IMPERIAL COLLEGE LONDON

DOCTORAL THESIS

Redox Stability and Ionic Conduction in Donor-Substituted $LaNbO_4$ under Hydrogen Environments

---

Author:
Kehan HUANG

Supervisor:
Prof Stephen J. SKINNER

A thesis submitted in fulfilment of the requirements
for the degree of Doctor of Philosophy

in the

Department of Materials

July 2025

Declaration of Authorship

I, Kehan HUANG, declare that this thesis and the work presented in it are my own. Information derived from other sources has been properly acknowledged and cited.

Kehan Huang
July 2025

The copyright of this thesis rests with the author. Unless otherwise indicated, its contents are licensed under a Creative Commons Attribution-Non Commercial 4.0 International Licence (CC BY-NC).

Under this licence, you may copy and redistribute the material in any medium or format. You may also create and distribute modified versions of the work. This is on the condition that: you credit the author and do not use it, or any derivative works, for a commercial purpose.

When reusing or sharing this work, ensure you make the licence terms clear to others by naming the licence and linking to the licence text. Where a work has been adapted, you should indicate that the work has been changed and describe those hanges.

Please seek permission from the copyright holder for uses of this work that are not included in this licence or permitted under UK Copyright Law.

Acknowledgements

The author conducted the majority parts of this work independently under the supervision of Prof. Stephen J. Skinner. However, the work cannot be completed without the help and suggestions of many others. The author would like to express a great appreciation for them and dedicate the first part of the acknowledgement to highlight their contributions to this work.

- **Prof Stephen J. Skinner** (Supervisor): Academic and financial support for this work. Nothing can be done without his supervision and support.
- **Dr Yidong Han** (Senior group member): Discussion, assisted in sample fabrications, and assisted in conducting TEM and XAS measurements.
- **Mr Chenyang Liao** (Group member): Assisted in conducting SIMS measurements and analysis.
- **Mr Yunfei Dang** (Collaborator in the Department of Chemistry, Imperial College London): Assisted in conducting ESR measurements and analysis.
- **Ms Luyang Wang** (Collaborator in the Department of Chemistry, University of Oslo): Conducted in *in-situ* TGA measurements and deuterium treatments.

(The author especially wishes that the above Mr. and Ms. can become Dr. in the near future!)

- **Dr Andrey V. Berenov** (Research facility manager of XRD): Assisted in conducting high-temperature XRD measurements.
- **Dr Gwilherm Kerherve** (Research facility manager of XPS): Assisted in conducting XPS measurements and fittings.
- **Dr Sarah Fearn** (Research facility manager of SIMS): Assisted in conducting SIMS measurements and analysis.
- **Dr Mahmoud Ardakani** (Research facility manager of Harvey Flowers electron microscopy suite): Assisted in conducting TEM measurements.
- **Dr Mark A. Isaacs** (Research Fellow at Harwell-XPS): Conducting benchtop XAS measurements.
- **Dr Donato Decarolis** and **Dr Diego Gianolio** (Beam line scientists of the B18 beam line at Diamond Light Source): Assisted in synchrotron XAS measurements and fittings.

- **Dr Matthew Krzystyniak** (Lead instrument scientist on the VESUVIO neutron spectrometer at the ISIS Neutron and Muon Source): Conducting NPD and NCS measurements and analysis; revising the corresponding contents of this work.

Beyond the academic area, I would like to express my great appreciation to my beloved family: my parents, my grandparents, and my little sister. I can achieve nothing without your support.

I also want to thank myself. That little country boy who had a seemingly unreachable dream to become a scientist finally made his tiny contribution to the scientific world. May this pure love and passion for science and nature accompany him throughout his life.

In the end, special thanks to **Ms Qian Cheng**. Sometimes life can be so bitter, but you make it taste like honey.

Abstract

Fergusonite-scheelite type $LaNbO_4$-based materials have presented promising potential for development as oxygen ionic or protonic conductors for solid oxide fuel cell (SOFC) and electrolysis cell (SOEC) applications. Among these material candidates, W- and Mo-substituted $LaNbO_4$ show acceptable oxygen ion conductivity and excellent chemical stability under atmospheric conditions. However, the properties and performances of these materials under reducing atmospheres remain unclear. Exploring W- and Mo-substituted $LaNbO_4$ under reducing atmospheres, especially under hydrogen conditions, is crucial for future SOFC/SOEC applications.

Therefore, this work aims to investigate the structural and redox stabilities of W- and Mo-substituted $LaNbO_4$ under hydrogen conditions and their corresponding changes in transport properties. The crystal structure of W-substituted $LaNbO_4$ is found to remain stable, while the structural symmetry of Mo-substituted $LaNbO_4$ is significantly reduced after hydrogen treatments. Multiple techniques have been used to attribute this difference in structural evolution to the redox stability of W cations and the instability of Mo cations under hydrogen conditions. X-ray absorption fine structure (XAFS) studies uncover the profound correlation between the crystal structure, the local coordination environment, and the oxidation state of cations. The neutron Compton scattering studies further provide a kinetic description of the elements.

The conductivity of both materials increases significantly under hydrogen conditions. The transport number of different charge species indicates the conductivity enhancement via distinct mechanisms. The increase in conductivity in W-substituted $LaNbO_4$ is attributed to proton incorporation and transport. Meanwhile, it has been confirmed that the increase in conductivity in Mo-substituted $LaNbO_4$ is partially due to electronic conduction. Attempts have been made to probe the hydrogen content in both materials directly, but these have proved inclusive. However, proton diffusion has been determined directly for the first time in W-substituted $LaNbO_4$ using isotope exchange and mass spectrometry techniques.

Contents

1 Research Background **1**

1.1 Energy crisis . . . 1

1.2 Hydrogen . . . 1

1.2.1 Hydrogen production . . . 2

1.2.2 Hydrogen storage and transport . . . 3

1.2.3 Hydrogen utilisation . . . 4

1.3 Fuel cell . . . 5

1.3.1 Solid oxide fuel cell (SOFC) . . . 6

1.3.2 Proton ceramic fuel cell (PCFC) . . . 7

2 Literature Review **9**

2.1 The proton-conducting mechanism in oxides . . . 9

2.1.1 Proton defect formation . . . 9

2.1.2 Proton solubility . . . 11

2.1.3 Proton transport . . . 12

2.1.4 Proton transport through grain boundary . . . 15

2.1.5 Hydride conductivity . . . 16

2.1.6 Summary . . . 17

2.2 Conventional proton-conducting oxides . . . 17

2.2.1 Perovskite type oxides . . . 17

2.2.2 Perovskite-related oxides . . . 19

2.2.3 Fluorite type oxides . . . 20

2.2.4 Fluorite-related oxides . . . 21

2.2.5 Summary . . . 22

2.3 Fergusonite-scheelite type oxides . . . 22

2.3.1 Hexavalent-substituted lanthanum orthoniobates . . . 27

2.3.2 Hexavalent-substituted lanthanum orthoniobates as ionic conductors . . . 29
2.3.3 Summary . . . 33

3 Methodology **34**
3.1 Preparation . . . 34
3.2 Density measurement . . . 35
3.3 X-ray related techniques . . . 36
3.3.1 X-ray powder diffraction . . . 37
3.3.2 X-ray powder diffraction refinement . . . 37
3.3.3 Experimental details of XRD . . . 39
3.3.4 X-ray photoelectron spectroscopy . . . 40
3.3.5 Experimental details of XPS . . . 41
3.3.6 X-ray absorption spectroscopy . . . 42
3.3.7 Experimental details of XAS . . . 45
3.4 Thermogravimetric analysis . . . 46
3.4.1 Experimental details of TGA . . . 46
3.5 Electron microscope techniques . . . 47
3.5.1 Experimental details of SEM & TEM . . . 48
3.6 Ultraviolet–visible spectroscopy . . . 49
3.6.1 Experimental details of UV-Vis-DRS . . . 50
3.7 Electron spin resonance . . . 51
3.7.1 Experimental details of ESR . . . 51
3.8 Secondary ion mass spectrometry . . . 52
3.8.1 Experimental details of SIMS . . . 54
3.9 Electrochemical techniques . . . 56
3.9.1 Electrochemical impedance spectroscopy . . . 56
3.9.2 Experimental details of EIS . . . 59
3.9.3 Hebb-Wagner polarisation method . . . 59
3.9.4 Experimental details of HW-method . . . 60
3.10 Neutron techniques . . . 61
3.10.1 Neutron scattering techniques . . . 61
3.10.2 Neutron Compton scattering . . . 62

3.10.3 Experimental details of NPD & NCS 64

4 Exploring the behaviours of W- and Mo-substituted $LaNbO_4$ under hydrogen atmospheres 66

4.1 Validation of synthesis 66
4.2 Structural and chemical studies 71
4.3 Redox study 75
4.3.1 XPS study 75
4.3.2 Spin resonance and thermogravimetric studies 80
4.3.3 XAS study 83
4.4 Coordination study 87
4.5 Conclusions 91

5 Electrochemical performances of W- and Mo-substituted $LaNbO_4$ under reducing conditions 92

5.1 Impedance study 92
5.2 Hebb-Wagner polarisation study 100
5.3 Conclusions 107

6 Proton incorporation study 108

6.1 Mass change study 108
6.2 Band structure study 110
6.3 Neutron study 113
6.4 Mass spectrometry study 117
6.5 Conclusions 122

7 Conclusions and future work 123

7.1 Conclusions 123
7.1.1 W-substituted $LaNbO_4$ 123
7.1.2 Mo-substituted $LaNbO_4$ 124
7.1.3 Overall conclusions 124
7.2 Future work 125
7.2.1 Proton transport 125
7.2.2 More electrochemical studies 125
7.2.3 Material modelling & simulation 126

Bibliography 127

A Publication record 147

B Copyright statement 148

List of Figures

1.1 Classification of hydrogen production routes by specific colours. Reproduced from [8] with permission under a Creative Commons Attribution-NonCommercial 3.0 Unported Licence. 2

1.2 Schematic diagram of the working principles in SOFC based on (a) oxide ion-conducting electrolyte and (b) proton-conducting electrolyte. Reproduced from [49] with permission from Royal Society of Chemistry. . 7

2.1 Helmholtz energy of proton transport of $BaCeO_3$ as a function of the O-O distance and the O-H$\cdots$O bond length. Reproduced from [74] with permission from Elsevier. 13

2.2 Proton migration pathways and their energy barriers in (a) Y-Zr-Y configuration and (b) Y-Zr-Zr configuration. Reproduced from [86] with permission from Springer Nature. 14

2.3 (a) Polycrystalline perovskite morphology, (b) enlarged grain boundary area, and (c) detailed schematic diagram. Reproduced from [94] with permission from American Chemical Society. 16

2.4 The proton-conducting mechanism in the ABO_3 perovskite structure. Reproduced from [48] with permission from Royal Society of Chemistry. 17

2.5 The structure of a $BaCeO_3$ cubic perovskite with Ba cation in A-site (green) at the centre surrounded by eight CeO_6 (yellow/red) octahedra. This figure is generated based on [112, 113] using VESTA software [116]. 18

2.6 Comparison of ionic conductivity of a series of solid oxide electrolytes. The solid line shows the protonic conductivity of the proton-conducting oxides, while the dashed line indicates the oxygen ionic conductivity of the comparative oxides. The arrow shows the optimising direction of solid oxide electrolytes, *i.e.*, higher ionic conductivity at lower working temperatures. Reproduced from [123] with permission from Springer Nature. 20

2.7 The total conductivity of nano-YSZ with different grain sizes measured under wet air (∼2.5% RH). Reproduced from [60, 98] with permission under a Creative Commons CC BY Licence. 21

2.8 Distorted NbO_6 octahedra (left) possesses four short Nb-O bonds similar to NbO_4 tetrahedra (middle) and two long Nb-O bonds, forming a corner-sharing configuration along *c* axis. Grey and green balls and dark green polyhedra denote O^{2-}, La^{3+} and NbO_4/NbO_6 polyhedra, respectively. Reproduced from [131] with permission from Elsevier. 23

2.9 Proton transport paths 1-4 in (a) t-$LaNbO_4$ and 1′-5′ in (b) m-$LaNbO_4$ (0 K). The green balls and green polyhedra denote La^{3+} cations and NbO_4 tetrahedra, respectively, while the black, white and grey balls denote the stable proton sites in both phases. The layer distance ratio between O1 and O2 in m-$LaNbO_4$ is 3:2. Reproduced from [133] with permission from Royal Society of Chemistry. 24

2.10 Linear thermal expansion of pristine $LaNbO_4$ and its corresponding monoclinic and tetragonal phase structures. Red and green balls and blue polyhedra denote O^{2-}, La^{3+} and NbO_4 tetrahedra, respectively. Reproduced from [48, 49, 135] with permission from Royal Society of Chemistry. 25

2.11 Phase diagrams of (a) LNW and (b) LNMo. Both phases were evaluated via *in-situ* X-ray powder diffraction (XRD) technique. Two temperature points extrapolated from dilatometry analysis are marked as "×" on the phase diagram of LNW. Reproduced from [151] with permission from American Chemical Society, and from [152] with permission under a Creative Commons Attribution-NonCommercial 3.0 Unported Licence. . 27

2.12 Schematic diagrams of (a) an ideal crystal lattice, (b) the (3+1)D-commensurately modulated structure along *a* axis, (c) the (3+1)D-incommensurately modulated structure along *a* axis, and their corresponding reciprocal lattice point patterns, respectively. Adapted from [47, 155] with permission from Imperial College London. 28

2.13 (a) XRD pattern of pristine $LaNbO_4$ and LNW08. The insert shows the satellite peaks marked as "asterisk" (*) from the modulated structure. (b) SAED pattern of LNW08 from [010] zone axis. The satellite reflections from the modulated structure are clearly observed. The estimated additional lattice vectors are $\boldsymbol{q_1} = 0.263\boldsymbol{a}^* + 0.106\boldsymbol{c}^*$ and $\boldsymbol{q_2} = 0.082\boldsymbol{a}^* + 0.243\boldsymbol{c}^*$. Reproduced from [138] with permission from Elsevier. 29

2.14 Total conductivity of LNW with a series of substitution levels (1%, 8%, 12% and 16%) under the ambient condition. The separate solid lines in LNW08 represent the activation energy difference between unmodulated and modulated scheelite structures, while such difference is diminished in LNW16. Reproduced from [161] with permission from Royal Society of Chemistry. 30

2.15 Schematic diagrams of different point defect conduction mechanisms. The solid blue balls represent the lattice oxygen ions, and the dashed balls represent the oxygen defects. (a) and (b) represent the typical vacancy and interstitial mechanisms, respectively. The oxygen vacancy and interstitial oxygen site are labelled as "v" and "i", respectively. (c) represents the interstitialcy mechanism, where the initial interstitial oxygen ion (1) occupies the lattice oxygen site (2), "kicking out" the lattice oxygen ion to become a new interstitial oxygen ion (2′). 31

2.16 Two short interstitial oxygen ion transport paths via interstitial mechanism along the *ab* plane, 1 and 3, and one long interstitial oxygen ion transport path via interstitialcy mechanism along the *c* axis, 4. The yellow and black balls represent the stable interstitial oxygen sites, while the blue balls represent the transition interstitial oxygen sites. For simplicity, the interstitialcy path 4 is represented by the blue lines. Path 2 is excluded due to its unfavourable energy barrier. Reproduced from [164] with permission from Royal Society of Chemistry. 32

3.1 Flow chart of the sample preparation procedure. 35

3.2 Schematic representative diagram of Bragg's law. 37

3.3 Flow diagram of Le Bail refinement process. 38

3.4 Schematic diagram of XPS measuring mechanism. 41

3.5 (a) Example Nb K-edge XAS spectrum, showing X-ray absorption near edge structure (XANES) region and extended X-ray absorption fine structure (EXAFS) region. The letter "n" represents the principal quantum number. (b) Example W L_3-edge XAS spectrum. 43

3.6 (a) The absorption process of an isolated atom. No EXAFS is raised. (b) The photoelectron is scattered by the electrons of the neighbouring atom, which interferes with the photoelectron at the absorbing atom, causing EXAFS. The photoelectron travels as a wave. Reproduced from [185] with permission under a Creative Commons Attribution-Share-Alike 3.0 Licence. 44

3.7 Schematic diagram of the electron-sample interaction volume. The typical information depth of each signal source was listed [192, 193]. The electron microscope techniques used in this work were highlighted in the bracket. 47
3.8 (a) Typical Tauc plot of an oxide; (b) Density of states $N(E)$ as a function of energy. Adapted from [204, 205] with permission from John Wiley and Sons. 50
3.9 Schematic diagram of the primary ion-sample interactions: (1) primary ion reflection, (2) primary ion implantation and (3) collision cascade [175, 212]. The positively charged primary ions are coloured in yellow, while the negatively charged secondary ions are coloured in blue. 53
3.10 Schematic diagram of the sample preparation required to obtain diffusion profiles from the line scan method [215]. 53
3.11 Schematic Nyquist plot of a typical EIS spectrum of a solid oxide electrolyte with metal electrodes and its corresponding equivalent circuit model [219]. The notation "gb" is short for grain boundary. 56
3.12 Schematic diagram of the bricklayer model. The notation "gb" is short for grain boundary. Adapted from [219] with permission from John Wiley and Sons. 57
3.13 Schematic configuration of the Hebb-Wagner polarisation cell used in this work. 60
3.14 Schematic comparison of the relative total cross sections of various elements for X-rays and neutrons. Reproduced from [230] with permission from Elsevier. 61
3.15 Schematic diagram of the kinematics of the neutron Compton scattering process [244]. 62
3.16 Schematic diagram of VESUVIO spectrometer. The foil changers are placed in between the sample and sensors to fix the value of the final energy of the neutrons in the so-called inverted-geometry configuration. Reproduced from [235] with permission from American Physical Society. 65

4.1 XRD patterns of LNW16 and LNMo16, together with monoclinic and tetragonal phases of pristine $LaNbO_4$ [132, 173]. The reflections from the modulated structure in LNW16 and LNMo16 are marked by the ∇ symbol. 67

4.2 Le Bail refinement results of (a) LNW16As and (b) LNMo16As. The small reflections from the modulated structure are excluded from the refinement, as only the unit cell is refined without considering the supercell. The extracted lattice parameters were summarised in Table 4.2. Adapted from [250] with permission under a Creative Commons Attribution-NonCommercial 3.0 Unported Licence. 68

4.3 *In-situ* high-temperature and RT XRD patterns of (a) LNW16As and (b) LNMo16As, respectively. The phase transition temperature of LNW16As and LNMo16As are around 200 and 300 °C, respectively. The patterns shift to a lower 2θ angle with increasing temperature due to thermal expansion of the lattice. The tilted patterns are due to the use of an auto-slit, which probes a larger sample volume at a higher 2θ angle. 69

4.4 (a) TEM image and (b) SAED pattern of LNW16As along the [010] zone axis; (c) TEM image and (d) SAED pattern of LNMo16As along the [110] zone axis. The calculated d-spacing is 1.75 nm for LNW16As and 1.90 nm for LNMo16As, respectively. Vectors, q_i, label the satellite reflections from modulated structures. Adapted from [250] with permission under a Creative Commons Attribution-NonCommercial 3.0 Unported Licence. 70

4.5 SEI and corresponding EDS mapping images of (a) LNW16As and (b) LNMo16As. The spectrum line and scale bar information on the bottom were relabelled for readability. 71

4.6 XRD patterns of LNW16As, LNW16H2 and elongating the hydrogen treatment time to 8, 16 and 24 hours, respectively. The 24-hour hydrogen-treated sample was then re-oxidised at 800 °C under ambient conditions for 4 hours and was labelled as "LNW16H2-Re". The modulated reflections are marked by the ∇ symbol. 72

4.7 XRD patterns of LNMo16As, LNMo16H2 and elongating the hydrogen treatment time to 8, 16 and 24 hours, respectively. The 24-hour hydrogen-treated sample was then re-oxidised at 800 °C under ambient conditions for 4 hours and was labelled as "LNMo16H2-Re". The modulated reflections are marked by the ∇ symbol. 73

4.8 Le Bail refinement results of (a) LNW16H2 and (b) LNMo16H2. The small reflections from the modulated structure are excluded from the refinement, as only the unit cell is refined without considering the supercell. The extracted lattice parameters were summarised in Table 4.2. Adapted from [250] with permission under a Creative Commons Attribution-NonCommercial 3.0 Unported Licence. 74

4.9 SEI and corresponding EDS mapping images of (a) LNW16H2 and (b) LNMo16H2. The spectrum line and scale bar information on the bottom were relabelled for readability. 74

4.10 Normalized XPS spectra of (a) La 3*d*, (b) Nb 3*d*; (c) fitted XPS spectra of W 4*f* in (top) LNW16As and (bottom) LNW16H2; (d) fitted XPS spectra of O 1*s* in (top) LNW16As and (bottom) LNW16H2. The "LF" in W 4*f* spectra represents the loss feature of W^{6+}. Adapted from [250] with permission under a Creative Commons Attribution-NonCommercial 3.0 Unported Licence. 77

4.11 Normalized XPS spectra of (a) La 3*d*, (b) Nb 3*d*; (c) fitted XPS spectra of Mo 3*d* in (top) LNMo16As and (bottom) LNMo16H2; (d) fitted XPS spectra of O 1*s* in (top) LNMo16As and (bottom) LNMo16H2. $\delta i+$ represents the valence state of Mo cations between 0 and +4. Adapted from [250] with permission under a Creative Commons Attribution-NonCommercial 3.0 Unported Licence. 78

4.12 Normalized XPS iteration spectra of (a) W 4*f* and (b) O 1*s* in LNW16As, and (c) Mo 3*d* and (d) O 1*s* in LNMo16As. The red arrow highlights the change tendency in spectra as a function of iteration time. Adapted from [250] with permission under a Creative Commons Attribution-NonCommercial 3.0 Unported Licence. 79

4.13 ESR spectra (100 K) of (a) LNW16 and (b) LNMo16; (c) Comparison of LNW16As and LNMo16As; (d) ESR spectra (100 K) of LNW16As after the heat treatment at Ar conditions (LNW16-Ar). The short dash lines in each spectrum from left to right indicate the positions of the g-factor at 2.061, 2.003, 1.960 and 1.875, respectively. 81

4.14 TGA results of (a) LNW16 and (b) LNMo16 collected from RT to 800 °C at flowing air conditions. The subtle mass difference in (a) falls within the instrumental uncertainty. The TGA result of pure indium metal reference is presented in the inset of (a), clearly indicating the buoyancy effect at the initial heating stage. Adapted from [250] with permission under a Creative Commons Attribution-NonCommercial 3.0 Unported Licence. 82

4.15 Normalized synchrotron XAFS spectra of (a) the Nb K-edge and (b) the W L_3-edge collected at ambient conditions. The vertical dashed line indicates the position of e_0 at 19003.8 eV in the Nb K-edge spectra and the white line at 10212.0 eV in W L_3-edge spectra, respectively. Adapted from [250] with permission under a Creative Commons Attribution-NonCommercial 3.0 Unported Licence. 84

4.16 Normalized synchrotron XAFS spectra of (a) the Nb K-edge and (b) the Mo K-edge collected at ambient conditions. The vertical dashed line indicates the position of e_0 at 19003.8 eV in the Nb K-edge spectra and e_0 at 20015.0 eV (orange) and 20017.0 eV (blue) in the Mo K-edge spectra, respectively. 85

4.17 Comparison of the Nb K-edge XAFS spectra. The vertical dashed line indicates the position of e_0 at 19003.8 eV. The pre-edge and edge features are highlighted by dotted boxes. 86

4.18 The EXAFS fitting results of the Nb K-edge in (a) LNW16As and (c) LNW16H2; the corresponding magnitude of Fourier-transform of (b) LNW16As and (d) LNW16H2. The vertical dashed line in each figure indicates the initial boundary of the fitting. 87

4.19 The EXAFS fitting results of the W L_3-edge in (a) LNW16As and (c) LNW16H2; the corresponding magnitude of Fourier-transform of (b) LNW16As and (d) LNW16H2. The vertical dashed line in each figure indicates the initial boundary of the fitting. 88

4.20 The EXAFS fitting results of the Nb K-edge in (a) LNMo16As and (c) LNMo16H2; the corresponding magnitude of Fourier-transform of (b) LNMo16As and (d) LNMo16H2. The vertical dashed line in each figure indicates the initial boundary of the fitting. 89

4.21 The EXAFS fitting results of the Mo K-edge in (a) LNMo16As and (c) LNMo16H2; the corresponding magnitude of Fourier-transform of (b) LNMo16As and (d) LNMo16H2. The vertical dashed line in each figure indicates the initial boundary of the fitting. 89

5.1 Example Nyquist plot of LNW16 measured at (a) 618 °C under dry air and (c) its corresponding fitting result from the KK test; example Nyquist plot of LNW16 measured at (b) 813 °C under dry 5% H_2 and (d) its corresponding fitting result from the KK test. The insert in (a) shows the corresponding equivalent circuit model. The inductance part in (b) was truncated to $-Z''\approx$-1 Ω/cm^2 figure readability and was excluded from the KK test in (d). 93

5.2 Total conductivity of LNW16 measured under different atmospheres. Adapted from [250] with permission under a Creative Commons Attribution-NonCommercial 3.0 Unported Licence. 94

5.3 Total conductivity of LNMo16 measured under different atmospheres. Adapted from [250] with permission under a Creative Commons Attribution-NonCommercial 3.0 Unported Licence. 95

5.4 Total conductivity of (a) LNW16 and (b) LNMo16 as a function of oxygen partial pressure. The scatters represent the conductivity measured in this work. The dashed lines correspond to the typical electronic enhanced conductivity under reducing conditions proposed by Canu *et al.* [153]. 97

5.5 Example Nyquist plots of (a) LNW16 and (b) LNMo16 measured at 570 °C under 5% H_2 conditions. The inductance parts in (b) were truncated to $-Z''\approx$-1 Ω/cm^2 for figure readability. 99

5.6 Example current relaxation curves of the Hebb-Wagner polarisation cell measured at different temperatures under dry 5% H_2 conditions. The applied voltage is 0.30 V. 101

5.7 Partial electronic conductivity of LNW16 measured by Hebb-Wagner polarisation method. The total conductivity of LNW16 under air and 5% H_2 conditions estimated from EIS measurements are replotted as dashed lines for direct comparison. The calculated activation energies of electrons are 1.09 eV (R-squared = 0.99) and 1.06 eV (R-squared = 0.99) for LNW16 measured under dry and wet 5% H_2 conditions, respectively. . . 102

5.8 Partial electronic conductivity of LNMo16 measured by Hebb-Wagner polarisation method. The total conductivity of LNMo16 under dry air and dry 5% H_2 conditions estimated from EIS measurements are replotted as dashed lines for direct comparison. The calculated activation energy of electrons is 0.44 eV (R-squared = 0.99). 103

5.9 (a) Extracted transport number of electrons in LNW16 under dry 5% H_2 conditions from Hebb-Wagner polarisation method. (b) Estimated transport number of protons in LNW16 under dry 5% H_2 conditions based on the assumption that the oxygen ionic conductivity under dry 5% H_2 conditions is the same as under dry air conditions. 104

5.10 (a) Extracted transport number of electrons in LNW16 under wet 5% H_2 conditions from Hebb-Wagner polarisation method. (b) Estimated transport number of protons in LNW16 under wet 5% H_2 conditions based on the assumption that the oxygen ionic conductivity under wet 5% H_2 conditions is the same as under wet air conditions. 105

5.11 (a) Extracted transport number of electrons in LNMo16 under dry 5% H_2 conditions from Hebb-Wagner polarisation method. (b) Estimated lower and upper limits of transport number of protons in LNMo16 under dry 5% H_2 conditions based on different assumptions. 106

6.1 *In-situ* TGA results of (a) LNW16As and (b) LNMo16As collected at 800 °C. The subtle mass change in (a) fails in the instrumental uncertainty and is likely due to the difference in buoyancy effect between different atmospheres. 109

6.2 Direct (allowed) band gap Tauc plots of (a) LNW16 and (c) LNMo16; XPS-VBM spectra of (b) LNW16 and (d) LNMo16. The dashed lines indicate the values of extrapolated band gaps or VBM. The red dashed circle in (d) highlights the pre-edge feature of LNMo16. 110

6.3 Schematic diagrams of estimated band structures of (a) LNW16 and (b) LNMo16. The inserts on top are the visual appearances of the pellet samples. 112

6.4 NPD data of (a) LNW16 and (b) LNMo16 collected on VESUVIO spectrometer at RT. 113

6.5 Backward and forward NCS spectra of the reduced (raw), the total fit and the elementary fitted spectra in (a) & (c) LNW16As and (b) & (d) LNW16H2 collected on VESUVIO spectrometer at RT. The peaks highlighted by red-shaded rectangular areas originate from the neutron-gamma resonances of tungsten and are excluded from the fittings [240]. 114

6.6 Backward and forward NCS spectra of the reduced (raw), the total fit and the elementary fitted spectra in (a) & (c) LNMo16As and (b) & (d) LNMo16H2 collected on VESUVIO spectrometer at RT. 116

6.7 (a) Depth profile for determining the correlation between sputtering time-depth in LNW16As. The spikes are due to the unstable beam current. (b) The crater depth was measured by coherence scanning interferometry from the slice indicated by the red arrow. 118
6.8 Depth profile of LNW16 samples. The spikes are due to the unstable beam current, which also causes the large fluctuation signals in LNW16D2-6h-Pt, especially for O^-. The large fluctuation of D^- is due to its relatively low ion counts. 119
6.9 2D ion images of $D^-/(H^- + D^-)$ in cross-sectional (a) LNW16D2-6h-Pt and (b) LNW16D2-6h, respectively. The corresponding normalized diffusion profiles of (c) LNW16D2-6h-Pt and (d) LNW16D2-6h, respectively. The red dashed line in (a) and (b) indicates the exchanged surface position before the cross-section. The brightness of (a) and (b) was increased by 50% for figure readability. 121
6.10 Fitted diffusion profile of LNW16D2-6h-Pt. The green dashed line indicates $C(x) = C_{bg}$. 121

List of Tables

1.1 Summary of fuel cell types. Adapted from [36–38] with permission from Elsevier. 6

2.1 Summary of single substituted $LaNbO_4$ reported up to now. Complicated co-substitution or multi-substitution cases are omitted. σ_e and σ_p denote electronic and protonic conductivity, respectively. Asterisk (*) marks dopants without available solubility data, and the reported highest substitution level was listed instead. 26

2.2 The activation energy of LNW with a series of substitution levels (1%, 8%, 12% and 16%). The activation energy reduces at around 600 °C. Reproduced from [47] with permission from Imperial College London. . 31

3.1 Summary of typical X-ray related techniques. Asterisk (*) highlights the techniques used in this work. 36

3.2 Capacitance value ranges and their possible corresponding response. Adapted from [219] with permission from John Wiley and Sons. 58

4.1 Normalized atomic ratios of B-site cations in LNW16As and LNMo16As, respectively. 69

4.2 Refined lattice parameters of all four samples from Le Bail refinements. Adapted from [250] with permission under a Creative Commons Attribution-NonCommercial 3.0 Unported Licence. 73

4.3 Normalized atomic ratios of W cations with different valence states and different oxygen species in LNW16As and LNW16H2 extracted from XPS fittings. The binding energy of each fitted W $4f_{7/2}$ and O 1*s* peak after C 1*s* calibration is listed in the brackets. Adapted from [250] with permission under a Creative Commons Attribution-NonCommercial 3.0 Unported Licence. 76

4.4 Normalized atomic ratios of Mo cations with different valence states and different oxygen species in LNMo16As and LNMo16H2 extracted from XPS fittings. $\delta i+$ represents the valence state of Mo cations between 0 and +4. The binding energy of each fitted Mo $3d_{5/2}$ and O $1s$ peak after C $1s$ calibration is listed in the brackets. Adapted from [250] with permission under a Creative Commons Attribution-NonCommercial 3.0 Unported Licence. 76

4.5 Extracted structural parameters of each sample from EXAFS fittings. N,R, and σ^2 represent the averaged coordination number, the bond length and the mean-square-displacement in the radial distance space, respectively. 90

5.1 Calculated activation energy of LNW16 measured under different atmospheres. T_c is ~570 °C. Adapted from [250] with permission under a Creative Commons Attribution-NonCommercial 3.0 Unported Licence. . 96

5.2 Calculated activation energy of LNMo16 measured under different atmospheres. Adapted from [250] with permission under a Creative Commons Attribution-NonCommercial 3.0 Unported Licence. 96

6.1 NMD widths, σ_M, together with their standard deviation of LNW16 extracted from NCS backward scattering fittings. The force constants, k_M, were deduced from the NMD widths using Equation 6.1. The standard deviation of k_M is estimated using the Monte Carlo error propagation. The NMD width of Al was pre-determined and removed from the table. 115

6.2 NMD widths, σ_M, together with their standard deviation of LNMo16 extracted from NCS backward scattering fittings. The force constants, k_M, were deduced from the NMD widths using Equation 6.1. The standard deviation of k_M is estimated using the Monte Carlo error propagation. The NMD width of Al was pre-determined and removed from the table. 117

6.3 Normalized isotopic fractions of hydrogen in each sample. The natural abundance of deuterium is 0.00015. The large error values are due to the low signal counts. 120

List of Abbreviations

AFC	Alkaline Fuel Cell
APT	Atom Probe Tomography
ASR	Area Specific Resistance
BCY	Yttrium-substituted Barium Cerate
BSE	Backscattered Electron
BZY	Yttrium-substituted Barium Zirconate
CB	Conduction Band
CBM	Conduction Band Minimum
CPE	Constant Phase Element
CSI	Coherence Scanning Interferometry
DFT	Density Functional Theory
DRS	Diffuse Reflectance Spectroscopy
EDS	Energy Dispersive X-ray Spectroscopy
EEC	Electrochemical Equivalent Circuit
EIS	Electrochemical Impedance Spectroscopy
EMF	Electromotive Force
EPR	Electron Paramagnetic Resonance
ESR	Electron Spin Resonance
EXAFS	Extended X-ray Absorption Fine Structure
FSE	Final State Effect
GDC	Gadolinium-Doped Ceria
GOF	Goodness-Of-Fitting
GPA	Gas Phase Analysis
HOR	Hydrogen Oxidation Reaction
HW	Hebb-Wagner Polarization Method
IB	Intermediate Band
KK	Kramers-Kronig Relation
LMIG	Liquid Metal Ion Gun
LNMo	Molybdenum(Mo)-substituted Lanthanum Orthoniobate
LNW	Tungsten(W)-substituted Lanthanum Orthoniobate

MCFC	Molten Carbonate Fuel Cell
MD	Molecular Dynamics
NCS	Neutron Compton Scattering
NMD	Nuclear Momentum Distribution
NMR	Nuclear Magnetic Resonance
NPD	Neutron Powder Diffraction
OCV	Open Circuit Voltage
ORR	Oxygen Reduction Reaction
PAFC	Phosphoric Acid Fuel Cell
PCFC	Proton Ceramic Fuel Cell
PEMFC	Proton-Exchange Membrane Fuel Cell
PTFE	Polytetrafluoroethylene
QENS	Quasi-Elastic Neutron Scattering
RH	Relative Humidity
RT	Room Temperature (298.15 K)
SAED	Selected Area Electron Diffraction
SEI	Secondary Electron Imaging
SEM	Scanning Electron Microscopy
SIMS	Secondary Ion Mass Spectrometry
SMR	Steam Methane Reforming
SOEC	Solid Oxide Electrolysis Cell
SOFC	Solid Oxide Fuel Cell
SS	Spot Size
TEM	Transmission Electron Microscopy
TGA	Thermogravimetric Analysis
TOF	Time-Of-Flight
UV-Vis	Ultraviolet-Visible Spectroscopy
VB	Valence Band
VBM	Valence Band Maximum
WD	Working Distance
WGSR	Water-Gas Shift Reaction
XANES	X-ray Absorption Near Edge Structure
XAFS	X-ray Absorption Fine Structure
XAS	X-ray Absorption Spectroscopy
XPS	X-ray Photoelectron Spectroscopy
XRD	X-ray Powder Diffraction
XRF	X-ray Fluorescence Spectroscopy
YSZ	Yttria-Stabilised Zirconate

Chapter 1

Research Background

1.1 Energy crisis

When the steam engine roared for the first time in the 1760s, human society consumed energy greedily and endlessly. This year, the entire world is expected to consume more than 600 EJ (1 EJ = 1×10^{18} J) to power cities, industries and homes, while 80% of the energy comes from fossil fuels, such as coal, oil, and natural gas [1].

However, every gift has its price. Last year, global CO_2 emissions were greater than 36 Gt (1 Gt = 1×10^{9} t), contributing to global warming and accelerating climate change [1]. Research shows that by 2030, more than 250,000 additional deaths are expected, with countless economic losses due to climate change [2].

In 2015, the Paris agreement was reached to limit global temperature rises to below 1.5 °C. Global CO_2 emissions must decrease by 43% by 2030 to achieve this ambitious target [3]. This emission reduction means that our society must dramatically reduce fossil fuel use while keeping the economy prosperous. Therefore, the development of green energy sources is crucial for our net-zero emission future.

In recent years, the prosperity of the battery industry offers a promising alternative to fossil fuels, especially in the transport sector. The market share of electric vehicles has increased from negligible to more than 13% worldwide in 2022 [4]. However, the booming market was dimmed by the heavy weight, degradation, and recycling challenges of batteries [5]. Therefore, while researchers are striving to develop batteries, other renewable energy sources continue to be sought.

1.2 Hydrogen

Hydrogen is superior among candidates for green energy sources due to its unique nature. First, hydrogen is the most abundant element in the universe. Hydrogen can be easily extracted from water via electrolysis, although not in a cost-efficient way

[6]. Second, water is the only by-product of using hydrogen, meaning that carbon is excluded from the hydrogen-using scenario. Third, hydrogen is not only a potential energy source, but also an essential raw material for fertiliser production and other processes [7]. Therefore, hydrogen-related research is currently a hot topic in academia and industry.

1.2.1 Hydrogen production

Hydrogen can be produced through various routes. These production routes are classified according to sources and processes (see Figure 1.1) [8]. Currently, most of the hydrogen is produced industrially by steam methane reforming (SMR, Equation 1.1) [9, 10]. The CO produced can also react with steam via the water-gas shift reaction (WGSR, Equation 1.2).

$$CH_{4(g)} + H_2O_{(g)} \rightarrow CO_{(g)} + 3H_{2(g)} \tag{1.1}$$

$$CO_{(g)} + H_2O_{(g)} \rightarrow CO_{2(g)} + H_{2(g)} \tag{1.2}$$

The produced hydrogen is called "grey" hydrogen, as the SMR route uses natural gas as a source and releases CO_2 as waste. Therefore, an alternative way of producing zero-carbon hydrogen, "green" hydrogen, is urgently needed.

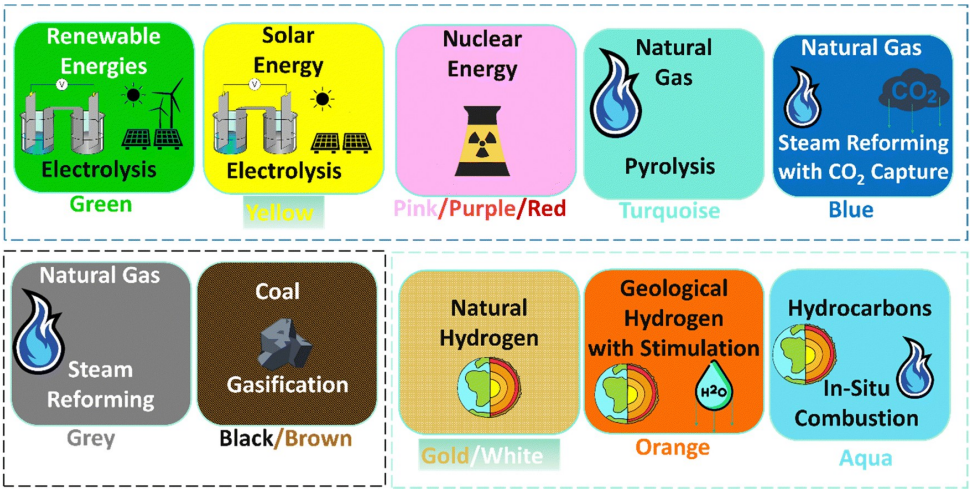


FIGURE 1.1: Classification of hydrogen production routes by specific colours. Reproduced from [8] with permission under a Creative Commons Attribution-NonCommercial 3.0 Unported Licence.

The easiest and most common way to produce "green" hydrogen is through water electrolysis. The mechanism behind this is simple. The input energy creates a minimum potential difference of 1.23 V at room temperature (RT) to split the water into hydrogen and oxygen (Equation 1.3) [6].

$$H_2O_{(l)} \rightarrow H_{2(g)} + \frac{1}{2}O_{2(g)} \tag{1.3}$$

The cathode forms hydrogen during this process, while the anode forms oxygen. A membrane electrolyser is placed between the two electrodes to split them.

Low-temperature electrolysers, including proton exchange membrane and alkaline water electrolysers, have been commercialised for decades. However, the proton exchange membrane electrolyser relies on costly noble metals, especially platinum, as catalysts, which hinders its broad application [11]. In contrast, the alkaline water electrolyser employs nickel-based catalysts. However, it suffers from the lower current density, slow response, and gas crossover issue due to its liquid alkaline electrolyte [12]. Another main drawback of low-temperature electrolysers is the overpotential originating from the reaction rate difference between cathodic and anodic reactions. The sluggish kinetics of the anodic reaction result in an input potential higher than 1.23 V to realise the water splitting [13].

In recent years, the solid oxide electrolyser cell (SOEC), which operates at high temperatures (400-900 °C), has received increasing attention. Unlike the proton exchange membrane electrolyser, with the aid of heat, noble metals can be replaced with earth-abundant materials, such as nickel [14]. Besides, heat accelerates the reaction rate, reducing the overpotential. However, heat also causes severe degradation issues for the SOEC's long-term operation [15]. Another main advantage of SOEC compared to the low-temperature electrolyser is its reversibility [16]. In SOEC mode, the cell consumes water and power to produce hydrogen and oxygen. In reverse mode, the cell consumes hydrogen and oxygen to generate power with by-products of water. This mode will be discussed in detail later.

In summary, SOEC offers a promising green hydrogen production route. Efforts have been made to lower the operating temperature to ensure the commercialisation of SOEC.

1.2.2 Hydrogen storage and transport

A typical lifetime scenario for hydrogen and any other energy source, such as gasoline and diesel, involves producing it in a factory, transporting it by pipeline or tank trucks, and using it in homes or passenger vehicles. From this example, one can easily find spatial and temporal separations between the production and usage ends, where the storage and transport become crucial. As the lightest element, hydrogen's gravimetric energy density of 120 MJ/kg is about three times higher than diesel or gasoline [17].

However, the extremely low density (0.089 kg/m^3) means its volumetric energy density of 10.7 MJ/m^3 is extremely low [18]. The highly flammable nature of hydrogen raises further safety concerns in the storage and transport of hydrogen.

Conventionally, hydrogen is stored in compressed gas or liquid form. Although storage in liquid form gives a high hydrogen density of 70 kg/m^3, the low storage temperature of -253 °C makes it practically unfavourable [19, 20]. However, the compressed gas form compromises the hydrogen density, but improves commercial availability. The highest hydrogen density was recorded at 23.3 kg/m^3 with a maximum pressure of 350 bar [21]. However, failure of such a high-pressure tank can be catastrophic.

To avoid the safety issues caused by direct hydrogen storage, developing hydrogen-containing chemical energy carriers such as methane, methanol and ammonia is an attractive option. Ammonia is the only carbon-free carrier among these energy carriers [22]. However, the main challenge in this area is the production of green ammonia because more than 99% ammonia is produced from the steam reforming process [23].

In addition to gas storage, hydrogen storage materials such as metal hydrides are developing rapidly. Taking the most developed material, $NaAlH_4$, as an example, hydrogen reacts with metal atoms to form hydrogen bonds (Al-H bonds) for storage [24]. Then, the reaction is reversed to break bonds and release hydrogen for use. However, the weight and cost efficiency still await further improvement [21]. It is worth mentioning that hydrogen storage in metal-organic frameworks recently ignited new research interest, but it is still in the early stages [25, 26].

1.2.3 Hydrogen utilisation

There are two distinct ways to use hydrogen. The first is to burn it in an internal combustion engine like a regular diesel or gasoline. In the late 20^{th} century, BMW and Mazda made prototype vehicles powered by hydrogen-fuelled internal combustion engines [27]. However, the combustion behaviour of hydrogen is distinct from that of diesel or gasoline, and this has yet to be fully understood [28]. This unique nature results in a dedicated engine design. In addition, the highly flammable nature of hydrogen means that direct combustion of hydrogen is always a safety concern.

The second is the use of hydrogen electrochemically through a fuel cell. Instead of combusting hydrogen, the fuel cell converts the chemical energy of hydrogen directly into electrical energy (Equation 1.4). The fuel cell has an energy efficiency of up to 85% higher than a diesel-based combustion engine (approximately 35%) [29]. In addition, the hydrogen fuel cell is a green energy conversion device since the only by-product is water. Moreover, the fuel cell is a static device, which means that its operation does

not produce noise and vibration [30]. However, the low power density and durability issues hinder the further development of fuel cell techniques [31].

$$H_{2(g)} + \frac{1}{2}O_{2(g)} \rightarrow H_2O_{(g)} \tag{1.4}$$

Apart from using hydrogen as an energy source, hydrogen is also an important industrial material in ammonia production and other industries [7]. Nevertheless, this is beyond the scope of this work.

1.3 Fuel cell

The fuel cell is not a brand-new invention. It was invented nearly two centuries ago [32]. The fuel cell was first used in space programmes, powering satellites and spacecraft [33]. The fuel cell was then commercialised as an auxiliary power unit or to power vehicles [34].

A fuel cell typically consists of three parts: anode, cathode, and electrolyte. The anode side experiences a hydrogen oxidation reaction (HOR), while the cathode side experiences an oxygen reduction reaction (ORR). Then, the ionic charge carriers, oxide ions, or protons, are transported through the electrolyte, while the electrons flow through the external load. Taking a fuel cell that conducts oxide ions as an example, these reactions can be written as Equation 1.5 and Equation 1.6:

$$HOR : H_{2(g)} + O^{2-} \rightarrow H_2O_{(g)} + 2e^- \tag{1.5}$$

$$ORR : \frac{1}{2}O_{2(g)} + 2e^- \rightarrow O^{2-} \tag{1.6}$$

The type of its electrolyte catalogues the fuel cell (see Table 1.1), such as the proton-exchange membrane fuel cell (also known as the polymer electrolyte membrane fuel cell, PEMFC), the phosphoric acid fuel cell (PAFC), the alkaline fuel cell (AFC), the molten carbonate fuel cell (MCFC), and the solid oxide fuel cell (SOFC). PEMFC is one of the primary research focuses. Like the proton-exchange membrane electrolyser, PEMFC requires noble metals, such as platinum, as catalysts. Worse, these noble metal catalysts are vulnerable to a small amount of impurities or contaminants in the hydrogen gas, especially CO [35]. This poisoning results in a significant PEMFC performance degradation. Another primary research focus, which is also the focus of this work, is the SOFC.

TABLE 1.1: Summary of fuel cell types. Adapted from [36–38] with permission from Elsevier.

	AFC	PEMFC	PAFC	MCFC	SOFC
Typical electrolyte	NaOH	Nafion	H_3PO_4	Na_2CO_3-Li_2CO_3	ZrO_2-Y_2O_3
Main charge carrier	OH^-	H^+	H^+	CO_3^{2-}	O^{2-}
Operating temperature	<70 °C	<80 °C	~200 °C	~650 °C	800-1000 °C
Fuel type	H_2	H_2	H_2	H_2, CO, CH_4	H_2, CO, CH_4
Energy efficiency	>60%	40%	40%	45%	65%

1.3.1 Solid oxide fuel cell (SOFC)

Table 1.1 presents the differences between PEMFC and SOFC. Compared with PEMFC, the main advantages of SOFC are similar to those of SOEC: noble metal catalysts can be replaced with earth-abundant materials. In addition, the energy efficiency of SOFC is higher than that of PEMFC.

However, given their solid oxide-based electrolyte, SOFCs require a high operating temperature, usually above 800 °C, to guarantee sufficient oxygen ionic conductivity [37, 38]. Although this high operating temperature expands the fuel viability from hydrogen to CO, CH_4 and so on, it presents a severe challenge in selecting the right materials [39]. In addition to high electrochemical performances, the materials must have a high thermal stability in long-term high-temperature operating cycles [15, 40–45]. The high temperature also means that conventional stainless steel cannot be used as a supporting material, increasing the fabrication cost [36]. Therefore, reducing the operating temperature of SOFC to the intermediate temperature range (400-700 °C) is intuitively reasonable. To achieve this intermediate operating temperature range, SOFC electrolyte materials that meet the following criteria are highly demanded [46, 47]:

1. The area specific resistance (ASR) is less than 0.15 Ω/cm^2.
2. The ionic conductivity is greater than 0.01 S/cm.

3. The operating temperature range is about 400-700 °C.
4. The thickness is less than 15 μm with an acceptable mechanical stability.
5. Performance degradation (*e.g.*, open circuit voltage, OCV) is less than 0.1% over 1000 h.

Note that despite these criteria being established for several decades, current SOFC electrolyte materials still struggle to simultaneously meet all requirements.

1.3.2 Proton ceramic fuel cell (PCFC)

In recent decades, a new type of SOFC electrolyte material that conducts protons instead of oxygen ions has become a hot research topic. This type of material is called the proton-conducting oxide, while the SOFC based on it is called the proton ceramic fuel cell (PCFC). Given the gravimetrically and volumetrically minor nature of a proton, the mobility of a proton is significantly higher than that of an oxygen ion at the same temperature [48]. This relatively high mobility has led to the development of PCFCs that operate at intermediate temperature.

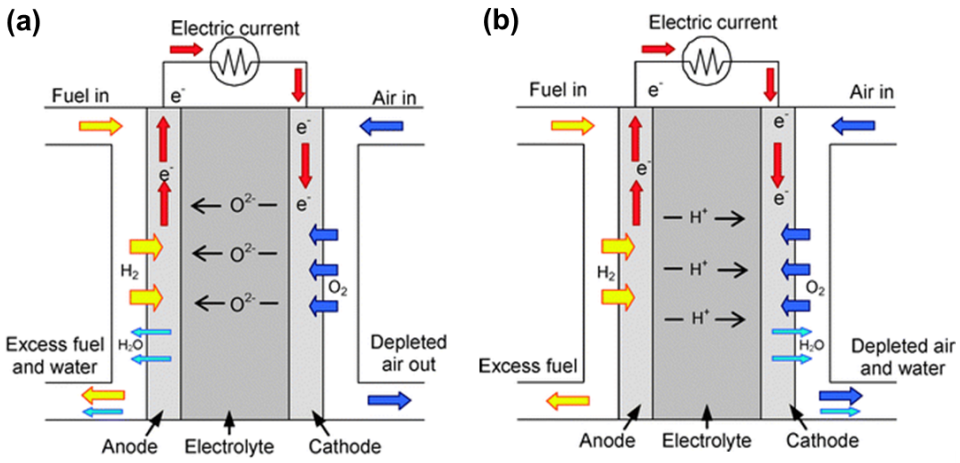


FIGURE 1.2: Schematic diagram of the working principles in SOFC based on (a) oxide ion-conducting electrolyte and (b) proton-conducting electrolyte. Reproduced from [49] with permission from Royal Society of Chemistry.

Figure 1.2 shows the differences in the working principles between conventional SOFC based on oxide-ion-conducting electrolytes and PCFC based on proton-conducting electrolytes [49]. Figure 1.2 also presents another main advantage of PCFC compared to SOFC: The water by-product is produced on the cathode side instead of the anode

side. This change reduces the complexity of the fuel cell system by preventing the hydrogen dilution issue [50].

However, the journey towards commercialising the PCFC is long and arduous. Typical proton-conducting oxides, such as barium zirconate substituted with yttrium (BZY) and barium cerate substituted with yttrium (BCY) are vulnerable to subtle CO_2 impurities in the air [51]. Their parasitic electronic conductivity deteriorates performance [52]. In addition, the lack of proper manufacturing methods prevents PCFCs from being mass-produced [53].

In recent years, another type of proton-conducting oxide, $LaNbO_4$-based materials, has shown good resistance to CO_2 and negligible electronic conductivity. In contrast, its protonic conductivity is orders of magnitude lower than that of BZY or BCY [54–56]. After the first exciting serial publications, the attraction for this type of material has largely declined. However, the potential of these $LaNbO_4$-based materials is worth further investigation. Therefore, this work will explore the stability and protonic conductivity in $LaNbO_4$-based materials, especially in hydrogen atmospheres.

Chapter 2

Literature Review

2.1 The proton-conducting mechanism in oxides

2.1.1 Proton defect formation

Although the proton is known to be an ubiquitous "impurity" in semiconductors, it is primarily regarded as an external atom in oxides [57, 58]. Therefore, protons must be introduced from the adjacent environment before protonic conductivity can be realised. Moreover, a proton cannot occupy a lattice site in most oxides but is covalently bonded to oxygen ions, which means that the proton is generally introduced as a hydroxide defect [48, 59, 60]. The most common and essential reaction for the introduction of protons into oxides is the interaction with water vapour or steam. This reaction is called hydration and can be written in Kröger–Vink notation as Equation 2.1 [61].

$$\begin{aligned} H_2O_{(g)} + V_O^{\cdot\cdot} + O_O^{\times} &\rightarrow 2OH_O^{\cdot} \\ K_W = [OH_O^{\cdot}]^2[V_O^{\cdot\cdot}]^{-1}(pH_2O)^{-1} \end{aligned} \tag{2.1}$$

Where K_W is the equilibrium constant of the hydration, and the square bracket indicates the concentration. The concentration of lattice oxygen ions ($[O_O^{\times}]$) in the mole fractional unit is regarded as one and omitted because $[O_O^{\times}] = const. >> [V_O^{\cdot\cdot}] + [OH_O^{\cdot}]$ [62]. Then, a correlation of $[OH_O^{\cdot}]$ as a function of $p(H_2O)^{1/2}$ is commonly observed. Note that oxygen vacancies ($V_O^{\cdot\cdot}$) are the prerequisite of this reaction, and the concentration of oxygen vacancies determines the upper limit of the concentration of protons as Equation 2.2.

$$[OH_O^{\cdot}] = K_W^{1/2}[V_O^{\cdot\cdot}]^{1/2}(pH_2O)^{1/2} \tag{2.2}$$

Oxygen vacancies are usually introduced by acceptor substitution. Taking Ca-substituted $LaNbO_4$ as an example, the substitution can be presented as Equation 2.3 [54, 55].

$$2CaO + 2La_{La}^{\times} + O_O^{\times} = 2Ca'_{La} + La_2O_3 + V_O^{\cdot\cdot} \tag{2.3}$$

During the hydration reaction, the concentration of each charge species in Ca-substituted $LaNbO_4$ should meet the electroneutrality condition as Equation 2.4.

$$[Ca'_{La}] = 2[V_O^{\cdot\cdot}] + [OH_O^{\cdot}] \tag{2.4}$$

However, Equation 2.1, 2.2 and 2.4 are simplified mainly based on the assumption of a constant concentration of oxygen vacancies determined by substitution level. For a more detailed analysis, the concentration of oxygen vacancies is also a function of oxygen partial pressure as Equation 2.5.

$$\begin{aligned} V_O^{\cdot\cdot} + \frac{1}{2}O_{2(g)} &= O_O^{\times} + 2h^{\cdot} \\ K_h &= [h^{\cdot}]^2[V_O^{\cdot\cdot}]^{-1}(pO_2)^{-1/2} \end{aligned} \tag{2.5}$$

Where K_h is the equilibrium constant of this reaction. Therefore, Equation 2.4 can be expanded as Equation 2.6.

$$[Ca'_{La}] + [e'] = 2[V_O^{\cdot\cdot}] + [OH_O^{\cdot}] + [h^{\cdot}] \tag{2.6}$$

Given the intrinsic excitation of electron-hole pairs, the concentration of electrons and holes can be written as Equation 2.7 [48, 63].

$$\begin{aligned} [h^{\cdot}] + [e'] &= null \\ K_{exc} &= [h^{\cdot}][e'] \end{aligned} \tag{2.7}$$

Where K_{exc} is the equilibrium constant of the excitation. Combining Equation 2.1, 2.4, 2.5 and 2.7, the concentration of each charge carrier can be written as Equation 2.8 [48].

$$\begin{aligned} [OH_O^{\cdot}] &= \frac{pH_2O \cdot K_W}{4}\left[\left(1 + \frac{8[Ca'_{La}]}{pH_2O \cdot K_W}\right)^{1/2} - 1\right] \\ [V_O^{\cdot\cdot}] &= \frac{pH_2O \cdot K_W}{16}\left[\left(1 + \frac{8[Ca'_{La}]}{pH_2O \cdot K_W}\right)^{1/2} - 1\right]^2 \\ [h^{\cdot}] &= \left(\frac{K_W K_h}{16}\right)^{1/2}(pO_2)^{1/4}(pH_2O)^{1/2}\left[\left(1 + \frac{8[Ca'_{La}]}{pH_2O \cdot K_W}\right)^{1/2} - 1\right] \\ [e'] &= K_{exc}\left(\frac{K_W K_h}{16}\right)^{-1/2}(pO_2)^{-1/4}(pH_2O)^{-1/2}\left[\left(1 + \frac{8[Ca'_{La}]}{pH_2O \cdot K_W}\right)^{1/2} - 1\right]^{-1} \end{aligned} \tag{2.8}$$

Equation 2.8 explicitly describes the concentration of each charge carrier in an acceptor-substituted oxide as the function of pH_2O and pO_2.

Apart from oxygen vacancies dominating hydration, there were fewer reports of other hydration or protonation mechanisms. If materials contain structural oxygen vacancies, hydration can be expressed as Equation 2.9 and Equation 2.10 [48, 59, 64]. These hydration mechanisms have been proposed to explain protonic conductivity in some oxides, such as $Ba_2In_2O_5$ and Y_2O_3 [65, 66]. However, their protonic conductivity is low as these positive and negative ions tend to be mutually neutralised.

$$H_2O_{(g)} + 2O_O^{\times} + V_O^{\times} = 2OH_O^{\cdot} + O_O'' \tag{2.9}$$

$$H_2O_{(g)} + 2O_O^{\times} + V_O^{\times} = OH_O^{\cdot} + OH_O' \tag{2.10}$$

The hydration can even be realised without oxygen vacancies by balancing the charge with holes as Equation 2.11 [48, 64].

$$H_2O_{(g)} + 2O_O^{\times} + 2h^{\cdot} = 2OH_O^{\cdot} + \frac{1}{2}O_{2(g)} \tag{2.11}$$

Moreover, complex defect species or associations have been proposed to realise hydration in some oxides, such as $LaNbO_4$, as Equation 2.12 states [67, 68].

$$H_2O_{(g)} + (Nb_2O_7)_{2NbO_4}^{\cdot\cdot} = 2(HNbO_4)_{NbO_4}^{\cdot} \tag{2.12}$$

Apart from taking protons from water, protons can also be taken directly from dry hydrogen gas, as in Equation 2.13 [62, 69].

$$H_{2(g)} + 2O_O^{\times} = 2OH_O^{\cdot} + 2e' \tag{2.13}$$

This was first reported for ZnO in the 1950s and, more recently, in $SmNiO_3$ [70, 71]. This mechanism is usually unfavoured for electrolytes due to the parasitic electronic conductivity. However, some latest works have found that electronic conductivity can be suppressed by electron/hole localisation via the Mott transition [71–73].

It is worth mentioning that the above contents still overlook the complicated surface interaction (water absorption, dissociation, and so on). These surface interactions primarily depend on electrodes and are beyond the scope of this work.

2.1.2 Proton solubility

The equilibrium constant of hydration (K_W) in Equation 2.1 can be expressed from a thermodynamic perspective as Equation 2.14.

$$k_B T ln K_W = T\Delta S - \Delta H \tag{2.14}$$

Where k_B is the Boltzmann constant (1.380649×10^{-23} J·K^{-1}), and ΔS and ΔH are the standard hydration entropy and enthalpy changes. Experimental ΔS values are negative in the range of -80 to -160 J/mol·K in oxides, dominated by the entropy loss of water vapour or steam [59]. Considering that Equation 2.1 is the sum of Equation 2.5 and 2.11, ΔH in Equation 2.14 is governed by the enthalpy change of proton dissolution and oxygen vacancy formation, while the latter is dominant and makes ΔH negative [59]. This indicates that oxygen vacancy formation is preferred in the high-temperature range, while hydration is preferred in the low-temperature range. Therefore, a balance between acceptable hydration capacity and sufficient oxygen vacancy concentration for a proton-conducting electrolyte has to be met at the operating temperature range (400-700 °C).

To increase the proton solubility at a fixed temperature, a proton-conducting oxide would need a more negative ΔH. This means a higher oxygen site basicity realised by reasonable material selection. A cation or a dopant with a lower electronegativity will result in a higher oxygen site basicity [74–76]. For example, the proton solubility of BCY is about six times higher than BZY due to the higher basicity of oxygen sites bonding with Ce cations [74].

Apart from basicity, crystal symmetry is another factor strongly affecting proton solubility. Different oxygen sites may result in selected hydration among those sites, thus reducing the proton solubility [74, 77, 78].

2.1.3 Proton transport

There are two distinct proton transport mechanisms: the vehicle and hopping mechanisms. H/D isotope effect measurements can determine the proton transport mechanism [79]. In the vehicle mechanism, the size and mobility differences between protons and deuterons are negligible, resulting in similar performances. In contrast, this isotope effect becomes more significant for the hopping mechanism. The transport of proton by vehicles, such as OH^-, H_3O^+, and NH_4^+, is mainly applicable in liquids and hydrides [59, 80]. For proton-conducting oxides, proton transport was described by the hopping mechanism (also known as the Grotthuss mechanism) [81].

After hydration, the Grotthuss mechanism includes two steps: (1) proton rotation and reorientation locally around the bonding oxygen ion; (2) proton transfers to a neighbouring oxygen ion [48, 82]. The energy barrier of the first step is less than 0.1 eV. On the other hand, the second step has a higher activation energy, usually larger than 0.5 eV, which suggests that it is the rate determining step [48, 59, 74, 77, 82].

The activation energy of the transfer step decreases as the distance between two neighbouring oxygen ions decreases. The structural O-O distance is usually 290 to 310 pm, while the O-H bond length is slightly smaller than 100 pm [74, 83]. Assuming a hydrated oxygen ion and its neighbouring oxygen ion are placed linearly, a transient O-H···O bond is formed with a variable bond length due to thermal vibration. If the O-O distance is reduced to below 280 pm by the transient O-H···O bond formation, the energy barrier of the proton transfer step could be reduced to even below 0.15 eV [77]. The energy barrier vanishes when the O-O distance is reduced to below 240 pm, resulting in tunnelling [59, 77].

However, the cation repulses the proton away from linear O-H···O configuration when O-O distance is below 250 pm, dramatically increasing the energy barrier for the reorientation step [74, 77]. Therefore, an optimal O-O distance is around 260 to 280 pm. Figure 2.1 shows an example of the Helmholtz energy of proton transport as a function of the O-O distance, where the negative value means thermodynamically favourable [74].

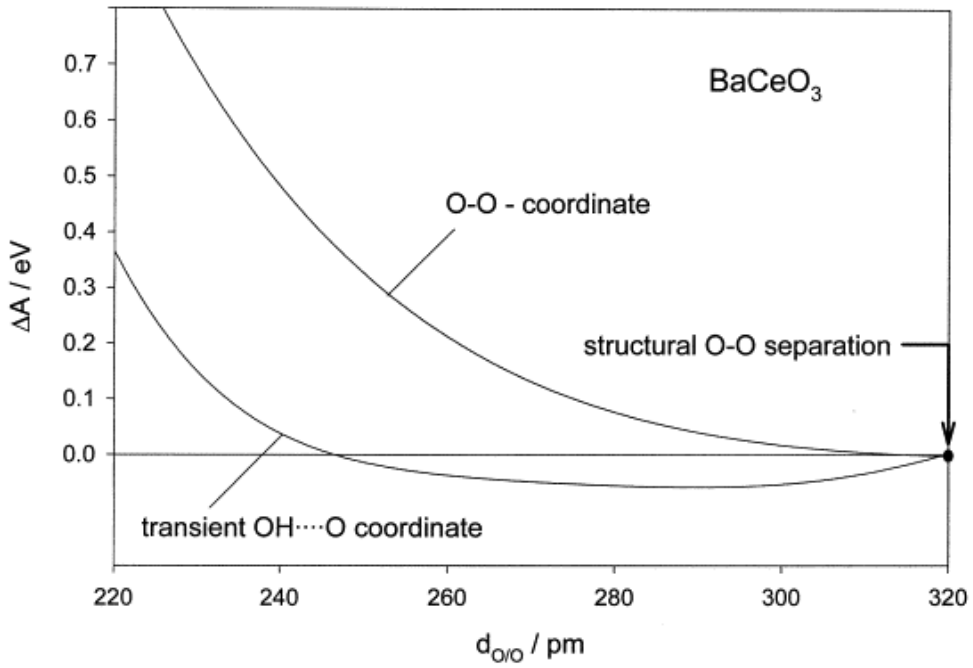


FIGURE 2.1: Helmholtz energy of proton transport of $BaCeO_3$ as a function of the O-O distance and the O-H···O bond length. Reproduced from [74] with permission from Elsevier.

From a material selection perspective, some criteria are critical for a suitable proton-conducting oxide with high proton mobility. Since a proton can only rotate and transfer in free space, a large free lattice volume is favourable, resulting in a lower activation energy [84]. A large free lattice volume also means a longer cation-oxygen ion bond length, which reduces the cation-proton repulsion [74, 77].

In addition, more neighbouring oxygen ions make proton transport easier. The activation energy of proton transport in MO_6 octahedra is significantly lower than in MO_4 tetrahedra or MO_5 pentahedra, where "M" represents the metallic cation [85]. Therefore, proton-conducting oxides prefer the MO_6 octahedra (corner-sharing oxygen framework) [84].

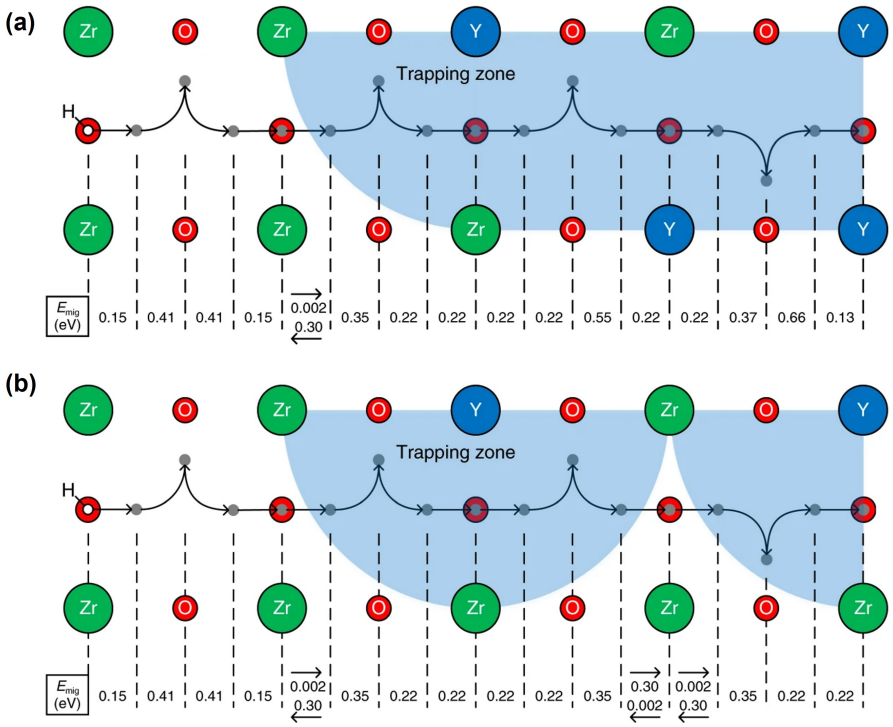


FIGURE 2.2: Proton migration pathways and their energy barriers in (a) Y-Zr-Y configuration and (b) Y-Zr-Zr configuration. Reproduced from [86] with permission from Springer Nature.

Moreover, crystal symmetry strongly affects proton transport, similar to what is discussed in Section 2.1.2. High symmetry minimises the difference in activation energy between each proton transport event, reducing the average activation energy [77]. In comparison, low symmetry leads to a long-range isotropic proton transport pathway breaking into isolated short-range anisotropic pathways, resulting in high-energy barriers between each pathway [78]. Local distortion caused by low symmetry might reduce the O-O distance below 240 pm, resulting in a dramatically increased activation energy of the reorientation step [78].

Crystal symmetry affects more than oxygen sites. The trapping or association effect also strongly correlates with crystal symmetry. This effect describes the association between negatively charged immobile dopants and positively charged charge carriers ($V_O^{\cdot\cdot}$ or $OH_O^{\cdot}$), which reduces the protonic conductivity [87]. Simulation studies found that an ordered local structure facilitates proton transport by reducing local energy barriers that hop protons [86, 88]. For example, Figure 2.2 shows that the local energy

barriers of proton hopping along oxygen sites adjacent to the Y-Zr-Y configuration (0.55 eV) are higher than those of the neighbouring Y-Zr-Zr configuration (0.35 eV) in BZY [86, 88]. Therefore, the protonic conductivity is enhanced because an ordered local structure possesses fewer Y-Zr-Y configurations.

2.1.4 Proton transport through grain boundary

The role of grain boundaries for proton transport is highly controversial. Due to the inevitable structural distortions, the grain boundaries are generally found to be highly resistive [77]. Many researchers tried to explain this high resistance using the space-charge layer theory [89, 90]. In this theory, the grain boundary is consistent with the grain boundary core and two adjacent space-charge layers. The width of the grain boundary cores is typically estimated to be around 1 nm, while the space charge layer can permeate further with a width of 4-5 nm [90–93].

For acceptor-substituted oxides, oxygen vacancies accumulate in the grain boundary core (oxygen vacancies accumulation zone). In contrast, oxygen vacancies are depleted in adjacent space-charge layers (oxygen vacancy depletion zone) [90]. The cations are also redistributed in the grain boundaries to balance the charge. Figure 2.3 shows the schematic diagram of the space charge layer in the grain boundary [94, 95]. This severe depletion of the charge carrier in the space charge layers results in a high potential barrier, causing the reduction of the protonic conductivity in the grain boundaries as in BZY [90, 96]. A recent study found that segregation of dopants in the grain boundaries could mitigate oxygen vacancy depletion in the space-charge layer, increasing protonic conductivity at the grain boundary [88, 97].

However, others reported that hydrated oxygen ions in grain boundary cores could realise fast and selective protonic conductivity along grain boundaries, such as in nano-yttria-stabilised zirconia (YSZ) [90, 98]. Moreover, Sha *et al.* reported that acceptors accumulate in the grain boundary cores instead of oxygen vacancies, resulting in fast ionic conductivity along the space-charge layers [92]. Some researchers even argued that the large void in the grain boundaries can realise vehicular proton transport [99].

Despite successfully explaining the protonic conductivity along the grain boundaries, many researchers still doubted that the effect of the space charge layer, if it exists, is negligible [96, 100]. They claimed that the segregation of impurities, such as silicon, in grain boundaries, even at the ppm level, acts as a blocking layer, dramatically reducing the protonic conductivity [96, 100, 101].

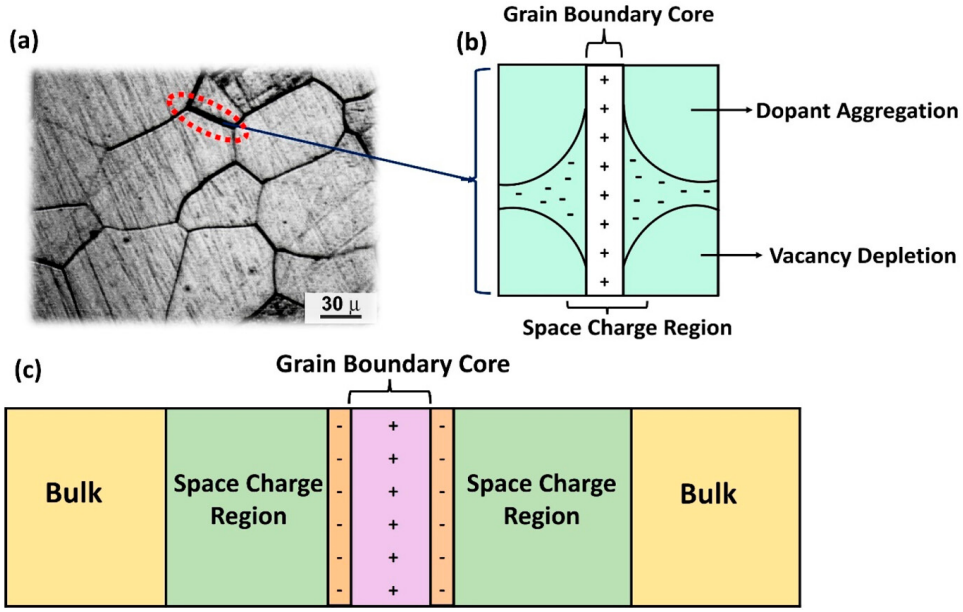


FIGURE 2.3: (a) Polycrystalline perovskite morphology, (b) enlarged grain boundary area, and (c) detailed schematic diagram. Reproduced from [94] with permission from American Chemical Society.

2.1.5 Hydride conductivity

In the past, hydride (H^-) conductivity had only been reported in a few metal hydrides [102, 103]. Recently, fast conductivity of hydrides has been revealed in many oxyhydrides, such as La_2LiHO_3 [104–106]. H^- is lighter and has a lower charge density than O^{2-} with a similar ionic radius (~1.46 $\AA$), achieving a fast hydride conductivity [105, 107]. In addition, hydrides can be taken directly from the dry hydrogen atmosphere as in Equation 2.15 [103].

$$H_{2(g)} + 2M_M^{\times} + 2e' = 2MH_M' \tag{2.15}$$

Where M represents the metallic cations. The resulting electrons were proposed to be trapped in the F-centres [103]. It is worth mentioning that there has long been speculation that hydrides exist widely in proton-conducting oxides, especially under hydrogen atmospheres, as Equation 2.16 [108, 109].

$$H_{2(g)} + M_M^{\times} + O_O^{\times} = MH_M' + OH_O^{\cdot} \tag{2.16}$$

However, the deconvolution of proton and hydride transport can be challenging as both show the H/D isotope effect [109].

2.1.6 Summary

The proton-conducting mechanism in oxides is summarised schematically in Figure 2.4 [48]. An excellent proton-conducting oxide should have high crystal symmetry with fewer defects or local distortions and a sizeable void space. The dopant selection should ensure a high oxygen vacancy concentration and a high oxygen site basicity. Ideally, proton-conducting oxides should form a corner-sharing oxygen framework, which facilitates proton transport. The grain boundary can be the primary source of resistance. Therefore, the preparation and sintering process should be optimised for polycrystalline oxides to reduce the grain boundary resistance. A brief review of the material aspect will be given in the next section.

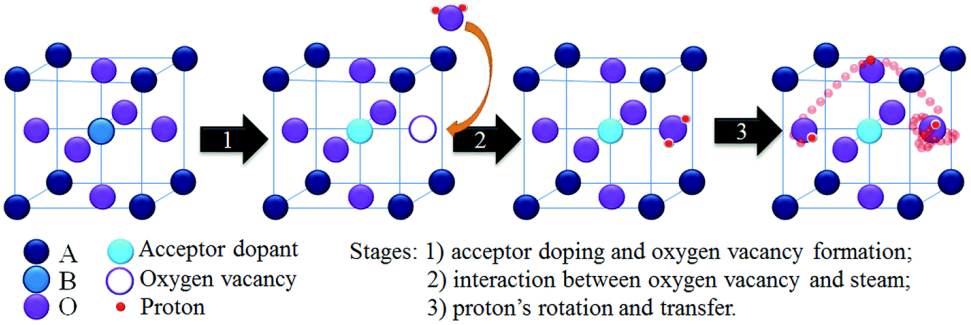


FIGURE 2.4: The proton-conducting mechanism in the ABO_3 perovskite structure. Reproduced from [48] with permission from Royal Society of Chemistry.

2.2 Conventional proton-conducting oxides

2.2.1 Perovskite type oxides

Acceptor-substituted barium cerates ($BaCeO_3$) are one of the first reported proton-conducting oxides [110, 111]. After decades of searching for proton-conducting oxides, $BaCeO_3$-based materials still exhibit the highest protonic conductivity among other oxides [48]. This type of oxide has a cubic perovskite structure (ABO_3, $Pm\bar{3}m$, #221) with many non-cubic variants, as shown in Figure 2.5 [112, 113]. The A-site cation is 12-coordinated, while the B-site cation is 6-coordinated. The Goldschmidt tolerance factor, t, can empirically predict the structure as Equation 2.17 [114].

$$t = \frac{r_A + r_O}{\sqrt{2}(r_B + r_O)} \tag{2.17}$$

Where r_A, r_B and r_O are the ionic radius of A and B site cations and oxygen ions, respectively. The tolerance factor of a cubic perovskite typically falls in the range of 0.9-1.0, while the factor reduces to 0.7-0.9 for a near-cubic orthorhombic or rhombohedral perovskite [114, 115]. Meanwhile, this tolerance factor can also be used to estimate the compatibility of dopants. The change of tolerance factor should be small to maintain the structure. The high crystal symmetry and corner-sharing oxygen framework of perovskite oxides offer favourable prerequisites for proton transport.

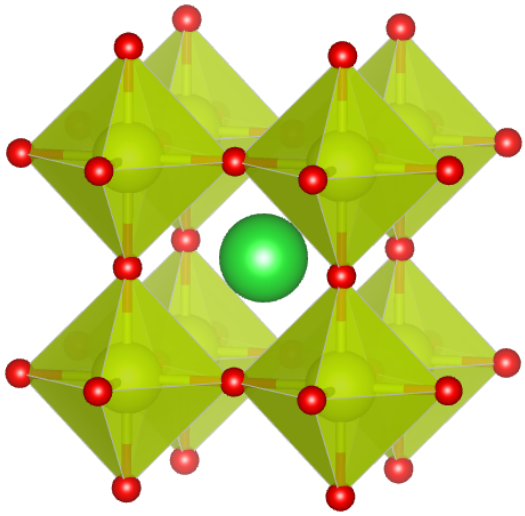


FIGURE 2.5: The structure of a $BaCeO_3$ cubic perovskite with Ba cation in A-site (green) at the centre surrounded by eight CeO_6 (yellow/red) octahedra. This figure is generated based on [112, 113] using VESTA software [116].

Trivalent acceptor dopants, such as yttrium, are commonly substituted into the Ce-site to introduce oxygen vacancies. The protonic conductivity of BCY increases with increasing dopant concentration and then decreases, with a maximum reported conductivity of 6.7×10^{-2} S/cm at 1000 °C under wet hydrogen atmospheres at the dopant concentration of 20% [49]. However, as Equations 2.18 and 2.19, BCY demonstrates low chemical stability in wet and acidic atmospheres and increased electronic conductivity in reducing atmospheres, which hinders its application.

$$BaCeO_3 + H_2O_{(g)} = Ba(OH)_2 + CeO_2 \tag{2.18}$$

$$BaCeO_3 + CO_{2(g)} = BaCO_3 + CeO_2 \tag{2.19}$$

Acceptor-substituted barium zirconates ($BaZrO_3$), on the other hand, exhibit better chemical stability due to the shorter and stronger Zr-O bonds compared with Ce-O

bonds [48]. BZY exhibits one of the highest bulk proton conductivities, with an acceptable chemical stability [117]. However, it requires a high sintering temperature (1800-2000 °C), which drives the acceptor to segregate along grain boundaries resulting in a large grain boundary resistance [48].

To balance BCY's poor chemical stability and BZY's low total protonic conductivity, a series of single-phase BCY-BZY mixed oxides has been prepared and widely studied. However, the properties of this type of material strongly depend on precise controls of substitution levels and preparation conditions, which can be challenging.

In addition to BCY-based and BZY-based materials, there are increasing research interests and reports in $SmNiO_3$-based materials. Nickel is widely regarded as an anodic element due to its multivalent nature and is unsuitable for electrolytes. However, Zhou *et al.* found that electrons can be localised via the Mott transition (metal-insulator transition), where the on-site electron-electron correlation potential suppresses the electronic conductivity [71, 72]. Therefore, protons can be incorporated directly from dry hydrogen atmospheres without parasitic electronic conductivity, as Equation 2.20.

$$Ni^{3+} + O_O^{\times} + \frac{1}{2}H_{2(g)} = Ni^{2+} + OH_O^{\cdot} \tag{2.20}$$

2.2.2 Perovskite-related oxides

As the substitution strategy inevitably introduces local structural distortion, which can significantly decrease protonic conductivity, oxides with structural (intrinsic) oxygen vacancies are of interest. Most of these oxides exhibit crystal structures derived from the perovskite structure, giving perovskite oxides flexible structural tunability. For example, brownmillerite oxides ($A_2B_2O_5 = ABO_{2.5}$, *Imma*, #74) possess one-sixth of oxygen deficiency [48]. Protonic conductivity has been reported in one of the brownmillerite oxides, $Ba_2In_2O_5$ [118]. However, its ordered oxygen vacancy framework raises a significant trapping effect, preventing fast ionic conductivity [49]. The crystal structure of $Ba_2In_2O_5$ undergoes a first-order phase transition to a cubic perovskite phase around 930 °C, resulting in a disordered oxygen vacancy framework and the corresponding fast ionic conductivity [119]. Researchers have tried to use the substitution strategy to stabilise the high temperature phase at lower temperatures [120]. However, it brings back the issue of local structural distortion, making this material less appealing.

Another research interest is in $SrCoO_3$-based materials. The application of an electric field allows the perovskite phase $SrCoO_3$ to be transformed to the brownmillerite phase $SrCoO_{2.5}$, resulting in significant oxygen vacancies for hydration [121, 122]. However, the phase stability of $SrCoO_{2.5}$ and hydrated $SrCoO_{2.5}$ awaits exploration.

Figure 2.6 compares the ionic conductivity of a series of solid oxide electrolytes, where the hydrated $SrCoO_{2.5}$ presents a significantly higher protonic conductivity at much lower temperatures [123].

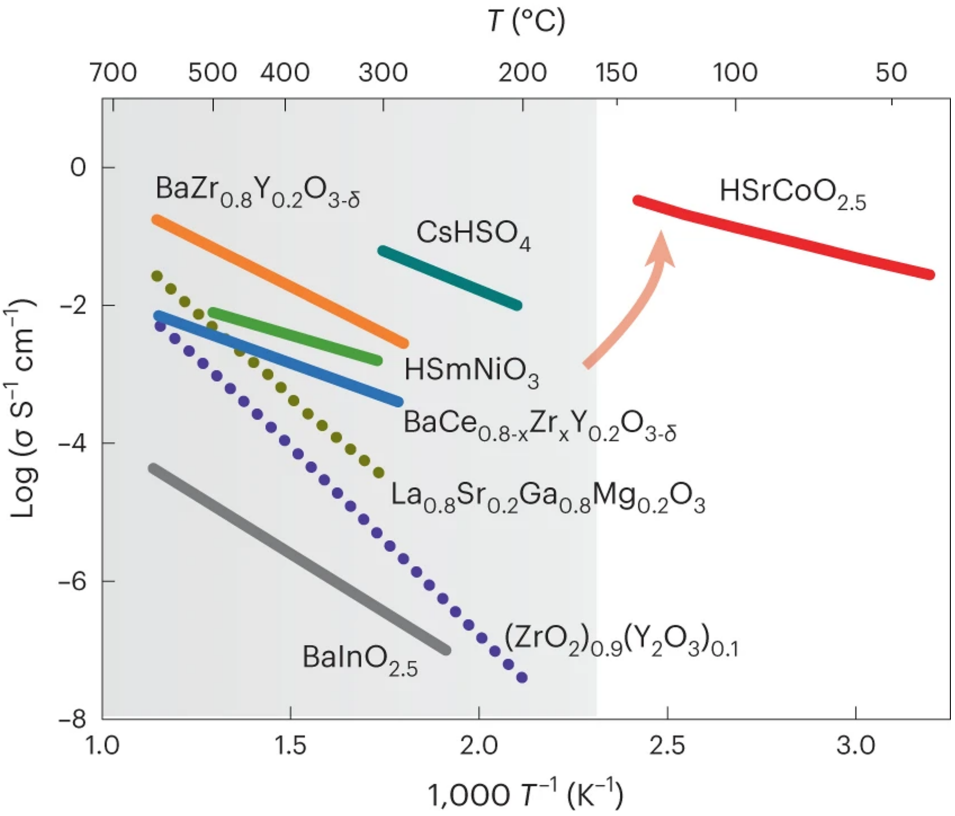


FIGURE 2.6: Comparison of ionic conductivity of a series of solid oxide electrolytes. The solid line shows the protonic conductivity of the proton-conducting oxides, while the dashed line indicates the oxygen ionic conductivity of the comparative oxides. The arrow shows the optimising direction of solid oxide electrolytes, *i.e.*, higher ionic conductivity at lower working temperatures. Reproduced from [123] with permission from Springer Nature.

2.2.3 Fluorite type oxides

Fluorite oxides (ABO_2, $Fm\bar{3}m$, #225), such as YSZ and gadolinium-doped ceria (GDC), are mainly considered as oxygen ion conductors with negligible protonic conductivity. However, as discussed in section 2.1.4, a selective grain boundary protonic conductivity reveals the potential of nanostructured YSZ and GDC to be proton-conducting oxides [60]. Figure 2.7 shows that this protonic conductivity prevails only below 120 °C, increasing dramatically with a decrease in grain size [60, 98]. Nano-YSZ shows a protonic conductivity dominated by absorbed water molecules via the vehicle mechanism in zone 1 [60]. Meanwhile, it exhibits proton transport in the form of hydroxyl

species via the Grotthuss mechanism in zone 2 [60]. The protonic conductivity is negligible in zone 3 [60]. Studies also indicated that protonic conductivity is invariant to the concentration of the dopant in the bulk, indicating selective conductivity through grain boundaries [124].

In addition to protonic conductivity through the grain boundary, recent studies have reported interfacial/surface protonic conductivity, especially in porous YSZ [125, 126]. A layered absorption of water on the surface of the oxide has been found, which consists of chemisorbed water layers and physisorbed water layers [126]. Apart from temperature dependence, interfacial/surface proton transport exhibits relative humidity (RH) dependence. It is through the Grotthuss mechanism in the chemisorbed water layers at <60% RH and change to the vehicle mechanism in the physisorbed water layers at ≥60% RH [126].

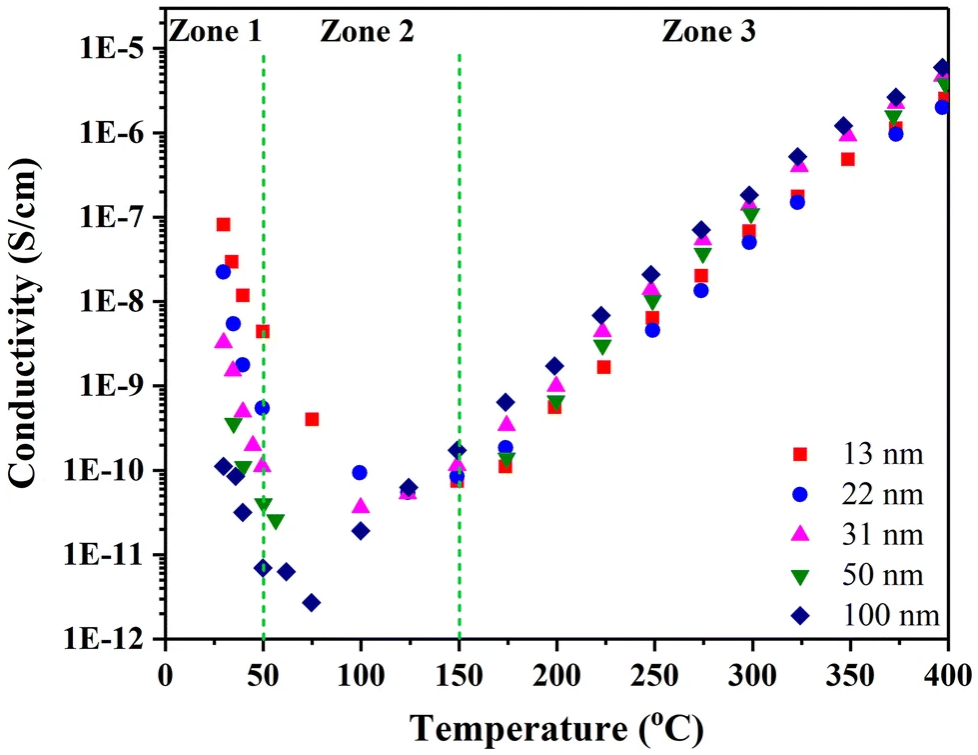


FIGURE 2.7: The total conductivity of nano-YSZ with different grain sizes measured under wet air (∼2.5% RH). Reproduced from [60, 98] with permission under a Creative Commons CC BY Licence.

2.2.4 Fluorite-related oxides

Rare-earth tungstates such as $La_{5.8}WO_{11.7}$ exhibited a recorded protonic conductivity of $\sim 5 \times 10^{-3}$ S/cm at 900 °C under wet hydrogen atmospheres [127]. These tungstates are not single-phase oxides, but solid solutions with a general composition of La_6WO_{12}

and a cubic structure related to fluorite [48]. Acceptor substitution strategies have been used to increase the oxygen vacancies. However, the high electronic conductivity and degradation to form La_2O_3 impurities through hydration make La_6WO_{12}-based oxides not suitable for proton-conducting electrolyte applications [128]. However, some studies intended to increase the electronic conductivity by substituting W^{6+} with Mo^{6+} for hydrogen separation membrane applications, where the electronic conductivity should be sufficient [128].

2.2.5 Summary

Although promising progress has been made in optimising and manufacturing conventional perovskite and fluorite oxides, they still demand further improvements to meet the requirements for commercialisation. Each material has its advantages and disadvantages. Perovskite oxides generally suffer from degradation issues and high grain boundary resistances, while fluorite oxides raise manufacturing challenges to nano-crystallisation. Nevertheless, studies of these conventional proton-conducting oxides deepen the understanding of the fundamental mechanism, which guides and stimulates new research interests in searching for new types of proton-conducting oxides.

2.3 Fergusonite-scheelite type oxides

While some strive to optimise conventional proton-conducting oxides, others start exploring the edge of new materials. One of these new oxides is fergusonite–scheelite type oxides (ABO_4), such as $LaNbO_4$, which exhibit excellent chemical stability, especially in CO_2-containing atmospheres [54, 55]. Pristine $LaNbO_4$ presents a monoclinic fergusonite phase ($C2/c$ or $I2/a$, #15, denoted as m-$LaNbO_4$) in RT and undergoes a phase transition to a tetragonal scheelite phase ($I4_1/a$, #88, denoted as t-$LaNbO_4$) around 500 °C [129]. The phase transition was initially proposed as a second-order transition due to a continuous volume change near the transition temperature range [129, 130]. However, recent studies found the coexistence of the monoclinic and tetragonal phases, suggesting a pseudo-second order phase transition with first-order phase transition natures [131, 132].

In $LaNbO_4$, La cations have an 8-fold coordinated environment in both phases, while Nb cations present a 4-fold coordinated environment in the t-$LaNbO_4$ and a 6-fold coordinated environment in the m-$LaNbO_4$ [131]. Figure 2.8 shows the relationship between NbO_4 tetrahedra and NbO_6 octahedra, where the latter can be considered as a

distorted NbO_4 tetrahedra with two longer Nb-O bonds forming corner-sharing NbO_6 octahedra along the *c* axis [131].

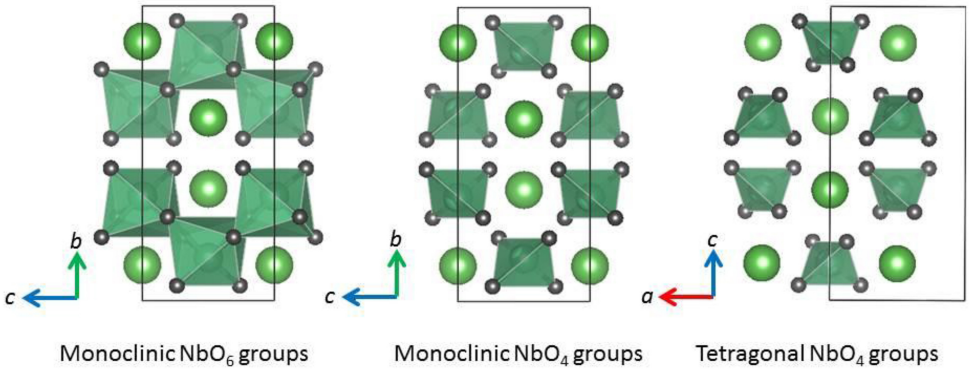


FIGURE 2.8: Distorted NbO_6 octahedra (left) possesses four short Nb-O bonds similar to NbO_4 tetrahedra (middle) and two long Nb-O bonds, forming a corner-sharing configuration along *c* axis. Grey and green balls and dark green polyhedra denote O^{2-}, La^{3+} and NbO_4/NbO_6 polyhedra, respectively. Reproduced from [131] with permission from Elsevier.

In 2006, Haugsrud *et al.* reported the first case of protonic conductivity in 1% Ca-substituted $LaNbO_4$ with a protonic conductivity recorded of ~1 mS/cm at 950 °C under wet air [54, 55]. Ca substitution introduces oxygen vacancies through Equation 2.3, allowing hydration and corresponding proton transport as Equation 2.1 [54, 55]. Some also proposed the hydration process via complex defect species or associations, such as Equation 2.12 [67, 68].

Later, a study of density functional theory (DFT) revealed that proton transport is highly anisotropic along the *ab* in-plane, as shown in Figure 2.9 [133]. For t-$LaNbO_4$, the energy barriers of the proton transport path are 0.04 eV, 0.06 eV, and 0.41 eV for the *ab* in-plane paths 1, 2 and 3, respectively, while the energy barrier is 0.74 eV for the *c* out-of-plane path 4 [133]. Due to the lower symmetry of m-$LaNbO_4$, the cation layers are divided into two types with different layer distances, resulting in non-identical oxygen sites (O1 and O2 sites) [133]. Therefore, for m-$LaNbO_4$, the energy barriers of the *ab* in-plane paths 1′, 2′ and 3′ are 0.04 eV, 0.17 eV, and 0.62 eV, respectively, while the energy barriers of the *c* out-of-plane paths 4′ and 5′ are 0.94 eV and 1.55 eV, respectively. The results suggested that proton transport becomes more anisotropic in m-$LaNbO_4$ [133]. It is worth mentioning that the m-$LaNbO_4$ structure was calculated at 0 K with NbO_4 tetrahedra, which is not directly comparable to the structure of m-$LaNbO_4$ with NbO_6 octahedra at RT [133].

The above promising results ignited more research on optimising the performance of $LaNbO_4$ through different doping strategies, as shown in Table 2.1. It is suggested that the proton conductivity of acceptor-substituted $LaNbO_4$ is limited mainly by the

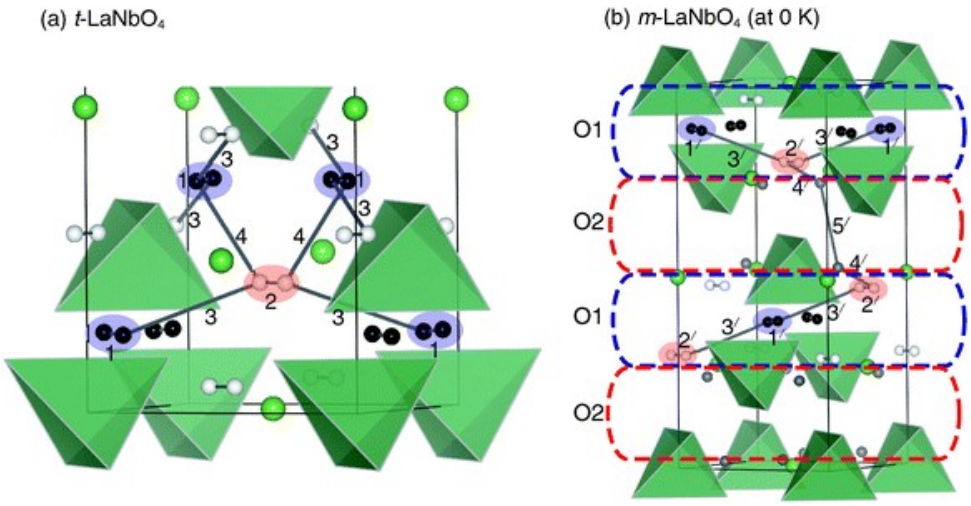


FIGURE 2.9: Proton transport paths 1-4 in (a) t-$LaNbO_4$ and 1′-5′ in (b) m-$LaNbO_4$ (0 K). The green balls and green polyhedra denote La^{3+} cations and NbO_4 tetrahedra, respectively, while the black, white and grey balls denote the stable proton sites in both phases. The layer distance ratio between O1 and O2 in m-$LaNbO_4$ is 3:2. Reproduced from [133] with permission from Royal Society of Chemistry.

low substitution solubility. The significant grain boundary resistance makes the total proton conductivity even lower [134]. On the other hand, donor-substituted $LaNbO_4$ generally shows much higher solubility, but the proton conductivity is negligible as donors cannot introduce oxygen vacancies.

Another main issue is the fergusonite–scheelite phase transition of $LaNbO_4$ with different thermal expansion coefficients. Figure 2.10 shows the fergusonite and scheelite structure of pristine $LaNbO_4$ with the corresponding linear thermal expansion coefficient [135]. This expansion difference leads to a thermal expansion mismatch between the electrolyte and adjacent layers (electrodes or interlayers), causing mechanical failure during thermal cycles [129].

Further studies found that, empirically, the high temperature tetragonal scheelite phase can be stabilised by substituting B-site cations with a higher electronegativity and a smaller ionic radius than Nb^{5+}, such as W^{6+} and Mo^{6+} [136, 137]. Table 2.1 also suggests that the solubility limit of these cations is much higher. This phase stabilisation capability with such high dopant solubility is intriguing.

However, as mentioned above, previous studies found that the proton conductivity of W- and Mo-substituted $LaNbO_4$ is negligible because W^{6+} and Mo^{6+} are donors that introduce interstitial oxygen ions instead of oxygen vacancies [138, 139]. Given the

multivalent nature of these cations, reducing W^{6+} and Mo^{6+} to the oxidation state below +5 could potentially introduce oxygen vacancies, thereby achieving protonic conductivity under reduced atmospheres. This oxidation state-templated protonic conductivity is not a new concept but has been reported for some perovskite oxides such as $SmNiO_3$ and $SrCoO_3$ [71, 72, 121, 122].

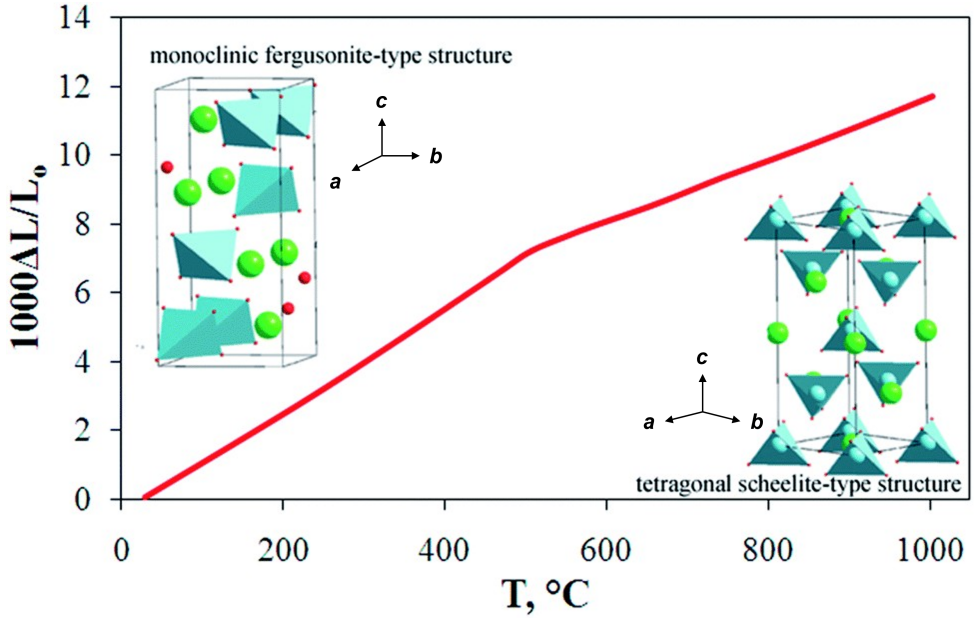


FIGURE 2.10: Linear thermal expansion of pristine $LaNbO_4$ and its corresponding monoclinic and tetragonal phase structures. Red and green balls and blue polyhedra denote O^{2-}, La^{3+} and NbO_4 tetrahedra, respectively. Reproduced from [48, 49, 135] with permission from Royal Society of Chemistry.

Until now, only one similar study has been reported suggesting a simultaneous increase in ionic and electronic conductivity in multivalent Sm^{2+}/Sm^{3+}, Gd^{2+}/Gd^{3+} and Yb^{2+}/Yb^{3+} substituted $LaNbO_4$ [140]. However, this work did not separate protonic and oxygen ionic conductivity, which weakens the argument of realising protonic conductivity under reducing atmospheres [140]. Moreover, the multivalent elements in these studies have only two oxidation states (+2/+3), compensating by introducing or not oxygen vacancies. In the W^{6+} and Mo^{6+} cases, they have at least three common oxidation states (+4/+5/+6), allowing for potentially more complicated anion compensation situations from oxygen vacancies to interstitial oxygen ions. Such complexities indicate more tunable conductivities among protonic, oxygen ionic (interstitial oxygen ions or oxygen vacancies), electronic, and mixed conductivities based on oxidation states.

TABLE 2.1: Summary of single substituted $LaNbO_4$ reported up to now. Complicated co-substitution or multi-substitution cases are omitted. σ_e and σ_p denote electronic and protonic conductivity, respectively. Asterisk (*) marks dopants without available solubility data, and the reported highest substitution level was listed instead.

Dopant	Substitution site	Dopant solubility	Drawbacks	Reference
Ca^{2+}	La^{3+}	2%	low solubility	[54, 55]
Sr^{2+}	La^{3+}	1%	low solubility	[137, 141, 142]
Ba^{2+}	La^{3+}	2%	low solubility	[142]
Mg^{2+}	La^{3+}	2%	low solubility	[143]
Zn^{2+}	La^{3+}	1%	low solubility	[144]
$Sm^{2+/3+}$	La^{3+}	10%*	increased σ_e	[140]
$Gd^{2+/3+}$	La^{3+}	10%*	increased σ_e	[140]
$Yb^{2+/3+}$	La^{3+}	10%*	increased σ_e	[140]
$Tb^{3+/4+}$	La^{3+}	30%*	negligible σ_p	[145]
$Pr^{3+/4+}$	La^{3+}	30%*	negligible σ_p	[146]
$Ce^{3+/4+}$	La^{3+}	30%*	negligible σ_p	[147]
Ga^{3+}	Nb^{5+}	3%	low solubility	[56]
Ti^{4+}	Nb^{5+}	3%	low solubility	[56]
Si^{4+}	Nb^{5+}	3%	low solubility	[56]
Ge^{4+}	Nb^{5+}	3%	low solubility	[56]
Al^{3+}	Nb^{5+}	3%	low solubility	[56]
Zr^{4+}	Nb^{5+}	2%	low solubility	[56]
Ta^{5+}	Nb^{5+}	40%	negligible σ_p	[130]
V^{5+}	Nb^{5+}	30%*	negligible σ_p	[136, 148]
Sb^{5+}	Nb^{5+}	30%*	negligible σ_p	[136, 148, 149]
As^{5+}	Nb^{5+}	30%*	negligible σ_p	[136]
W^{6+}	Nb^{5+}	20%	negligible σ_p	[150, 151]
Mo^{6+}	Nb^{5+}	30%	negligible σ_p	[139, 152]

2.3.1 Hexavalent-substituted lanthanum orthoniobates

The hexavalent-substituted lanthanum orthoniobates can be written as Equation 2.21 and Equation 2.22.

$$2WO_3 + 2Nb_{Nb}^{\times} = 2W_{Nb}^{\cdot} + Nb_2O_5 + O_i'' \tag{2.21}$$

$$2MoO_3 + 2Nb_{Nb}^{\times} = 2Mo_{Nb}^{\cdot} + Nb_2O_5 + O_i'' \tag{2.22}$$

There are abundant studies on the crystal structure and the tetragonal phase stabilising capability of W- and Mo-substituted $LaNbO_4$ [150–152]. Herein, W- and Mo-substituted $LaNbO_4$ are denoted below as LNW and LNMo, respectively. The number will be added for W- and Mo-substituted $LaNbO_4$ with a specific substitution level. For example, 10% Mo-substituted $LaNbO_4$ ($LaNb_{0.9}Mo_{0.1}O_{4.05}$) is denoted as LNMo10.

Figure 2.11 shows the phase diagrams of LNW and LNMo, indicating the tetragonal scheelite phase can be stabilised at RT with ≥16% of W^{6+} or ≥20% of Mo^{6+} substitution [151, 152]. However, the actual phases of LNW and LNMo are sensitive to sintering and any followed heat treatment conditions [152, 153]. Auckett *et al.* found that the lattice parameters of LNMo20 are not fully reversible after a thermal cycle [152]. This hysteresis effect is likely due to the slow phase transition kinetics, which traps the tetragonal phase at a lower temperature [152].

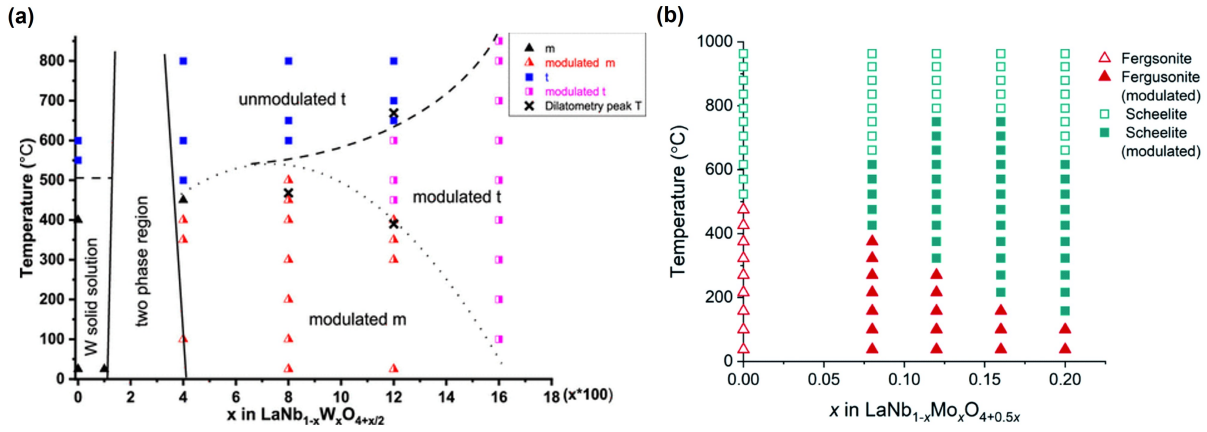


FIGURE 2.11: Phase diagrams of (a) LNW and (b) LNMo. Both phases were evaluated via *in-situ* X-ray powder diffraction (XRD) technique. Two temperature points extrapolated from dilatometry analysis are marked as "×" on the phase diagram of LNW. Reproduced from [151] with permission from American Chemical Society, and from [152] with permission under a Creative Commons Attribution-NonCommercial 3.0 Unported Licence.

In addition to the phase stabilising capacity, both LNW and LNMo have incommensurately modulated structures [151, 152]. The modulated structure describes the derivation from the ideal lattice sites with superimposed long-range-ordered lattice periodicity, as shown in Figure 2.12 [47, 154, 155]. If this long-range-ordered lattice periodicity equals integral n-times of the primary lattice periodicity, then it is called the commensurately modulated structure [154]. If not, it is called the incommensurately modulated structure [154]. Therefore, the conventional lattice notation system cannot describe the modulated structure. De Wolff *et al.* developed the super-lattice approach to fully describe the modulated structure, where an additional lattice vector $\boldsymbol{q_i} = h\boldsymbol{a}^* + k\boldsymbol{b}^* + l\boldsymbol{c}^*$ is introduced [156, 157]. The simplest example is presented in Figure 2.12(b) with the additional lattice vector $\boldsymbol{q_i} = h\boldsymbol{a}^*$. This case is called (3+1)D commensurately modulated structure.

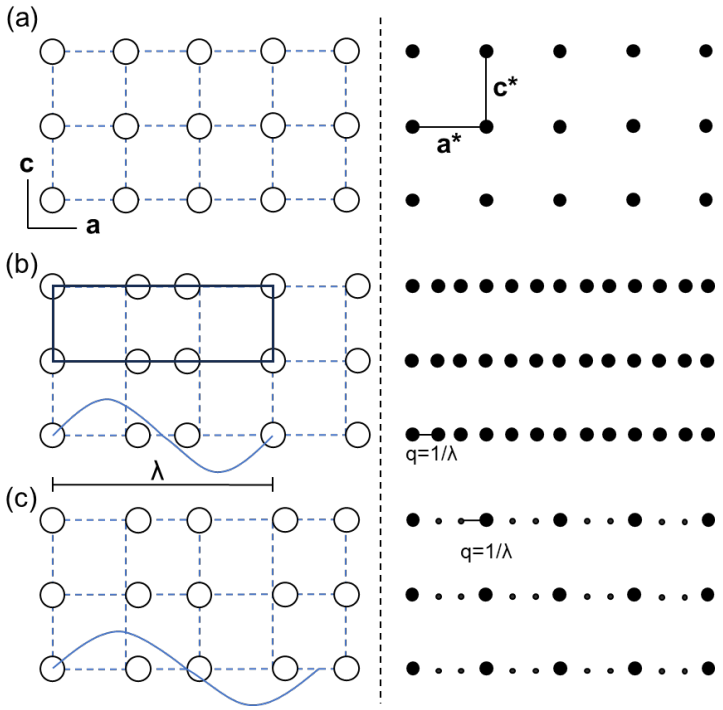


FIGURE 2.12: Schematic diagrams of (a) an ideal crystal lattice, (b) the (3+1)D-commensurately modulated structure along a axis, (c) the (3+1)D-incommensurately modulated structure along a axis, and their corresponding reciprocal lattice point patterns, respectively. Adapted from [47, 155] with permission from Imperial College London.

XRD and selected area electron diffraction (SAED) techniques can evaluate the modulated structure presented as satellite peaks/reflections, as shown in Figure 2.13. Studies on $CeNbO_{4+\delta}$ proposed that the modulated structure in scheelite oxides is highly correlated with interstitial oxygen ions [158, 159]. The modulated structure also substantially impacts conductivity and other properties [47]. For example, Han *et al.* found

that the modulated structure in LNMo10 negatively affects the oxygen ionic conductivity [160]. The activation energy of 1.53 eV in modulated LNMo10 is significantly higher than that of 0.64 eV in unmodulated LNMo10 [160]. This poorer performance is likely due to the reduced symmetry of the modulated structure [160].

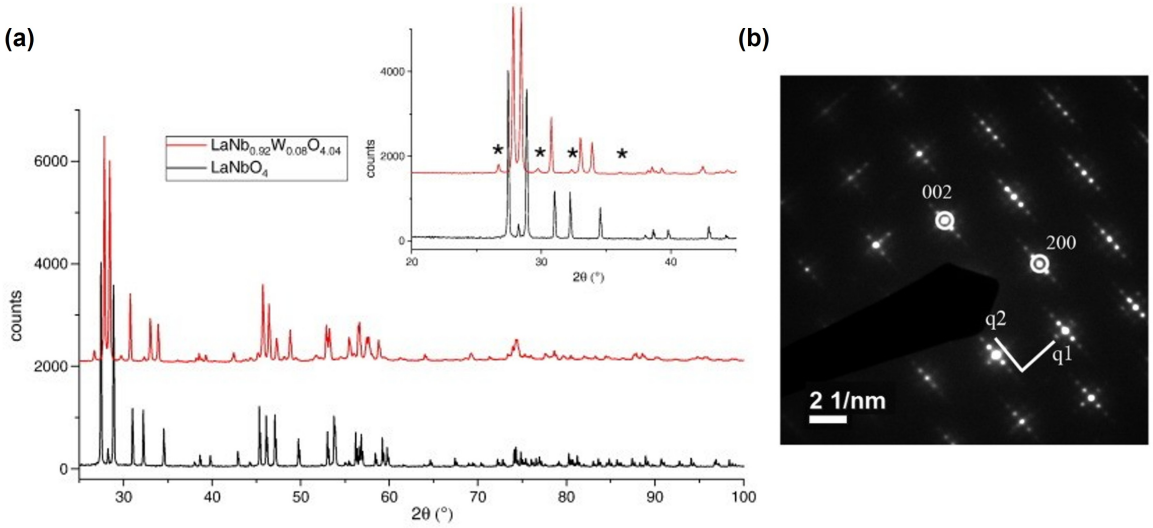


FIGURE 2.13: (a) XRD pattern of pristine $LaNbO_4$ and LNW08. The insert shows the satellite peaks marked as "asterisk" (*) from the modulated structure. (b) SAED pattern of LNW08 from [010] zone axis. The satellite reflections from the modulated structure are clearly observed. The estimated additional lattice vectors are $\boldsymbol{q_1} = 0.263\boldsymbol{a}^* + 0.106\boldsymbol{c}^*$ and $\boldsymbol{q_2} = 0.082\boldsymbol{a}^* + 0.243\boldsymbol{c}^*$. Reproduced from [138] with permission from Elsevier.

2.3.2 Hexavalent-substituted lanthanum orthoniobates as ionic conductors

LNW and LNMo are good oxygen ion conductors due to the presence of interstitial oxygen ions. Li *et al.* studied the conductivity of LNW with a series of substitution levels (1%, 8%, 12% and 16%) under ambient conditions [161]. The results suggested that LNW is a pure oxygen ion conductor, while LNW08 reaches the highest conductivity, as shown in Figure 2.14 [161]. The oxygen ion conductivity in LNW is achieved through an interstitialcy mechanism, indicating a similar mobility between interstitial oxygen ions and lattice oxygen ions, as shown in Figure 2.15(c) [161]. In addition, similar activation energies listed in Table 2.2 suggest that modulated structure rather than substitution level mainly governs conductivity [47]. Canu *et al.* proposed an increased electronic conductivity of LNW16 under hydrogen atmospheres due to the reduction

of W^{6+} cations [153]. However, direct measurement of the oxidation state was missing and this hypothesis did not explain the conductivity behaviour under hydrogen atmospheres.

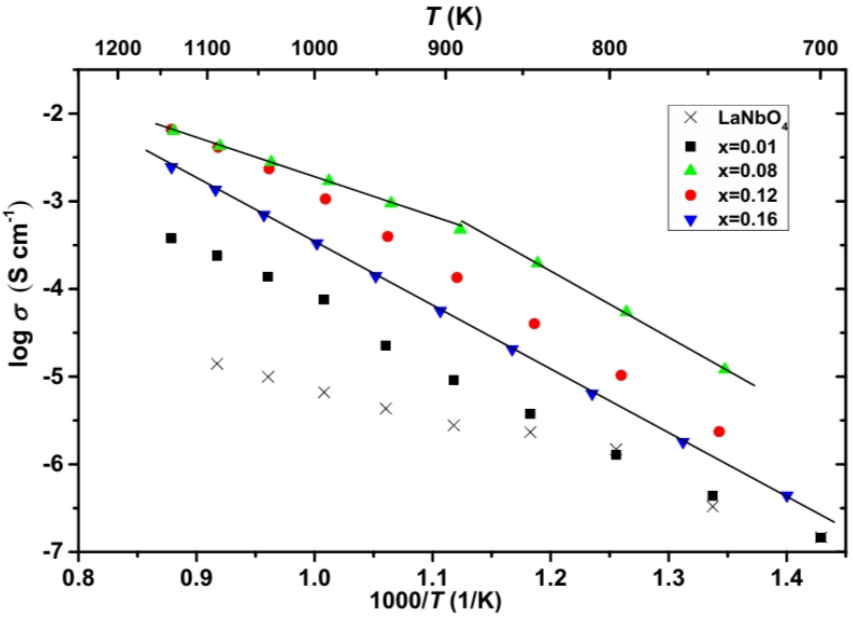


FIGURE 2.14: Total conductivity of LNW with a series of substitution levels (1%, 8%, 12% and 16%) under the ambient condition. The separate solid lines in LNW08 represent the activation energy difference between unmodulated and modulated scheelite structures, while such difference is diminished in LNW16. Reproduced from [161] with permission from Royal Society of Chemistry.

Meanwhile, Johansen *et al.* reported the formation of $LaNb_{0.95}W_{0.05}O_{4+\delta-x}H_x$ oxyhydride via the reaction between LNW05 and CaH_2 [162]. XRD, gas phase analysis (GPA), and thermogravimetric analysis (TGA) strongly indicate the presence of hydrogen in LNW05 after reaction [162]. Although this study indicates the potential of LNW as a protonic conductor, it neither offers conclusive evidence of oxyhydride formation nor conducts the study of potential hydride conductivity.

In addition to the experimental results, DFT and molecular dynamics (MD) studies provided a theoretical description of the oxygen ionic conductivity in LNW at the atomic level [163, 164]. The interstitial oxygen ion in t-$LaNbO_4$ prefers to be located between two NbO_4 tetrahedra, forming a Nb_2O_9 unit [164]. In LNW cases, the interstitial oxygen ion should prefer to form a Nb_2O_9 or W_2O_9 or $NbWO_9$ unit, assuming a random distribution of dopants [163].

Figure 2.16 shows two short interstitial oxygen ion transport paths through the interstitial mechanism along the *ab* plane and one long interstitial oxygen ion transport path through the interstitialcy mechanism along the *c* axis [164]. However, in contrast to the

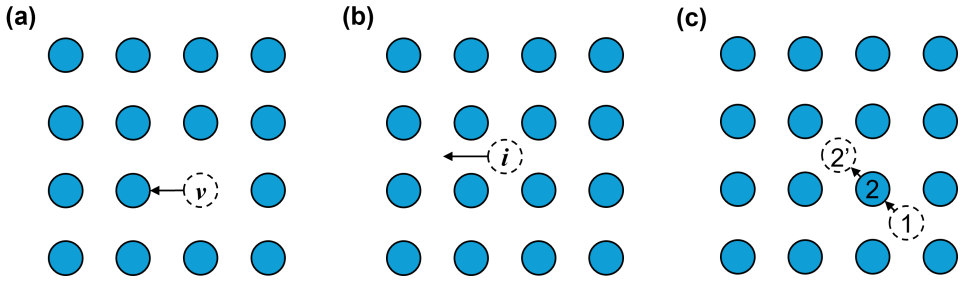


FIGURE 2.15: Schematic diagrams of different point defect conduction mechanisms. The solid blue balls represent the lattice oxygen ions, and the dashed balls represent the oxygen defects. (a) and (b) represent the typical vacancy and interstitial mechanisms, respectively. The oxygen vacancy and interstitial oxygen site are labelled as "v" and "i", respectively. (c) represents the interstitialcy mechanism, where the initial interstitial oxygen ion (1) occupies the lattice oxygen site (2), "kicking out" the lattice oxygen ion to become a new interstitial oxygen ion (2′).

reported anisotropic proton conductivity in $LaNbO_4$, the long-range pathways along the *ab* plane in Figure 2.16(a) and along the *c* axis in Figure 2.16(b) present the similar energy barriers of ∼0.40 eV, indicating the isotropic oxide-ion conductivity [164]. These simulation works also suggested that the reduced conductivity in LNW with high substitution levels is likely due to the trapping effect [163, 164]. In contrast, this effect should be suppressed more in LNMo [164].

TABLE 2.2: The activation energy of LNW with a series of substitution levels (1%, 8%, 12% and 16%). The activation energy reduces at around 600 °C. Reproduced from [47] with permission from Imperial College London.

Composition	E_a at low T (eV)	E_a at high T (eV)
LNW01	1.21±0.03	1.05±0.01
LNW08	1.58±0.01	0.89±0.05
LNW12	1.49±0.02	1.29±0.03
LNW16	1.43±0.02	

To my knowledge, there are only two publications on LNMo [139, 152]. Auckett *et al.* investigated the total conductivity of LNMo16 and LNMo20, which are higher than that of LNW16 and LNW20, suggesting the suppressed trapping effect [152]. DFT simulations revealed that a similar interstitialcy mechanism dominated interstitial oxygen ion transport to LNW [152].

Cao *et al.* reported the reduction of Mo^{6+} cations in LNMo20 under reducing atmospheres, transforming the tetragonal phase into the monoclinic phase analogous to the pristine $LaNbO_4$ [139]. This reduction is fully reversible [139]. The total conductivity in reduced atmospheres is three orders higher than in ambient conditions due to the enhancement of electronic conductivity [139]. The oxidation states of the Mo^{6+} cations

were proposed to reduce to below +4, indicating the potential creation of oxygen vacancies [139]. However, reduced oxidation states were examined only by X-ray photoelectron spectroscopy (XPS), which provides the surface ($\leq$10 nm) compositional and redox information [139]. The actual oxidation states in the bulk of LNMo20 remain unknown. Furthermore, this work claimed that LNMo20 is a mixed oxygen ionic, protonic, and electronic conductor despite the negligible difference in conductivity between dry and wet conditions [139]. This contradiction weakens the credibility of the argument, requiring a profound re-evaluation.

Despite the insufficient research on LNW and LNMo, one can empirically conclude that LNW has better phase stabilising capability while LNMo shows a higher ionic conductivity. Therefore, Han *et al.* utilised the co-doping strategy in $LaNb_{0.8}W_xMo_{0.2-x}O_{4.1}$ (x = 0, 0.02, 0.04, 0.10, 0.16, 0.18, 0.20) to balance phase stabilisation capability and ionic conductivity [165]. The results agree with the above empirical conclusion suggesting that the tetragonal phase can be stabilised in RT when the W substitution level, x, $\geq$0.04, while the total conductivity increases with the increase in the Mo substitution level [165]. Like LNW and LNMo, the modulated structure negatively affects the total conductivity, increasing the activation energy [165]. However, unlike LNW and LNMo, having only one (3+2)D modulated structure, the (3+2)D and (3+1)D modulated structures coexist on these co-doped $LaNbO_4$ [165].

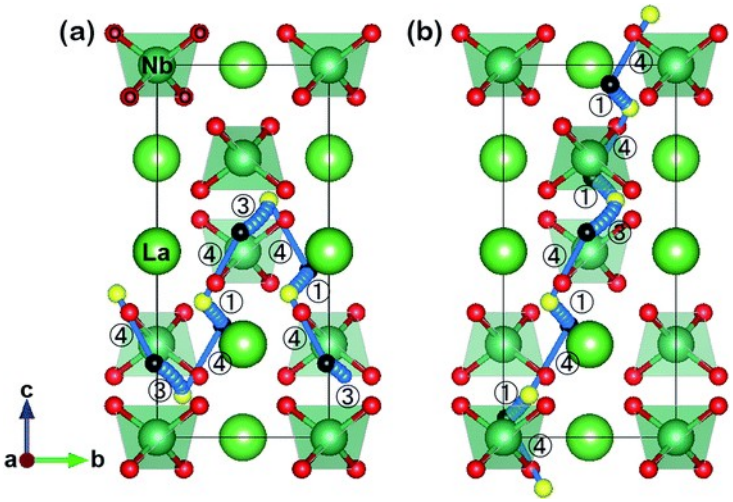


FIGURE 2.16: Two short interstitial oxygen ion transport paths via interstitial mechanism along the *ab* plane, 1 and 3, and one long interstitial oxygen ion transport path via interstitialcy mechanism along the *c* axis, 4. The yellow and black balls represent the stable interstitial oxygen sites, while the blue balls represent the transition interstitial oxygen sites. For simplicity, the interstitialcy path 4 is represented by the blue lines. Path 2 is excluded due to its unfavourable energy barrier. Reproduced from [164] with permission from Royal Society of Chemistry.

2.3.3 Summary

Lanthanum orthoniobates exhibit excellent chemical stability with acceptable ionic conductivity. The protonic conductivity of the acceptor-substituted $LaNbO_4$ is promising. However, the low solubility and the monoclinic-tetragonal phase transition hinder the application of this type of material as a proton-conducting electrolyte.

A two-birds-with-one-stone strategy is the donor substitution in $LaNbO_4$, showing a higher solubility and stabilising capacity of the tetragonal phase. Although the modulated structure in donor-substituted $LaNbO_4$ negatively affects the ionic conductivity, it also offers an excellent opportunity to understand the relationship between structure and conductivity. Moreover, the modulated structure can be adjusted by changing substitution species and levels, which provides a wide templating ability of conductivity in these materials.

Nevertheless, the drawbacks of donor substitution are significant. The substituted donors are compensated by interstitial oxygen ions rather than by oxygen vacancies, resulting in negligible hydration and the corresponding protonic conductivity. Therefore, donor substitution in $LaNbO_4$ was initially regarded a good oxygen ionic conductor. However, donor dopants such as W^{6+} and Mo^{6+} are multivalent, indicating the potential of varying oxidation states in reducing atmospheres. This variation might be crucial for the realisation of protonic conductivity. Although there are abundant publications on the crystal structure and interstitial oxygen conductivity of LNW and LNMo under ambient conditions, the study of these materials in reducing atmospheres is largely overlooked.

Inspired by the potential and insufficient research on W- and Mo-substituted $LaNbO_4$, I will focus on exploring the crystal structures, oxidation states, and conductivities of these materials in hydrogen atmospheres. Hopefully, this work could deepen the understanding of W- and Mo-substituted $LaNbO_4$, especially under hydrogen atmospheres, and promote the search for proton-conducting oxides beyond acceptor-substituted oxides.

Chapter 3

Methodology

3.1 Preparation

Commercial oxide powders, La_2O_3 (99.90%, Alfa Aesar), Nb_2O_5 (99.99%, Sigma-Aldrich), WO_3 (99.80%, Alfa Aesar), and MoO_3 (99.95%, Alfa Aesar), were chosen as starting materials. Due to the hydration nature of La_2O_3, the raw powder could contain a level of $La(OH)_3$. Therefore, La_2O_3 was first dehydrated at 1000 °C for 12 hours [166]. Then, all powders were weighed with an accuracy of 0.001 g and appropriately mixed in a rotary ball mill with acetone (≥99%, VWR) for 24 hours. The mixture was first oven dried at 95 °C for 48 hours and then calcined at 400 °C for 12 hours to completely remove acetone. The collected precursors were pressed to form pellets with a diameter of 13 mm using a uniaxial press held at 360 MPa for 3 minutes. The pellet samples were sintered at 1400 °C for 10 hours with a ramping rate of 10 °C/min. The pellet samples were manually smashed, ground and passed through a 53-μm sieve to obtain the powder samples.

The rest of the pellets were ground for the first time with successive grades of SiC papers (Struers Ltd., UK). Then, they were polished sequentially to 0.25 μm using a semi-automated polisher (TegraPol-15, Struers Ltd., UK) with water-based diamond suspensions (Struers Ltd., UK). After polishing, the samples were ultra-sonicated in acetone and deionised water, then calcined at 400 °C for 4 hours with a ramping rate of 10 °C/min. These two processes are used to remove contaminants introduced during the grinding and polishing processes.

The hydrogen treatment was realised by annealing the pellet or powder samples under 1 bar of 5% H_2 (5% hydrogen in nitrogen gas, BOC) in a tube furnace (TS1-1200, Carbolite Gero Ltd., UK). The tube was initially purged for at least 15 minutes to remove residual air. The samples were then heated to 800 °C for 2 hours with a ramping rate of 10 °C/min. Humidity was controlled by pumping gas through a commercial gas dryer (Drierite 26800 Drying column, $pH_2O \approx 10^{-5}$ atm) for dry atmosphere or through an external water bubbler at room temperature ($pH_2O \approx 0.025$ atm) for wet atmosphere.

The sample preparation processes are summarised as a flow chart shown in Figure 3.1.

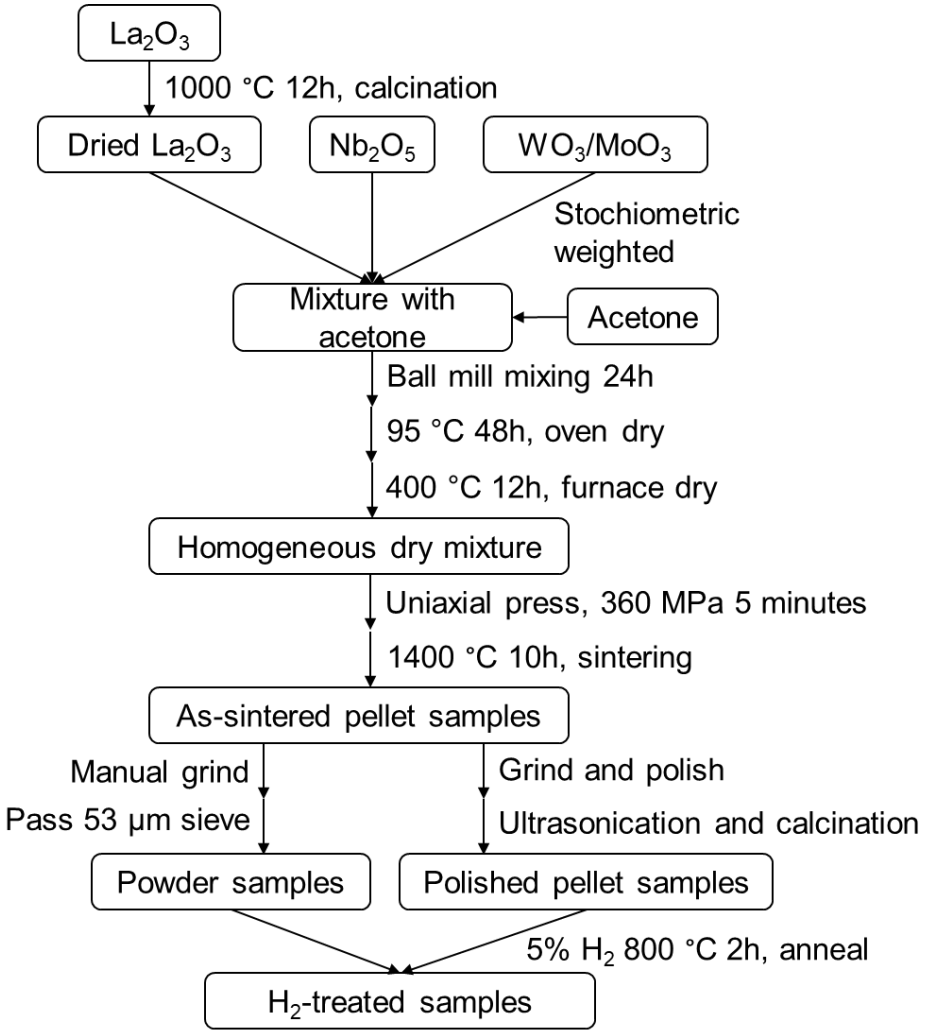


FIGURE 3.1: Flow chart of the sample preparation procedure.

3.2 Density measurement

The density of a solid sample (ρ) can be extracted by Equation 3.1.

$$\rho = \frac{W_a \cdot \rho_l}{W_a - W_l} \tag{3.1}$$

Where W_a and W_l are the weight of the solid sample in air and liquid, and ρ_l is the density of the liquid. Considering the air buoyancy and instrumental error, Equation 3.1 can be rewritten as Equation 3.2.

$$\rho = \frac{W_a \cdot [\rho_l - \rho_a]}{f_i \cdot [W_a - W_l]} + \rho_a \tag{3.2}$$

Where ρ_a and f_i are air density under ambient conditions and the instrumental correction factor, respectively.

In practice, the density of the pellet samples was measured using a laboratory balance (CP124S, Sartorius Ltd., UK) and the density determination kit (YDK 01, Sartorius Ltd., UK). The instrumental correction factor, f_i, is 0.99983 given by Sartorius Ltd. First, the sample mass under ambient conditions was weighted. Then, the sample was immersed in deionised water and boiled for 2 hours to remove air from the surface entirely. After cooling down, the sample was transferred into the density determination kit with deionised water, and the sample mass in the liquid was weighed. The temperature reader recorded the liquid temperature during the measurements with 0.1 °C accuracy. Both masses under ambient conditions and in the liquid were weighed multiple times to reduce error.

3.3 X-ray related techniques

When an incident X-ray beam reaches a material, it will be scattered, absorbed, or transmitted. Suppose that the scattering event is elastic, meaning that the scattered X-ray beam only changes direction. This scattering is called coherent scattering. If the recoil electron is generated during the scattering event, which reduces the energy of the X-ray beam, this scattering is called incoherent scattering. Meanwhile, X-ray absorption is caused by the valence electron hopping, resulting in a photoelectron, Auger electron, or fluorescent X-ray. The outgoing X-ray beam and the electron emitted contain essential information about the material. Therefore, multiple X-ray related techniques have been developed for materials characterisation, summarised in Table 3.1.

TABLE 3.1: Summary of typical X-ray related techniques. Asterisk (*) highlights the techniques used in this work.

Signal source	Output signal	Technique
Scattering	Coherent scattering	X-ray powder diffraction (XRD)*
	Incoherent scattering	-
Absorption	Photoelectron	X-ray photoelectron spectroscopy (XPS)*
	Auger electron	Auger electron spectroscopy
	Fluorescent X-ray	X-ray fluorescence spectroscopy (XRF) & X-ray absorption spectroscopy (XAS-fluorescent)
Transmission	Transmitted X-ray	X-ray absorption spectroscopy (XAS-transmission)*

3.3.1 X-ray powder diffraction

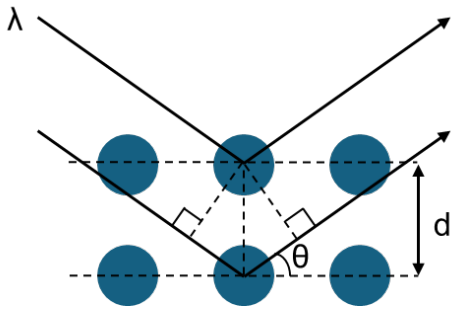


FIGURE 3.2: Schematic representative diagram of Bragg's law.

X-ray powder diffraction (XRD) is selective coherent scattering in a specific direction, and it is one of the most powerful techniques for studying crystal structure. The coherently scattered X-ray beams are usually weak and featureless. However, given the periodicity of the crystal materials, in some specific directions, the X-ray beams interfere constructively with each other, resulting in intensive diffraction phenomena. The well-known Bragg's law has established the relationship between diffraction and crystal structure shown in Figure 3.2 and Equation 3.3 [167].

$$2dsin\theta = n\lambda \tag{3.3}$$

Where n is an integer, λ is the wavelength of the incident X-ray beam, d is the interplanar distance of the hkl plane, and θ is the Bragg angle.

It is worth mentioning that scattered X-ray beams that fulfil Bragg's law are not necessarily observable. Bragg's law only considers the Bragg angle, ignoring the diffraction intensity. In some cases, the diffraction intensity might be eliminated by destructive interference. Equation 3.4 shows the structure factor $F_{(hkl)}$, which governs constructive or destructive interference.

$$F_{(hkl)} = \sum_{i=1}^{N} f_i exp[2\pi i(hx_i + ky_i + lz_i)] \tag{3.4}$$

Where the unit cell contains N atoms, f_i is the atomic scattering factor and x_i, y_i, z_i are the fractional unit cell coordinates.

3.3.2 X-ray powder diffraction refinement

The relative intensity of any diffraction peak can be calculated using Equation 3.5.

$$I = P{\cdot}F^2_{(hkl)}{\cdot}\frac{1 + cos^2 2\theta}{sin^2\theta cos\theta}{\cdot}e^{-2M}{\cdot}A(\theta) \tag{3.5}$$

Where P is the multiplicity factor that depends on the crystal symmetry, $F_{(hkl)}$ is the structure factor mentioned in Equation 3.4, and $\frac{1+cos^2 2\theta}{sin^2 \theta cos\theta}$, e^{-2M}, $A(\theta)$ are the angle, temperature, and absorption corrections. Therefore, one can calculate the diffraction pattern of the reference structure and refine the structure to mimic the measured structure by minimising the weighted sum of squared difference, S_y, as shown in Equation 3.6 [168].

$$S_y = \sum_i w_i (y_{obs,2\theta} - y_{cal,2\theta})^2 \tag{3.6}$$

Where $y_{obs,2\theta}$ and $y_{cal,2\theta}$ are the observed and calculated intensity at the i^{th} observation, respectively [168]. w_i is the weight attributed to the i^{th} observation, which is defined as $1/\sigma_i^2$, while σ_i is the estimated uncertainty [168]. This refinement method was first proposed in 1969 and named Rietveld refinement [168].

However, Rietveld refinement requires a reasonable reference structure, which is often challenging. Later, Armel Le Bail proposed a whole pattern fitting, Le Bail refinement, which does not require a reference structure [169]. Instead, it treats all peak intensities to an arbitrary value, using lattice parameters as the primary input parameters [169]. A set of intensities is then calculated for the least-squares fit to extract new lattice parameters, as shown in Figure 3.3 [169]. This process is equivalent to a self-consistent converged steepest descent minimisation [169]. There are more advantages of Le Bail refinement. It can easily be compiled into existing Rietveld refinement algorithms and converges faster [169].

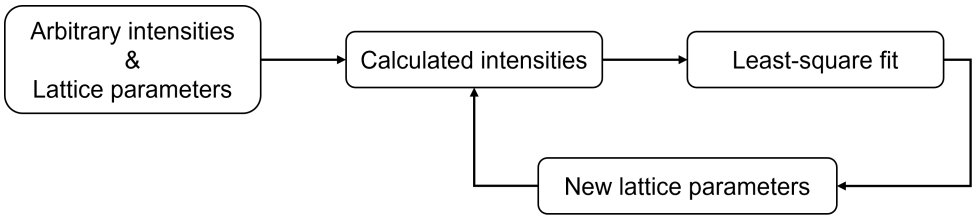


FIGURE 3.3: Flow diagram of Le Bail refinement process.

In addition to the refinement methods, statistical methods are required to check whether the results are good enough. There are three widely used R-factors to evaluate the quality of refinement results [170]. Equations 3.7, 3.8, and 3.9 show the profile residual (R_p), the weighted profile residual (R_{wp}) and the expected profile residual (R_{exp}), respectively.

$$R_p = \frac{\sum |y_{obs,2\theta} - y_{cal,2\theta}|}{\sum y_{obs,2\theta}} \tag{3.7}$$

$$R_{wp} = \left\{ \frac{\sum_i w_i (y_{obs,2\theta} - y_{cal,2\theta})^2}{\sum_i w_i (y_{obs,2\theta})^2} \right\}^{\frac{1}{2}} \tag{3.8}$$

$$R_{exp} = \left\{ \frac{N - P}{\sum_i w_i (y_{obs,2\theta})^2} \right\}^{\frac{1}{2}} \tag{3.9}$$

Where N is the number of observations, and P is the number of refined parameters. The ratio of R_{wp} and R_{exp} is then defined as a goodness-of-fitting factor (GOF), as shown in Equation 3.10.

$$GOF = \frac{R_{wp}}{R_{exp}} \tag{3.10}$$

One should expect the GOF not to be smaller than 1 [170]. For an ideal structure, the numerator of R_{wp} is equal to N, leading GOF to be equal to $\frac{N}{N-P}$, where the minimum value of P is 0 [170]. Generally, a refinement with a GOF smaller than 5 is sufficient [170].

3.3.3 Experimental details of XRD

Powder samples were used for XRD measurements. Room temperature XRD patterns were collected using a PANalytical X'Pert PRO diffractometer (Cu Kα radiation with a nickel filter, $\lambda = 1.5418$ $\AA$) under ambient conditions. The samples were placed on top of a commercial Si (911) XRD sample holder (Bruker). This holder is cut perpendicular to the [911] axis, producing a very low background signal [171]. The 2θ range was set to 20° to 60° with a step size of 0.017° and a holding time of 150 seconds per step.

In-situ high-temperature XRD patterns were collected using a PANalytical Empyrean diffractometer (Cu Kα radiation with a nickel filter, $\lambda = 1.5418$ $\AA$) under flowing compressed air conditions. The samples were loaded on top of a commercial Al_2O_3 high-temperature XRD sample holder (Malvern Panalytical). The measuring temperature was controlled by a high temperature oven chamber (HTK 1200N, Anton Paar) and its built-in water cooling system. The 2θ range was set to 20° to 60° with a step size of 0.013° and a holding time of 150 seconds per step. The samples were heated to 800 °C with a heating rate of 60 °C/min. The high temperature XRD data was then collected from 800 °C to 100 °C with an interval of 100 °C/min. The final RT data were collected after fully cooling. The cooling rate was 20 °C/min. After reaching each measuring temperature, the samples were equilibrated for 20 minutes to ensure thermal homogeneity.

The XRD refinement was performed to determine the lattice parameters using the GSAS-II software [172]. The Rietveld refinement method was first used to obtain the

initial lattice parameters for the Le Bail refinements. Then, the Le Bail refinement was executed to determine more accurate lattice parameters. The reference structures were pristine $LaNbO_4$ at room temperature (ICSD collection code: 430884) and 500 °C (ICSD collection code: 430897) [132, 173].

3.3.4 X-ray photoelectron spectroscopy

X-ray photoelectron spectroscopy (XPS) is a surface sensitive and non-destructive analytical technique. The photoelectron is generated by X-ray absorption. Suppose an incident high-energy X-ray beam hits a valence electron surrounding an atom. The energy from the X-ray might excite this electron from the ground state to the excited state. If this excited electron is close to the surface, it might travel to the surface, eventually overcoming the work function and being released into the vacuum. Based on the above processes, the kinetic energy of the photoelectron is expressed as Equation 3.11.

$$E_K = h\upsilon - E_B - \Phi_{sample} \tag{3.11}$$

Where E_K and E_B are the kinetic and binding energy of the photoelectron, respectively. $h\upsilon$ is the energy of the incident X-ray beam, and Φ_{sample} is the work function of the sample. A spectrometer is used to measure the kinetic energy of the photoelectron. Given that the spectrometer has its work function $\Phi_{spectrometer}$, the sample is electrically connected to the spectrometer, resulting in the contact potential. This potential will accelerate the photoelectron. Therefore, the measured kinetic energy of the photoelectron can be deduced as Equation 3.12.

$$\begin{aligned} E_{K,measured} &= h\upsilon - E_B - \Phi_{sample} + \Phi_{sample} - \Phi_{spectrometer} \\ &= h\upsilon - E_B - \Phi_{spectrometer} \end{aligned} \tag{3.12}$$

Figure 3.4 shows the above correlation between the sample and the spectrometer. Since $h\upsilon$ and $\Phi_{spectrometer}$ terms are known, the binding energy can be determined by measuring the kinetic energy. The energy level of the valence band maximum can also be determined.

The binding energy of the valence electron is affected not only by its surrounding atom but also strongly by the neighbouring bonding environment. This binding energy variation allows XPS to investigate the local bonding environment. For example, a metal oxide cation with a higher valence state, such as W^{6+}, possesses a higher binding energy due to its higher electronegativity [174]. Meanwhile, one can compare the ratio of different elements by comparing the intensity of different valence electrons. The

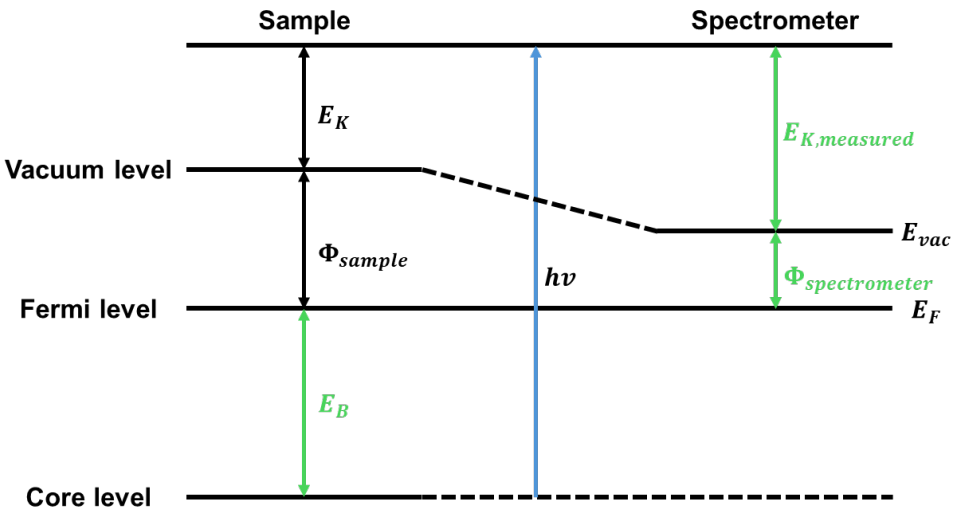


FIGURE 3.4: Schematic diagram of XPS measuring mechanism.

empirical quantitative analysis compares the peak area in the XPS spectra, as shown in Equation 3.13.

$$C_i = \frac{A_i/s_i}{\sum_{i=1}^{n}(A_i/s_i)} \tag{3.13}$$

Where C_i is the molar concentration of the element i, A_i is the peak area, and s_i is the relative sensitivity factor.

It is worth mentioning that since the photoelectrons have to be released from the sample surface, the valence electrons close to the surface have a higher probability of detection. The signal intensity of XPS is empirically described by the Beer-Lambert law, where 95% of all photoelectrons are from the depth from 1 to 10 nm for the normal XPS using Al K_α radiation [175].

3.3.5 Experimental details of XPS

The polished pellet samples were used for XPS measurements. XPS spectra were collected using a K-Alpha XPS instrument (Thermo Fisher Scientific). A monochromatic Al K_α (1486.6 eV) X-ray source generated an incident X-ray beam with a spot size of 400 μm^2. The energy resolution was set to 0.1 eV. A dual beam flood gun (Ar^+ and e^-) compensated for surface charge accumulation and was further corrected by reference to the C 1*s* signal (284.8 eV). The measuring chamber was under high vacuum (<5×10^{-7} mbar) conditions. The iteration XPS spectra were collected by repeated measurements every 30 or 60 minutes. The collected spectra were analysed and the peak fitted using Avantage software (Thermo Fisher Scientific). The relative sensitivity factor, s_i of each peak was experimentally determined by Thermo Fisher Scientific and

built into the software. The Voigt function and the Shirley background function were applied during the peak-fitted processes.

3.3.6 X-ray absorption spectroscopy

X-ray absorption is expressed as Equation 3.14.

$$I_t = I_0 exp(-\mu t) \tag{3.14}$$

Where I_0 and I_t are the incident and transmitted X-ray intensities, respectively. μ is the linear absorption coefficient, and t is the thickness of the sample. The linear absorption coefficient can be estimated using Equation 3.15.

$$\mu \approx \frac{\rho Z^4}{AE^3} \tag{3.15}$$

Where ρ is the sample density, Z is the atomic number, A is the atomic mass, and E is the incident X-ray energy. Therefore, the linear absorption coefficient for a given element increases with the incident X-ray energy decreases. However, the linear absorption coefficient becomes discontinuous when the incident X-ray energy equals the binding energy of valence electrons, especially those on the K and L shells. This strong absorption is called absorption edge, and it is due to the photoelectron effect. The excited valence electrons will relax rapidly, resulting in Auger electrons or fluorescent X-rays. Therefore, there are two modes of X-ray absorption spectroscopy (XAS): one is measuring the transmitted X-ray, and the other is measuring the fluorescent X-ray.

Absorption peaks or oscillations are observed in proximity to the absorption edge, extending over a range of several hundred electron volts on the high-energy side. These structures are called X-ray absorption fine structures (XAFS). XAFS is further divided into two regions: from the pre-edge to approximately 30 eV above the edge, it is referred to as X-ray absorption near edge structure (XANES), while after that, it is termed extended X-ray absorption fine structure (EXAFS) [176].

Figure 3.5(a) presents an example of the XAFS spectrum in Nb K-edge, where the photoelectrons are all excited from 1s orbitals (K-shell). A small pre-edge feature is raised before the absorption edge for transition elements like Nb. This feature is due to the transition of electrons from 1s orbitals to the unoccupied 4d orbitals [177–179]. The double-peak feature after the edge position is called the post-edge feature and usually contains information about the coordination environment [155, 180–182].

The absorption phenomena can be different for the XAFS spectra of other edges. Figure 3.5(b) presents an exemplified XAS spectrum of W L_3-edge. A strong absorption

peak dominates the spectrum called the white line, and it is due to the photoelectrons transitioning from $2p_{3/2}$ orbitals (L-shell) to the unoccupied $5d$ orbitals [183, 184].

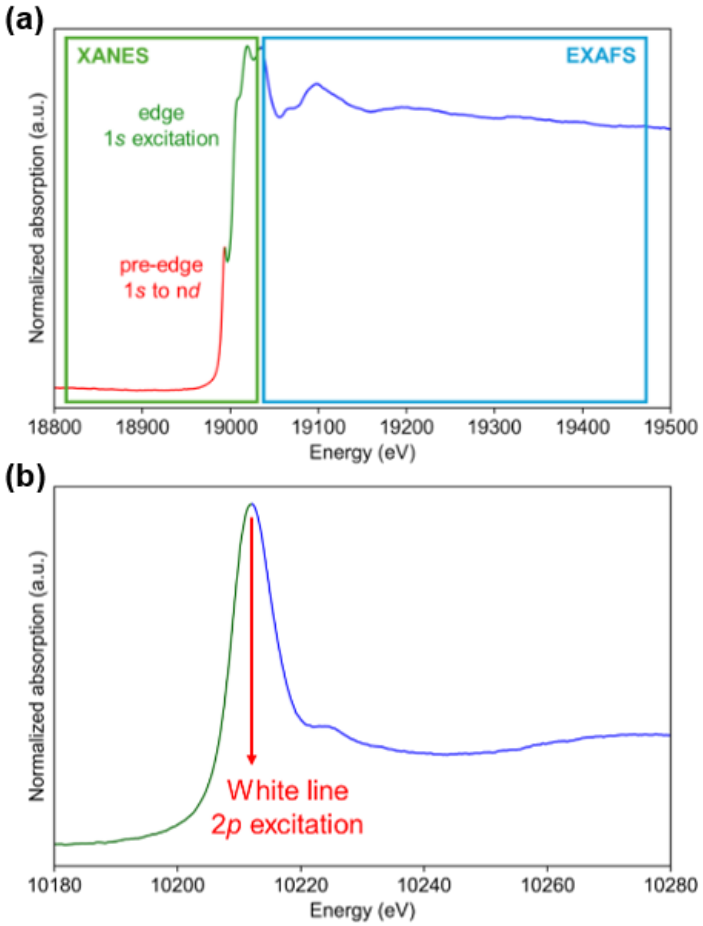


FIGURE 3.5: (a) Example Nb K-edge XAS spectrum, showing X-ray absorption near edge structure (XANES) region and extended X-ray absorption fine structure (EXAFS) region. The letter "n" represents the principal quantum number. (b) Example W L_3-edge XAS spectrum.

The quantitative description of XANES remains challenging [176]. However, the edge position tends to change linearly with the valence states [176, 177]. Therefore, the energy position of the absorption edge in the XANES spectrum can be used to determine the valence states.

Meanwhile, there is a well-developed, though complicated, quantitative description of EXAFS. The oscillations in the EXAFS regions originate from the scattering of photoelectrons by the electrons of the neighbouring atoms, as shown in Figure 3.6 [185]. Therefore, the linear absorption coefficient can be expressed as Equation 3.16 [185].

$$\mu(E) = \mu_0(E)[1 + \chi(E)] \tag{3.16}$$

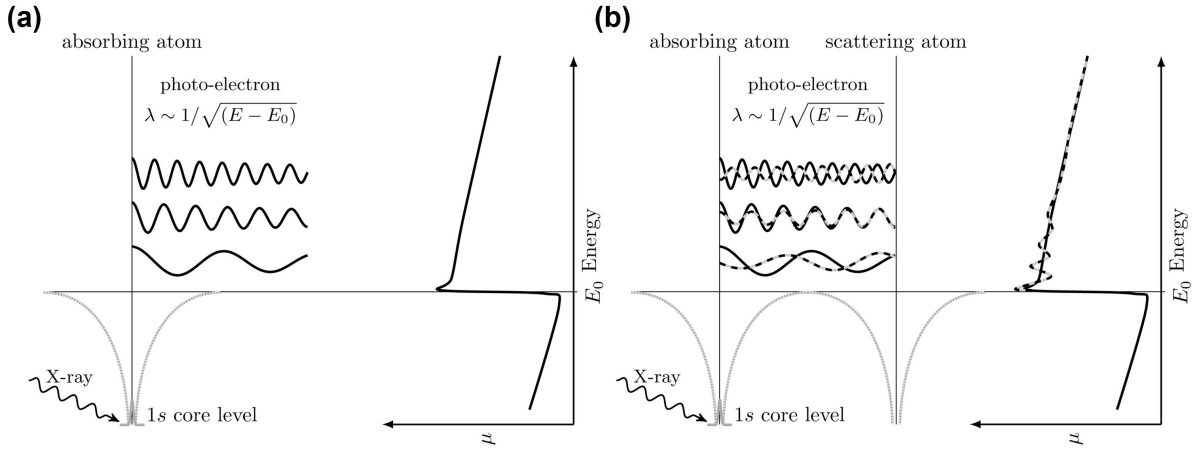


FIGURE 3.6: (a) The absorption process of an isolated atom. No EXAFS is raised. (b) The photoelectron is scattered by the electrons of the neighbouring atom, which interferes with the photoelectron at the absorbing atom, causing EXAFS. The photoelectron travels as a wave. Reproduced from [185] with permission under a Creative Commons Attribution-ShareAlike 3.0 Licence.

Where $\mu_0(E)$ is the smooth background representing the absorption of an isolated atom. The measured $\chi(E)$ from EXAFS spectra can be isolated using Equation 3.16.

$\chi(E)$ in the energy domain can be converted into $\chi(\boldsymbol{k})$ in the kinetic domain based on the wave-particle duality of photoelectrons, as shown in Equation 3.17 [185].

$$\boldsymbol{k} = \left(\frac{2m(E-E_0)}{\hbar^2}\right)^{\frac{1}{2}} \tag{3.17}$$

Where $\boldsymbol{k}$ is the wavevector of the photoelectron, and $\hbar$ is the reduced Planck constant, respectively. Suppose the most straightforward scattering event, in which one photoelectron is scattered by only one neighbouring atom at 0 K, $\chi(\boldsymbol{k})$ can be expressed as Equation 3.18 [185].

$$\chi(\boldsymbol{k}) = \frac{f(\boldsymbol{k})}{\boldsymbol{k}R^2} sin2\boldsymbol{k}R + \delta(\boldsymbol{k}) \tag{3.18}$$

Where R is the distance between two atoms, $f(\boldsymbol{k})$ and $\delta(\boldsymbol{k})$ are the scatter amplitude and scatter phase-shift for the neighbouring atom, respectively. In a more practical scenario, the absorbing atom will be surrounded by many atoms with different types and distances. The interatomic distances also keep changing due to the thermal vibrations. Therefore, Equation 3.18 can be rewritten as Equation 3.19 [185].

$$\chi(\boldsymbol{k}) = \sum_j \frac{N_j f_j(\boldsymbol{k}) e^{-2k^2\sigma_j^2}}{\boldsymbol{k}R_j^2} sin[2\boldsymbol{k}R_j + \delta_j(\boldsymbol{k})] \tag{3.19}$$

Where N is the coordination number, and σ_j^2 is the mean-square-displacement in the interatomic distance to correct the thermal vibration effect. Further considering inelastic scattering events, Equation 3.19 can be rewritten as Equation 3.20 [185].

$$\chi(\boldsymbol{k}) = \sum_j \frac{N_j f_j(\boldsymbol{k}) e^{-2\boldsymbol{k}^2\sigma_j^2} e^{-2R_j/\lambda(\boldsymbol{k})}}{\boldsymbol{k}R_j^2} sin[2\boldsymbol{k}R_j + \delta_j(\boldsymbol{k})] \tag{3.20}$$

Where $\lambda(\boldsymbol{k})$ represents the mean free path of the photoelectron, determining how far it can move before being scattered inelastically. $\lambda(\boldsymbol{k})$ is primarily independent of the samples with a typical value of 3 to 30 $\AA$ [185]. Therefore, EXAFS can only provide information less than 5 $\AA$ because of $\lambda(\boldsymbol{k})$ and R_j^{-2} terms [185]. The above deduction only considers a single excited core-level electron. For multi-excitation, an amplitude reduction term, S_0^2, is introduced. This factor is fully correlated with N with a typical value of 0.7 to 1.0 [185]. Therefore, the final EXAFS equation can be expressed as Equation 3.21.

$$\chi(\boldsymbol{k}) = \sum_j \frac{N_j S_0^2 f_j(\boldsymbol{k}) e^{-2\boldsymbol{k}^2\sigma_j^2} e^{-2R_j/\lambda(\boldsymbol{k})}}{\boldsymbol{k}R_j^2} sin[2\boldsymbol{k}R_j + \delta_j(\boldsymbol{k})] \tag{3.21}$$

The terms in Equation 3.21 can be separated into two parts: those in red are correlated with scattering processes, while those in blue are local structure information. In 1991, Rehr developed the FEFF program, calculating $f(\boldsymbol{k})$ and $\delta(\boldsymbol{k})$ from a known crystal structure [186]. Then, the local structure information can be fitted accordingly [185].

It is worth mentioning that Equation 3.21 only considers the single scattering event where the photoelectron is scattered only once and returns to the absorbing atom [185]. The multiple scattering event, where the the photoelectron is scattered many times before returning, is more complicated. However, the effect of the multiple scattering events is negligible for the first shell analysis of EXAFS [185].

3.3.7 Experimental details of XAS

The synchrotron XAS spectra of the Mo K-edge and the W L_3-edge were collected 6 times in transmission mode with an energy step size of 0.35 eV and a beam spot size of 1×1 mm on the B18 core beamline at Diamond Light Source (DLS, UK) [187]. Since Nb cations have a much higher concentration in the samples, the synchrotron XAS spectra of the Nb K-edge were collected 3 times in transmission mode with identical setups. The energy shift was calibrated using the XAS spectra of Nb (18986 eV), Mo (20000 eV) and W (10207 eV) metal foils, pristine $LaNbO_4$ powder, Nb_2O_5, MoO_3, and WO_3 commercial oxide powders.

Powder samples were used for these measurements. All samples were diluted with cellulose powder (Sigma-Aldrich) and then pressed into pellets with a diameter of 13 mm and a thickness of approximately 1 mm. For the spectra of the Nb K-edge and the Mo K-edge, the sample and cellulose were mixed in a mass ratio of 1:2, while for the W L_3-edge, the sample and cellulose were mixed in a mass ratio of 1:6.

The collected data were calibrated and analysed using Athena software (Demeter software package) [188]. The EXAFS data were fitted using the Artemis software (Demeter software package) [188]. $f(\boldsymbol{k})$ and $\delta(\boldsymbol{k})$ were determined by the in-built FEFF6 program using crystal structures obtained from The Material Project [113]. The amplitude reduction term, S_0^2, and the energy shift calibration term, ΔE_0, are extracted from the EXAFS fittings of Nb_2O_5, MoO_3, and WO_3 commercial oxide powders. The quality of the fit was estimated using an R-factor as presented in Equation 3.22. Usually, an EXAFS fitting with an R-factor ≤ 0.02 is regarded a suitable fitting [185].

$$R - factor = \frac{\sum|\chi_{exp}(\boldsymbol{k}) - \chi_{fit}(\boldsymbol{k})|^2}{\sum|\chi_{exp}(\boldsymbol{k})|^2} \tag{3.22}$$

3.4 Thermogravimetric analysis

Thermogravimetric analysis (TGA) measures the change in mass as a function of temperature and time. Any gas-related reaction that occurs will result in mass changes. For oxides, mass changes are highly correlated with the change in oxygen stoichiometry during oxidation or reduction reactions. For proton-conducting oxides, it could also be correlated with the absorption or release of protons in the form of H_2O or H_2. Therefore, TGA has been widely used to determine the proton content in proton-conducting oxides [189, 190]. However, the buoyancy effect compromises the precise determination of the mass change and, therefore, the actual proton content [191]. Moreover, the mass change might be below the detection limit for oxides with a subtle proton incorporation capability.

3.4.1 Experimental details of TGA

The TGA measurements were performed using an STA 449 F5 Jupiter simultaneous thermal analyser (Netzsch GmbH, Germany) with a mass accuracy of 0.01 mg. Approximately 30 mg of powder samples were used during each measurement. *In situ* TGA measurements were performed using an STA 449 F3 Jupiter simultaneous thermal analyser (Netzsch GmbH, Germany) in the Department of Chemistry, University of Oslo, with a mass accuracy of 0.1 mg. Approximately 1000 mg of powder samples

were used during each *in situ* measurement. The ramp rate was 10 °C/min. The gas flow rate was 50 mL/min for the compressed air purge gas (BOC) in the analytical chamber and 20 mL/min for the protective gas of argon (BOC) in the balance chamber. The blank baseline was collected using Al_2O_3 powder (99.99%, Sigma-Aldrich). An indium-metal reference determined the buoyancy effect at the initial heating stage. The data obtained were analysed using Proteus software (Netzsch GmbH, Germany).

3.5 Electron microscope techniques

Like the incident X-ray beams, incident electron beams can interact with samples, resulting in different informative output signals. The electron-sample interactions are summarised in Figure 3.7 [192, 193].

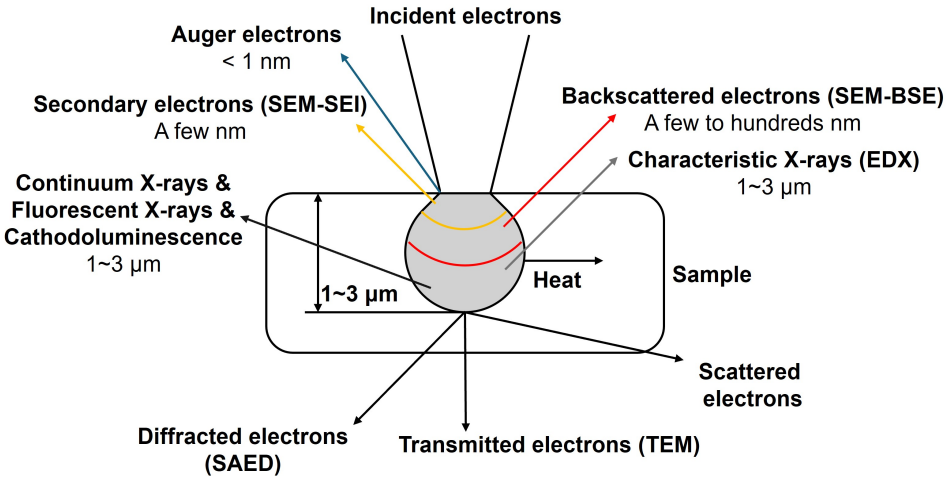


FIGURE 3.7: Schematic diagram of the electron-sample interaction volume. The typical information depth of each signal source was listed [192, 193]. The electron microscope techniques used in this work were highlighted in the bracket.

Scanning electron microscopy (SEM) has two detection modes: secondary electron imaging (SEI) and backscattered electron (BSE) modes. The SEI mode can provide surface morphology images because the secondary electrons are primarily from the surface and are affected mainly by the surface morphology. Meanwhile, backscattered electrons come from the deeper layers and strongly depend on the scattering atoms' atomic number. Therefore, BSE images can indicate compositional homogeneity.

Under incident electron beams, the valence electrons in the outer shell might relax to fill the empty inner orbitals left by excited valence electrons and release characteristic X-rays. The intensity of the characteristic X-rays is proportional to the concentration of the elements in the samples. Therefore, energy-dispersive X-ray spectroscopy

(EDS), which collects the characteristic X-rays, is widely used for compositional analysis. However, the quantitative accuracy of EDS is relatively low, with a general relative error of ±5 wt% in the standard-free analysis mode [194].

Transmission electron microscopy (TEM) is a microscopy technique that detects transmitted electrons. It uses an electron source with an applied voltage of 100 to 300 kV much higher than that of SEM of less than 20 kV to allow sufficient electrons to transmit the sample. The spatial resolution of electron microscopy is proportional to the wavelength of incident electrons, while the wavelength of the incident electrons, λ_e, can be expressed as Equation 3.23.

$$\lambda_e = \frac{hc}{\sqrt{eV(2m_0c^2 + eV)}} \tag{3.23}$$

Where h is the Planck constant, m_0 is the electron's intrinsic mass, e is the charge of an electron, c is the speed of light, and V is the applied voltage [195]. Therefore, the spatial resolution of TEM at the sub-nm level is much higher than that of SEM at >1 nm [192, 193].

Selected area electron diffraction (SAED) is a TEM in-built crystallographic technique. Unlike XRD, SAED can only diffract a user-selected small area by changing apertures and positions. Based on Equation 3.3, the short wavelength of incident electrons gives a measurable d-spacing smaller than the size of an atom.

3.5.1 Experimental details of SEM & TEM

SEM and EDS spectra measurements were performed using a LEO-1525 FEGSEM instrument (Zeiss) with an implemented EDS spectrometer (Oxford Instruments). To avoid electron accumulation, the unpolished pellet samples were sputter coated with a 15-nm chromium layer. The applied voltage was set to 20 kV. The magnification, working distance (WD) and spot size (SS) were optimised to ×2000, 15 mm and 50 nm, respectively. The grain size of each sample was determined using the line intercept method using ImageJ software [196]. The EDS spectrometer was calibrated using a well-polished Cr metal. The EDS spectra and mappings were analysed using INCA software (Oxford Instruments). For readability, the sharpness, brightness, and contrast of each mapping image were adjusted to -25%, 40%, and -40%, respectively.

The TEM images and SAED patterns were obtained using a JEM-2100Plus TEM instrument (JEOL) operated at 200 kV. The powder samples were first dispersed in isopropanol (≥99%, VWR) and ultra-sonicated for 30 minutes. The suspension was then dropped into a TEM copper grid (Ted Pella, Inc.) and dried under ambient conditions.

The d-spacing value and the Miller indices were determined using GMS 3 (Gatan Microscopy Suite) and ImageJ software [196].

3.6 Ultraviolet–visible spectroscopy

Ultraviolet-visible spectroscopy (UV-Vis) is an analytical technique that measures the absorption of light in ultraviolet-visible light regions. Similarly to X-ray absorption, light absorption can be expressed as Equation 3.14, light absorption can be expressed as Equation 3.24.

$$I_t = I_0 exp(-\alpha t) \tag{3.24}$$

Where α and t are the absorption coefficient and the sample thickness, respectively. Given the low energy of UV-Vis lights, the absorption is primarily due to the electron excitation between the valence band (VB) and the conduction band (CB) in the information depth of a few μm [197, 198]. Therefore, UV-Vis spectroscopy has been widely used to estimate the optical band gap of samples via the Tauc method. This method is expressed as Equation 3.25.

$$(\alpha \cdot h\upsilon)^{1/\gamma} = B(h\upsilon - E_g) \tag{3.25}$$

Where h is the Planck constant, υ is the photon's frequency, E_g is the optical band gap, and B is a constant [199, 200]. γ depends on the nature of the optical band gap. If it is a direct band gap, γ is 1/2. If it is an indirect band gap, γ is 2. The experimental assignment of the band gap type is often challenging, especially for materials with flat bands [201]. Therefore, the band gap type is mostly determined using DFT calculations [197]. It is worth mentioning that the optical band gap is not exactly equal to the electronic band gap, but the difference is often marginal [202].

However, measuring the absorption coefficient for opaque samples can be challenging. Alternatively, the sample's reflectance is measured using a diffuse reflectance sphere called UV-Vis-diffuse reflectance spectroscopy (UV-Vis-DRS). The sphere's interior surface is coated by highly reflective white polytetrafluoroethylene (PTFE)-based material, reflecting the lights from the sample to the detector. The measured UV-Vis-DRS spectra can be converted to the corresponding absorption spectra using the Kubelka-Munk function, as Equation 3.26 [203].

$$\alpha \approx F(R_\infty) = \frac{(1 - R_\infty)^2}{2R_\infty} \tag{3.26}$$

Where R_∞ is the relative sample reflectance compared to the standard reference. Therefore, the optical band gap can be extrapolated from UV-Vis-DRS using Equation 3.27.

$$(F(R_\infty)\cdot hv)^{1/\gamma} = B(hv - E_g) \tag{3.27}$$

Figure 3.8(a) presents a typical Tauc plot of an oxide [204, 205]. The absorption curve is analogous to a vertical line for an ideal crystal [204, 205]. The Urbach tail raises due to the presence of defects, as presented in Figure 3.8(a) and (b) [204–206]. The Urbach tail will further deviate to form a pre-edge if the defect concentration is large enough to form inter-band gap defect levels [204–206].

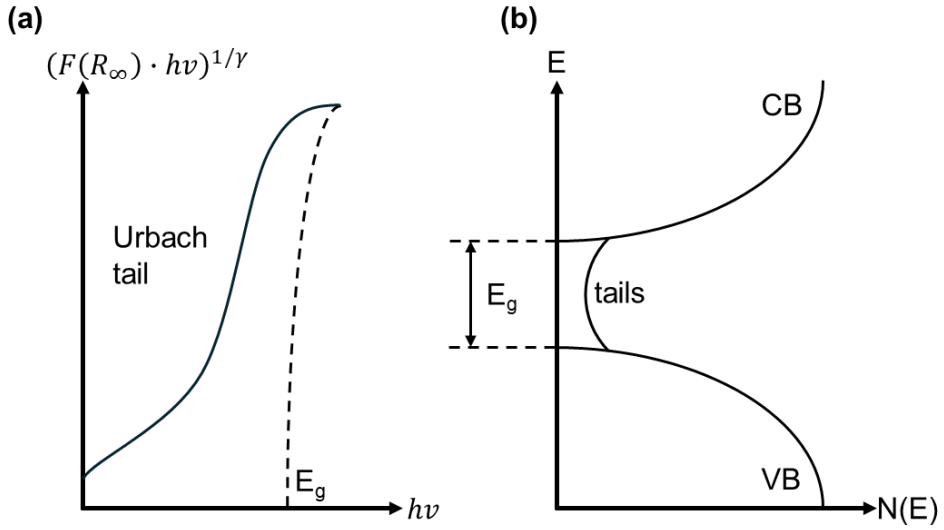


FIGURE 3.8: (a) Typical Tauc plot of an oxide; (b) Density of states $N(E)$ as a function of energy. Adapted from [204, 205] with permission from John Wiley and Sons.

3.6.1 Experimental details of UV-Vis-DRS

The diffuse reflectance spectra were collected from 800 to 200 nm using a Cary-5000 spectrophotometer (Agilent Technologies, Inc.) with a diffuse reflectance sphere accessory and WinUV software (Agilent Technologies, Inc.). The energy interval and the acquisition time per step were set at 0.5 nm and 1 second, respectively. A data glitch at 350 nm was observed in every spectrum due to the light source changeover. A PTFE reference disk (Agilent Technologies, Inc.) was used to calibrate the reflectance baseline. Polished pellet samples were used for UV-Vis-DRS measurements.

3.7 Electron spin resonance

Electron spin resonance (ESR), also known as electron paramagnetic resonance (EPR), is a technique for detecting unpaired electrons. Each atomic orbital can only be occupied by two electrons with a spin quantum number m_s of $\frac{1}{2}$ and $-\frac{1}{2}$. Typically, the energy levels of these two electrons are the same. However, when the external magnetic field is applied, the Zeeman effect will split the energy level into low-energy antiparallel ($m_s = -\frac{1}{2}$) and high-energy parallel ($m_s = \frac{1}{2}$) levels [207]. Suppose a microwave field is applied perpendicular to the external magnetic field. In that case, the unpaired electron in an atomic orbital can be excited from the antiparallel to the parallel level, resulting in a paramagnetic resonance absorption [207]. Equation 3.28 summarises this electron paramagnetic resonance mechanism [207].

$$\Delta E = h\upsilon = \mu_b g B \tag{3.28}$$

Where ΔE is the energy difference between the antiparallel and parallel energy levels. $h\upsilon$ represents the energy of the microwave field. μ_b, g and B are the Bohr magnetron constant (9.274×10^{-24} J/T), g-factor and the external magnetic field, respectively.

The g-factor shifts depending on the electronic configuration of the surrounding atoms. For a free electron, the g-factor, g_e, is equal to 2.003 [207]. For samples containing transition metals with unpaired electrons, the g-factor is typically smaller than 2 [208, 209]. Therefore, each species containing unpaired electrons has a single unique g-factor [207]. The g-factor can even be utilised to identify defects such as oxygen vacancies since defects might trap free electrons [210, 211]. It is worth mentioning that at low temperatures, the g-factor becomes an anisotropic tensor, g_{xx}, g_{yy}, g_{zz} [207]. Besides, the unpaired electrons might interact with neighbouring nuclei, resulting in hyperfine coupling [207]. However, these situations are not applicable to this work and, therefore, are omitted from the discussion.

3.7.1 Experimental details of ESR

The ESR spectra were collected using a Magnettech CW-ESR5000 benchtop spectrometer (Bruker) at 100 K. The microwave frequency and power were set to ~9.4 GHz (X-band) and 2.0 mW (17 dB), respectively. The modulation amplitude and frequency for the absorption resonance spectra were set at 0.5 mT and 100 kHz, respectively. The scanning magnetic field range was set from 290 to 390 mT with a sweep time of 200 seconds. Each spectrum was measured five times. The collected spectra were analysed using the ESRStudio software (Bruker). The ESR spectrum of the empty quartz tube

was collected and used as the correction baseline. Powder samples were used in the ESR measurements.

3.8 Secondary ion mass spectrometry

Mass spectrometry techniques measure the mass-to-charge ratio of charged species. When an electrical field is applied perpendicular to the direction of the charged species, the species are accelerated, and therefore separated as a function of their mass-to-charge ratio. There are three types of mass spectrometer: the magnetic sector mass spectrometer, the quadrupole mass spectrometer, and the time-of-flight (TOF) mass spectrometer. The quadrupole mass spectrometer selectively allows ions of a specific mass-to-charge ratio to reach the detector by modulating the electrical field, while the TOF mass spectrometer detects all ions simultaneously by measuring their flight times. Compared to sector field instruments, which offer high resolution but slower scanning and larger size, TOF provides faster analysis, higher sensitivity, and broader mass range coverage, making it ideal for high-throughput and complex sample analysis.

Secondary ion mass spectrometry (SIMS) is a mass spectrometry technique that collects the signals of secondary ions bombarded by charged primary ion beams. Figure 3.9 schematically summarises the potential interactions when the high energy primary ion beams bombard the surface of a sample under high vacuum conditions [175, 212]. During this bombardment process, a small amount of sputtered species, usually less than 1%, will be ionised and become secondary ions, which is presented as scenario (3) in Figure 3.9 [213, 214]. The SIMS signals obtained from these secondary ions, including ions or ion clusters, can be expressed by Equation 3.29.

$$I_S^x = I_P C_x S \gamma F \tag{3.29}$$

Where I_S^x and I_P are the secondary ion current of the charged species, x, and the primary ion beam current, respectively. C_x is the concentration of the charged species, S is the sputter yield, γ is the ionisation efficiency, and F is the instrumental transmission. The S and γ terms are dependent on the surrounding environment of the secondary ions, also known as the matrix effect. This effect makes quantitive analysis of SIMS results challenging. However, utilising isotopes can bypass this issue since the surrounding environment of isotopes is almost the same. Therefore, SIMS is an ideal technique for studying the proton diffusion process, as the intensities of the proton and deuteron are directly proportional to the concentration in the samples. The diffusion profile in depth can also be studied by combining the primary ion gun with the sputter gun. This method is known as depth profiling.

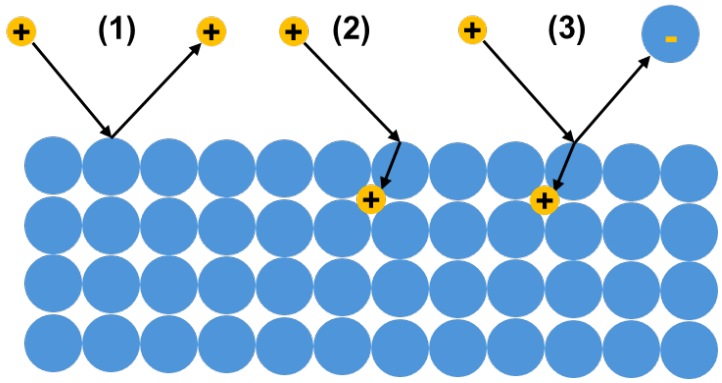


FIGURE 3.9: Schematic diagram of the primary ion-sample interactions: (1) primary ion reflection, (2) primary ion implantation and (3) collision cascade [175, 212]. The positively charged primary ions are coloured in yellow, while the negatively charged secondary ions are coloured in blue.

However, a typical diffusion profile can range from a few to a couple of hundred μm, requiring an extremely long time of sputtering, which is not practical [215]. Therefore, a method called line scan was developed to measure cross-sectional samples, as presented in Figure 3.10 [215].

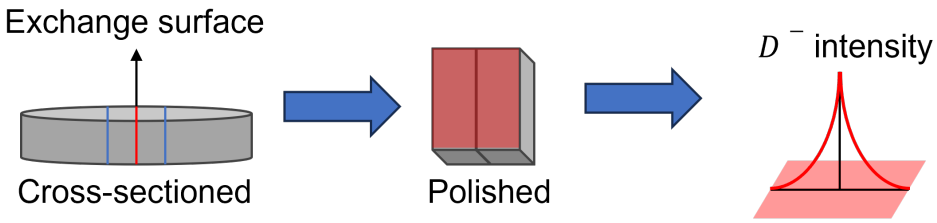


FIGURE 3.10: Schematic diagram of the sample preparation required to obtain diffusion profiles from the line scan method [215].

Crank developed a semi-infinite solution to fit the diffusion profile [216]. The normalized isotopic fraction of deuteron can be expressed as Equation 3.30.

$$\begin{aligned} C'(x,t) &= \frac{C(x,t) - C_{bg}}{C_g - C_{bg}} \\ &= erfc\left[\frac{x}{2\sqrt{D^*t}}\right] - \left[exp(\frac{kx}{D^*} + \frac{k^2t}{D^*}) \times erfc(\frac{x}{2\sqrt{D^*t}} + k\sqrt{\frac{t}{D^*}})\right] \end{aligned} \tag{3.30}$$

Where $C'(x,t)$ is the normalized isotopic fraction of deuteron ($C(x,t)$) corrected by the isotopic background (C_{bg}) and the isotopic fraction of the annealing gas (C_g). x and t are the distance from the surface of the sample and the time spent on the isotopic annealing process. D^* and k are the tracer diffusion coefficient and the surface exchange coefficient. $erfc$ is the complementary error function in mathematics expressed

as Equation 3.31.

$$erfc(x) = 1 - \frac{2}{\sqrt{\pi}} \int_0^x e^{-t^2} dt \tag{3.31}$$

When $x = 0$, $erfc(x) = 1$. Equation 3.30 can be simplified by assuming $x' = \frac{x}{2\sqrt{D^* t}}$ and $h' = \frac{k}{D^*}\sqrt{D^* t}$, as Equation 3.32.

$$C'(x,t) = erfc(x') - [exp(2x'h' + h'^2) \times erfc(x' + h')] \tag{3.32}$$

At the surface, *i.e.*, x=0, Equation 3.32 can be written as Equation 3.33.

$$C'(0,t) = 1 - [exp(h'^2) \times erfc(h')] \tag{3.33}$$

D^* and k can be extrapolated using a non-linear least squares fitting.

The random walk model gives the theoretical description of an uncorrelated and independent ion diffusion event, as Equation 3.34 [84].

$$D_r = \frac{a^2 v_0}{b} exp(\frac{\Delta S}{k_B}) exp(-\frac{\Delta H}{k_B T}) \tag{3.34}$$

Where a is the diffusion distance, v_0 is the attempt frequency, and b is the geometry factor of 2, 4, or 6 for one-, two-, or three-dimensional diffusion, respectively. ΔS, ΔH, k_B, and T are the activation entropy, the activation enthalpy, the Boltzmann constant, and the temperature, respectively. This random diffusion coefficient, D_r, is usually applicable at the microscopic level and can be determined using quasielastic neutron scattering (QENS) and nuclear magnetic resonance (NMR).

Meanwhile, the macroscopic long-range ion diffusion coefficient can be determined by the Nernst-Einstein equation:

$$D_\sigma = \frac{k_B T \sigma}{c q^2} \tag{3.35}$$

Where c and q are the concentration and the charge of the ion. σ is the ionic conductivity. The tracer diffusion coefficient, D^*, obtained from SIMS is also regarded as a macroscopic long-range ion diffusion coefficient [84]. However, it is worth emphasising that D_σ and D^* are not directly comparable due to the ambiguity in the definition of the ion concentration [84].

3.8.1 Experimental details of SIMS

For surface exchange-limited samples, the coating is preferred to ensure a sufficiently detectable diffusion profile [47, 217]. Therefore, the one-sided polished pellet samples

were divided into five groups. Two groups were hand-brushed with Pt paste (Pt 76.3 wt%, fuelcellmaterials) on the polished surface and then fired at 900 °C for one hour with a ramp rate of 1 °C/min. One group was used as the as-sintered references. One uncoated group and one coated group were used for hydrogen treatments, while the rest of the uncoated and coated groups were used for deuteron treatments. After treatments, the Pt paste was carefully removed.

The hydrogen treatments were taken at 800 °C for 6 hours under 1 bar of 5% H_2 gas (BOC) using a tube furnace. Deuteron treatments were taken at 800 °C for 6 hours under 50 mbar of D_2 gas (Linde) in a sealed home-made quartz tube in the Department of Chemistry, University of Oslo.

SIMS data were collected using a TOF-SIMS 5 instrument (ION-TOF GmbH, Germany). The SIMS sample chamber with loaded samples was pumped overnight prior to measurements to remove any surface-absorbed species. The measurements were operated under a high vacuum condition (<1×10^{-8} mbar). The primary ion gun was a Bi_3^+ liquid metal ion gun (LMIG), while the sputter ion gun was Cs^+. An electron flood gun was turned on during the measurements to compensate for the charge accumulation as a result of the low electronic conductivity.

The depth profile measuring area was limited to 100×100 μm, while the sputtering area was set to 300×300 μm to avoid geometric interference. For line scan measurements without sputtering, the measurement area was set to 500×500 μm to cover a long depth range. It should be mentioned that the spatial resolution of the TOF-SIMS 5 instrument is 256×256 pixels. Therefore, the resolution of the depth profile is 25 times better than the line scan measurements, which might result in data inconsistency between the two methods. The collected SIMS data were analysed using SurfaceLab 7 software (ION-TOF GmbH, Germany). The surface roughness and depth of the crater after SIMS measurements were checked by coherence scanning interferometry (CSI) using a Zygo instrument (AMETEK, Inc.).

It is worth mentioning that TOF-SIMS 5 is a dual-ion beam SIMS instrument, which allows the collection of positive or negative ions. Although the proton is a positively charged species, the yield of the SIMS signal of H^+ was found to be lower than H^- [214]. The reason for this difference remains unclear, since the ionisation process is complex without a mature physical description [214]. In this work, the negatively charged SIMS signals were collected to ensure sufficient signal yields.

3.9 Electrochemical techniques

3.9.1 Electrochemical impedance spectroscopy

Electrochemical impedance spectroscopy (EIS) is a widely used technique for measuring electrical properties. Unlike DC measurements, this AC method can deconvolve the impedance responses from different parts of the sample, such as the bulk, the grain boundary, and the surface, according to their time-constant differences [218]. The impedance of a sample at a specific frequency, $Z(\omega)$, can be expressed as Equation 3.36.

$$Z(\omega) = |Z|cos\varphi - i|Z|sin\varphi = Z' - iZ'' \tag{3.36}$$

Where i is the imaginary unit. Z', Z'', $|Z|$ and φ are the real and imaginary parts of the impedance, the magnitude and phase angle of the impedance, respectively.

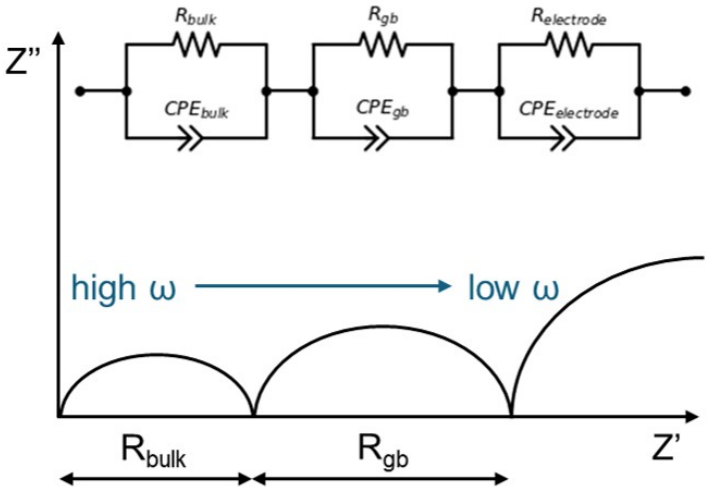


FIGURE 3.11: Schematic Nyquist plot of a typical EIS spectrum of a solid oxide electrolyte with metal electrodes and its corresponding equivalent circuit model [219]. The notation "gb" is short for grain boundary.

Usually, an impedance response contains resistive and reactive components simplified by a resistance (R) and a capacitance (C) in parallel [219]. Then, the time constant, τ, of the response is defined as Equation 3.37.

$$\tau = RC \tag{3.37}$$

However, the reactive component is never ideal. Therefore, a hypothetical electrical component, the constant phase element (CPE) is proposed to replace the capacitance. The impedance of a CPE is determined as Equation 3.38.

$$Z(\omega)_{CPE} = \frac{1}{T(i\omega)^P} \tag{3.38}$$

Where T and P are the pseudo-capacitance and phase angle, respectively. The phase angle is used to evaluate how analogous a CPE is to an ideal capacitance with a value range between 0 and 1. The CPE reduces to an ideal capacitance when $P = 1$. The model, which consists of a resistance and a constant phase element in parallel, is called the R-CPE component. The effective capacitance of a CPE in an R-CPE component can be deduced as Equation 3.39.

$$C = \frac{(RT)^{\frac{1}{P}}}{R} \tag{3.39}$$

Figure 3.11 presents a typical EIS spectrum of a solid oxide with metal electrodes consisting of three impedance responses: bulk, grain boundary and electrode/interfacial responses [219]. This figure is also called the Nyquist plot. The spectrum can be simplified using an electrochemical equivalent circuit (EEC) model consisting of a series of R-CPE elements [219].

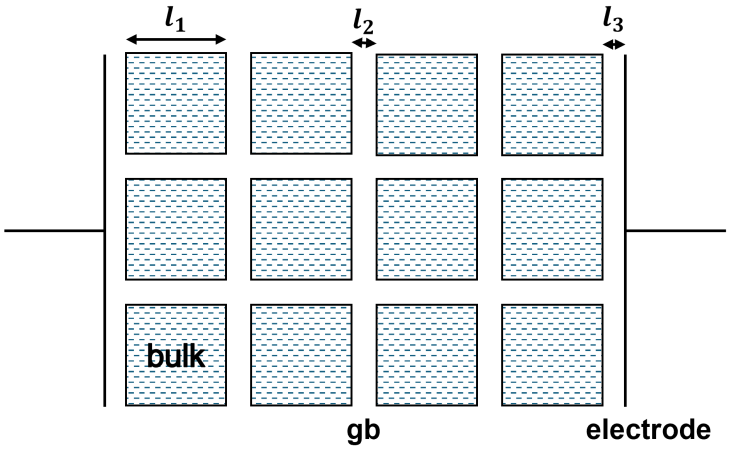


FIGURE 3.12: Schematic diagram of the bricklayer model. The notation "gb" is short for grain boundary. Adapted from [219] with permission from John Wiley and Sons.

Suppose an ideal solid oxide electrolyte composed of cube-shaped grains, "bricks", as shown in Figure 3.12. The length of each grain is l_1, while the length of the grain boundaries is l_2, and the length of the electrode/interfaces is l_3. Given the inverse correlation between the capacitance and the thickness, the capacitance ratio of each response can be expressed as Equation 3.40.

$$\frac{C_{bulk}}{C_{gb}} = \frac{l_2}{l_1}$$
$$\frac{C_{gb}}{C_{electrode}} = \frac{l_3}{l_2} \tag{3.40}$$

Therefore, Irvine *et al.* utilised this bricklayer model to assign the capacitance value ranges to each impedance response, as presented in Table 3.2 [219]. By fitting the obtained EIS spectra with a proper EEC model, one can estimate the capacitance of each semicircle and assign it to the electrochemical impedance response. Meanwhile, the resistance of each response can also be separated for detailed analysis. To directly compare the resistance of different samples, the resistance is often normalized to the area-specific resistance (ASR) to exclude the dimensional differences.

TABLE 3.2: Capacitance value ranges and their possible corresponding response. Adapted from [219] with permission from John Wiley and Sons.

Capacitance (F)	Impedance response
$10^{-12} - 10^{-11}$	Bulk
$10^{-11} - 10^{-8}$	Grain boundary
$10^{-9} - 10^{-7}$	Surface
$10^{-7} - 10^{-5}$	Sample-electrode interface

Before analysing an EIS spectrum, it is essential to validate the quality of the collected data. An ideal EIS spectrum should be a linear, time-invariant, and causal system [220]. The real part of this system can be calculated mathematically from its imaginary part using the Kramers-Kronig (KK) relations and vice versa, as Equation 3.41 [220]. Therefore, for example, one can separate the real part of an EIS spectrum and use the KK relations to calculate the ideal imaginary part [220]. If the data quality is sufficient, the residual between the obtained and calculated imaginary parts should be reasonably small. This validation also works vice versa.

$$Z_{Re} = \frac{2}{\pi}\int_0^\infty \frac{\omega' \cdot Z_{Im}(\omega')}{\omega^2 - \omega'^2} d\omega'$$
$$Z_{Im} = \frac{2}{\pi}\int_0^\infty \frac{\omega' \cdot Z_{Re}(\omega')}{\omega^2 - \omega'^2} d\omega' \tag{3.41}$$

The temperature dependence of the total conductivity of a solid oxide electrolyte can be described as a classical Arrhenius equation, as Equation 3.42.

$$ln\sigma = -\frac{E_a}{k_B T} + lnA \tag{3.42}$$

Where E_a is the activation energy in the unit of eV or kJ/mol and A is the pre-exponential factor, respectively. k_B and T are the Boltzmann constant and temperature, respectively.

Therefore, by plotting $ln\sigma$ as a function of $-\frac{1000}{T}$, one can extrapolate the activation energy from the slope of $-\frac{E_a}{k_B \cdot 1000}$. The activation energy is an important factor in determining the type of charge carriers and their mobilities. For instance, the activation energy of a proton-conducting oxide is usually of $\leq$0.5 eV, while the activation energy of an oxygen ion-conducting oxide is higher [48, 85].

3.9.2 Experimental details of EIS

The EIS spectra were collected using a Solartron 1260A frequency analyser implemented with a Solartron 1296 dielectric interface (Solartron Analytical Ltd.). The sample holder was home-made in a two-probe configuration. The measuring temperature range was 400 to 900 °C with an interval of 50 °C. The spectra of the heating and cooling processes were both collected. After reaching the highest temperature, the samples were dwelled for 2 hours before measuring the spectra of the cooling process. A K-type thermocouple was placed beside the sample to record the exact temperature. The frequency range was 1 MHz to 1 Hz with 30 sampling points per logarithmic decade. The AC potential was set to 100 mV during measurements without DC bias. The measuring atmospheres were controlled by pumping gas from the cylinders (O_2, compressed air, N_2 and 5% H_2, BOC) through the sample holder. Humidity was controlled by pumping gas through a commercial gas dryer (Drierite 26800 Drying column, $pH_2O \approx 10^{-5}$ atm) for dry atmosphere or through an external water bubbler at room temperature ($pH_2O \approx 0.025$ atm) for wet atmosphere. The oxygen partial pressure of dry N_2, dry and wet 5% H_2 was calibrated simultaneously using a ZrO_2 tube oxygen sensor [221].

The Pt paste (Pt 76.3 wt%, fuelcellmaterials) was hand-brushed on both sides of the polished pellet samples and then fired at 900 °C for 1 hour with a ramp rate of 1 °C/min. The area of the Pt electrode for both sides was limited to 0.28 cm^2. The thickness of the samples was measured using a micrometre screw.

The obtained spectra were validated by the KK-test using Lin-KK software (KIT.edu) and analysed using ZView4 software (v4.0h, Scribner Associates) [220].

3.9.3 Hebb-Wagner polarisation method

The total conductivity, σ_{tot}, of a typical solid oxide electrolyte is the sum of ionic, σ_i, and electronic, σ_e, conductivities. The ratio of each partial conductivity to the total conductivity is defined as the transport number, t, as Equation 3.43.

$$t_e = 1 - t_i = \frac{\sigma_e}{\sigma_i + \sigma_e} = \frac{\sigma_e}{\sigma_{tot}} \tag{3.43}$$

Where t_e and t_i are the transport number of electrons and ionic charge carriers, respectively. Given that σ_{tot} can be estimated from EIS spectra, one can determine t_e and t_i if partial conductivities can be separated from each other. Hebb-Wagner polarisation method (HW-method) is one of the most convenient and widely used methods for separating partial conductivities [222–228]. The key idea of this method is to use a blocking electrode layer to screen ionic conductivity, or vice versa [222–225]. A dense metal disk, such as Pt, is usually used as an ionic blocking layer, and a typical Hebb-Wagner polarisation cell configuration is **(dense Pt disk|solid oxide electrolyte|porous Pt electrode)** [224, 225]. The airtight adhesive further covers the side of the dense Pt disk to prevent any electrode response. When a DC bias is applied, a current perturbation can be observed, and it generally becomes stable. However, if there is a gas leakage on the adhesive, the current cannot reach stability, and the transport number is ill-estimated [227].

3.9.4 Experimental details of HW-method

Figure 3.13 presents the schematic configuration of the Hebb-Wagner polarisation cell used in this work. A dense pure Pt disk with a thickness of 0.2 mm was used as the ion blocking layer and was firmly attached on one side of the polished pellet sample. High-temperature ceramic adhesive (Aremco Ceramabond 885) was used to ensure the polarisation cell was airtight on the blocking side. The Pt paste (Pt 76.3 wt%, fuelcellmaterials) was hand-brushed on the other side to be used as a porous electrode. The electrode area was limited to 0.28 cm^2. The thickness of the samples was measured using a micrometre screw. Before measurements, the fabricated cell was first dried at RT for 2 hours and then heated to 900 °C for 1 hour with a ramping rate of 1 °C/min.

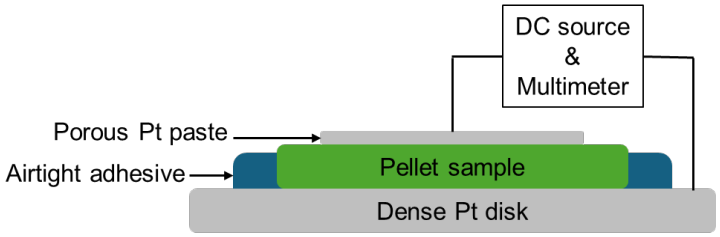


FIGURE 3.13: Schematic configuration of the Hebb-Wagner polarisation cell used in this work.

Measurements were taken in a ceramic heater sample stage (Nextron Corporation). A K-type thermocouple was placed beside the sample to record the exact temperature.

The measuring atmospheres and humidities were controlled by the same setup discussed in Section 3.9.2. A constant DC voltage was applied to the cell using the ModuLab XM ECS Electrochemical System (Solartron Analytical Ltd.) and the DC current data as a function of time were collected using the same electrochemical system.

3.10 Neutron techniques

3.10.1 Neutron scattering techniques

Directly probing hydrogen is a challenging task due to the small size and light mass nature of hydrogen. For laboratory-based X-ray-related techniques, the likelihood of interaction, known as the cross section, between an incident X-ray beam and a target shows a strong element dependence [190]. Therefore, the proton is often untraceable under X-rays [190]. In contrast, the neutron beam has the largest total cross section with protons of 82.02 barns (1 barn = 10^{-24} cm^2), which is significantly larger than other elements [229]. Figure 3.14 presents the schematic comparison of the relative total cross sections of various elements for X-rays and neutrons, clearly indicating the high sensitivity of protons in neutron techniques [230].

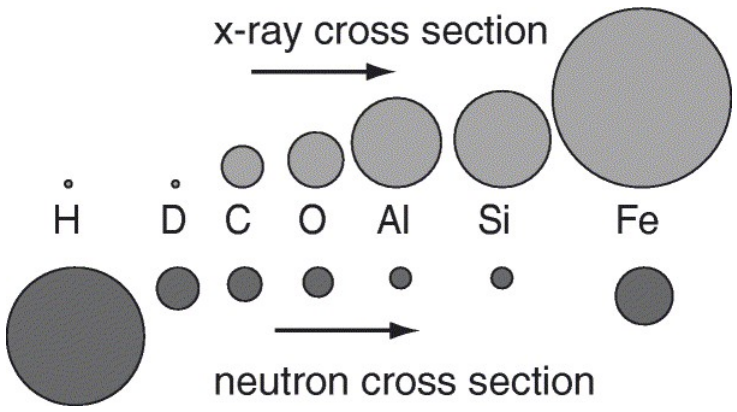


FIGURE 3.14: Schematic comparison of the relative total cross sections of various elements for X-rays and neutrons. Reproduced from [230] with permission from Elsevier.

Elastic neutron scattering for crystal materials is also called neutron powder diffraction (NPD), as it is similar to X-ray diffraction and contains structural information [231]. However, in contrast to XRD, NPD has an additional incoherent scattering intensity mainly affected by the isotope and/or non-zero nuclear spins [229, 231]. More specifically, the coherent scattering analogy to XRD contains the collective structural information of the whole lattice. In contrast, incoherent scattering contributes to the remaining

intensity of individual nucleus behaviours, which mainly affects the background intensity [231]. Most elements are dominated by coherent scattering, while hydrogen is an exception [229, 231]. The coherent and incoherent cross sections of hydrogen are 1.76 and 80.26 barns, respectively. This vast cross-sectional difference means that the NPD background intensity of a protonated material should be significantly higher than its deprotonated counterpart [232, 233]. Therefore, the NPD background intensity change can be used as a direct indicator to investigate the protonation or hydration process [190, 232, 233].

3.10.2 Neutron Compton scattering

Recently, a new type of mass-selective inelastic neutron spectroscopy technique, neutron Compton scattering (NCS), has shown its potential in probing protons [234–241]. The neutron Compton effect describes the inelastic interaction between a neutron and a nucleus, as presented in Figure 3.15 [242–244].

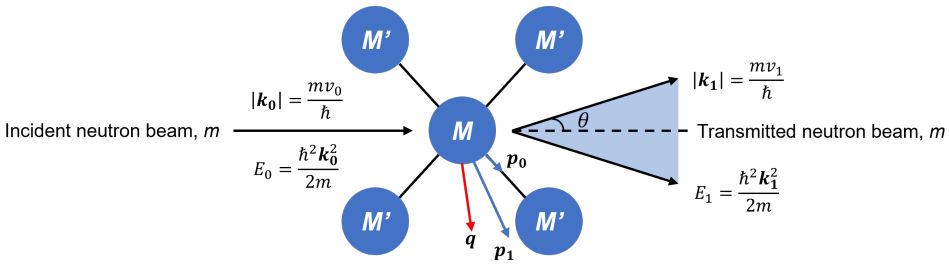


FIGURE 3.15: Schematic diagram of the kinematics of the neutron Compton scattering process [244].

When the incident neutron of mass m interacts with the target nucleus of mass M, which bonds locally with neighbouring nuclei of mass M' and has the initial momentum of $\boldsymbol{p_o}$, the energy transferred from neutron to nucleus is $\omega = E_0 - E_1$. The associated momentum transfer is $\boldsymbol{q} = \boldsymbol{k_1} - \boldsymbol{k_0}$ with the magnitude of $|\boldsymbol{q}| = (\boldsymbol{k_0}^2 + \boldsymbol{k_1}^2 - 2\boldsymbol{k_0}\boldsymbol{k_1}cos\theta)^{1/2}$ and the scattering angle of θ [242–244]. In practice, energy transfer can be detected using a TOF neutron spectrometer, as expressed in Equation 3.44 [242–244].

$$t = \frac{L_0}{v_0} + \frac{L_1}{v_1} + t_0 \tag{3.44}$$

Where v_0 and v_1 are neutron velocities before and after the scattering process, respectively. L_0 and L_1 are the distance from the beam source to the sample holder and from the sample holder to the detector at scattering angle of θ. t_0 is the predetermined spectrometer dead time. Therefore, for a TOF detector placed at a fixed scattering angle, θ, with a fixed final neutron energy, E_1, the energy and momentum of the incident neutron beam and the energy transfer can be extrapolated [242–244]. The count rate

of $C(t)$ in the TOF domain can then be transformed into the dynamic structure factor of $S(|\boldsymbol{q}(t)|, \omega(t))$, where one should observe a recoil peak Doppler-broadened by the nuclear momentum distribution (NMD) [242–244]. Such broadening often leads to an overlap between the recoil peaks of different nucleus species. To ensure good mass resolution, placing a set of detectors at different scattering angles with a preference for high-angle is necessary.

The high momentum transfer from the epithermal neutron to a nucleus, $\boldsymbol{q}(t)$, leads to a dynamic structure factor, $S(|\boldsymbol{q}(t)|, \omega(t))$, which can be described by the so-called impulse and incoherent approximation and convolution approximation. Within these approximations, scattering occurs so rapidly that the distinction between the coherent and incoherent cross-section becomes immaterial. In consequence, the coherent and incoherent structure factors merge into the so-called total structure factor, which depends only on the total scattering cross-section. This unique feature renders the NCS technique sensitive to every scattering event, thus improving the detection limit [242–244]. Based on these approximations, the total count rate of a given sample can be expressed as Equation 3.45 [242–244].

$$\begin{aligned} C(t) &= [E_0(t)I(E_0(t))] \sum_{i_M} A_{i_M} S_{i_M}(|\boldsymbol{q}(t)|, \omega(t)) \\ &= \frac{E_0(t)I(E_0(t))}{\hbar^2 |\boldsymbol{q}(t)|} \sum_{i_M} A_{i_M} M J_{i_M}(y_{i_M}(t)) \end{aligned} \tag{3.45}$$

Where the prefactor, $E_0(t)I(E_0(t))$, is the normalization of the NCS spectrum to the incident neutron spectrum. $\hbar$ is the reduced Planck constant. A_{i_M} is the proportionality constant representing the contribution from the nucleus species indexed i_M, and it is proportional to the product of the stoichiometry of the species in the sample and the total cross section of this species. $S_{i_M}(|\boldsymbol{q}(t)|, \omega(t))$ can be approximated to $\frac{M}{\hbar^2 |\boldsymbol{q}(t)|} J_{i_M}(y_{i_M}(t))$ by applying the impulse approximation [242, 244]. This approximation assumes that a neutron recoils freely after being struck by a nucleus, meaning that the neutron travels along a straight line and with a constant velocity [242, 244].

The so-called West scaling variable, $y_{i_M}(t)$, can be interpreted as the longitudinal momentum of a given nucleus, as expressed in Equation 3.46 [242–244].

$$y_{i_M}(t) = \frac{M}{\hbar^2 |\boldsymbol{q}(t)|} \left(\omega(t) - \frac{\hbar^2 |\boldsymbol{q}(t)|^2}{2M} \right) \tag{3.46}$$

A nucleus with a mass of M possesses a fixed momentum at a given moment. Every time a neutron scatters another nucleus of the same type in the sample, it randomly samples the momentum distribution of this nucleus. After many such collisions, the sum of different scattering processes from individual neutrons leads to

a probability distribution termed the longitudinal momentum distribution or NMD, $J_{i_M}(y_{i_M})$ [242–244]. The most common expression of the NCS profile is an isotropic single-dimensional Gaussian, as Equation 3.47 showed [242–244].

$$J_{i_M}(y_{i_M}) = \frac{1}{\sqrt{2\pi\sigma^2}} exp\left(-\frac{y^2}{2\sigma^2}\right) \tag{3.47}$$

Where σ is the standard deviation of NMD.

The impulse approximation is not practical due to the effects originating from the neighbouring nuclei [244]. An additive term called the final state effect (FSE) correction needs to be added to Equation 3.47. In practice, the FSE correction is generated automatically based on the shape of $J_{i_M}(y_{i_M})$, and is proportional to the third derivative of $J_{i_M}(y_{i_M})$ over y_{i_M} for each nucleus [242–244]. Further considering the instrumental mass-dependent resolution, the final NCS expression can be written in Equation 3.48 [242–244].

$$C(t) = \frac{E_0(t)I(E_0(t))}{\hbar^2|\boldsymbol{q}(t)|} \sum_{i_M} A_{i_M} M \left(J_{i_M}(y_{i_M}(t)) - \frac{\sigma\sqrt{2}}{12|\boldsymbol{q}(t)|} \frac{d^3 J_{i_M}(y_{i_M}(t)}{dy_{i_M}(t)^3} \right) \times R_{i_M}(y_{i_M}(t)) \tag{3.48}$$

Where $R_{i_M}(y_{i_M}(t))$ is the resolution function [242–244].

Importantly, in the NCS technique, there is no need to assign peaks. Given a sample composition, the mass of each nucleus uniquely determines the peak position. The position of a recoil peak is given by Equation 3.49 [243].

$$\frac{v_1(t)}{v_0(t)} = \frac{cos\theta + \sqrt{(M/m)^2 - sin\theta^2}}{M/m + 1} \tag{3.49}$$

Where M and m are the mass of neutrons and nuclei, θ is the scattering angle, $v_0(t)$ and $v_1(t)$ are the initial and velocities of neutrons, and t is the TOF flight. Therefore, one can expect that when $M = m$, *i.e.*, the neutron scattering from a proton, this equation reduces to $v_1/v_0 = cos\theta/2$. Therefore, the proton can only be measured at forward scattering angles, while the rest of the heavier nuclei dominate the backscattering angles [243]. This selective measurement of protons offers a unique advantage in proton-related studies.

3.10.3 Experimental details of NPD & NCS

NCS and NPD measurements were performed concurrently on a neutron Compton scattering spectrometer, VESUVIO, at the ISIS Neutron and Muon Source, Rutherford

Appleton Laboratory, UK [242]. The instrumental configuration of the VESUVIO spectrometer is presented schematically in Figure 3.16 [235]. The powder samples of ∼30 g each were loaded into square-shaped Al containers of 0.1 mm wall thickness and measured at RT. The cross-sectional area between the neutron beam and a sample is about 20 cm^2, while the proton detection limit of neutron Compton scattering in VESUVIO is 38.4 $\mu mol/cm^2$ [238, 245].

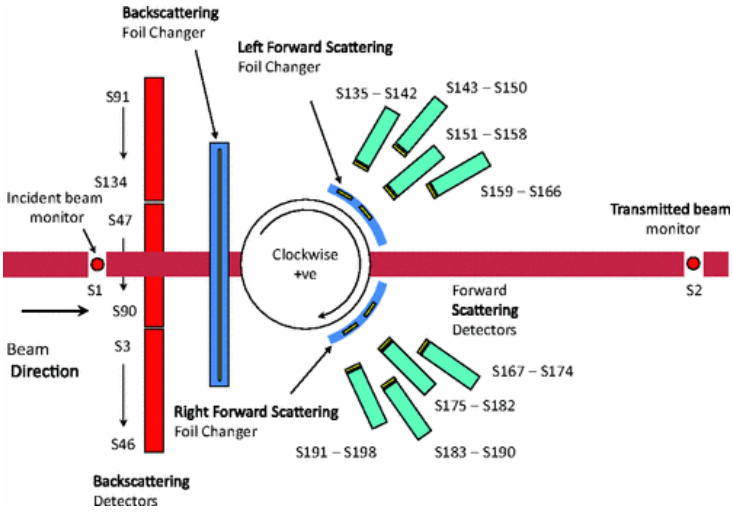


FIGURE 3.16: Schematic diagram of VESUVIO spectrometer. The foil changers are placed in between the sample and sensors to fix the value of the final energy of the neutrons in the so-called inverted-geometry configuration. Reproduced from [235] with permission from American Physical Society.

The raw data from NPD were processed and visualised using Mantid software [246]. NCS raw data were reduced and fitted using the "VESUVIO analysis" algorithm implemented in Mantid software [247]. The mathematical expression for the single-dimensional Gaussian fitting process was given in the previous section. The transmission coefficient required for NCS fittings was estimated using a Beer-Lambert law-based "VESUVIO Transmission" algorithm implemented in Mantid software [248]. The initial guessed NMD width of each element was estimated using the "VESUVIO Peak Prediction" algorithm implemented in Mantid software, which is based on a bond-free single nucleus model [247]. The relative intensity ratio of each element except H and Al was predetermined using the techniques mentioned above. The NMD width of Al, which is the sample container, was determined from the blank measurement and fixed to 13.5±0.5 $\AA^{-1}$.

Chapter 4

Exploring the behaviours of W- and Mo-substituted $LaNbO_4$ under hydrogen atmospheres

This chapter presents a comprehensive study exploring the behaviours of W- and Mo-substituted $LaNbO_4$ under hydrogen atmospheres from mainly crystal structural, compositional, and redox perspectives. First, the successful synthesis of the target samples was confirmed. The pristine samples were then treated with hydrogen and investigated using multiple techniques, such as XRD, XPS, and SEM. The excellent stability of W-substituted $LaNbO_4$ was uncovered compared to the strong reduction of Mo-substituted $LaNbO_4$.

4.1 Validation of synthesis

The relationship between unit cell parameters, miller indices and d-spacings for monoclinic and tetragonal phases can be expressed as Equation 4.1.

$$\begin{aligned} Monoclinic: \frac{1}{d^2} &= \frac{1}{sin^2\beta}\left(\frac{h^2}{a^2} + \frac{k^2 sin^2\beta}{b^2} + \frac{l^2}{c^2} - \frac{2hlcos\beta}{ac}\right) \\ Tetragonal: \frac{1}{d^2} &= \frac{h^2+l^2}{a^2} + \frac{k^2}{b^2} \end{aligned} \tag{4.1}$$

Where h, k, l, and d are the Miller index and d-spacing. a, b, c and β are lattice parameters. One can find that when $\beta = 90°$ and $a = c$, there is a change to 4-fold symmetry, and the monoclinic phase will transition to the tetragonal phase. A progressively changed β angle has been reported in the *in-situ* high-temperature XRD studies of pristine $LaNbO_4$ [132, 173]. The β angle changes from $\sim$94° at RT to eventually 90° becoming a tetragonal phase [132, 173]. Therefore, the β angle was suggested to be used as an indicator of the symmetry of $LaNbO_4$ based materials [132, 151, 152, 249].

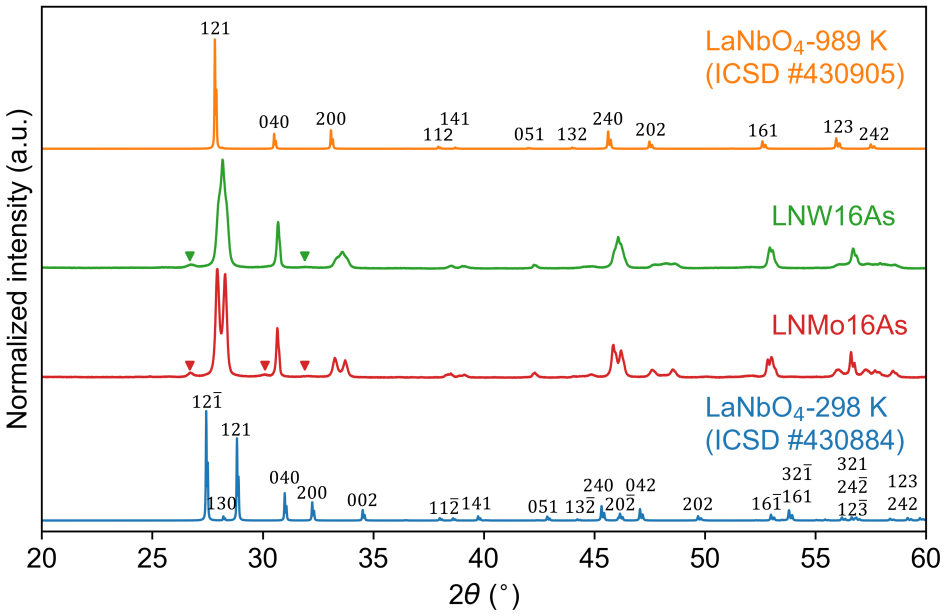


FIGURE 4.1: XRD patterns of LNW16 and LNMo16, together with monoclinic and tetragonal phases of pristine $LaNbO_4$ [132, 173]. The reflections from the modulated structure in LNW16 and LNMo16 are marked by the ∇ symbol.

Figure 4.1 presents the as-sintered 16% W- and Mo-substituted $LaNbO_4$, hereinafter denoted as LNW16As and LNMo16As, respectively. Compared to the pristine monoclinic fergusonite phase $LaNbO_4$ at RT, one noticeable feature of LNW16As and LNMo16As is that many peaks are closer to each other, more similar to the pristine tetragonal scheelite phase $LaNbO_4$ at high temperatures. Especially for LNW16As, the peak with the highest intensity becomes inseparable. This peak merging proves the high-temperature phase stabilising ability of W^{6+} and Mo^{6+} substitution in $LaNbO_4$ [136, 137, 151, 152]. Le Bail refinements were conducted to extract the β angle of both samples, as shown in Figure 4.2. The β angle of LNW16As and LNMo16As is 90.663(3)° and 90.968(3)°, respectively, suggesting a relatively better high-temperature phase stabilising ability of W^{6+} substitution than Mo^{6+} substitution. However, the β angle of >90° also suggests that the tetragonal phase does not fully stabilise in RT.

Figure 4.3 shows *in-situ* high-temperature XRD patterns of LNW16As and LNMo16As. The patterns shift to a lower 2θ angle with increasing temperature due to thermal expansion of the lattice. The higher background intensity at the higher 2θ angle is due to the use of an auto-slit, which probes a larger sample volume at a higher 2θ angle. For LNW16As, the phase becomes fully tetragonal at 200 °C, while for LNMo16As, the transition occurs at 300 °C. These transition temperatures are inconsistent with the phase diagrams presented in Figure 2.11 [151, 152]. In addition, it was observed that the RT patterns in Figure 4.3 are not exactly the same as the patterns in Figure 4.1.

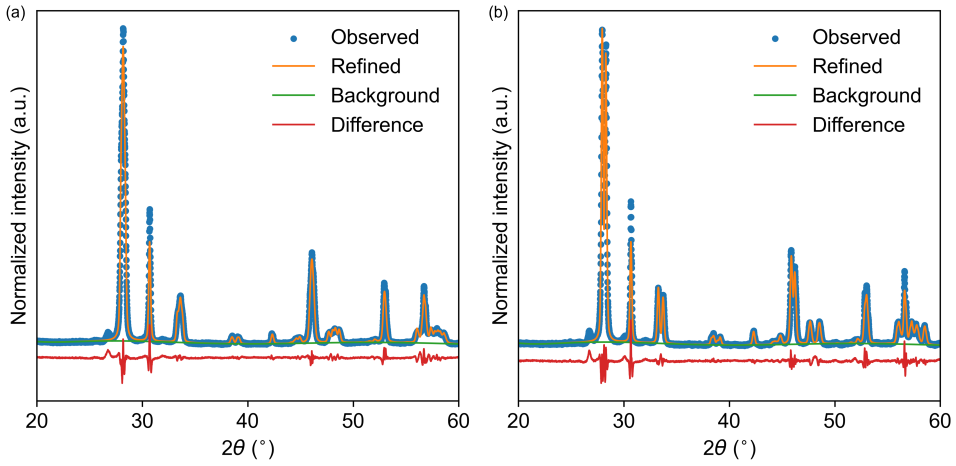


FIGURE 4.2: Le Bail refinement results of (a) LNW16As and (b) LNMo16As. The small reflections from the modulated structure are excluded from the refinement, as only the unit cell is refined without considering the supercell. The extracted lattice parameters were summarised in Table 4.2. Adapted from [250] with permission under a Creative Commons Attribution-NonCommercial 3.0 Unported Licence.

The refined β angles are 90.311(8)° and 90.846(4)° for LNW16As and LNMo16As, respectively. Similar phenomena have been reported in other works, indicating that the actual phases of LNW16As and LNMo16As are sensitive to heat treatments [151, 152]. This hysteresis effect is probably due to the slow kinetics of the phase transition, which traps the tetragonal phase at a lower temperature [152].

Another interesting feature presented in Figure 4.1 and 4.3 is the small reflections from the modulated structure. These small reflections are maintained throughout the measuring temperature range except LNMo16As at 800 °C, in accordance with the phase diagrams presented in Figure 2.11 [151, 152]. The modulated structure was further investigated using TEM and SAED. Figure 4.4 (a) and (b) present the TEM image and corresponding SAED diffraction pattern of LNW16As with a (3+2)D-modulated structure. The calculated d-spacing of 1.75 nm refers to the modulated structure indexed by the modulated vectors of $\boldsymbol{q_1}\approx 0.23\boldsymbol{a} + 0.18\boldsymbol{c}$ and $\boldsymbol{q_2}\approx -0.15\boldsymbol{a} + 0.22\boldsymbol{c}$. For LNMo16As, a (3+1)D-modulated structure was found in Figure 4.4 (c) and (d). The calculated d-spacing of 1.90 nm refers to the modulated structure indexed by the modulated vectors of $\boldsymbol{q_1}\approx 0.38\boldsymbol{a} + 0.25b + 0.02\boldsymbol{c}$. These satellite peaks in SAED patterns clearly confirm the existence of the modulated structure in both samples. Although only a (3+1)D-modulated structure in LNMo16As was visualised, the (3+2)D- and (3+1)D-modulated structures could coexist in both samples as suggested by the previous work [165].

The above XRD results suggested that LNW16As and LNMo16As have been successfully synthesised without the sign of a secondary phase in XRD patterns. Figure 4.5 shows the SEI and EDS mapping images of LNW16As and LNMo16As, respectively.

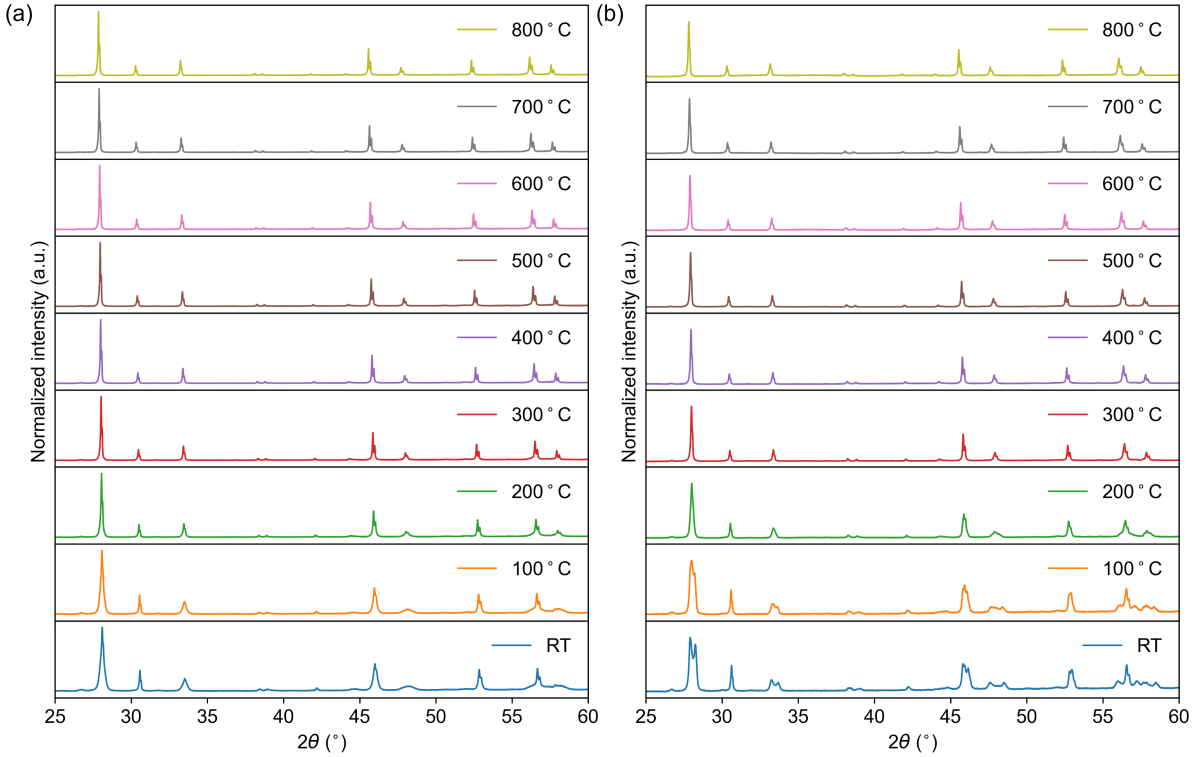


FIGURE 4.3: *In-situ* high-temperature and RT XRD patterns of (a) LNW16As and (b) LNMo16As, respectively. The phase transition temperature of LNW16As and LNMo16As are around 200 and 300 °C, respectively. The patterns shift to a lower 2θ angle with increasing temperature due to thermal expansion of the lattice. The tilted patterns are due to the use of an auto-slit, which probes a larger sample volume at a higher 2θ angle.

TABLE 4.1: Normalized atomic ratios of B-site cations in LNW16As and LNMo16As, respectively.

Cation	LNW16As (at%)	LNW16H2 (at%)	Theoretic (at%)
Nb	84.7±0.3	84.6±0.3	84.0
W	15.3±0.2	15.4±0.3	16.0
Cation	LNMo16As (at%)	LNMo16H2 (at%)	Theoretic (at%)
Nb	84.6±0.5	84.0±0.5	84.0
Mo	15.4±0.6	16.0±0.6	16.0

The average grain size of LNW16As and LNMo16As is 4.25±0.60 μm and 6.07±1.17 μm, respectively. Compared to LNMo16As, LNW16As presents a smaller average grain size with a more unified size distribution, suggesting better sintering. The relative density difference, 95.6% of LNW16As and 93.0% of LNMo16As, further confirms this sintering difference. However, pores were rare to observe in Figure 4.5, suggesting a suitable overall sintering condition for both samples. The EDS mapping images in Figure 4.5 indicate a good homogeneity of the compositional distribution. The W- and

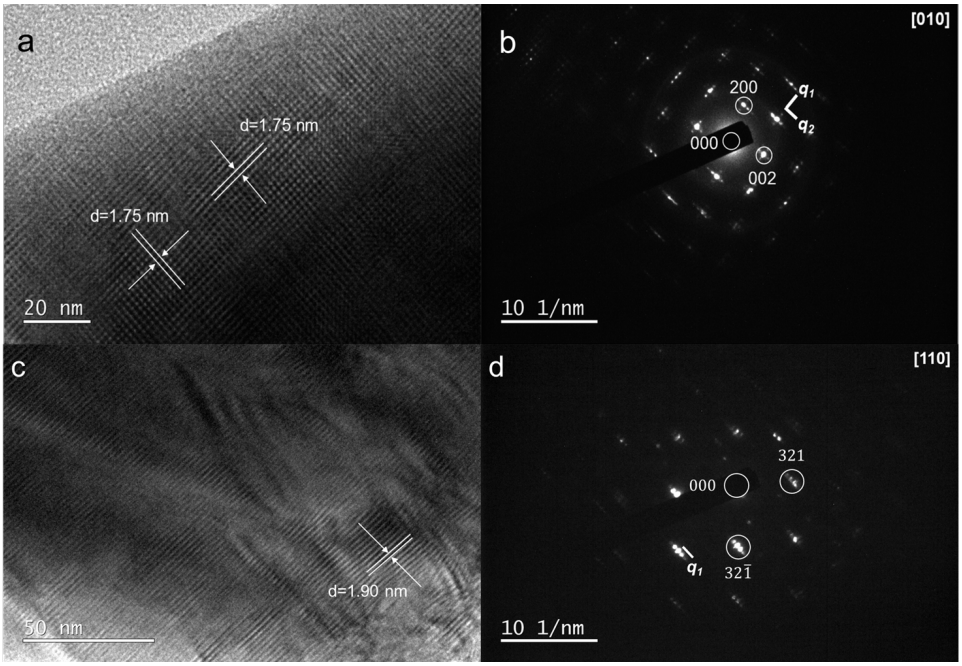


FIGURE 4.4: (a) TEM image and (b) SAED pattern of LNW16As along the [010] zone axis; (c) TEM image and (d) SAED pattern of LNMo16As along the [110] zone axis. The calculated d-spacing is 1.75 nm for LNW16As and 1.90 nm for LNMo16As, respectively. Vectors, $\boldsymbol{q_i}$, label the satellite reflections from modulated structures. Adapted from [250] with permission under a Creative Commons Attribution-NonCommercial 3.0 Unported Licence.

Mo-substitution concentrations were analysed and summarised in Table 4.1. Although the atomic ratios deviate from theoretical values, these ratios are still reasonable within the instrumental uncertainty range of the EDS, suggesting that the target substitution concentration is achieved.

In summary, both samples possess a monoclinic phase ($C2/c$ or $I2/a$, #15). The previously reported modulated structure was confirmed in both samples. The phases of both samples are homogeneous with an expected substitution concentration of $\sim$16 at%. The above results validate the successful synthesis of the starting materials in this work.

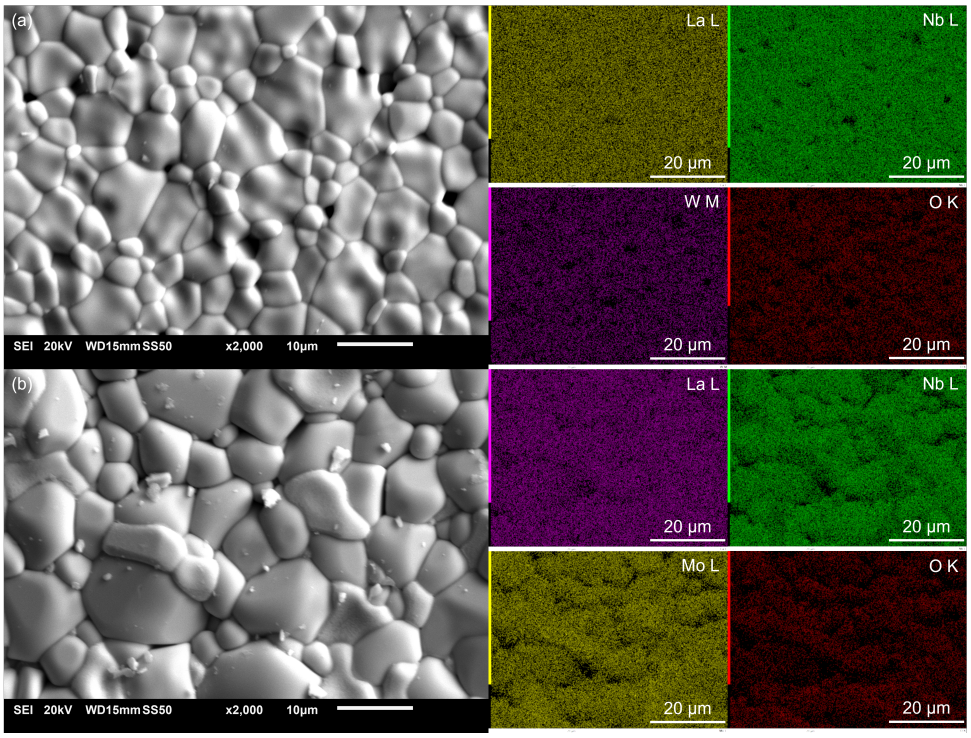


FIGURE 4.5: SEI and corresponding EDS mapping images of (a) LNW16As and (b) LNMo16As. The spectrum line and scale bar information on the bottom were relabelled for readability.

4.2 Structural and chemical studies

To explore the potential effect of hydrogen atmospheres on the samples, both LNW16As and LNMo16As underwent heat treatments at 800 °C under 5% H_2 conditions for different holding times, as presented in Figure 4.6 and 4.7. The temperature of 800 °C was chosen as it is the upper limit operating temperature for most PCFCs [46, 47]. In addition, Figure 4.6 and 4.7 also indicate that treatment with hydrogen at 800 ° C for 2 hours is sufficient. The extension of the treatment time did not lead to significant changes in the samples. Therefore, hereinafter, LNW16As and LNMo16As that underwent heat treatments at 800 °C under 5% H_2 conditions for 2 hours are denoted as LNW16H2 and LNMo16H2, respectively.

For LNW16As, the XRD patterns in Figure 4.6 are almost identical, suggesting an excellent structural stability of LNW16As. The modulated reflections exist in each pattern, suggesting that the hydrogen treatment does not affect the modulated structure. However, a subtle difference in peak width can be observed, where the peak width of hydrogen-treated samples is narrower than that of LNW16As. Figure 4.8(a) presents the Le Bail refinement of LNW16H2. The refined β angle of LNW16H2 is 90.390(4)° slightly smaller than of LNW16As. This difference is likely due to the above-mentioned

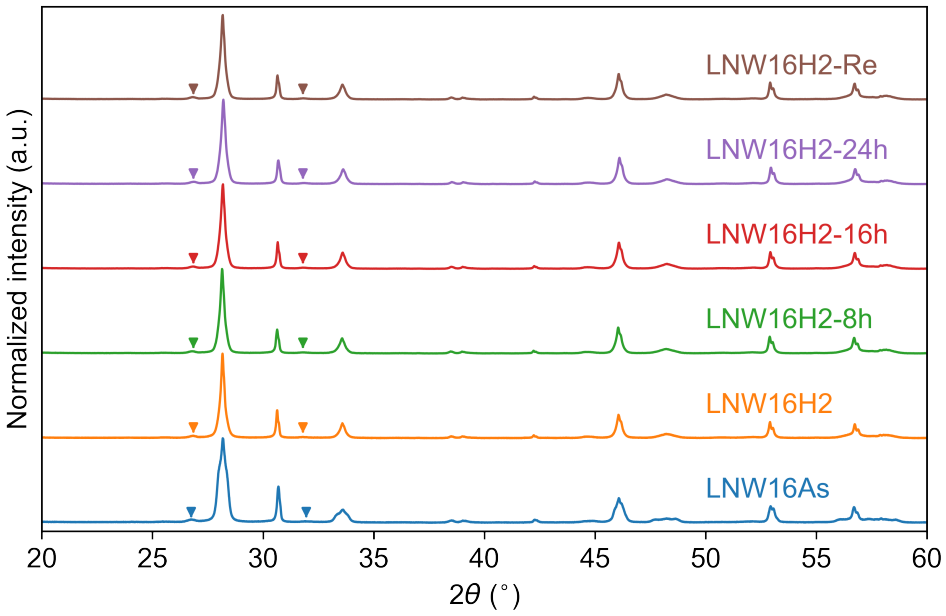


FIGURE 4.6: XRD patterns of LNW16As, LNW16H2 and elongating the hydrogen treatment time to 8, 16 and 24 hours, respectively. The 24-hour hydrogen-treated sample was then re-oxidised at 800 °C under ambient conditions for 4 hours and was labelled as "LNW16H2-Re". The modulated reflections are marked by the ∇ symbol.

hysteresis effect. To further validate this effect, the 24-hour hydrogen-treated sample was re-oxidised at 800 °C under ambient conditions for 4 hours. The sharp peak is maintained with the refined β angle of 90.432(3)°, indicating that the sample and its modulated structure are unaffected by the reduction treatment.

However, the structural change is significant for LNMo16As. After hydrogen treatments, the near-tetragonal phase transited to a fully monoclinic phase analogous to the pristine $LaNbO_4$. Figure 4.8(b) presents the Le Bail refinement of LNMo16H2. The refined β angle of LNMo16H2 is 94.004(1)° again analogous to that of pristine $LaNbO_4$. The modulated reflections also diminished after hydrogen treatments. The modulated structure in this type of material has been reported to be highly correlated with interstitial oxygen defects [158, 159]. Therefore, the disappearance of the modulated reflections and the monoclinic transition strongly suggest the reduction of LNMo16As under hydrogen conditions. The same re-oxidation procedure was conducted for a 24-hour hydrogen-treated sample, and the reduction was found to be fully reversible. The refined β angle of LNMo16H2-Re is 90.956(2)°. The slight pattern and β angle differences are again due to the hysteresis effect.

Figure 4.9 presents the SEI images and their corresponding EDS mapping images of LNW16H2 and LNMo16H2, respectively. The average grain sizes of LNW16H2 and LNMo16H2 are 5.10±0.65 μm and 5.53±0.85 μm, respectively. Table 4.1 summarised

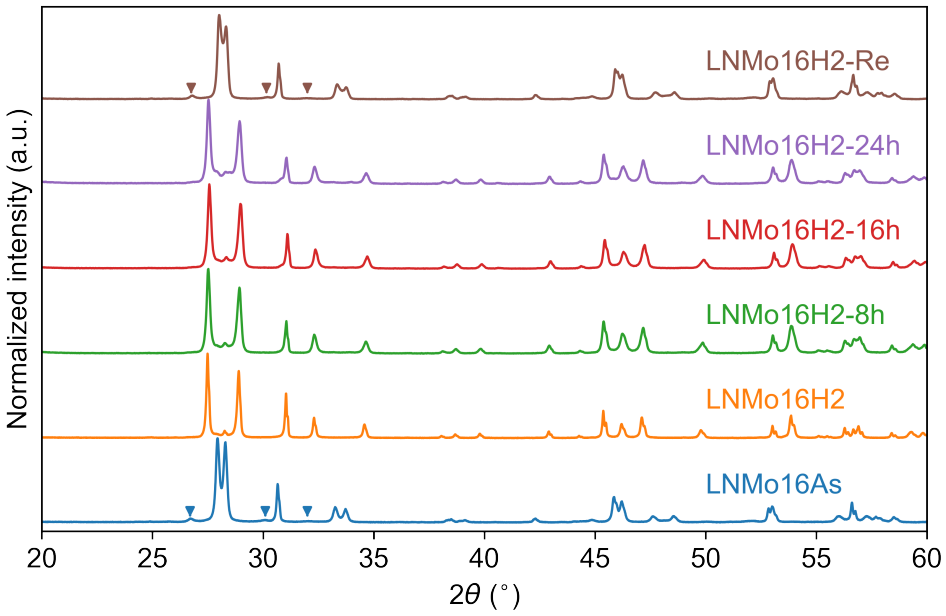


FIGURE 4.7: XRD patterns of LNMo16As, LNMo16H2 and elongating the hydrogen treatment time to 8, 16 and 24 hours, respectively. The 24-hour hydrogen-treated sample was then re-oxidised at 800 °C under ambient conditions for 4 hours and was labelled as "LNMo16H2-Re". The modulated reflections are marked by the ∇ symbol.

the concentrations of W and Mo substitution of both samples. There is no noticeable difference between the as-sintered and hydrogen-treated samples from the morphology and compositional points of view.

TABLE 4.2: Refined lattice parameters of all four samples from Le Bail refinements. Adapted from [250] with permission under a Creative Commons Attribution-NonCommercial 3.0 Unported Licence.

	LNW16As	LNW16H2	LNMo16As	LNMo16H2
$a(Å)$	5.3694(2)	5.3474(3)	5.3834(2)	5.5583(1)
$b(Å)$	11.6707(4)	11.6848(4)	11.6555(7)	11.5333(2)
$c(Å)$	5.3238(2)	5.3463(3)	5.3140(2)	5.2023(1)
$\beta(^\circ)$	90.663(3)	90.390(4)	90.968(3)	94.004 (1)
$V(Å^3)$	333.58(1)	334.05(1)	333.38(2)	332.68(1)
$R_{wp}(\%)$	8.28	9.81	8.35	9.51
GOF	3.45	3.93	3.46	3.90

For the sake of direct comparison, the refined lattice parameters were summarised in Table 4.2. The relatively poor refinement qualities imply the coexistence of the monoclinic and tetragonal phases [131, 132]. It is intriguing to see such structural differences realised by simply changing the substitution species. W and Mo are generally regarded as vulnerable elements in the form of binary oxides, WO_3 and MoO_3, easily changing

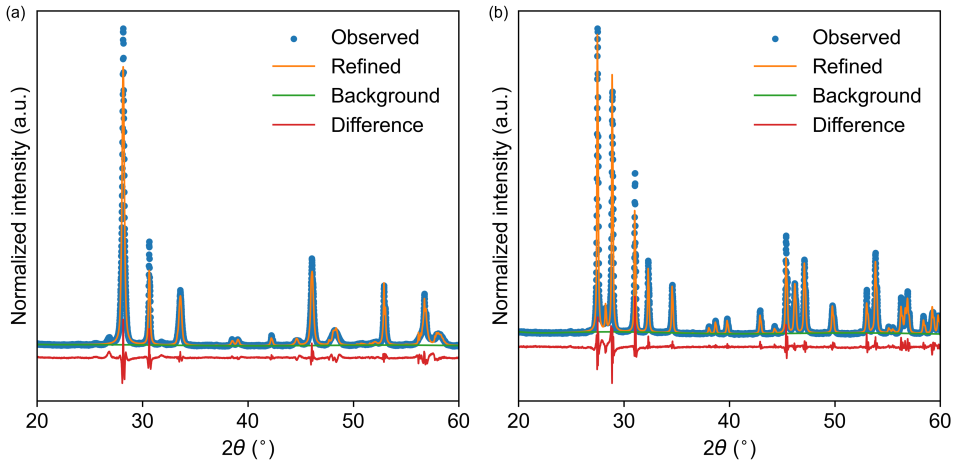


FIGURE 4.8: Le Bail refinement results of (a) LNW16H2 and (b) LNMo16H2. The small reflections from the modulated structure are excluded from the refinement, as only the unit cell is refined without considering the supercell. The extracted lattice parameters were summarised in Table 4.2. Adapted from [250] with permission under a Creative Commons Attribution-NonCommercial 3.0 Unported Licence.

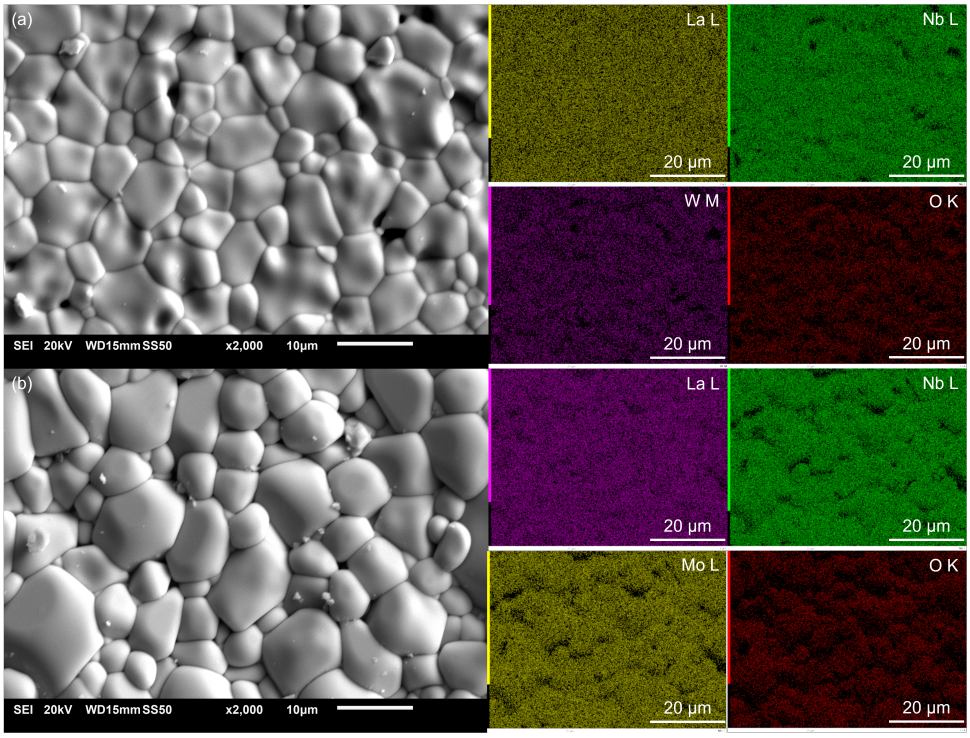


FIGURE 4.9: SEI and corresponding EDS mapping images of (a) LNW16H2 and (b) LNMo16H2. The spectrum line and scale bar information on the bottom were relabelled for readability.

their valence state [174, 251]. However, there are very few publications investigating the behaviour of W and Mo in the form of substitution in hydrogen atmospheres. Marrero-Lopez *et al.* studied W-substituted $La_2Mo_2O_9$ and Mo-substituted $La_2W_2O_9$

suggesting W has better redox stability than Mo [252, 253]. However, the materials studied in these works are not in a single phase comprising their arguments. The conclusion may not be applicable for $LaNbO_4$ based materials, given the structural difference. So far, there has been only one publication that reported phase reduction of Mo-substituted $LaNbO_4$ without further detailed analyses [139]. Therefore, the redox behaviour of W and Mo in $LaNbO_4$-based materials is worth exploring in detail.

4.3 Redox study

4.3.1 XPS study

Potential reductions can be expressed in Equation 4.2, assuming that W^{6+} and Mo^{6+} were only reduced to W^{5+} and Mo^{5+} [254]. The charge is compensated for by simultaneous oxygen loss, as expressed in Equation 4.3 [254]. To verify these equations, one would need to determine the valence states of the cations and the oxygen stoichiometry of the samples.

$$\begin{aligned} W_{Nb}^{\cdot} + e' &= W_{Nb}^{\times} \\ Mo_{Nb}^{\cdot} + e' &= Mo_{Nb}^{\times} \end{aligned} \tag{4.2}$$

$$\begin{aligned} H_{2(g)} + O_i'' &= H_2O_{(g)} + 2e' \\ H_{2(g)} + O_O^{\times} &= H_2O_{(g)} + V_O^{\cdot\cdot} + 2e' \end{aligned} \tag{4.3}$$

XPS is an easy-accessible technique for determining the valence state. Figure 4.10 and 4.11 present the normalized XPS spectra of all samples. The La 3*d* spectra in Figure 4.10(a) and 4.11(a) are more complex than other spectra due to the multiplet-splitting, making fitting these spectra challenging. However, the energy difference between each split peak was reported to be a good indicator for determining the valence state [255–257]. For all samples, the energy difference is the same, $\Delta_1 = \Delta_2 \approx 4.6$ eV, suggesting a La^{3+} cation state. The Nb 3*d* spectra in Figure 4.10(b) and 4.11(b) showed clear doublet peaks, suggesting a Nb^{5+} cation state. Note that the doublet peaks in Nb 3*d* spectra of LNMo16H2 are wider than other samples, suggesting more disordered Nb-O bonds with a binding energy more deviated from the average.

The W 4*f* XPS spectra of LNW16As and LNW16H2 both showed shoulders representing W cations with a valence state lower than +6. The spectra were adequately fitted by three sets of double peaks representing W^{6+}, W^{5+}, and W^{4+}, respectively. The fitting results are summarised in Table 4.3. After hydrogen treatments, the atomic fraction of W^{6+} was slightly reduced with a subtle increase in W^{5+} and W^{4+} cations. In addition, a peak of the hydroxyl group (-OH) was observed in the O 1*s* spectrum of LNW16H2,

TABLE 4.3: Normalized atomic ratios of W cations with different valence states and different oxygen species in LNW16As and LNW16H2 extracted from XPS fittings. The binding energy of each fitted W $4f_{7/2}$ and O 1*s* peak after C 1*s* calibration is listed in the brackets. Adapted from [250] with permission under a Creative Commons Attribution-NonCommercial 3.0 Unported Licence.

Valence state	LNW16As (at%)	LNW16H2 (at%)
W^{6+}	67.7 (35.8 eV)	63.0 (35.8 eV)
W^{5+}	26.2 (34.7 eV)	29.8 (34.7 eV)
W^{4+}	6.1 (33.5 eV)	7.2 (33.5 eV)
Oxygen species	LNW16As (at%)	LNW16H2 (at%)
$[O]_{lattice}$	89.7 (530.5 eV)	77.8 (530.6 eV)
$[O]_{surface}$	10.3 (531.5 eV)	11.1 (531.6 eV)
$-OH$	-	11.1 (532.9 eV)

TABLE 4.4: Normalized atomic ratios of Mo cations with different valence states and different oxygen species in LNMo16As and LNMo16H2 extracted from XPS fittings. $\delta i+$ represents the valence state of Mo cations between 0 and +4. The binding energy of each fitted Mo $3d_{5/2}$ and O 1*s* peak after C 1*s* calibration is listed in the brackets. Adapted from [250] with permission under a Creative Commons Attribution-NonCommercial 3.0 Unported Licence.

Valence state	LNMo16As (at%)	LNMo16H2 (at%)
Mo^{6+}	46.4 (233.1 eV)	30.0 (233.2 eV)
Mo^{5+}	35.6 (231.8 eV)	34.0 (231.9 eV)
Mo^{4+}	7.4 (230.4 eV)	11.9 (230.6 eV)
$Mo^{\delta 1+}$	4.8 (229.8 eV)	9.5 (229.9 eV)
$Mo^{\delta 2+}$	5.8 (229.1 eV)	10.0 (229.5 eV)
$Mo^{\delta 3+}$	-	4.6 (227.9 eV)
Oxygen species	LNMo16As (at%)	LNMo16H2 (at%)
$[O]_{lattice}$	91.3 (530.4 eV)	74.8 (530.5 eV)
$[O]_{surface}$	8.7 (531.6 eV)	12.7 (531.3 eV)
$-OH$	-	12.5 (532.4 eV)

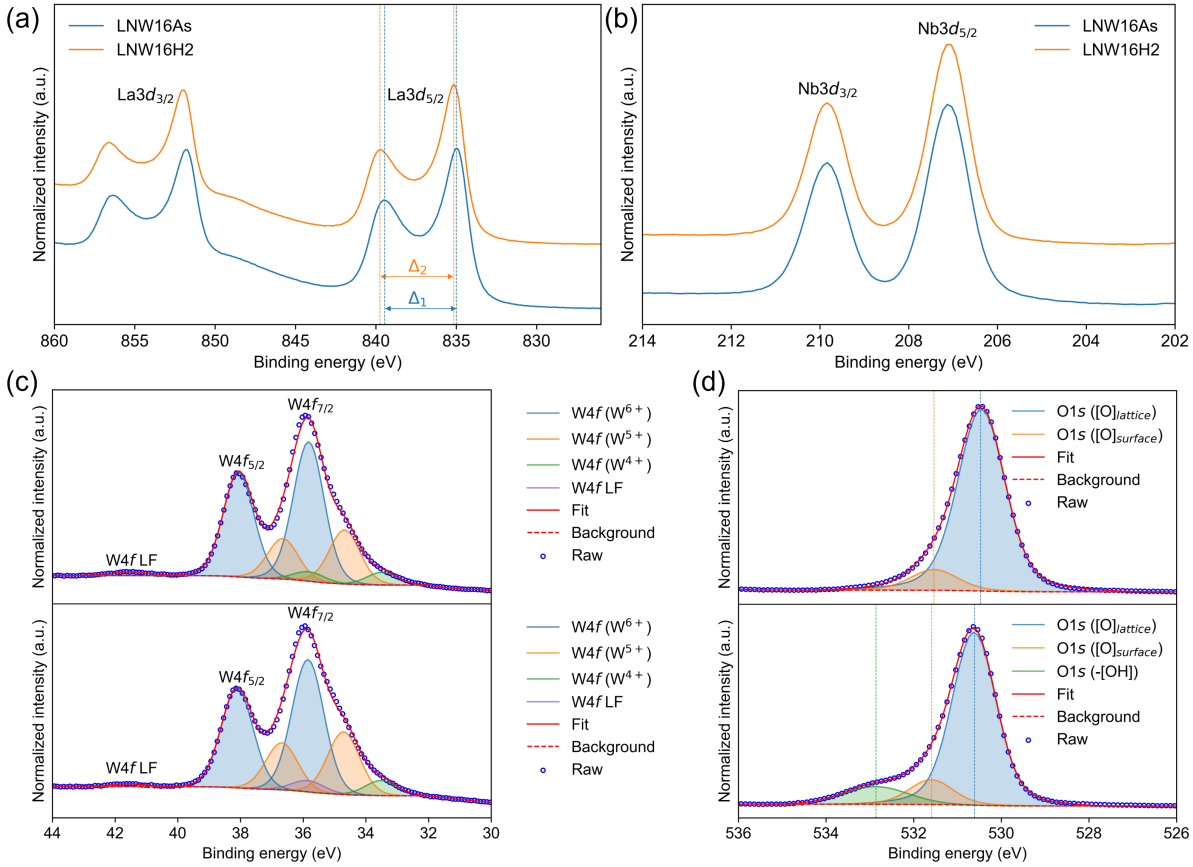


FIGURE 4.10: Normalized XPS spectra of (a) La 3*d*, (b) Nb 3*d*; (c) fitted XPS spectra of W 4*f* in (top) LNW16As and (bottom) LNW16H2; (d) fitted XPS spectra of O 1*s* in (top) LNW16As and (bottom) LNW16H2. The "LF" in W 4*f* spectra represents the loss feature of W^{6+}. Adapted from [250] with permission under a Creative Commons Attribution-NonCommercial 3.0 Unported Licence.

indicating the formation of metal hydroxide. The proton incorporation mechanism can explain this formation as shown in Equation 2.13 [70, 71]. However, given that XPS is a surface-sensitive technique, it is not feasible to determine whether the hydroxide is surface-limited or can penetrate deeper into the bulk.

The Mo 3*d* XPS spectra of LNMo16As and LNMo16H2 are more complicated with dominant shoulder characteristics. The fitting results are summarised in Table 4.4. Due to the difficulty in assigning Mo cations with a low valence state, the notation of $Mo^{\delta i+}$ was used to represent the valence state of Mo cations between 0 and +4. After hydrogen treatments, the atomic fraction of Mo^{6+} was reduced dramatically from 46.4 at% to 30.0 at%, while the double peaks representing lower valence states increased significantly. These changes clearly indicate the reduction of Mo cations under hydrogen conditions. Similarly to LNW16H2, a peak of the hydroxyl group (-OH) was observed in the O 1*s* spectrum of LNMo16H2 with a higher atomic fraction than LNW16H2. This

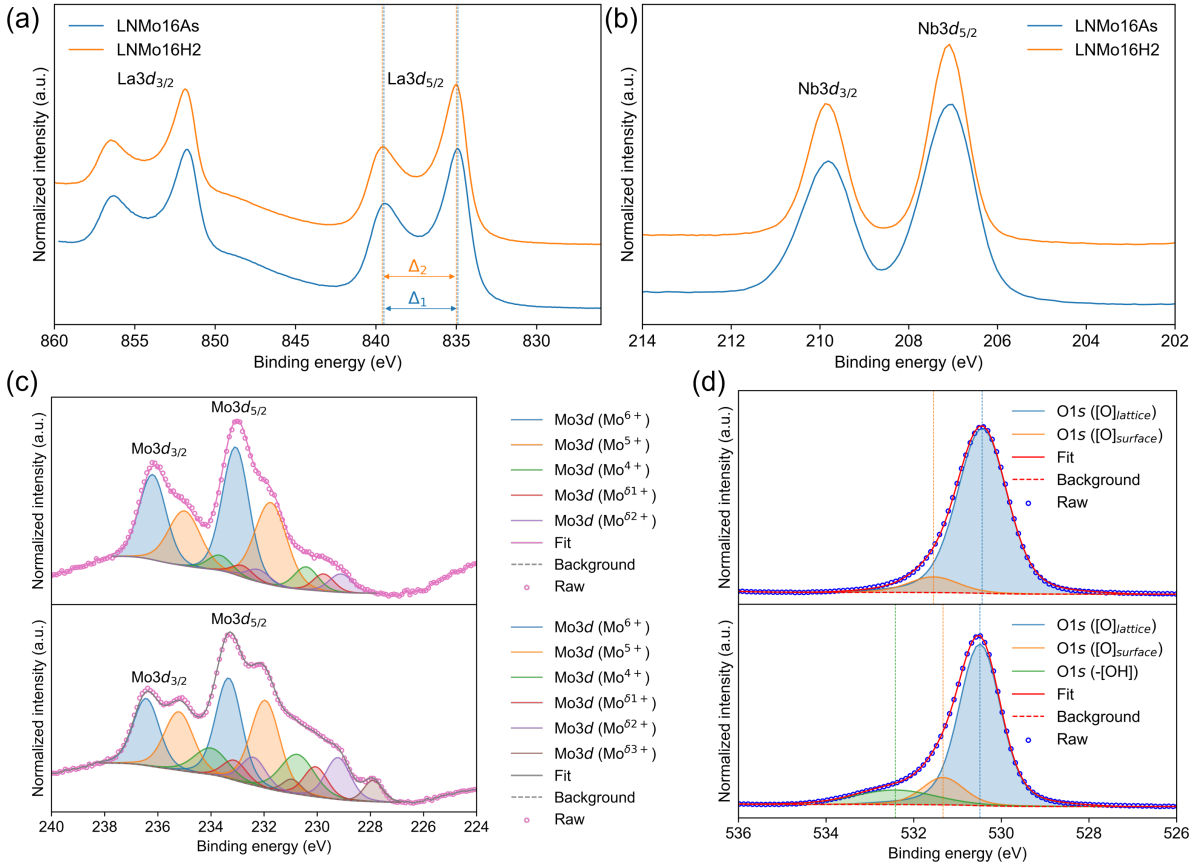


FIGURE 4.11: Normalized XPS spectra of (a) La 3*d*, (b) Nb 3*d*; (c) fitted XPS spectra of Mo 3*d* in (top) LNMo16As and (bottom) LNMo16H2; (d) fitted XPS spectra of O 1*s* in (top) LNMo16As and (bottom) LNMo16H2. $\delta i+$ represents the valence state of Mo cations between 0 and +4. Adapted from [250] with permission under a Creative Commons Attribution-NonCommercial 3.0 Unported Licence.

higher fraction is in line with the heavier reduction of Mo^{6+} cations, also suggesting a better proton incorporation capability. The shift towards a lower binding energy of the peak representing $O_{surface}$ in Figure 4.11(d) further indicates the dramatic change of the local bonding environment due to the substantial reduction of Mo cations on the surface.

The above results suggest that both LNW16As and LNMo16As were reduced under hydrogen atmospheres. However, many studies have argued that XPS technique might not be ideal for determining the valence state of some elements, such as W and Mo, due to high vacuum measuring conditions and the use of the flood gun [174, 258]. These measuring conditions might reduce cations, resulting in incorrect estimation of valence states. To verify this argument, XPS iteration spectra were collected, as presented in Figure 4.12.

For the XPS iteration for the W 4*f* spectra in Figure 4.12(a) and (b), a small shoulder was

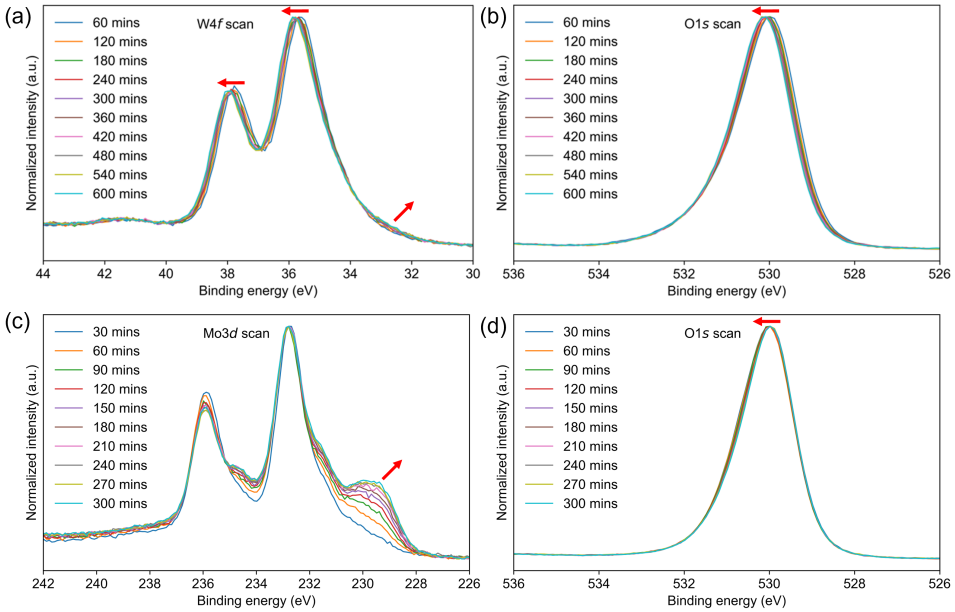


FIGURE 4.12: Normalized XPS iteration spectra of (a) W 4*f* and (b) O 1*s* in LNW16As, and (c) Mo 3*d* and (d) O 1*s* in LNMo16As. The red arrow highlights the change tendency in spectra as a function of iteration time. Adapted from [250] with permission under a Creative Commons Attribution-NonCommercial 3.0 Unported Licence.

raised on the low binding energy side, indicating the spontaneous reduction of W^{6+} under the XPS measuring conditions. The main double peaks, which represent W^{6+}, also shifted to a higher binding energy. A similar shift phenomenon was also found in O 1*s* iteration spectra of LNW16As. Given the highly insulating nature of LNW16As, this shift is likely due to the surface charge accumulation with the measuring time, which was not observed in the similar iteration measurement of WO_3 [174].

For the XPS iteration for the Mo 3*d* spectra, the shoulder features were more significant and grew faster with the measuring time. The energy shift was not presented in the Mo 3*d* spectra and became subtle in the O 1*s* iteration spectra of LNMo16As. This energy shift difference between LNW16As and LNMo16As is likely due to the relatively higher surface conductivity of LNMo16As after reduction compared to LNW16As.

The XPS iteration spectra clearly demonstrated the limitation of precisely determining the valence states of W and Mo cations. The exact atomic fractions might be incorrectly estimated due to the spontaneous reduction triggered by XPS measuring conditions. However, the XPS spectra still indicated the redox stability difference between the W and Mo cations. The redox stability of LNW16 is clearly much better than that of LNMo16 under hydrogen atmospheres.

4.3.2 Spin resonance and thermogravimetric studies

The electronic structure of the W and Mo cations offers an excellent opportunity to probe the valence states indirectly using the ESR technique. Reducing W^{6+} and Mo^{6+} to W^{5+} and Mo^{5+} will introduce a single unpaired electron, generating an ESR signal with a unique g-factor under an applied magnetic field. Figure 4.13(a) shows the ESR spectra of LNW16As and LNW16H2 measured at 100 K in air. Three unpaired electron signals with a g-factor of 2.061, 2.003 and 1.960 were found. Similar signals were also found in LNMo16As with the same g-factors, as shown in Figure 4.13(c), suggesting these signals do not originate from cations. The signal of 2.003 comes from the semi-free electron trapped in the surface defects [207]. Meanwhile, previous studies have reported that the signals of 2.061 and 1.960 originate from the superoxide ion, O_2^-, and the singly ionised oxygen vacancy, $V_O^{\cdot}$ in bulk and/or on the surface of the samples [210, 211, 259]. The ESR spectra of Ar-treated LNW16As further verified this statement, as presented in Figure 4.13(d). The sample was calcined at 800 °C for 2 hours in pure Ar atmospheres, and then the ESR spectra were collected under the same measurement conditions. The fully flat spectra suggested that all three signals were from surface defects and could be easily removed under mild conditions.

Both LNW16As and LNW16H2 did not show a signal in the range of 1.500 to 1.800, indicating that the valence state of W cations is entirely +6 before and after hydrogen treatments. Another distinct feature in Figure 4.13(a) is the intense signal of 2.003 in LNW16H2. Because the surface oxygen defects were removed after hydrogen treatments, this semi-free electron signal can no longer be explained as trapped in those surface oxygen defects. Many studies have reported this signal as a so-called F-centre that represents surface-trapped electrons correlated with surface hydrogen defects [102, 103, 260, 261]. This hypothetical F-centre signal is consistent with the emergence of hydroxyl groups in the above XPS measurements, further increasing the credibility of the proton incorporation mechanism in Equation 2.13. However, the detailed identification of this signal is too complex and beyond the scope of this work.

In contrast, Figure 4.13(b) shows a intensive signal of 1.876 in LNMo16H2 while absent in LNMo16As. This g-factor aligns with the values in the literature, suggesting the formation of Mo^{5+} cations [208, 209]. The intensity of this signal is about 25 times higher than that of the others. All measuring samples were approximately equal in mass and the intensity of the EPR signal was proportional to the square root of the concentration. Therefore, this signal is strong evidence that indicates the valence state of Mo cations is entirely +6 in the as-sintered sample and is largely reduced to +5 after hydrogen treatments. In addition, the signal intensity of 1.876 is so intense that the F-centre signal was immersed, becoming undetectable.

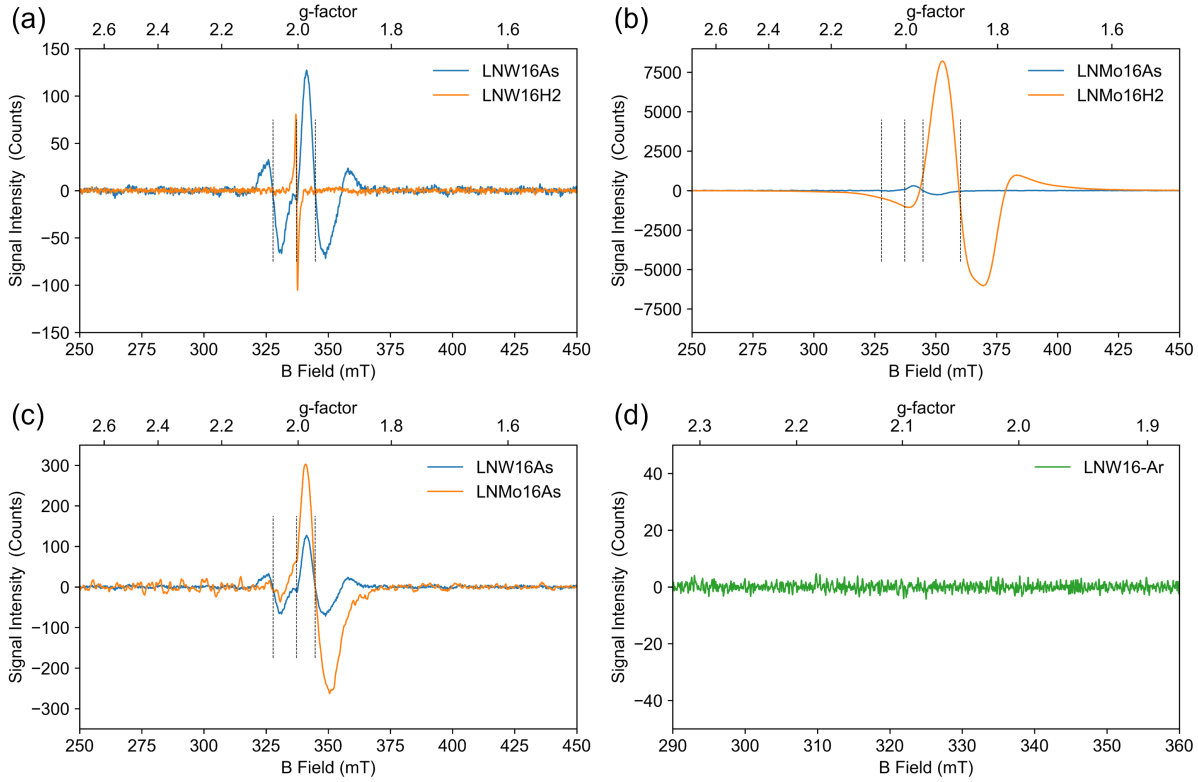


FIGURE 4.13: ESR spectra (100 K) of (a) LNW16 and (b) LNMo16; (c) Comparison of LNW16As and LNMo16As; (d) ESR spectra (100 K) of LNW16As after the heat treatment at Ar conditions (LNW16-Ar). The short dash lines in each spectrum from left to right indicate the positions of the g-factor at 2.061, 2.003, 1.960 and 1.875, respectively.

The above ESR results are consistent with the XPS studies, suggesting a better redox stability of LNW16 than LNMo16. However, quantifying the valence state using ESR remains challenging.

Another indirect method to determine the valence state is to evaluate the oxygen stoichiometry. As expressed in Equation 4.3, a change in oxygen stoichiometry causes a mass change, which is measurable using the TGA technique. Figure 4.14 shows the mass change of all samples measured under flowing air conditions. All samples showed a non-negligible increase in mass of ∼0.1 wt% from RT to around 180 °C. This increase in the initial heating stage was attributed to the buoyancy effect owing to the thermal ingredient in the measuring chamber. The insert of Figure 4.3(a) presents the TGA result of the pure indium metal reference, where a similar increase in mass was found, demonstrating the impact of the buoyancy effect.

After excluding the initial increase in mass, the changes in mass for both LNW16As and LNW16H2 were less than 0.04 wt%, which is below the instrumental uncertainty. This subtle difference suggests that the reduction of LNW16H2 is negligible, resulting in a negligible re-oxidation during TGA measurements with a negligible mass change.

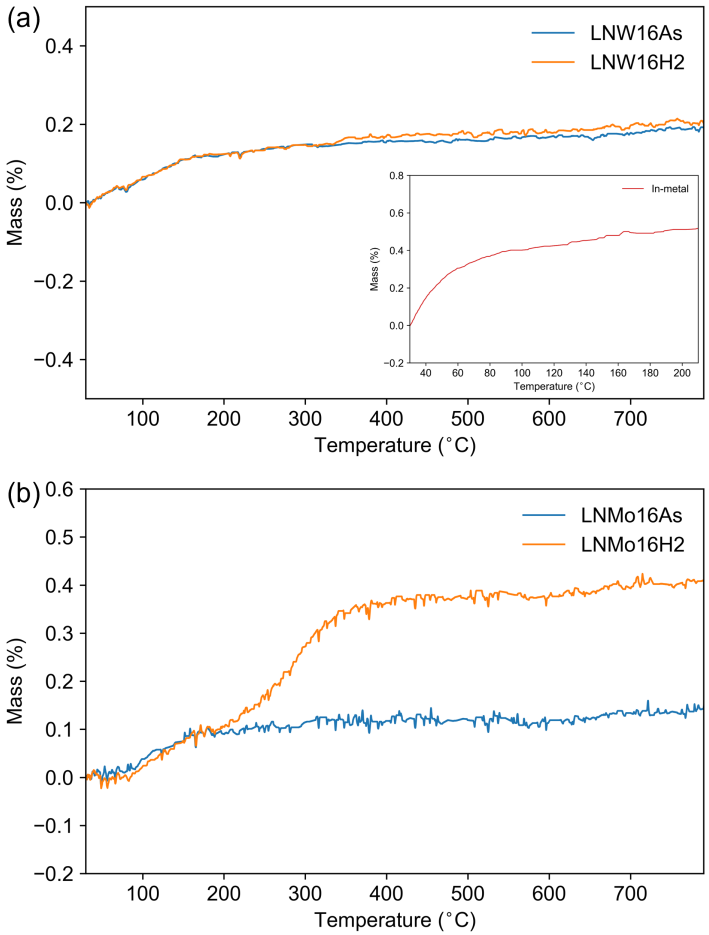


FIGURE 4.14: TGA results of (a) LNW16 and (b) LNMo16 collected from RT to 800 °C at flowing air conditions. The subtle mass difference in (a) falls within the instrumental uncertainty. The TGA result of pure indium metal reference is presented in the inset of (a), clearly indicating the buoyancy effect at the initial heating stage. Adapted from [250] with permission under a Creative Commons Attribution-NonCommercial 3.0 Unported Licence.

This result is consistent with the above ESR results, suggesting that the W^{6+} cations remained stable before and after hydrogen treatments.

In contrast, the TGA result of LNMo16H2 showed a significant mass gain of 0.28 wt%, suggesting the Mo cations were re-oxidised during the TGA measurement. This result also suggested that the oxidation started above 200 °C. As suggested by ESR results, assuming the valence state of the Mo cations in LNMo16H2 was fully re-oxidised back to +6, then the valence state of Mo cations in LNMo16H2 was estimated to be +5.35, giving a nominal composition of $LaNb_{0.84}Mo_{0.16}O_{4.028}$.

In conclusion, the average valence state of W and Mo cations was determined from the TGA results, indicating excellent redox stability of LNW16 while LNMo16 cannot be reduced to below +5. However, given the unavoidable buoyancy effect, limited

instrumental accuracy, and absorption/desorption of surface species, the valence state extrapolated from TGA is often found to deviate from the actual value. An approach that can directly determine the valence state of cations is favourable.

4.3.3 XAS study

The XAS technique is one of the very few techniques that allows direct determination of the valence state at ambient conditions. The valence state of an element can be easily determined by locating either the edge position, e_0, or the white line. Figure 4.15(a) and Figure 4.16(a) presented the XAFS spectra of the Nb K edge in all samples. The edge position, e_0, of each sample is located at 19003.8 eV, aligning well with the position of the $LaNbO_4$ and Nb_2O_5 reference samples. This suggests that Nb cations in all samples maintain a valence state of +5 regardless of any change. The energy uncertainty of all edge positions and white lines in Figure 4.15 and Figure 4.16 is estimated well below the energy step size of 0.35 eV and therefore not given in this work.

Apart from the edge position, there are apparent geometrical differences in the pre-edge and post-edge areas. Therefore, the Nb K-edge spectra were reconstructed in Figure 4.17 for direct comparison. The pre-edge shoulder and the separated double-peak feature in the post-edge area were found to be highly correlated with the local coordination structures [177–180, 262, 263]. The pre-edge shoulder originated from the forbidden 1*s*-4*d* transitions becoming allowed due to the 5*p*-4*d* hybridisation [180, 264]. This allowed transition can be enhanced by charge transfer between Nb 4*d* orbitals and O 2*p* orbitals [180, 264]. Such intense pre-edge shoulder may reflect highly disordered environments around Nb cations [180]. Meanwhile, post-edge features were assigned to the 1*s*-4*p* transitions, which is highly correlated with the distortion of the NbO_6 octahedra [180–182]. Typically, materials that contain the NbO_6 octahedra possess a well-separated double-peak feature [155, 180–182]. Therefore, this feature can be used to determine the existence of the NbO_6 octahedra.

In Figure 4.17, LNMo16H2 exhibits the most intense pre-edge shoulder and a well-resolved post-edge feature, similar to pristine $LaNbO_4$, suggesting a highly disordered coordination environment of NbO_6. In contrast, LNMo16As possessed a more ordered NbO_4 coordination environment suggested by both flat features. Interestingly, both LNW16As and LNW16H2 possessed less flat post-edge features with intense pre-edge shoulders, suggesting a disordered NbO_4 coordination environment for both samples. It should be mentioned that there is no direct correlation between the intensity of the pre-edge shoulder and the coordination number, which has been proved by *in-situ* high-temperature XAFS experiments of LNMo10 [155].

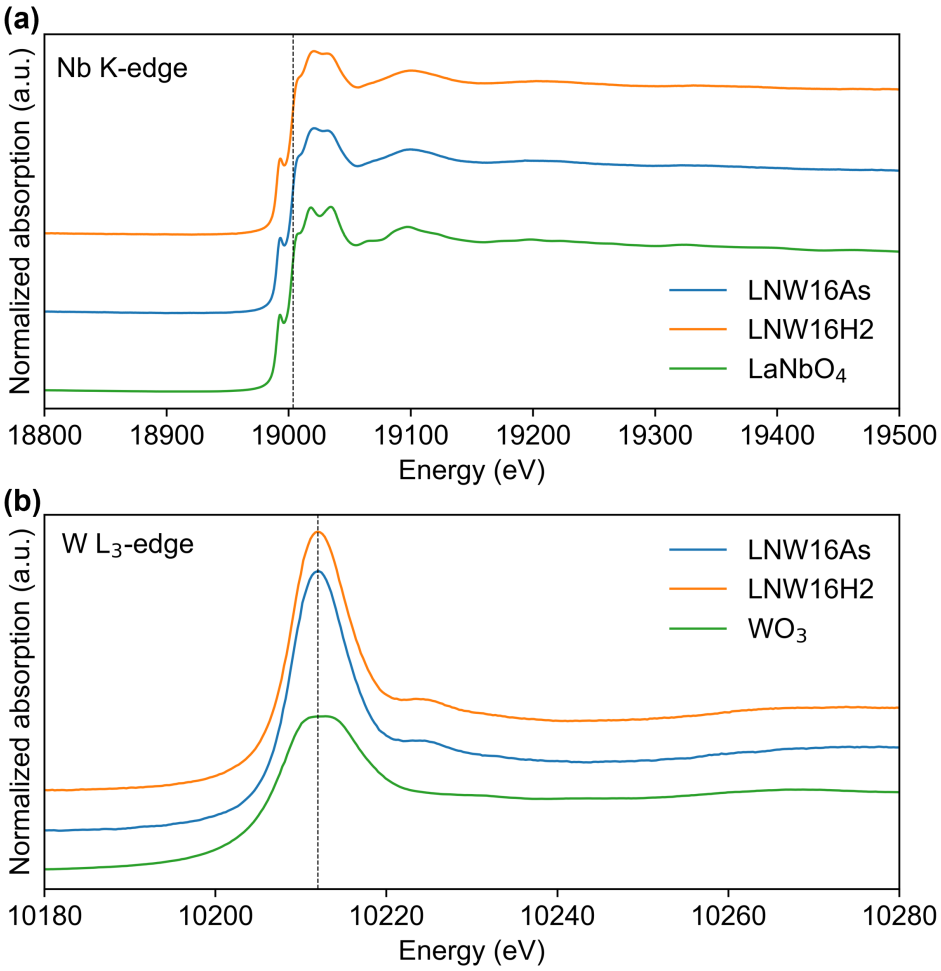


FIGURE 4.15: Normalized synchrotron XAFS spectra of (a) the Nb K-edge and (b) the W L_3-edge collected at ambient conditions. The vertical dashed line indicates the position of e_0 at 19003.8 eV in the Nb K-edge spectra and the white line at 10212.0 eV in W L_3-edge spectra, respectively. Adapted from [250] with permission under a Creative Commons Attribution-NonCommercial 3.0 Unported Licence.

Unlike the Nb K-edge, the XAFS spectra of the W L_3-edge in Figure 4.15(b) presented a distinctly different shape. The intense absorption peak is called the white line, originating from the dominant $2p$-$5d$ transitions [265–267]. The white line position of both samples overlapped well with the position of WO_3 at 10212.0 eV, suggesting that the valence state of the W cations in both samples was purely +6. This result is in line with the above results from ESR and TGA and is consistent with the previous study [267]. Meanwhile, the shape of the white line peak in the W L_3-edge depends strongly on the coordination environment [265–267]. The single, relatively sharp peak indicates a WO_4 tetrahedral coordination environment, while a WO_6 octahedral coordination environment results in a flat peak or even double peaks due to the $t_{2g} - e_g$ orbital splitting [265–267]. Therefore, the single, relatively sharp peak of both samples indicates their

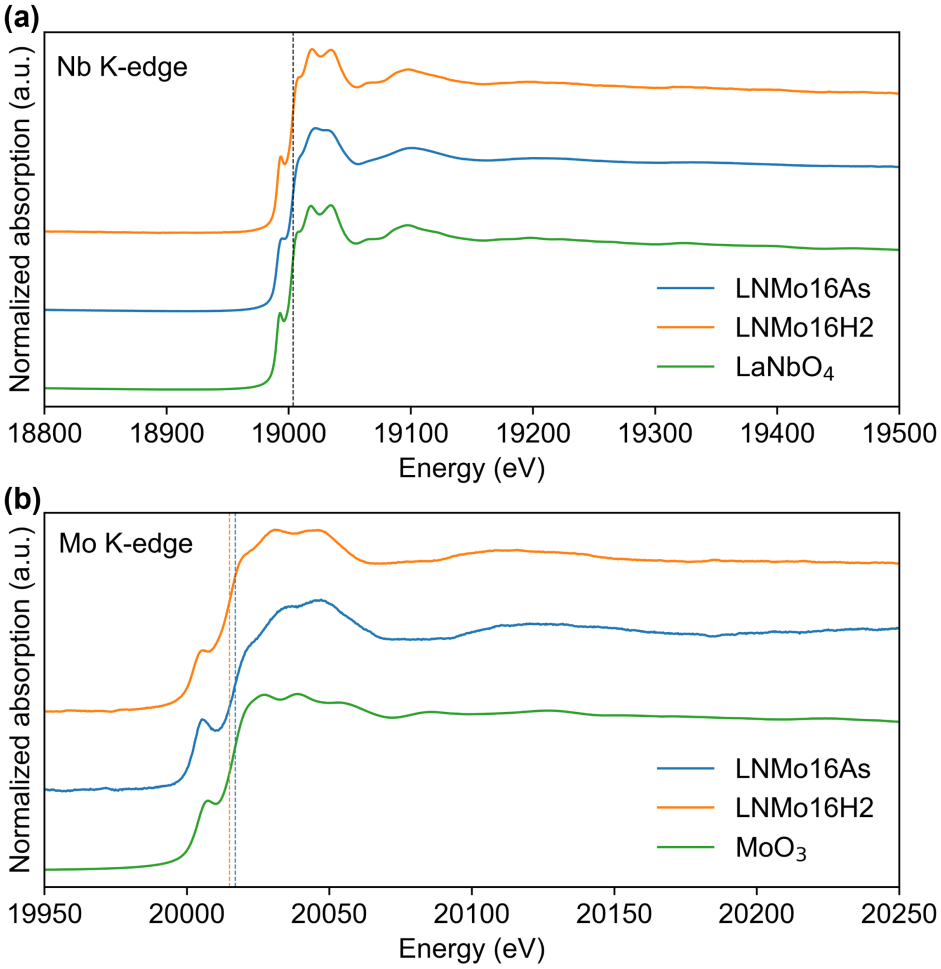


FIGURE 4.16: Normalized synchrotron XAFS spectra of (a) the Nb K-edge and (b) the Mo K-edge collected at ambient conditions. The vertical dashed line indicates the position of e_0 at 19003.8 eV in the Nb K-edge spectra and e_0 at 20015.0 eV (orange) and 20017.0 eV (blue) in the Mo K-edge spectra, respectively.

WO_4 tetrahedral coordination environment, while the flat peak of WO_3 with the WO_6 octahedral configuration further credits this conclusion.

In Figure 4.16(b), the edge position was shifted from 20017.0 eV in LNMo16As to 20015.0 eV in LNMo16H2. The Mo^{6+} cations in MoO_3 possess the same edge position at 20017.0 eV, suggesting the reduction of LNMo16 after hydrogen treatments. Zhou *et al.* investigated a variety of Mo-containing materials, suggesting a linear relationship between the edge position and the valence state, as expressed by Equation 4.4 [268, 269].

$$\Delta E = 3\delta - 1 \tag{4.4}$$

Where ΔE is the edge position difference between Mo metal (20000 eV) and the measured sample, and δ is the valence state of the sample. This relation has been validated in a study of LNMo10 [155]. The extracted valence state of Mo cations in LNMo16H2 was +5.33, which is in good agreement with the valence state of +5.35 extracted from TGA results. Meanwhile, the XAFS spectra of the Mo K-edge showed pre-edge and post-edge features similar to those of the Nb K-edge with similar origins [155, 180, 264]. The well-separated post-edge double-peak also functions as an indicator of the MoO_6 octahedra [155, 180, 264]. However, unlike the XAFS spectra from the Nb K-edge, the intensity of the pre-feature shoulder of the Mo K-edge was reported to be correlated with the coordination number, and more intense in the MoO_4 tetrahedral environment than in the MoO_6 octahedral environment [155, 264, 270]. Therefore, Figure 4.16(b) clearly indicates the transition from MoO_4 tetrahedra to MoO_6 octahedra after hydrogen treatments.

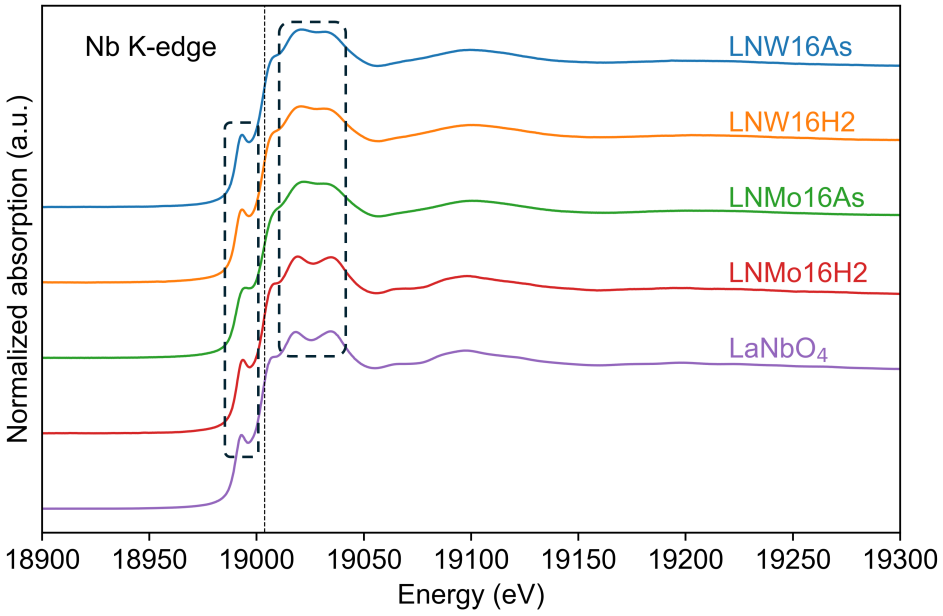


FIGURE 4.17: Comparison of the Nb K-edge XAFS spectra. The vertical dashed line indicates the position of e_0 at 19003.8 eV. The pre-edge and edge features are highlighted by dotted boxes.

In conclusion, the valence states of Nb, W and Mo cations in each sample were directly determined using the XAS technique. The excellent redox stability of LNW16 was proved for the first time, while LNMo16 can be reduced easily with the valence state of Mo cations not below +5. The XAFS spectra further suggested the change in the coordination environment, which can be essential in understanding the behaviours of these materials under the hydrogen atmospheres.

4.4 Coordination study

The synchrotron XAFS spectrum is valuable because it can not only determine the valence state of the absorbing atoms from the XANES part but also fit the local coordination environments from the EXAFS part. Figures 4.18-4.21 present the EXAFS fitting results of the Nb, W, and Mo cations in all samples. The different noise levels in the higher wave number space were due to the slightly unstable input energy from the synchrotron source, negligibly affecting the overall fitting results. The amplitude reduction factor, S_0^2, and the energy shift correction term, ΔE_0 of each element were determined from the EXAFS fittings of Nb_2O_5, WO_3, and MoO_3 commercial powders. The values of S_0^2 were fitted to be 1.00, 0.72, and 0.80 for Nb, W, and Mo, respectively, which have also been reported and used in other EXAFS studies [155, 180, 271, 272].

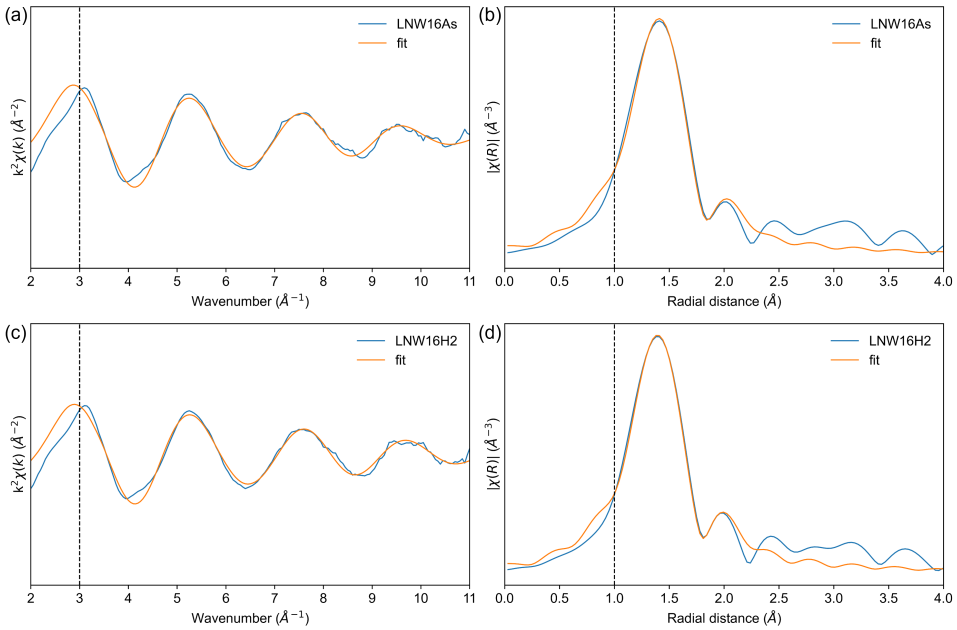


FIGURE 4.18: The EXAFS fitting results of the Nb K-edge in (a) LNW16As and (c) LNW16H2; the corresponding magnitude of Fourier-transform of (b) LNW16As and (d) LNW16H2. The vertical dashed line in each figure indicates the initial boundary of the fitting.

All EXAFS fittings were limited in the first neighbouring $MO_\times$ coordination environment. A typical $M-O$ bond length is greater than 1 $\AA$. Therefore, the fitting ranges started from 1 $\AA$ in the radial distance space indicated by the vertical dashed line in the figures. The intensity below 1 $\AA$ is probably due to background signal noise. Meanwhile, the initial fit ranges in the photoelectron wave number space were set at 3 $\AA^{-1}$ to minimise multiple scattering and background interference from the XANES parts. The fitting results are summarised in Table 4.5. N and R represent the averaged coordination number and the bond length, respectively. The mean-squared-displacement,

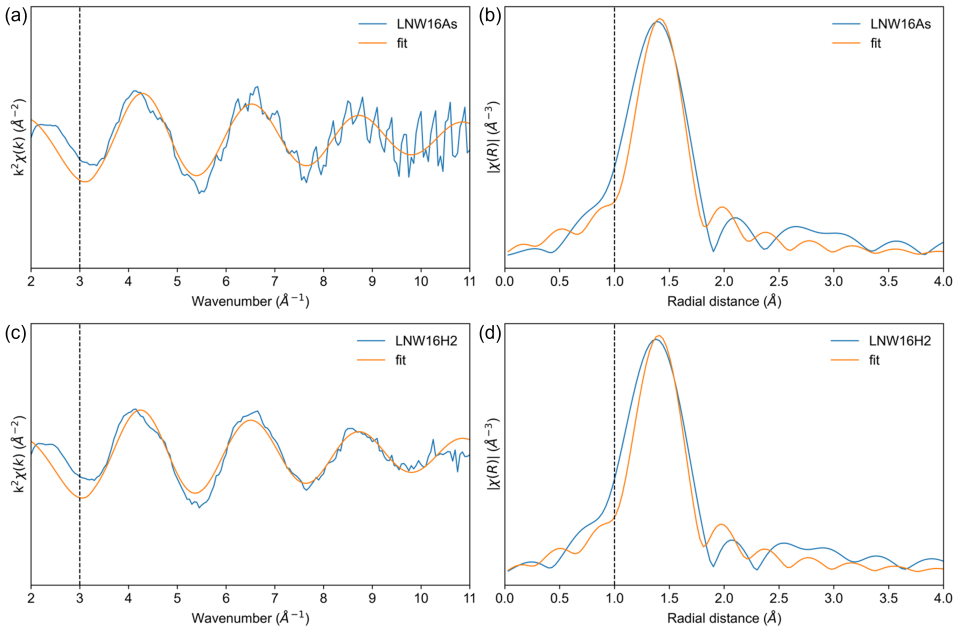


FIGURE 4.19: The EXAFS fitting results of the W L_3-edge in (a) LNW16As and (c) LNW16H2; the corresponding magnitude of Fourier-transform of (b) LNW16As and (d) LNW16H2. The vertical dashed line in each figure indicates the initial boundary of the fitting.

σ^2, works as an indicator of the degree of disorder if the measurements were taken at the same temperature [267]. Due to the lower concentration of W and Mo cations in the samples, the EXAFS fitting quality of W L_3- and Mo K-edge was relatively lower than that of the Nb K-edge.

For LNW16, the coordination number of Nb cations in both samples was fitted to be ~4.5. This fractional coordination number suggests that the interstitial oxygen ions were located between two NbO_4 units, forming a Nb_2O_9 unit, which is consistent with other experimental and computational studies [155, 164]. This near-tetrahedral configuration agrees well with the flat post-edge features in Figure 4.17. The $Nb-O$ bond length of LNW16As was ~1.89 $Å$, which is in good agreement with previous neutron diffraction studies, while the bond length of LNW16H2 was ~1.88 $Å$ [47, 151]. Therefore, these similar values in the coordination number and the bond length suggest a similar local environment of Nb cations in both samples.

The situation of W cations in both samples was roughly the same. The coordination number of the W cations was ~4.0 with a bond length of ~1.80 $Å$. This WO_4 tetrahedral configuration is in line with the sharp white line of both samples in Figure 4.15, and is in good agreement with the previous study [267]. The slightly shorter $W-O$ bond length compared to $Nb-O$ bond length is reasonable since W cations prefer a WO_4 tetrahedral configuration. Meanwhile, the smaller σ^2 of the W cations suggests that this WO_4 tetrahedral configuration is more ordered than the Nb_2O_9 configuration.

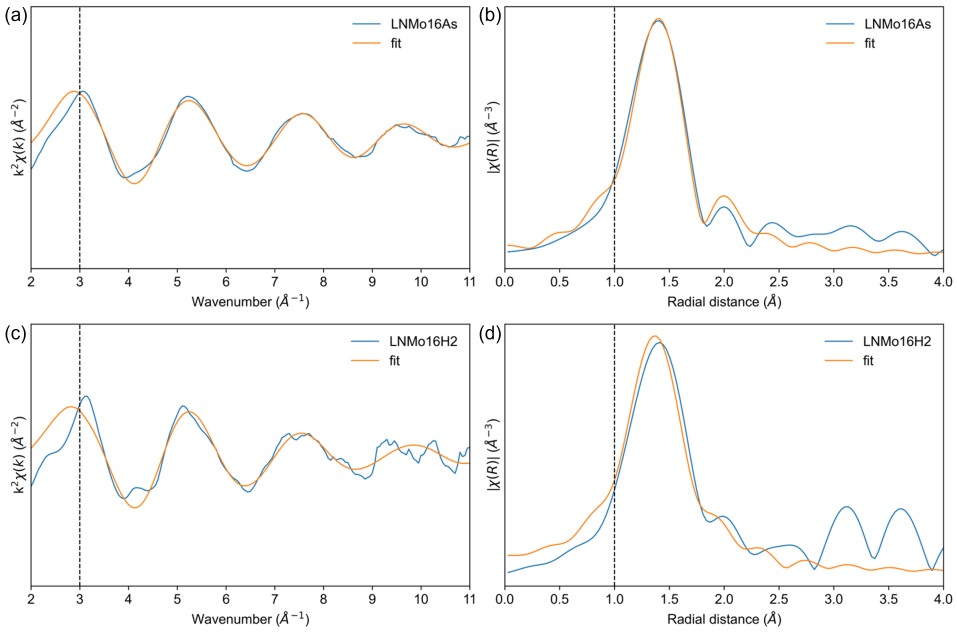


FIGURE 4.20: The EXAFS fitting results of the Nb K-edge in (a) LNMo16As and (c) LNMo16H2; the corresponding magnitude of Fourier-transform of (b) LNMo16As and (d) LNMo16H2. The vertical dashed line in each figure indicates the initial boundary of the fitting.

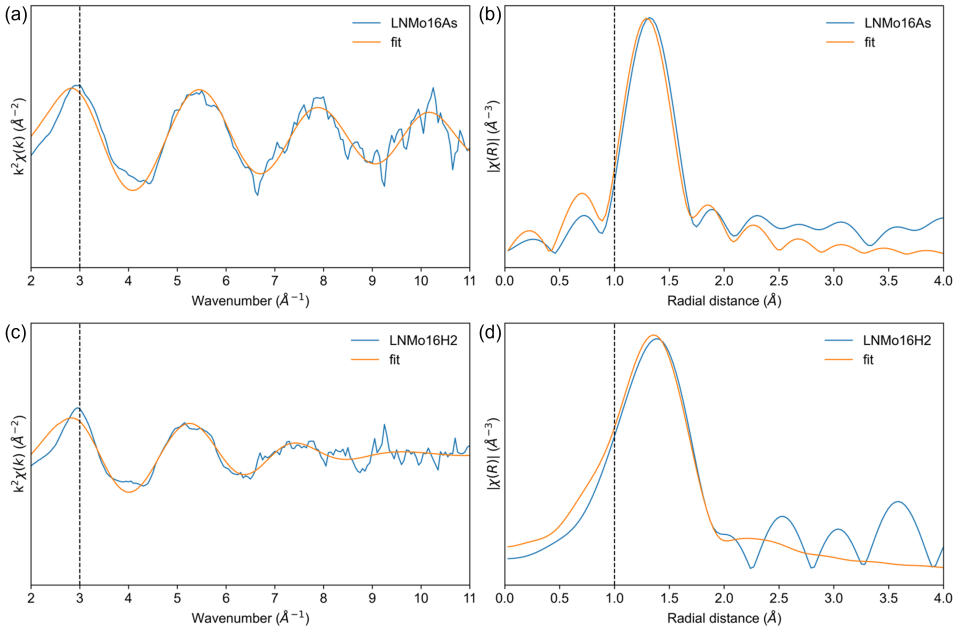


FIGURE 4.21: The EXAFS fitting results of the Mo K-edge in (a) LNMo16As and (c) LNMo16H2; the corresponding magnitude of Fourier-transform of (b) LNMo16As and (d) LNMo16H2. The vertical dashed line in each figure indicates the initial boundary of the fitting.

In contrast, the coordination number of the Nb cations was fitted to ∼4.0 and ∼5.0 in LNMo16As and LNMo16H2, respectively. The value of ∼4.0 clearly indicates a NbO_4 tetrahedral configuration in LNMo16As, while the 5-coordinated environment in LNMo16H2 is averaged from NbO_4 and NbO_6 units, as suggested in a previous DFT study [152]. The difference in the bond length of ∼0.02 $\AA$ is negligible and could be due to the average between the shorter and longer bond lengths of NbO_4 and NbO_6 units in LNMo16H2.

Similar changes can also be observed in the EXAFS fittings of Mo cations. The MoO_4 tetrahedral configuration with a bond length of ∼1.78 $\AA$ in LNMo16As changed significantly to the 5-coordinated environment with a longer bond length of ∼1.87 $\AA$ in LNMo16H2. This dramatic change is consistent with the pre-edge shoulder and the post-edge feature in Figure 4.16, strongly indicating the reduction of LNMo16 with the change in the coordination environment of the Mo cations. The vast increase in σ^2 also suggests a highly disordered $MoO_\times$ coordination environment in LNMo16H2.

TABLE 4.5: Extracted structural parameters of each sample from EXAFS fittings. N,R, and σ^2 represent the averaged coordination number, the bond length and the mean-square-displacement in the radial distance space, respectively.

	Edge	N	R ($\AA$)	σ^2 ($\AA^2$)	R-factor
LNW16As	Nb-K	4.67±0.22	1.891±0.005	0.006±0.001	0.012
LNW16H2	Nb-K	4.44±0.19	1.880±0.004	0.005±0.001	0.009
LNMo16As	Nb-K	4.09±0.13	1.886±0.003	0.004±0.001	0.005
LNMo16H2	Nb-K	5.17±0.29	1.865±0.002	0.006±0.001	0.014
LNW16As	W-L_3	3.96±0.23	1.806±0.005	0.002±0.001	0.037
LNW16H2	W-L_3	4.06±0.25	1.803±0.005	0.002±0.001	0.034
LNMo16As	Mo-K	3.93±0.18	1.784±0.002	0.001±0.001	0.019
LNMo16H2	Mo-K	4.82±0.20	1.872±0.010	0.007±0.004	0.030

It is worth highlighting that many factors inevitably compromise the EXAFS fittings. The selection of the window function and the fitting cut-off range, the mathematical process of the lower and upper boundaries of the fitting data, the choice of the initial structure for the single-scattering path calculations, and the exclusion of the multi-scattering events all affect the fitting results. Therefore, EXAFS cannot resolve a perfect local coordination environment. For example, the EXAFS fittings of LNMo16As failed to locate the interstitial oxygen ions, since both the Nb and Mo cations were fitted to be 4-coordinated.

However, the above EXAFS results clearly showed the distinct behavioural differences between LNW16H2 and LNMo16H2, which is in good agreement with the results from

other techniques. This consistency increased the credibility of the fitting results and the arguments drawn on the basis of them.

In conclusion, the EXAFS fitting results agree well with the description of the coordination environment suggested by the XANES spectra. The coordination environment of LNW16 remains stable after hydrogen treatments, while LNMo16 was dramatically reduced, changing from a tetrahedral to a mixed tetrahedral and octahedral coordination configuration.

4.5 Conclusions

This chapter uses multiple techniques to examine how LNW16 and LNMo16 could change under hydrogen atmospheres from structural, compositional, and redox perspectives. Overall, the results agreed well with each other, suggesting that LNW16 is surprisingly stable under hydrogen atmospheres. In contrast, LNMo16 can be significantly reduced, changing the structure and reducing the valence state of Mo cations. This behavioural difference sparked research interest in examining the influence of these changes on performance, especially conductivity.

Chapter 5

Electrochemical performances of W- and Mo-substituted $LaNbO_4$ under reducing conditions

This chapter focuses on electrochemical performance studies of W- and Mo-substituted $LaNbO_4$, especially under reducing conditions. A strong correlation between the redox effects discussed above and the conductivity changes was clearly demonstrated. The proton conductivity, which uptakes protons directly from dry hydrogen atmospheres, was presented and investigated.

5.1 Impedance study

Figure 5.1 presents two example Nyquist plots from LNW16. At lower temperatures, the Nyquist plot showed two separable semicircles representing the grain boundary and the electrode responses. Ideally, a "perfect" Nyquist plot should present three responses from bulk, grain boundary, and electrode, as presented schematically in Figure 3.11. However, the bulk response is usually tricky to detect due to the requirement of a very high measurement frequency. The relation between the time constant, τ, and the frequency, f, can be expressed as Equation 5.1.

$$f = \frac{1}{2\pi\tau} \tag{5.1}$$

Given the upper limit frequency of 1 MHz in this work, the lower limit time constant of the response is $\sim 1.6\times10^{-7}$ s. Then, assuming the bulk response has a typical capacitance of $\sim 1\times10^{-12}$ F and based on Equation 3.37, the bulk resistance of larger than 1.6×10^{5} Ω is required to allow the corresponding semicircle to become visible [219]. This high bulk resistance is not feasible at high temperatures. Therefore, for Nyquist plots similar to Figure 5.1(a), the total resistances of the electrolyte were extracted using

the equivalent circuit model presented in the insert of Figure 5.1(a). At higher temperatures, given the reduced resistance of the grain boundary, its semicircle diminished, leaving only semicircles representing electrode responses visible. Therefore, the total resistances of the electrolyte can only be estimated from the high-frequency intercepts.

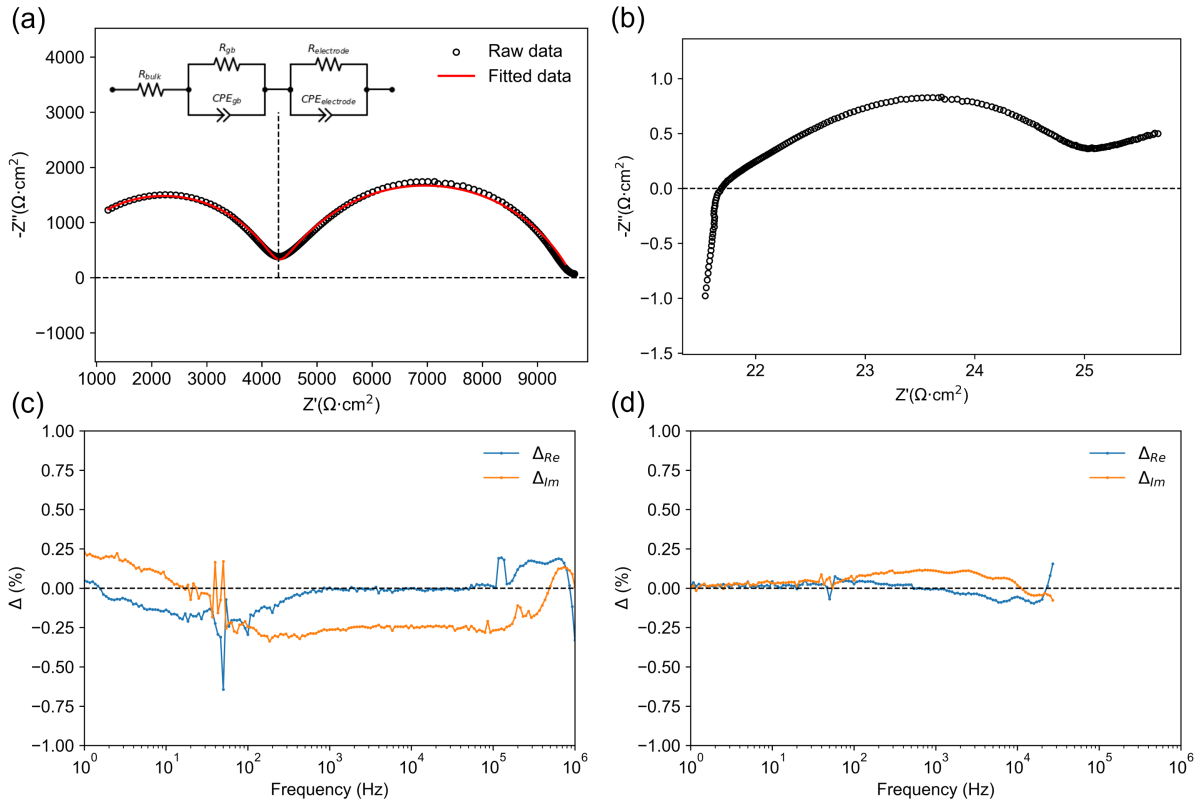


FIGURE 5.1: Example Nyquist plot of LNW16 measured at (a) 618 °C under dry air and (c) its corresponding fitting result from the KK test; example Nyquist plot of LNW16 measured at (b) 813 °C under dry 5% H_2 and (d) its corresponding fitting result from the KK test. The insert in (a) shows the corresponding equivalent circuit model. The inductance part in (b) was truncated to $-Z''\approx$-1 Ω/cm^2 figure readability and was excluded from the KK test in (d).

Each EIS measurement was repeated multiple times to guarantee reproducibility. The KK test further validated the obtained spectra, as presented in Figure 5.1(c) and (d). Both measurements presented residuals smaller than 0.5% throughout the frequency range, suggesting valid spectra with good quality [220]. It was noted that there was a subtle imaginary residual bias, especially in Figure 5.1(c), where the residual consistently deviated from zero. This bias usually indicates an invalid time-variance nature [220]. However, elongating the delay time and repeating the measurements did not show any noticeable change. In addition, the measuring temperature kept oscillating slightly during the measurements. Therefore, this bias is likely due to fluctuations in $\pm$3 °C in the furnace temperature, and the EIS spectra were in general validated.

Figures 5.2 and 5.3 show the total conductivities of LNW16 and LNMo16 obtained from the EIS spectra. For both LNW16 and LNMo16, the conductivity measured at elevated temperatures under non-reducing conditions overlapped with each other, suggesting pure ionic conduction. The proton conductivity under non-reducing conditions was negligible, as there was no increase in conductivity under wet conditions. Both samples showed a linear conductivity increase with the temperature under non-reducing conditions, suggesting that they remained stable under measured temperature and atmosphere conditions. The activation energy of each measurement was summarised in Table 5.1 and Table 5.2. The higher activation energy of ∼1.50 eV for both samples suggested their oxygen ion conducting nature [48, 85]. All these results were consistent with the above discussions and previous studies, indicating that both samples were good pure oxygen ion conducting electrolytes in the intermediate temperature range under non-reducing conditions [138, 139, 152, 153, 250].

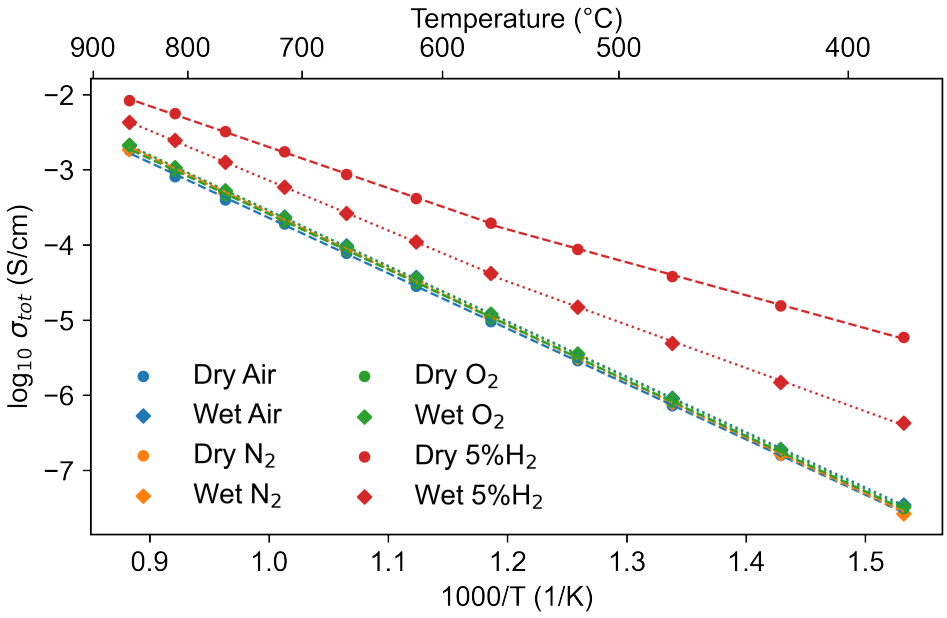


FIGURE 5.2: Total conductivity of LNW16 measured under different atmospheres. Adapted from [250] with permission under a Creative Commons Attribution-NonCommercial 3.0 Unported Licence.

Despite the similar activation energy, the total conductivity of LNMo16 is about five times higher than that of LNW16 under the same measuring conditions, suggesting a higher concentration of charge carriers. Given that the concentration of interstitial oxygen ions in both samples should be the same, as demonstrated in Chapter 4, this conductivity difference strongly suggests the suppressed trapping effect on LNMo16, resulting in a higher charge carrier concentration [152].

When it comes to reducing conditions, the conductivity behaviour of both samples is

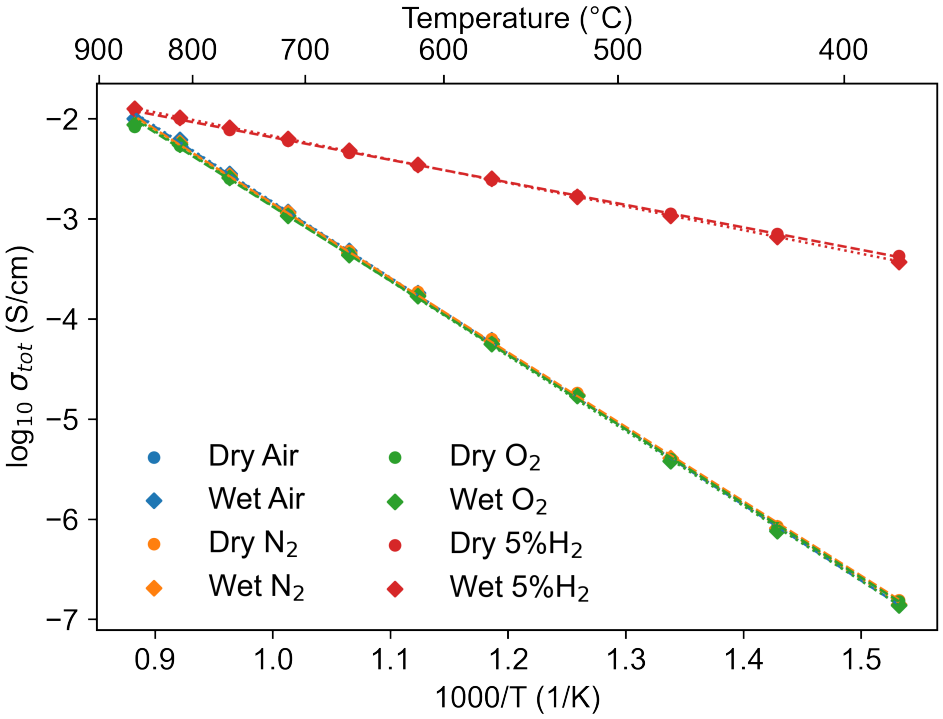


FIGURE 5.3: Total conductivity of LNMo16 measured under different atmospheres. Adapted from [250] with permission under a Creative Commons Attribution-NonCommercial 3.0 Unported Licence.

significantly different from that under non-reducing conditions, showing a considerable conductivity enhancement. Typically, the conductivity increases under reducing conditions for electrolytes is attributed to the reduction of oxygen anions, as Equation 2.5 suggested [48, 273]. In this work, since both samples possess interstitial oxygen ions, the reduction is more likely to be expressed as Equation 5.2.

$$H_{2(g)} + O_i'' = H_2O_{(g)} + 2e' \tag{5.2}$$

To correlate electronic conductivity with oxygen partial pressure, Equation 5.2 can be rewritten to a more general form, as expressed in Equation 5.3.

$$O_i'' = \frac{1}{2}O_{2(g)} + 2e' \tag{5.3}$$

Equation 5.3 clearly indicates the electronic conductivity increase as a function of $pO_2^{-1/4}$ [48, 273].

Canu *et al.* investigated the conductivity behaviour of LNW16, reporting a similar conductivity increase under reducing conditions [153]. They attributed the increase to the above reduction process and proposed an estimated total conductivity change as a function of oxygen partial pressure, as replotted in Figure 5.4 [153]. To validate this

TABLE 5.1: Calculated activation energy of LNW16 measured under different atmospheres. T_c is ~570 °C. Adapted from [250] with permission under a Creative Commons Attribution-NonCommercial 3.0 Unported Licence.

Atmosphere	Humidity	E_a (eV)	R-squared
Air	Dry	1.46	0.99
	Wet	1.46	0.99
N_2	Dry	1.48	1.00
	Wet	1.48	0.99
O_2	Dry	1.46	0.99
	Wet	1.47	1.00
5% H_2	Dry	0.87 (<T_c)	0.99
		1.08 (>T_c)	0.99
	Wet	1.14 (<T_c)	0.99
		1.32 (>T_c)	1.00

TABLE 5.2: Calculated activation energy of LNMo16 measured under different atmospheres. Adapted from [250] with permission under a Creative Commons Attribution-NonCommercial 3.0 Unported Licence.

Atmosphere	Humidity	E_a (eV)	R-squared
Air	Dry	1.50	0.99
	Wet	1.50	0.99
N_2	Dry	1.47	0.99
	Wet	1.48	0.99
O_2	Dry	1.47	0.99
	Wet	1.49	0.99
5% H_2	Dry	0.45	0.99
	Wet	0.47	0.99

estimation, the oxygen partial pressure of each EIS measurement must be determined. For oxygen-rich gases such as air and pure O_2, the partial pressure can be determined easily by their oxygen fraction. However, for oxygen-poor gases such as N_2 and 5% H_2, the determination is challenging as minor effects such as measuring chamber gas leakage and humidity can change the partial pressure significantly. For example, water molecules might split into hydrogen and oxygen, increasing the oxygen partial pressure, as expressed in Equation 5.4.

$$\begin{aligned} H_2O_{(g)} &= H_{2(g)} + \frac{1}{2}O_{2(g)} \\ pO_2 &= \left(\frac{K_w \cdot pH_2O}{pH_2}\right)^2 \end{aligned} \tag{5.4}$$

Where K_w is the equilibrium constant of this reaction changing with the temperature. This humidity effect is more significant in hydrogen conditions.

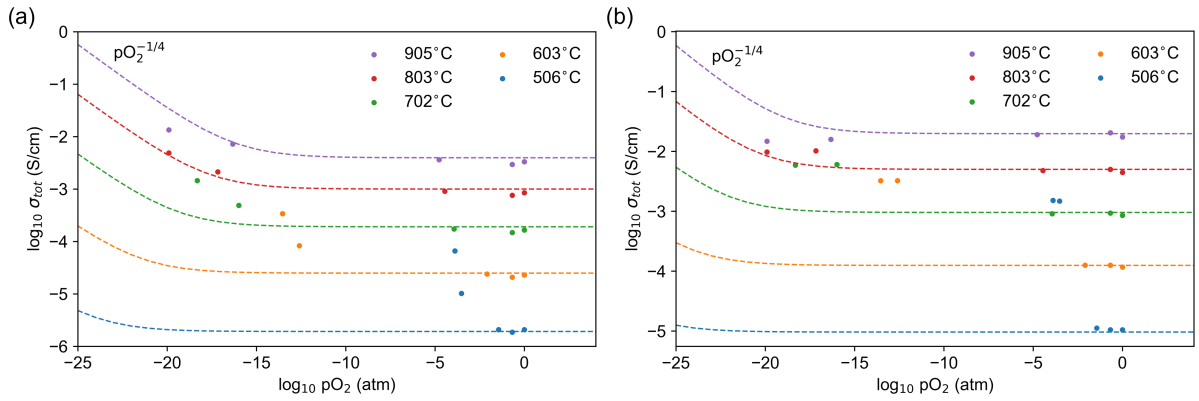


FIGURE 5.4: Total conductivity of (a) LNW16 and (b) LNMo16 as a function of oxygen partial pressure. The scatters represent the conductivity measured in this work. The dashed lines correspond to the typical electronic enhanced conductivity under reducing conditions proposed by Canu *et al.* [153].

In this work, the actual oxygen partial pressures were recorded using a ZrO_2 oxygen sensor and the total conductivity presented in Figure 5.2 and Figure 5.3 were replotted in Figure 5.4(a) and (b), respectively. It is worth mentioning that only the oxygen partial pressures of the oxygen-poor gases were recorded, while the oxygen partial pressures of air and oxygen were directly estimated from their oxygen fractions. Besides, for an ideal sealed measuring chamber, the oxygen partial pressure of an oxygen-poor gas should be increased with the increase of the temperature due to the larger equilibrium constant. However, the tendency was reversed in this work because flowing gases were used, and the measuring chamber was connected with the ambient atmosphere. Higher temperatures increased the flow rate, extruding more outer air from the chamber.

Figure 5.4 suggested that the conductivity behaviour of both LNW16 and LNMo16 deviated from the estimation, indicating other conductivity enhancement mechanisms. This -1/4 power law dependence did not apply to LNMo16 as it assumed that cations remain stable. However, as has been extensively discussed in Chapter 4, Mo^{6+} cations will be reduced under reducing conditions, generating electrons as expressed in Equation 4.2 and 4.3. The activation energies of ∼0.46 eV also suggested that the conductivity of LNMo16 under reducing conditions is electronic-dominated, which is in line with the previous study [139]. Therefore, a complete description of the conductivity behaviour of LNMo16 as presented in Figure 5.3 can be given.

The reduction of Mo^{6+} cations increased the electronic conductivity while reducing the oxygen ionic conductivity as the loss of interstitial oxygen ions. At low temperatures, the electronic mobility is significantly higher than that of the interstitial oxygen

ions, resulting in a considerable conductivity enhancement. However, at high temperatures, the mobility of the interstitial oxygen ions generally became comparable with electrons, minimising the conductivity difference between reducing and non-reducing conditions. It is reasonable to expect that electronic conductivity under reducing conditions will eventually fail to fully compensate for the loss of oxygen ionic conductivity, resulting in a smaller conductivity at a higher temperature, *e.g.*, 900 °C, compared to that under non-reducing conditions. This swap of conductivity has been reported in LNMo10 [155].

However, the deviation of LNW16 in Figure 5.4 is somewhat surprising as W^{6+} cations remain stable under reducing conditions. The conductivity behaviour of LNW16 under reducing conditions presented a humidity dependence and a non-linear temperature dependence. The conductivity under wet 5% H_2 is lower than that under dry 5% H_2 but still higher than that under non-reducing conditions. The activation energies under dry 5% H_2 were 0.87 eV at low temperatures (<570 °C) and 1.08 eV at high temperatures (>570 °C), while the activation energies under wet 5% H_2 were 1.14 eV and 1.32 eV for low and high temperatures, respectively. Similar to LNMo16, the conductivity difference between reducing and non-reducing conditions decreased with the increase in temperature. The above results strongly indicated a distinct different conduction mechanism of LNW16 under reducing conditions.

Since the typical -1/4 power law dependence and the electronic conduction raised by cation reductions was ruled out, the potential conduction contribution from protons should be considered. One possible proton conducting mechanism can be expressed as Equation 5.5, similar to Equation 2.13.

$$\begin{aligned} H_{2(g)} + 2O_i'' &= 2OH_i' + 2e' \\ H_{2(g)} + 2O_O^{\times} &= 2OH_i^{\cdot} + 2e' \end{aligned} \tag{5.5}$$

The evidence of this protonation mechanism has been shown in section 4.3.1 and will be investigated comprehensively in Chapter 6. Given that the protonation process is exothermic, possessing a negative enthalpy, it is preferred at low temperatures, lowering the activation energy [62]. At higher temperatures, the increase of oxygen ionic conduction contribution minimised the conductivity difference between reducing and non-reducing conditions and enlarged the activation energy. Besides, by a rule of thumb, the activation energy of proton conduction is expected to be 2/3 of the value for oxygen ionic conduction [274, 275]. The activation energy difference in LNW16 agrees well within this ratio, strengthening the protonation mechanism. What is more, if the protonation process in LNW16 is surface exchange limited, then the dependence on humidity could be explained by the surface environment difference between dry and wet 5% H_2 conditions. This surface exchange limiting nature has been reported in

LNW16 for oxygen incorporation due to the lack of surface electrons, which is likely also the case in protonation [47].

Another indicator of conducting species is the geometry of the corresponding electrode responses, more specifically, the interface between the sample and the electrode [219]. The initial stage of the electrode responses in Figure 5.1(a) presented a tail with a slope of $\sim$45° associating with the diffusion of oxygen species through the electrode. Usually, electrode polarisation resistance is considerable due to the slow oxygen diffusion process [219]. Given the relatively faster proton diffusion, its electrode polarisation resistance is reduced. This suppressed resistance has been reported in Ca-substituted $LaNbO_4$ under wet air [275]. Because platinum electrodes were used, there was a negligible impedance barrier to charge transfer for electrons. Therefore, electrode responses should be vastly reduced [219].

Figure 5.5 presents example Nyquist plots of LNW16 and LNMo16 measured at 570 °C under 5% H_2 conditions. Both LNW16 measured under dry and wet 5% H_2 conditions possessed a reduced electrode response with an effective capacitance of 8.39×10^{-5} F and 4.46×10^{-6} F, respectively, suggesting their ionic conducting nature. In comparison, the diminished electrode response in LNMo16 under dry 5% H_2 clearly indicates that the dominant conducting species are electrons. The subtle electrode response in LNMo16 under wet 5% H_2 combined with a lower resistance appears to suggest proton conduction via the hydration process. This phenomenon can be reasonable, as the reduction might create a small amount of oxygen vacancies. However, this resistance decline might also be due to the smaller temperature difference between the measurements. In general, both LNMo16 measured under dry and wet 5% H_2 conditions possessed a decreased electrode response, suggesting an electronic conducting nature.

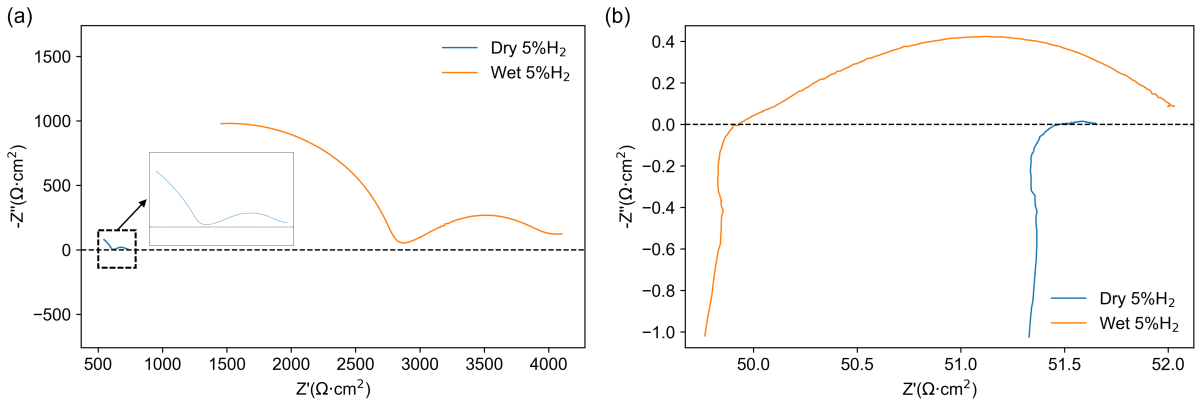


FIGURE 5.5: Example Nyquist plots of (a) LNW16 and (b) LNMo16 measured at 570 °C under 5% H_2 conditions. The inductance parts in (b) were truncated to $-Z''\approx$-1 Ω/cm^2 for figure readability.

Although the conduction mechanisms under 5% H_2 are different between LNW16 and

LNMo16, the conductivity changes were found to be reversible. The total conductivity of LNW16 and LNMo16 under 5% H_2 can be reduced quickly to the level under non-reducing conditions after switching the atmospheres from 5% H_2 to air and vice versa. For LNW16, this fast conduction reversibility suggests relatively fast protonation and deprotonation processes. For LNMo16, this fast conduction reversibility suggests that the reduction of Mo^{6+} cations is reversible, which is consistent with the conclusion drawn in Chapter 4.

5.2 Hebb-Wagner polarisation study

In addition to protonation, Equation 5.5 also implied simultaneously generated electrons, which might lead to an increase in electronic conduction. One might argue that, though the protonation process occurs, the conductivity enhancement can be from electrons, protons, or both. Therefore, the separation of the conductivity contribution from each charge carrier, oxygen ions, protons, and electrons, is required to fully understand the conductivity enhancement of both samples under 5% H_2 conditions. In this work, the partial conductivity of electrons, σ_e, under 5% H_2 conditions was determined using the Hebb-Wagner polarisation method. A dense pellet metal disk was used to block the ion conduction totally. Therefore, the transport number of electrons can be extracted using Equation 3.43, where the total conductivity can be estimated from the above EIS spectra. Given the pure oxygen ion conduction nature of both samples under non-reducing conditions, the partial conductivity of oxygen ions can also be estimated from the above EIS spectra. Therefore, the transport number of protons can be deduced using Equation 5.6.

$$t_p = \frac{\sigma_p}{\sigma_O + \sigma_p + \sigma_e} = 1 - \frac{\sigma_O + \sigma_e}{\sigma_{tot}} \tag{5.6}$$

One key factor in guaranteeing a valid Hebb-Wagner polarisation measurement is the airtightness of the ion-blocking electrode side. A subtle air leakage will result in an incomplete ion-blocking effect, incorrectly increasing the extracted electronic conductivity. A simple method to check the airtightness is to evaluate the current relaxation curve under a constant applied voltage [227]. Figure 5.6 presents three example current relaxation curves of the Hebb-Wagner polarisation cell measured at different temperatures under dry 5% H_2 conditions. The applied voltage was 0.30 V. The steadily decreased current relaxation curve to a specific value represents the typical relaxation response, suggesting good airtightness [227].

Figures 5.7 and 5.8 presented the measured electronic conductivity of LNW16 and LNMo16 in comparison with their corresponding total conductivity estimated from

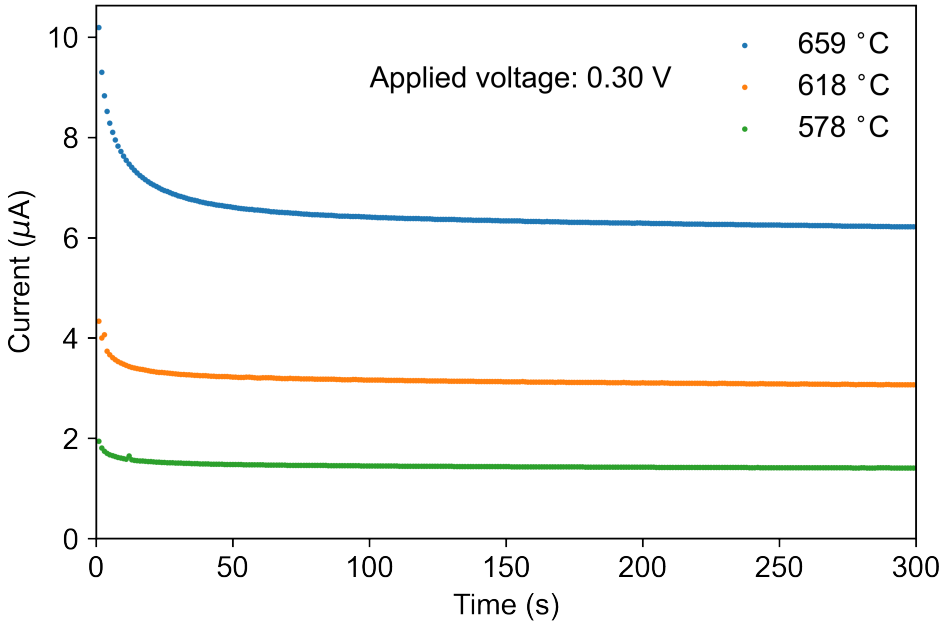


FIGURE 5.6: Example current relaxation curves of the Hebb-Wagner polarisation cell measured at different temperatures under dry 5% H_2 conditions. The applied voltage is 0.30 V.

EIS spectra, respectively. For LNW16, the electronic conductivity at low temperatures was at the same level as the total conductivity in air conditions, suggesting an increased electronic conduction. However, the increased electronic conductivities were significantly lower than the total conductivities under dry and wet 5% H_2 conditions, suggesting an enormous protonic conduction contribution. The calculated partial activation energies of 1.09 eV (R-squared = 0.99) and 1.06 eV (R-squared = 0.99) were more significant than the values of other $LaNbO_4$ based materials with mixed electronic and ionic conductivity [67]. These larger values suggested that the samples were still highly electronic-resistive under 5% H_2 conditions, while the electrons were likely generated from the protonation process. The similar electronic conductivities under dry and wet 5% H_2 conditions indicated that the large total conductivity difference was mainly from the difference in protonic conductivities. One possible explanation is that the surface coverage of hydroxyl species originating from H_2O blocks the absorption sites for the protonation, which has been reported repeatedly in the studies of hydrogen surface exchange [276, 277]. However, further validation of this hypothesis requires detailed surface analysis studies, which is beyond the scope of this work.

In contrast, the significantly enhanced electronic conductivity in LNMo16 under dry 5% H_2 conditions with an activation energy of 0.44 eV (R-squared = 0.99) clearly indicated the electronic-dominated conducting nature originating from cation reductions. Nevertheless, the electronic conductivity was still about half an order lower than the

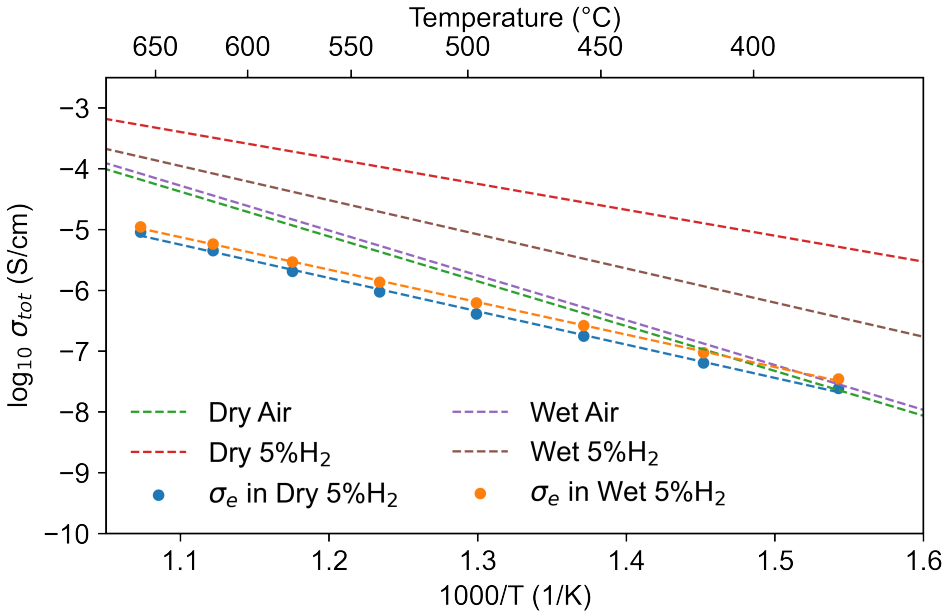


FIGURE 5.7: Partial electronic conductivity of LNW16 measured by Hebb-Wagner polarisation method. The total conductivity of LNW16 under air and 5% H_2 conditions estimated from EIS measurements are replotted as dashed lines for direct comparison. The calculated activation energies of electrons are 1.09 eV (R-squared = 0.99) and 1.06 eV (R-squared = 0.99) for LNW16 measured under dry and wet 5% H_2 conditions, respectively.

total conductivity, suggesting the presence of proton conductivity in LNMo16. This protonation-reduction co-effect might be summarised as Equation 5.7.

$$2H_{2(g)} + Mo_{Nb}^{\cdot} + O_i'' + 2O_O^{\times} = Mo_{Nb}^{\times} + H_2O_{(g)} + 2OH_O^{\cdot} + 3e' \tag{5.7}$$

Figures 5.9(a) and 5.10(a) present the extracted transport number of electrons in LNW16 under dry and wet 5% H_2 conditions, respectively. For dry conditions, the electronic conduction contribution increased with increasing temperature, but was less than 2% throughout the measuring temperature range. Given the excellent structural and redox stabilities of LNW16, the oxygen ionic conductivity under 5% H_2 conditions is likely to be the same as that under non-reducing conditions. The estimated transport number of protons was surprisingly high, indicating a protonic-dominated conductivity of LNW16 under dry 5% H_2 conditions. The protonic conduction contribution decreased with the increase in temperature, which can be due to the fast increase in oxygen ionic conduction.

Unlike conductivity behaviours under dry 5% H_2 conditions, the transport number of electrons in LNW16 under wet 5% H_2 conditions was more significant and reduced with increasing temperature. Applying the same procedure resulted in a suppressed

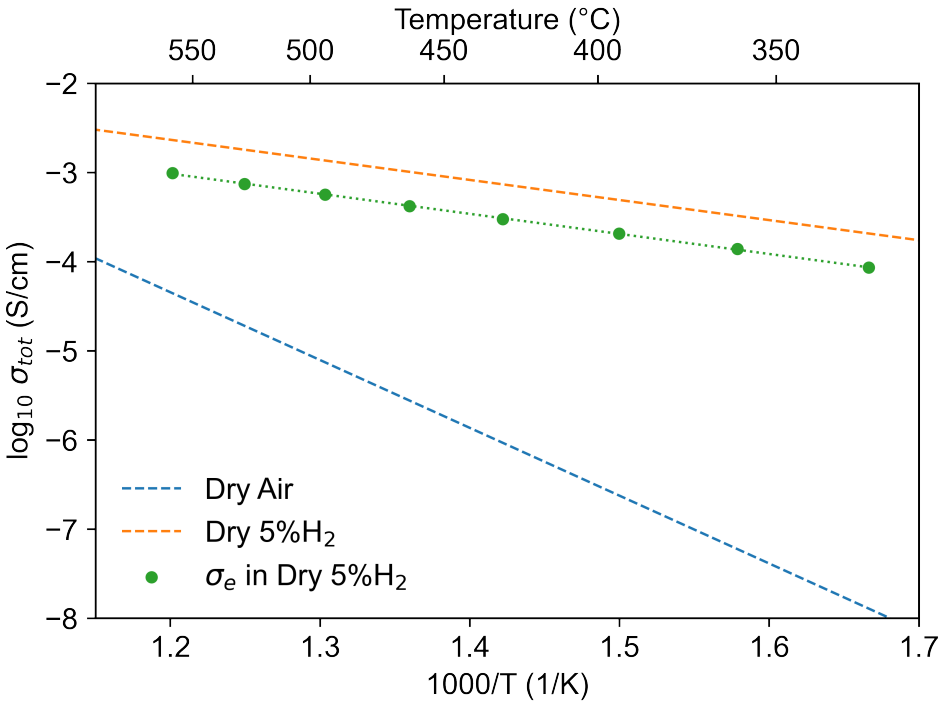


FIGURE 5.8: Partial electronic conductivity of LNMo16 measured by Hebb-Wagner polarisation method. The total conductivity of LNMo16 under dry air and dry 5% H_2 conditions estimated from EIS measurements are replotted as dashed lines for direct comparison. The calculated activation energy of electrons is 0.44 eV (R-squared = 0.99).

proton conduction contribution of less than 50% at high temperatures, suggesting a water blocking effect for protonation.

It is worth noting that the assumption of unchanged oxygen ionic conductivity under 5% H_2 conditions may lead to an overestimation of the protonic conduction contribution. The oxygen ionic conductivity could increase due to the relaxation of the trapping effect induced by proton incorporation. However, validating this hypothesis requires separating oxygen ionic and protonic conductivity, which would introduce significant additional challenges in selecting a suitable blocking layer. Further polarisation measurements or alternative electromotive force (EMF) measurements are planned for future work.

When it comes to LNMo16, the transport number of electrons was somewhat insensitive to temperatures at about 42%. This value is consistent with the value of about 49% from the previous study of LNMo20, suggesting the mixed oxygen ionic, protonic and electronic conducting nature of LNMo16 [139]. Given its poorer structural and redox stabilities, the estimation of oxygen ionic conductivity from the total conductivity under non-reducing conditions is not viable. However, the upper and lower limits of the

protonic conduction contribution can be extracted by assuming oxygen ionic conductivity is negligible and oxygen ionic conductivity is the same as under air, respectively. The blue area in Figure 5.11 indicates the possible values for the transport number of protons in LNMo16 under dry 5% H_2 conditions. The protonic conduction contribution remained steady throughout the measuring temperature range at approximately 58%. The potential contribution from oxygen ionic conduction was reasonably minor, as charge carriers, interstitial oxygen ions, were largely removed from the sample under reducing conditions.

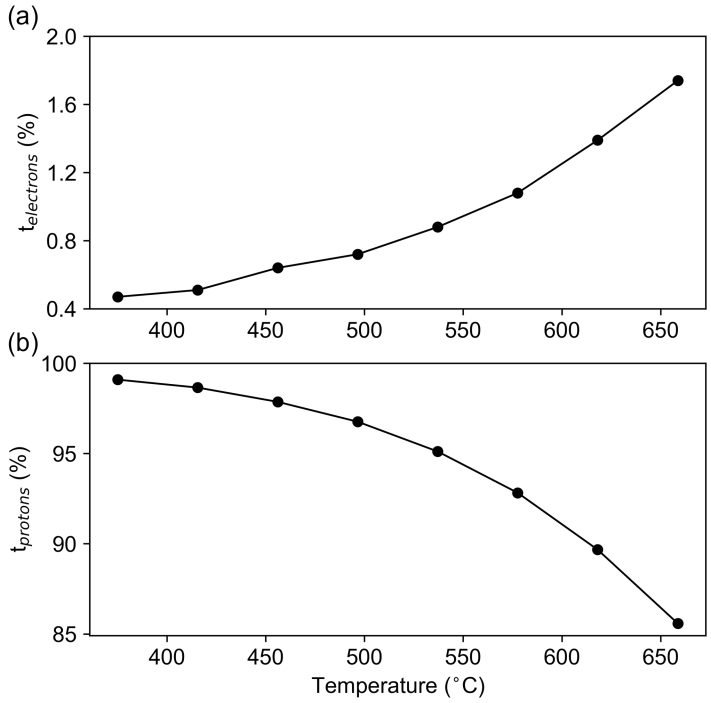


FIGURE 5.9: (a) Extracted transport number of electrons in LNW16 under dry 5% H_2 conditions from Hebb-Wagner polarisation method. (b) Estimated transport number of protons in LNW16 under dry 5% H_2 conditions based on the assumption that the oxygen ionic conductivity under dry 5% H_2 conditions is the same as under dry air conditions.

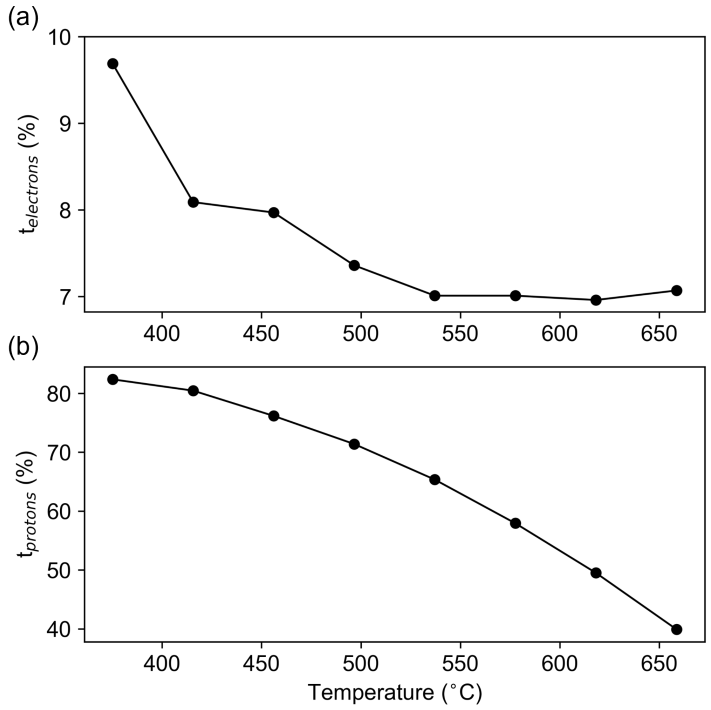


FIGURE 5.10: (a) Extracted transport number of electrons in LNW16 under wet 5% H_2 conditions from Hebb-Wagner polarisation method. (b) Estimated transport number of protons in LNW16 under wet 5% H_2 conditions based on the assumption that the oxygen ionic conductivity under wet 5% H_2 conditions is the same as under wet air conditions.

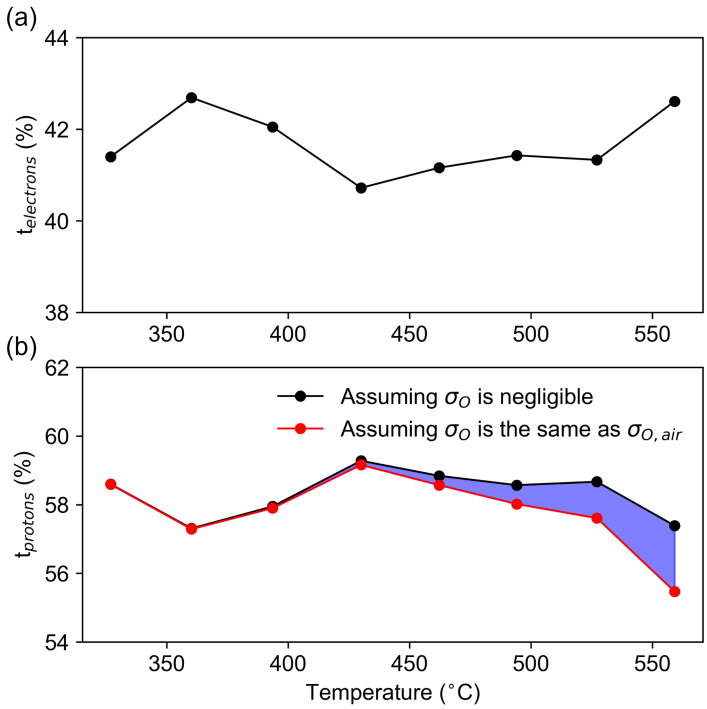


FIGURE 5.11: (a) Extracted transport number of electrons in LNMo16 under dry 5% H_2 conditions from Hebb-Wagner polarisation method. (b) Estimated lower and upper limits of transport number of protons in LNMo16 under dry 5% H_2 conditions based on different assumptions.

5.3 Conclusions

In this chapter, the total conductivities and the transport numbers of LNW16 and LNMo16 under reducing conditions were successfully estimated by combining EIS and Hebb-Wagner polarisation measurements. An impressive protonic-dominated conductivity was confirmed in LNW16 under reducing conditions for the first time, implying its potential application as a proton-conducting electrolyte. However, the mixed protonic-electronic conducting nature of LNMo16 under reducing conditions was found, implying its application as a proton-conducting electrode.

Meanwhile, the above results highlight the potential protonic conduction contribution via protonation instead of conventional hydration under reducing conditions, which has been reported in other oxides [69]. This direct protonation from dry hydrogen atmospheres could explain the abnormal conductivity enhancement in some proton-conducting oxides, such as BZY and BCY, under wet hydrogen atmospheres compared to wet air atmospheres, which are often simply assumed to be electronic conduction [278].

Furthermore, electrochemical studies of both samples uncovered a profound correlation between redox behaviour and electrochemical performance under reducing conditions. Hopefully, the above results can provide helpful guidelines for future selection strategies in substitutions and materials.

Chapter 6

Proton incorporation study

This chapter presents the attempts to directly probe proton incorporation and transport in LNW16H2 and LNMo16H2. In many of the upcoming studies, the proton content remained undetectable due to the low proton concentration and limited instrumental availability. However, there are still promising results that provide direct evidence of proton incorporation in this type of material for the first time.

6.1 Mass change study

Proton incorporation and release will cause the mass change of the samples. Therefore, it is possible to investigate proton incorporation via *in-situ* thermogravimetric analysis by switching the atmospheres. Figure 6.1 presents the *in-situ* TGA results of both LNW16As and LNMo16As. For LNW16As, similar to the *ex-situ* TGA results, the mass change of -0.004 wt% was negligible below the instrumental uncertainty, indicating an excellent redox stability of LNW16. Unfortunately, however, this change also indicates that there was no noticeable mass increase induced by proton incorporation. The measurable mass increase in conventional proton-conducting oxides originates from the incorporation of hydroxyl groups [189, 190]. In LNW16 and LNMo16, hydrogen is more likely to be incorporated in the form of protons, resulting in undetectable mass changes below instrumental uncertainty. In addition, the increase in mass from proton incorporation could be overshadowed by the buoyancy effect and the potential desorption of surface oxygen species, as indicated by the ESR results presented in Figure 4.13. One might argue that such a small amount of proton incorporation should not be able to enhance the conductivity by exceeding two orders of magnitude. However, studies of 1% Ca-substituted $LaNbO_4$ ($La_{0.99}Ca_{0.01}NbO_{3.995}$) have shown around an order of magnitude increase in maximum conductivity, while the upper limit hydration level was only 1% ($La_{0.99}Ca_{0.01}NbO_4H_{0.01}$) [54, 279].

In contrast, the mass loss in LNMo16As of approximately -0.418 wt% was significant

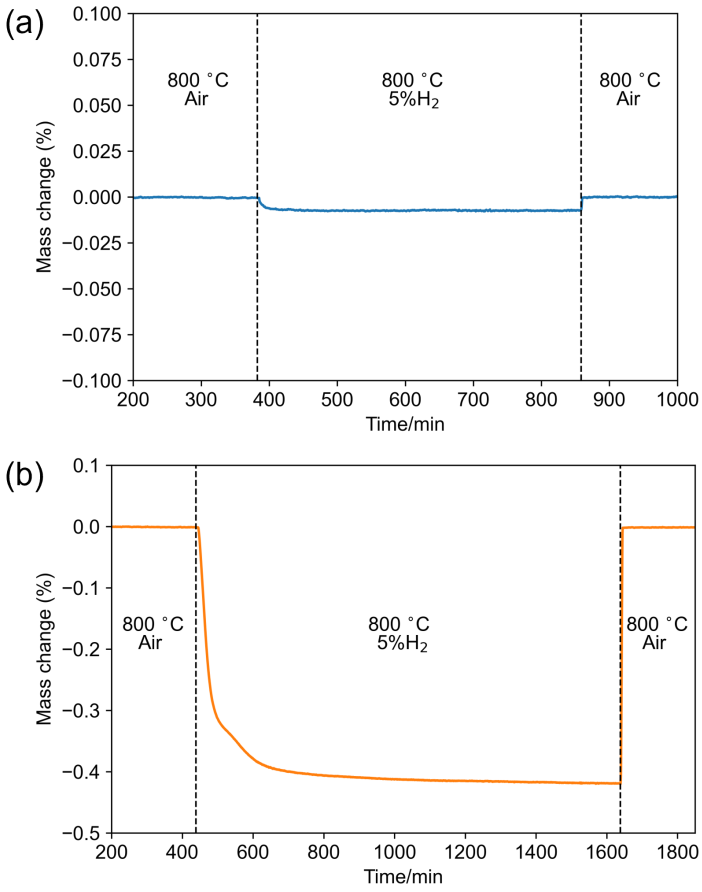


FIGURE 6.1: *In-situ* TGA results of (a) LNW16As and (b) LNMo16As collected at 800 °C. The subtle mass change in (a) fails in the instrumental uncertainty and is likely due to the difference in buoyancy effect between different atmospheres.

due to the reduction, making the estimation of the proton content not viable. However, this result is an excellent supplement to the previous results. Assuming that the valence state of the Mo cations in LNMo16As was +6 and the mass change induced by proton incorporation is negligible, LNMo16As was reduced to ∼+5.025 after more than 20 hours of hydrogen treatment at 800 °C. Given that the mass continued to decrease, it is reasonable to predict that the valence state might eventually reduce to fully +5 with an extended treatment period. After switching back to air, the mass increased dramatically to roughly the same mass as before hydrogen treatment in 30 minutes, suggesting that the reduction is fully reversible, which is in line with the XRD results presented in Figure 4.7. The steep decrease and increase when switching the gases further suggest a swift redox reaction process of LNMo16, highlighting its potential to be developed as a high-temperature gas sensor.

6.2 Band structure study

After hydrogen treatments, the colour of both samples changed from green to black. This colouration effect suggested a change in the band structure, usually reducing the band gap and becoming electronically conductive. [280, 281]. On the one hand, this colouration effect and its corresponding band gap reduction are commonly seen in reduced metal oxides, such as reduced MoO_3 [251, 282]. On the other hand, a similar colouration effect has been reported in many oxides after reacting to the corresponding oxyhydrides [162, 232]. In addition, it has been widely studied in the semiconductor area that subtle hydrogen incorporation can strongly modify the band structure [57, 58, 283]. Therefore, the change in the band structure can be an informative indicator of the reduction and/or proton incorporation.

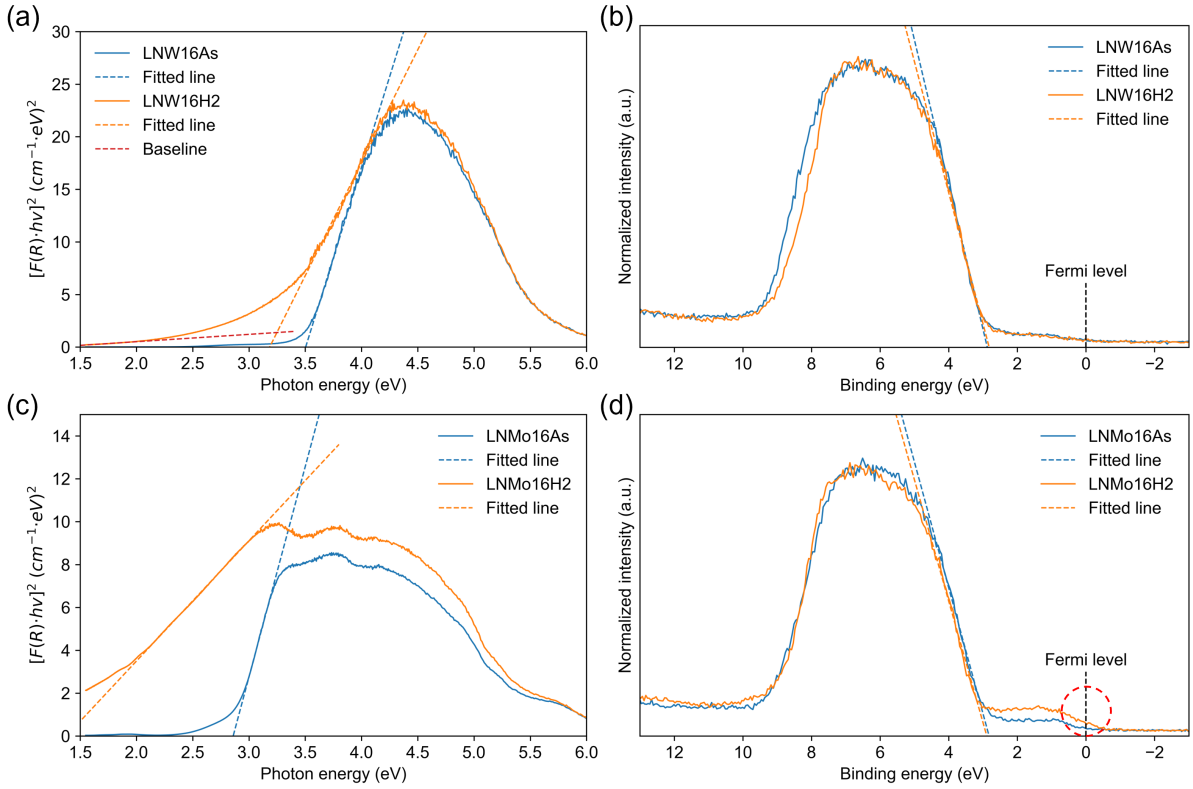


FIGURE 6.2: Direct (allowed) band gap Tauc plots of (a) LNW16 and (c) LNMo16; XPS-VBM spectra of (b) LNW16 and (d) LNMo16. The dashed lines indicate the values of extrapolated band gaps or VBM. The red dashed circle in (d) highlights the pre-edge feature of LNMo16.

Figures 6.2(a) and (c) present band gap Tauc plots calculated from UV-vis-DRS reflectance spectra by applying Equations 3.25, 3.26 and 3.27. Notice that the value of $1/\gamma$ is 2 in Figure 6.2, suggesting a direct (allowed) band gap nature. Strictly speaking, the nature of the band gap, direct or indirect, should be pre-determined by DFT calculations, which can be challenging. However, many comprehensive studies on the band

gap of rare-earth niobates, including pristine and substituted $LaNbO_4$, have reported a negligible energy difference between direct and indirect band gaps [197, 284–287]. Therefore, the band gap nature in LNW16 and LNMo16 was assumed to be a direct band gap.

The more tilted Urbach tail and the rise of the pre-edge in both samples after hydrogen treatments indicate an increased defect concentration [197, 205]. Considering the unchanged nature of LNW16, the increased defects can only be attributed to protons, resulting in a subtle change in Figure 6.2(a). In contrast, the more pronounced change in Figure 6.2(c) is clearly demonstrated in LNMo16 mainly due to the reduction with a potential effect of proton incorporation.

The band gap of LNW16As and LNMo16As can be extrapolated directly from the Tauc method, as the Urbach tail feature in both samples is marginal. However, when it comes to LNW16H2, the enormous Urbach tail pre-edge will lead to an inaccurate estimation [288]. Therefore, the widely recognised baseline method proposed by Makuła *et al.* was used to extract a more accurate band gap from LNW16H2 [288]. For LNMo16H2, due to the limited measurement range, the baseline position is unrecognisable, resulting in an unclear band gap value. However, the range of band gap values can still be estimated since the baseline is located between the Urbach tail pre-edge and the flat line.

The extrapolated band gap of LNW16As and LNMo16As was 3.5 eV and 2.9 eV, respectively. These large band gaps highlighted their electronically insulating nature as a pure ionic conductor in non-reducing atmospheres. After hydrogen treatments, the band gap of LNW16H2 reduced slightly to 3.2 eV with an Urbach tail pre-edge, indicating the presence of intermediate bands (IBs) introduced by proton incorporation. In comparison, LNMo16H2 reduced significantly to the range of 1.4 to 2.0 eV with an outstanding Urbach tail pre-edge, indicating the existence of distinct intermediate bands mainly due to the reduction. The colouration effect is highly likely to be due to the presence of these IBs. In addition, these band gap reductions were consistent with the above redox and electrochemical studies: LNW16 is stable and electronically insulated, while LNMo16 will be reduced and becomes electronically conductive under hydrogen atmospheres.

Figures 6.2(b) and (d) present the XPS-valence band maximum (VBM) spectra of both samples. The VBM energy position of LNW16 remained stable before and after hydrogen treatments at 2.8 eV. In contrast, the VBM of LNMo16 increased slightly from 2.8 to 2.9 eV after hydrogen treatments. Given that the dominant O 2*p* orbitals comprise the VBM, this change indicated the loss of oxygen due to reduction, which altered the VBM [197]. More interestingly, a pre-edge can be found in the VBM spectrum of LNMo16H2

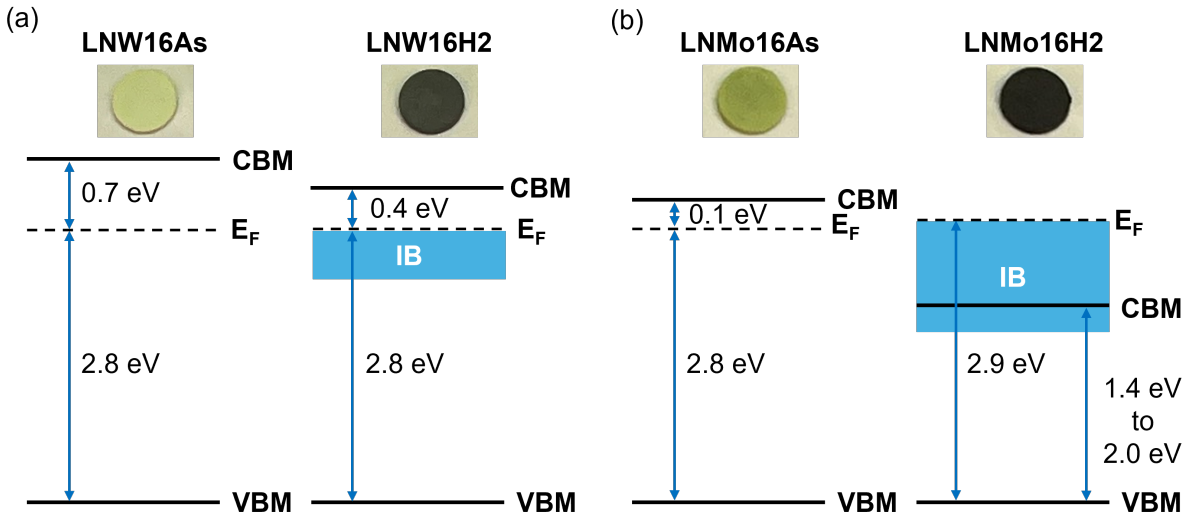


FIGURE 6.3: Schematic diagrams of estimated band structures of (a) LNW16 and (b) LNMo16. The inserts on top are the visual appearances of the pellet samples.

raised before binding energy at 0 eV, which is the Fermi level. A similar but more subtle feature can also be found in LNMo16As, probably due to the reduction of Mo^{6+} during XPS measurements. Nevertheless, this largely increased pre-edge feature highlighted the metallic nature of LNMo16H2. Similar counter-intuitive electron emission above the Fermi level has been attributed to the reduction of Mo^{6+} in reduced MoO_3, shifting the Fermi level into the conduction band [251, 289].

The above studies are instructive, and the estimated band structure of both samples can be depicted accordingly in Figure 6.3. The slightly narrowed band gap in LNW16H2, together with the Fermi level closer to the conduction band minimum (CBM), suggested that protons act as shallow donors, giving rise to intermediate bands within the band gap [251, 290, 291]. In contrast, the significantly reduced band gap of LNMo16H2 was due to reduction and, potentially, proton incorporation. In particular, the high degree of reduction created pronounced IBs mainly comprised by Mo 4*d* orbitals, which shifted the Fermi level into the conduction band, resulting in the metallic nature of LNMo16H2 [251, 289]. It should be emphasised that the band structures presented in Figure 6.3 are largely simplified and were adapted from the well-determined band structures of WO_3 and MoO_3 [251, 289]. The actual band structures in LNW16 and LNMo16 might be different.

6.3 Neutron study

Figure 6.4 presents NPD data of both samples recorded at RT. The rise in the background intensity clearly indicated the proton incorporation in both samples. The almost identical diffraction patterns shown in Figure 6.4(a) with the exception of the difference in the background contribution suggested excellent stability of LNW16, which is consistent with the XRD results in Section 4.2. In contrast, the diffraction pattern in Figure 6.4(b) shows a peak splitting after hydrogen treatments, indicating a reduction in LNMo16, as observed with the XRD results in Section 4.2. The slightly higher increase in background intensity in LNMo16 compared to LNW16 suggests a higher proton incorporation level in LNMo16. However, a quantitative determination of the proton content using NPD results is not feasible. Furthermore, since VESUVIO is not optimised for NPD measurements, the limited experimental resolution does not allow meaningful refinement.

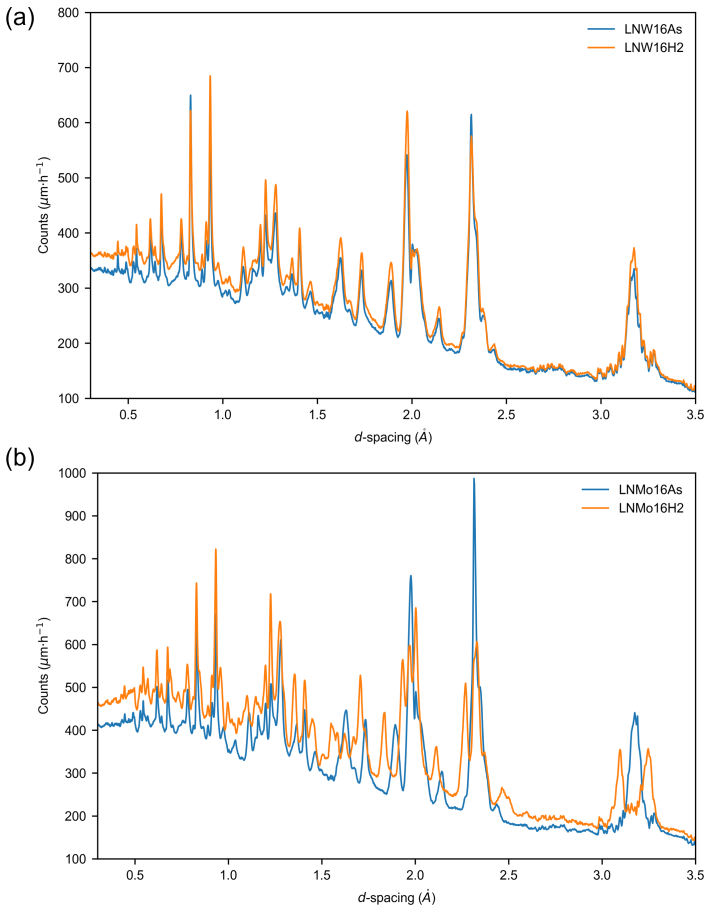


FIGURE 6.4: NPD data of (a) LNW16 and (b) LNMo16 collected on VESUVIO spectrometer at RT.

Figures 6.5 and 6.6 present the backward and forward neutron Compton scattering spectra of LNW16 and LNMo16, respectively. In contrast to NPD results, the forward

NCS spectra of both samples did not present the recoil peak of the proton. However, the relatively poor detection limit for the proton of 1.92 μmol makes this unnoticeable proton content still reasonable [238, 245]. Taking into account the mass of ~30 g used in the measurements for each sample, the proton concentration should be larger than ~0.02, *i.e.*, $LaNb_{0.84}W_{0.16}O_{4.08}H_{0.02}$ and $LaNb_{0.84}Mo_{0.16}O_{4.03}H_{0.02}$ to beyond the detection limit. In addition, in practice, the recoil peak of the proton is broader than the peaks of other elements because of the relatively fast kinetics of the proton. This broader peak might be immersed in the background noise, therefore requiring the proton content to be much higher than the detection limit for a clear peak resolution. In contrast, the detection limit of NPD depends on specific instruments, but is usually much better than NCS, which might explain the inconsistency between NPD and NCS data [292].

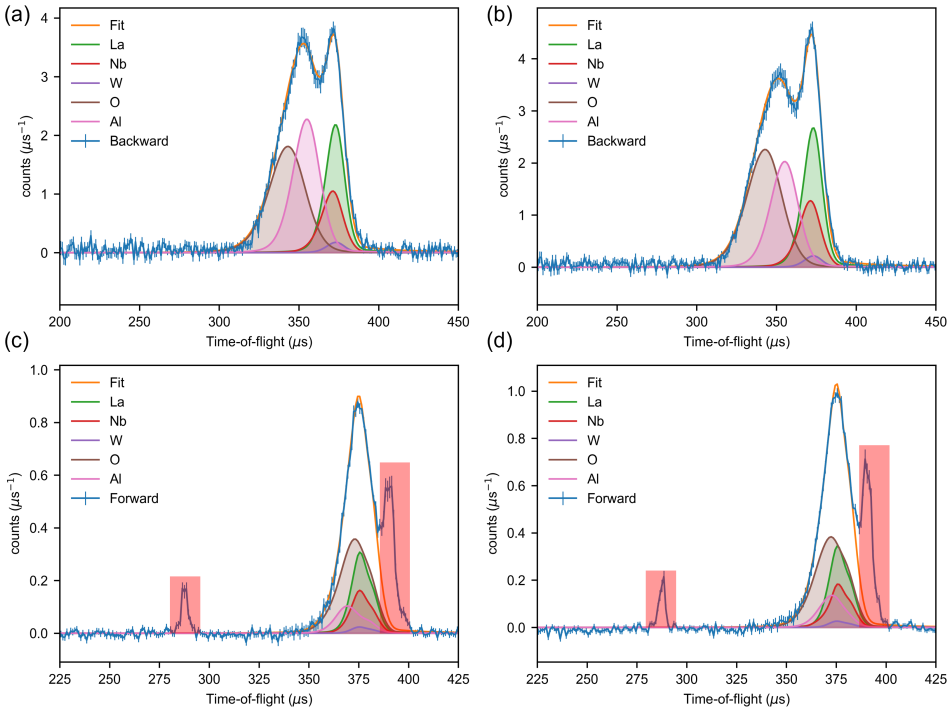


FIGURE 6.5: Backward and forward NCS spectra of the reduced (raw), the total fit and the elementary fitted spectra in (a) & (c) LNW16As and (b) & (d) LNW16H2 collected on VESUVIO spectrometer at RT. The peaks highlighted by red-shaded rectangular areas originate from the neutron-gamma resonances of tungsten and are excluded from the fittings [240].

It is worth mentioning that the recoil peaks on the forward scattering spectra presented a non-Gaussian-like shape. The spectra presented in Figures 6.5 and 6.6 were convolved from multiple detectors. Therefore, the slight angle misalignment of each detector will be propagated, resulting in the peak shape distortion. This distortion did not affect the single-dimensional Gaussian fitting process since the recoil peaks in each

spectrum from an individual detector for fittings presented a Gaussian shape. Given the configuration difference between forward and backward scattering detectors, this distortion is suppressed in backward scattering spectra. In addition, neutron-gamma resonances are more popular in the forward scattering angle region for heavier elements. Therefore, this resonance was not presented in the NCS spectra of LNMo16.

TABLE 6.1: NMD widths, σ_M, together with their standard deviation of LNW16 extracted from NCS backward scattering fittings. The force constants, k_M, were deduced from the NMD widths using Equation 6.1. The standard deviation of k_M is estimated using the Monte Carlo error propagation. The NMD width of Al was pre-determined and removed from the table.

LNW16As	σ_M ($\AA^{-1}$)	k_M ($eV \cdot \AA^{-2}$)	LNW16H2	σ_M ($\AA^{-1}$)	k_M ($eV \cdot \AA^{-2}$)
La	38.63±2.62	16.37±5.22	La	38.29±2.81	15.70±5.55
Nb	30.53±3.04	9.24±4.71	Nb	38.35±3.85	23.17±7.65
W	34.55±1.09	1.47±1.46	W	34.46±1.04	1.31±1.36
O	12.57±1.63	1.53±1.01	O	11.83±1.65	1.06±0.89

Despite the failure to directly probe proton content using NCS, the extracted NMD widths still provided meaningful and unique kinetic information. Tables 6.1 and 6.2 summarised the fitted NMD widths of LNW16 and LNMo16, respectively. Employing the mean force function, which assumes the average force acting on an atom while keeping other atoms in the system fixed, one can deduce the effective force constant from the NMD width, as presented in Equation 6.1 [293, 294].

$$k_M = \left|\frac{(k_B T)^2 M}{\hbar^2} - k_B T \cdot \sigma_M^2\right| \tag{6.1}$$

Where k_M and σ_M are the effective force constant and the NMD width, respectively. M, k_B, and $\hbar$ are the mass of a given nucleus, the Boltzmann constant, and the reduced Planck constant, respectively. Importantly, this equation is not valid in the low-temperature limit, *i.e.*, $T \rightarrow 0$ K, but has been applied well to describe the mean force at 100 K and 300 K [293, 294].

For LNW16, this effective force constant change suggested that protons prefer to be incorporated with oxygen ions that are around Nb cations. This proton-induced effective force constant has been reported in another NCS study, where the effective force constant increases with the increased trapping rate of protons around Nb [241]. In addition, the study on acceptor-substituted $LaNbO_4$ materials has proposed preferred hydration on Nb_2O_7 units, suggesting that similar polyhedra, Nb_2O_9 units, in LNW16 could be the key to achieving proton incorporation [67]. For LNMo16, a similar change could be due to the same protonation effect. However, the simultaneous reduction makes the contribution of protonation inseparable.

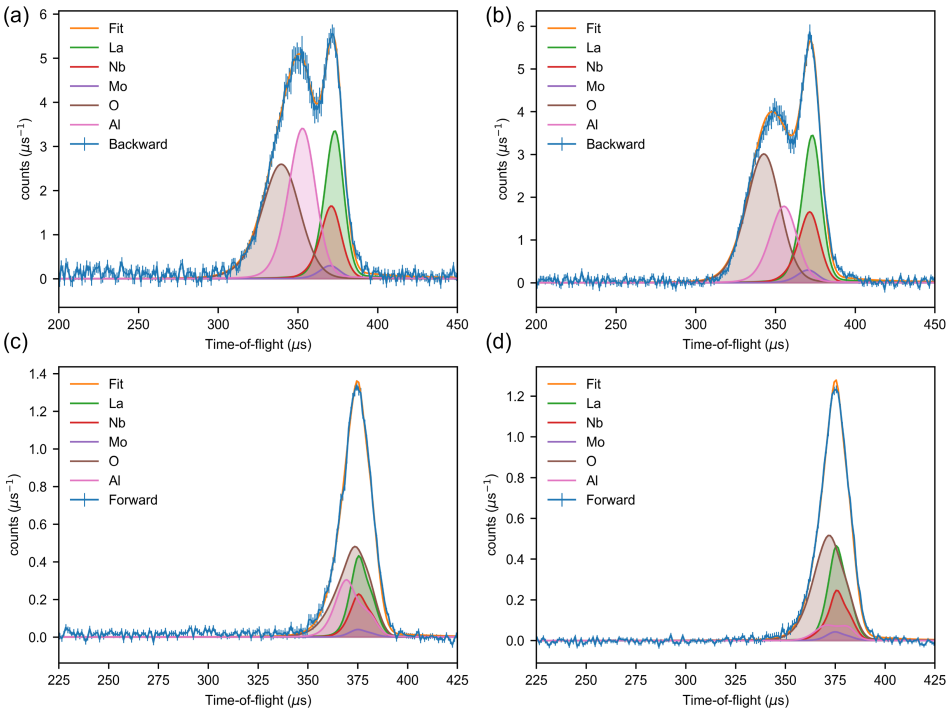


FIGURE 6.6: Backward and forward NCS spectra of the reduced (raw), the total fit and the elementary fitted spectra in (a) & (c) LNMo16As and (b) & (d) LNMo16H2 collected on VESUVIO spectrometer at RT.

Both materials show an effective force constant reduction in oxygen anions after hydrogen treatments. For LNW16, this subtle reduction could also be due to proton incorporation, which probably relaxes the trapping effect among the M-O framework. Interestingly, this relaxation could lead to an enhancement in oxygen ionic conduction under hydrogen conditions, suggesting a potential overestimation of the proton transport number measured under 5% H_2 conditions in section 5.2. More detailed research is required to clarify this hypothesis in the future. In contrast, for LNMo16, the relatively larger effective force constant reduction is clearly due to the tetrahedral to octahedral transformation. However, similar to the case for Nb cations, the potential contribution of protonation is inseparable.

The relatively large standard deviation of the effective force constants in W and Mo is due to the limited beam time and the multiple isotope nature of these elements. Ideally, each isotope of W and Mo should be treated as an individual recoil peak, but this treatment will significantly increase the fitting complicity and, therefore, was not feasible. To avoid misinterpretation, the changes in the effective force constant in W and Mo were excluded from the discussion.

In summary, although NCS did not provide solid evidence of proton incorporation, it offered unique results of the effective force constant, which can be determined by far

TABLE 6.2: NMD widths, σ_M, together with their standard deviation of LNMo16 extracted from NCS backward scattering fittings. The force constants, k_M, were deduced from the NMD widths using Equation 6.1. The standard deviation of k_M is estimated using the Monte Carlo error propagation. The NMD width of Al was pre-determined and removed from the table.

LNMo16As	σ_M ($\AA^{-1}$)	k_M ($eV \cdot \AA^{-2}$)	LNMo16H2	σ_M ($\AA^{-1}$)	k_M ($eV \cdot \AA^{-2}$)
La	38.86±2.19	16.83±4.40	La	38.45±2.68	16.07±5.34
Nb	31.12±4.03	10.18±6.29	Nb	38.68±3.49	23.83±7.00
Mo	26.07±2.09	2.23±2.20	Mo	25.53±1.71	1.51±1.67
O	13.92±1.96	2.45±1.39	O	11.59±1.47	0.92±0.77

only experimentally using NCS. A more realistic MD simulation model can be configured based on these values to describe the dynamics of LNW16 and LNMo16 in the future.

6.4 Mass spectrometry study

To obtain a reliable and valid diffusion profile, a sample with a density exceeding 95% of the theoretical density is required [215]. At this density level, the sample can effectively be considered pore-free, as the open porosity is negligible [215, 295]. Therefore, LNW16 (relative density of 95.6%) is valid for the exchange and diffusion analysis, while, unfortunately, the low density (relative density of 93.0%) and relatively poor surface roughness invalidate LNMo16 for this analysis. Meanwhile, given the low level of proton incorporation suggested by the above results, the samples were deuterium treated at 800 °C for 6 hours under 50 mbar of D_2 gas and denoted as LNW16D2-6h. The same treatment processes were performed under atmospheres 5% H_2 for direct comparison, and the samples were denoted as LNW16H2-6h. Furthermore, given the expected poor surface exchange capacity of LNW16, two samples were brush coated with Pt and denoted as LNW16H2-6h-Pt and LNW16D2-6h-Pt, respectively [47, 217]. After hydrogen/deuterium treatments, the Pt coating layer exhibited poor adhesion and could be easily peeled off by wiping.

Figure 6.7 presents a depth profile to determine the correlation between sputtering time and depth. To sputter a detectable crater ($\geq$3 μm), a long depth profiling for more than 4000 s is required. Therefore, only LNW16As was used for long depth profiling measurements, and the sputtering time-depth correlations of other samples were estimated by assuming that the hardness of the samples remained the same. The long depth profiling measurements also suggested a homogeneous composition with a thin surface layer. This homogeneity allowed for a reduced depth profile time, since the

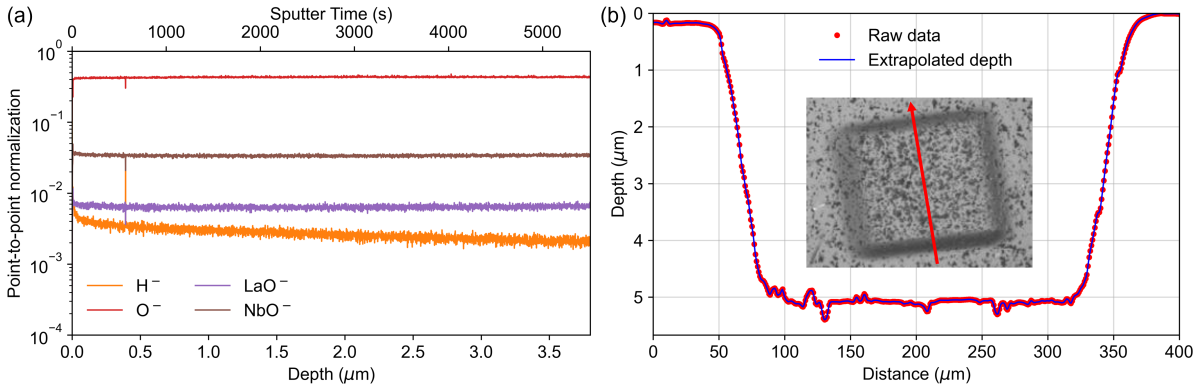


FIGURE 6.7: (a) Depth profile for determining the correlation between sputtering time-depth in LNW16As. The spikes are due to the unstable beam current. (b) The crater depth was measured by coherence scanning interferometry from the slice indicated by the red arrow.

fractional composition at a depth greater than 0.025 μm is representative of the composition deeper in bulk.

In contrast to the steady ion count of O^- and cation species, the ion count of H^- showed a steady decrease. This H^- signal is common in depth profiling measurement, since hydrogen is a widely spread impurity that is almost impossible to remove from the sample and the measurement chamber. This high ion count of H^- also highlighted the unreliability of investigating hydrogen-related properties using SIMS and highlighted the demand for isotopic exchange.

Figure 6.8 presents the depth profile of each sample. A significantly increased ion count of D^- can be observed for both deuterium-treated samples, strongly suggesting proton (deuterium) incorporation. The slightly tilted profile shape of D^- in both deuterium-treated samples indicated their surface exchange limited diffusion nature [47, 217]. However, unfortunately, the diffusion coefficient cannot be estimated from these depth profiles.

The isotopic fractions of hydrogen in each sample are summarised in Table 6.3. The isotopic fraction of D^- in both deuterium-treated samples was more than ten times larger than the natural abundance of deuterium. Meanwhile, LNW16D2-6h-Pt possessed more than a doubled D^- fraction than LNW16D2-6h. This significantly enhanced incorporation highlighted the surface exchange limited diffusion nature of LNW16. For pristine and hydrogen-treated samples, the isotopic fractions of D^- were all below the natural abundance of deuterium, validating these results.

Given the high isotopic fraction of D^- in both deuterium-treated samples, the samples were cross-sectioned and polished for further SIMS measurements using the line scan method. Figure 6.9 presents the 2D ion images of cross-sectional samples and

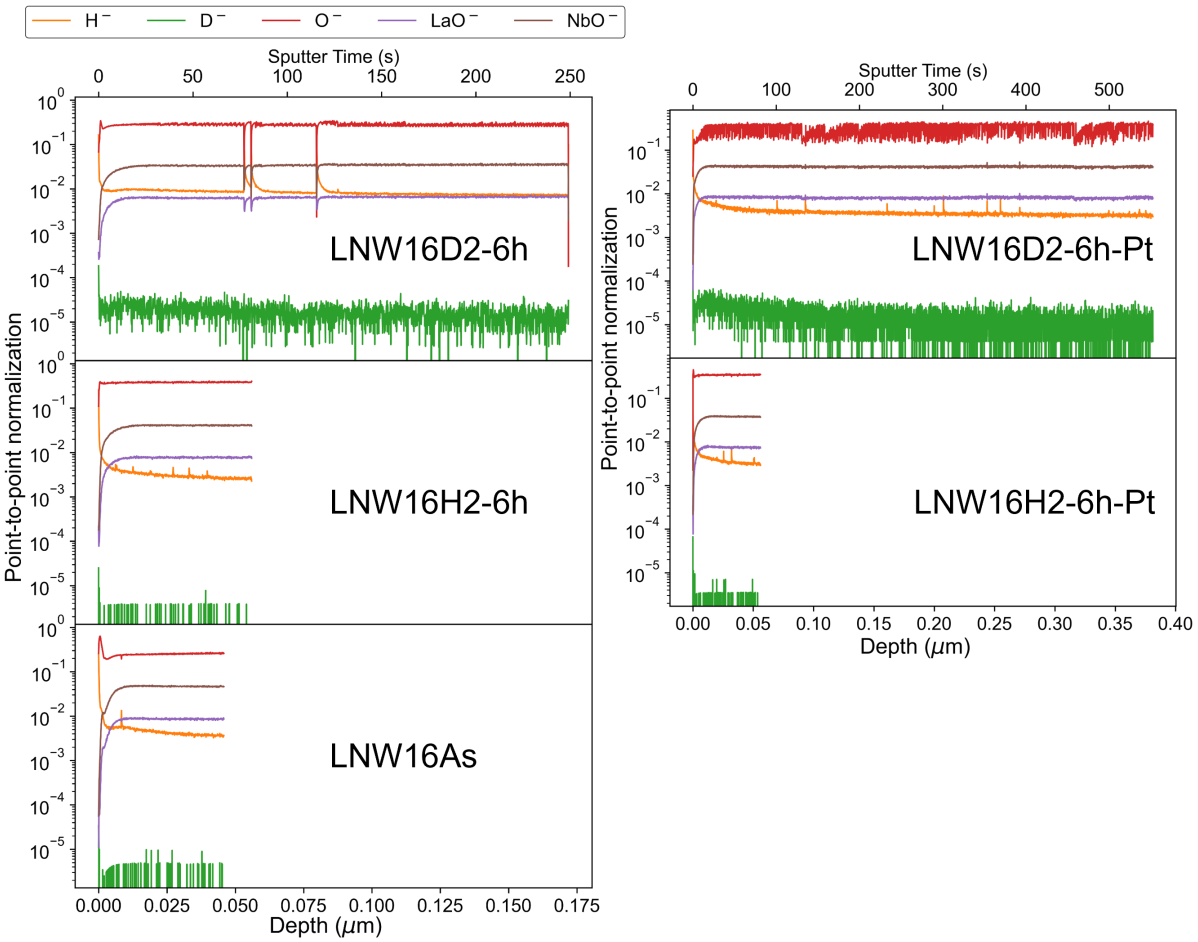


FIGURE 6.8: Depth profile of LNW16 samples. The spikes are due to the unstable beam current, which also causes the large fluctuation signals in LNW16D2-6h-Pt, especially for O^-. The large fluctuation of D^- is due to its relatively low ion counts.

their corresponding normalized diffusion profiles. Note that the isotopic fraction of both samples near the surface is much lower than the fraction obtained from the depth profile measurements. This difference is due to subtle surface damage during line scan preparations, the difficulty in determining the precise position of the exchange surface, and the resolution difference between depth profile and line scan methods. However, the isotopic fraction of LNW16D2-6h-Pt and LNW16D2-6h is higher than the natural abundance, indicating that the deuterium actually diffused into the bulk.

The smaller isotopic fraction near the surface in LNW16D2-6h presented in Figure 6.9(d) could be due to the geometric effect on the edge, since the height of two sample pieces was slightly misaligned. This misalignment will scatter part of the secondary ions away from the detector. Other potential reasons could be the release of protons from the surface during post-processes after deuterium treatments or surface segregation when the surface is exposed directly to reducing conditions. However, more

TABLE 6.3: Normalized isotopic fractions of hydrogen in each sample. The natural abundance of deuterium is 0.00015. The large error values are due to the low signal counts.

	$D^-/(H^-+D^-)$
LNW16As	0.00014±0.00038
LNW16H2-6h	0.00011±0.00036
LNW16H2-6h-Pt	0.00013±0.00034
LNW16D2-6h	0.00195±0.00088
LNW16D2-6h-Pt	0.00386±0.00221

surface characterisations are needed in the future. In contrast, a clear diffusion profile can be observed in LNW16D2-6h-Pt compared to LNW16D2-6h, indicating the surface exchange limited nature of LNW16. Therefore, a reasonable diffusion profile fitting in LNW16D2-6h-Pt can be obtained applying Equation 3.30, as presented in Figure 6.10. It should be mentioned that since Pt was coated on the surface, the surface exchange coefficient, k, is altered and does not represent the surface exchange ability of the sample. Meanwhile, the isotopic background in LNW16D2-6h-Pt should be negligible, as the hydrogen content in the sample is negligible prior to deuterium treatment. However, since the ubiquitous hydrogen impurity in SIMS, C_{bg} can be set to the natural abundance (0.00015) to reflect the instrumental isotopic background. Furthermore, the actual C_{bg} was found to be slightly higher than the natural abundance, suggesting a saturated incorporation of deuterium under this treatment condition. Therefore, the actual C_{bg} was set to where $D^-/(H^-+D^-)$ ratio reaches plateau. Although the above experimental limitations could compromise the credibility of the extracted tracer diffusion coefficient, this result is still valuable as this is the first direct evidence to prove the proton (deuterium) incorporation in LNW16.

The tracer diffusion coefficient of $\sim 4.0\times10^{-9}$ cm^2/s at 800 °C is found to be about three orders of magnitude lower than conventional proton-conducting oxides, such as $BaZr_{0.1}Ce_{0.7}Y_{0.1}Yb_{0.1}O_{3-\delta}$ ($\sim 1.8\times10^{-6}$ cm^2/s) [296, 297], but similar to the oxygen ion conducting counterparts, such as $GdBaCo_2O_{5+\delta}$ ($\sim 2.5\times10^{-9}$ cm^2/s) [298] and $LaNb_{0.88}W_{0.12}O_{4.06}$ ($\sim 5.0\times10^{-9}$ cm^2/s) [161]. Therefore, such a diffusion coefficient value indicates a different proton transport mechanism in LNW16 from the conventional proton-conducting oxides. A similar level of proton and oxygen diffusion coefficients of W-substituted $LaNbO_4$ appears to suggest proton transport in the vehicle mechanism, at least in the high temperature ranges. However, the vehicle mechanism fails to explain the conductivity behaviour of LNW16 in low-temperature ranges. More comprehensive experiments are needed to uncover the proton transport mechanism in this type of material.

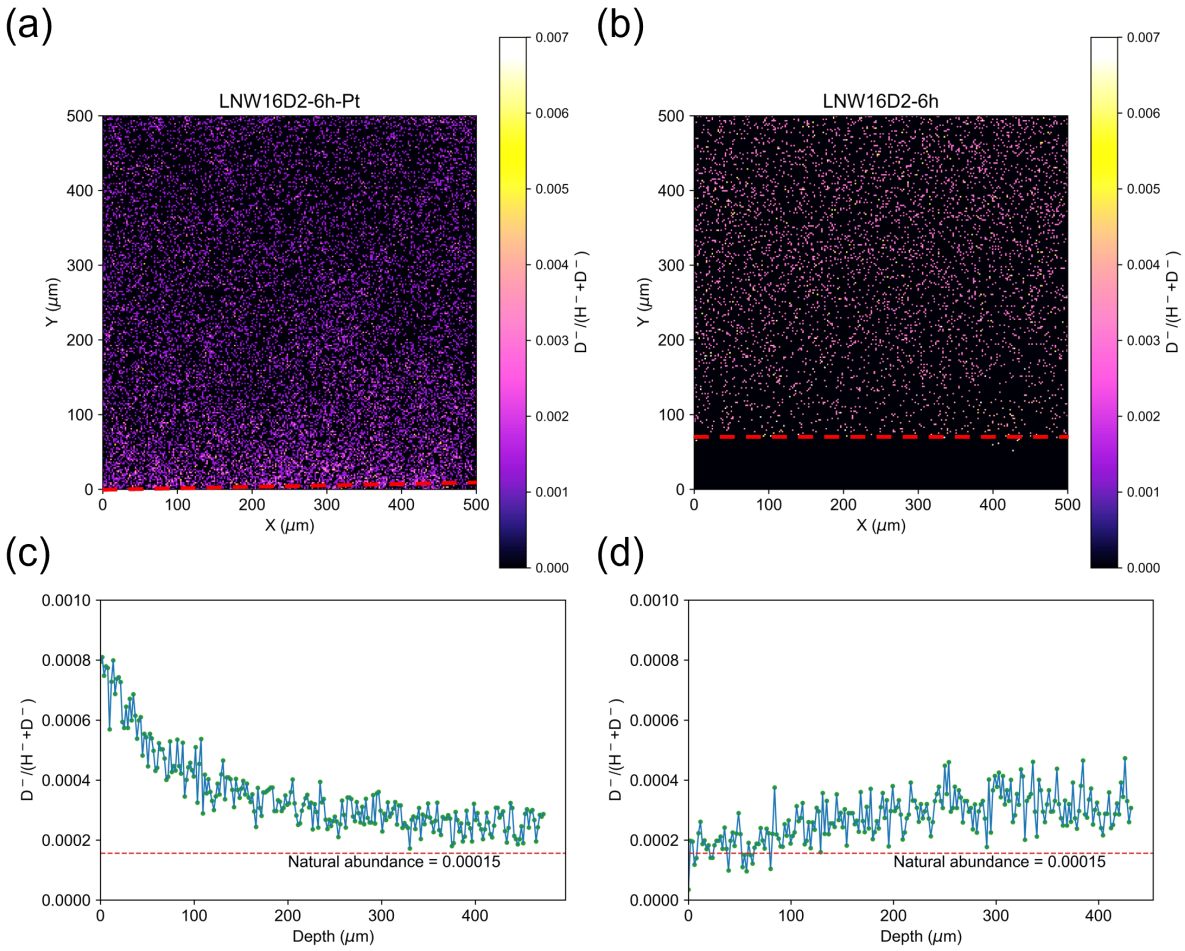


FIGURE 6.9: 2D ion images of $D^-/(H^- + D^-)$ in cross-sectional (a) LNW16D2-6h-Pt and (b) LNW16D2-6h, respectively. The corresponding normalized diffusion profiles of (c) LNW16D2-6h-Pt and (d) LNW16D2-6h, respectively. The red dashed line in (a) and (b) indicates the exchanged surface position before the cross-section. The brightness of (a) and (b) was increased by 50% for figure readability.

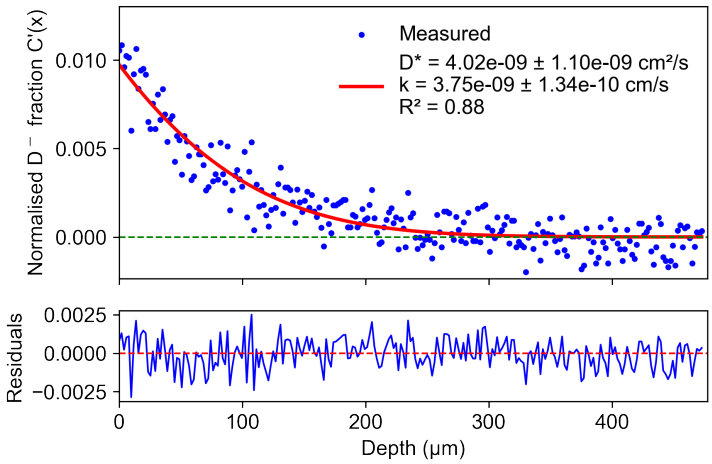


FIGURE 6.10: Fitted diffusion profile of LNW16D2-6h-Pt. The green dashed line indicates $C(x) = C_{bg}$.

6.5 Conclusions

In this chapter, proton incorporation was investigated using multiple techniques, providing abundant indirect or direct information to help understand the incorporation. The first direct proof of proton incorporation in LNW16 under hydrogen atmospheres was presented using NPD and isotopic exchange depth profiling/line scan techniques. It was admitted that many studies in this chapter were not sufficient due to the limited instrumental accessibility and the difficulty of probing protons. These results were instructive for future optimised research.

Chapter 7

Conclusions and future work

In this work, 16 at% W- and Mo- substituted $LaNbO_4$ materials have been successfully synthesised as starting materials via the solid-state reaction route. The redox stability and ionic conductivity of these materials in hydrogen environments have been investigated, demonstrating a strong correlation. Moreover, proton incorporation and conduction in these materials have been first characterised.

7.1 Conclusions

7.1.1 W-substituted $LaNbO_4$

Pristine 16 at% W-substituted $LaNbO_4$ possesses a monoclinic structure that closely resembles the high-temperature tetragonal phase. The phase remains stable from RT to high temperatures. A (3+2)D-incommensurately modulated structure was observed in this material. The oxidation state of the B-site dopant was found to be pure +6, giving a nominal composition of $LaNb_{0.84}W_{0.16}O_{4.08}$. EXAFS studies suggested that interstitial oxygen ions tend to be located near Nb cations, forming Nb_2O_9 polyhedra. Pure oxygen ionic conduction was determined under non-reducing atmospheres with an activation energy of $\sim$1.5 eV.

LNW16 shows excellent redox stability in hydrogen environments. The crystal structure, composition, oxidation state of the cations, and oxygen stoichiometry remain stable. However, the total conductivity increases significantly in hydrogen environments. The partial electronic conduction raised from the reduction cannot explain this enhancement in conductivity. With evidence of proton incorporation from XPS, a novel proton conduction mechanism was proposed.

Many techniques have been used in attempts to probe the hydrogen content directly. The proton diffusion profile was observed, proving proton transport in this type of material for the first time. The proton diffusion coefficient is 4.2×10^{-9} cm^2/s at 800 °C comparable with the oxygen ionic diffusion coefficient, probably suggesting a vehicle

transport mechanism. In addition, the proton incorporation was found to significantly affect the band structure and kinetics of the atoms.

7.1.2 Mo-substituted $LaNbO_4$

Pristine 16 at% Mo-substituted $LaNbO_4$ possesses a monoclinic crystal structure. The phase transition to the tetragonal structure occurs at above 200 °C. The presence of a (3+1)D-incommensurately modulated structure was confirmed in this material. The oxidation state of the B-site dopant was found to be pure +6, giving a nominal composition of $LaNb_{0.84}Mo_{0.16}O_{4.08}$. B-site cations possess a disordered tetrahedral environment. Pure oxygen ionic conduction was determined under non-reducing atmospheres with an activation energy of ∼1.5 eV. The conductivity is about five times higher than its W-substituted counterpart, indicating the relaxed trap effect in LNMo16.

The Mo^{6+} cations were found to be reduced to a minimum of Mo^{5+} in hydrogen environments. This reduction causes a phase transition to the analogue of pure $LaNbO_4$ and a loss of interstitial oxygen ions. The coordination of Nb and Mo cations changes from tetrahedral to octahedral on reduction. The increase in electronic conduction due to reduction converts LNMo16 from a pure ionic conductor to a mixed ionic and electronic conductor. The profound change in the band structure results in the metallic nature of the material. The transport number studies of LNMo16H2 further imply potential protonic conduction in conduction enhancement under hydrogen environments. The reduction and corresponding conductivity change were found to be quickly and fully reversible, suggesting its potential to be developed as a high-temperature sensor.

7.1.3 Overall conclusions

The novel proton incorporation and transport mechanism reported in this work suggests that potential proton-conducting electrolyte candidates extend far beyond conventional vacancy-dominated perovskite oxides. This discovery could shift research focus from a limited class of traditional oxides to a broader range of new materials. Additionally, proton incorporation from dry hydrogen atmospheres relaxes the rigorous humidity requirements for SOFCs and SOECs, reducing the complexity of the cell systems. By further elucidating this mechanism, a new selection strategy can be developed to identify materials that meet all the criteria for proton-conducting electrolytes at intermediate operating temperatures.

7.2 Future work

7.2.1 Proton transport

Although proton incorporation and transport in LNW16 have been discovered, the optimal hydrogen treatment that could maximise hydrogen content and corresponding effects has not yet been determined. The proton diffusion coefficient at lower temperatures remains unknown. Therefore, the next step is to optimise the treatment conditions and perform deuterium exchanges and SIMS measurements at different temperatures covering the EIS measuring temperature range.

The sintering condition was optimised for LNW16 and kept the same for LNMo16 to ensure direct comparison. However, this condition results in a relatively low density and a high porosity of LNMo16, which prevents it from being studied using SIMS. In the future, an optimisation of the preparation for LNMo16 is planned to obtain dense material for similar isotopic exchange SIMS measurements as LNW16.

Exploring the proton incorporation process on the surface is another future focus. One of the unsolved questions of the current work is why the conduction of LNW16 under a wet hydrogen environment is largely suppressed compared to that under a dry hydrogen environment. The surface exchange-limited nature of LNW16 implies that this suppression is due to the presence of water molecules on the surface. However, the proof of this claim is missing, and more surface studies are needed.

Other techniques that can directly probe protons, such as QENS and atom probe tomography (APT), were not used in the current work due to the challenges in their availability. However, with the current evidence of proton incorporation and transport, the likelihood of accessing these instruments is expected.

7.2.2 More electrochemical studies

Current electrochemical tests failed to separate the conduction contribution from the bulk and grain boundary. Therefore, the next step is to expand the measuring frequency, attempting to make these contributions separable. This separation is crucial in determining the preferred proton transport pathway through the bulk or grain boundary.

Meanwhile, current polarisation work only separated the electronic and ionic conductions. The protonic conductivity under hydrogen environments was estimated by assuming that the oxygen ionic conductivity remains the same as under non-reducing conditions. However, this assumption could lead to an overestimation of protonic

conduction since the potential trapping effect relaxation cannot be ruled out. This relaxation might enhance oxygen ionic conduction. Therefore, the next step is to perform more polarisation or, alternatively, electromotive force measurements, which allow the separation of all charge carriers (electrons, oxygen ions, and protons). Hydrogen permeation is another alternative measurement that provides a direct quantitative result of protonic conduction.

7.2.3 Material modelling & simulation

With the relatively abundant experimental studies currently available, modelling and simulations are what one should expect in the future. Some DFT simulations have been performed with promising initial results. However, these results still require further validations and optimisations and thus are not given in this work.

Computational studies could help explain the distinct behaviour difference between W and Mo dopants in hydrogen environments from an atomic scale. For example, the formation energy difference between reduction and proton incorporation is suspected to be the reason for the behaviour difference. DFT studies could identify potential transport pathways and local transport barriers.

As understanding of these materials from experiments and DFT simulations builds up, large-scale MD modelling will become feasible. Especially with unique interatomic force constants obtained from NCS measurements, more realistic modelling could assist in explaining the experimentally discovered phenomenon from atomic perspectives.

Bibliography

[1] *World Energy Outlook 2022 – Analysis - IEA*. URL: https://www.iea.org/reports/world-energy-outlook-2022.

[2] *Climate change*. URL: https://www.who.int/news-room/fact-sheets/detail/climate-change-and-health.

[3] *The Paris Agreement | UNFCCC*. URL: https://unfccc.int/process-and-meetings/the-paris-agreement.

[4] *Electric vehicle sales leapt 55% in 2022, with China in front | World Economic Forum*. URL: https://www.weforum.org/agenda/2023/05/electric-vehicles-ev-sales-growth-2022/.

[5] Paul B. MacCready. "The Case for Battery Electric Vehicles". *The Hydrogen Energy Transition: Cutting Carbon from Transportation*. Academic Press, Jan. 2004, pp. 227–233. ISBN: 9780126568813. DOI: 10.1016/B978-012656881-3/50016-2.

[6] Shannon W. Boettcher et al. *ACS Energy Letters* 6.1 (Jan. 2021), pp. 261–266. ISSN: 23808195. DOI: 10.1021/acsenergylett.0c02443.

[7] Christine Mansilla et al. "Hydrogen Applications: Overview of the Key Economic Issues and Perspectives". *Hydrogen Supply Chain: Design, Deployment and Operation*. Academic Press, Jan. 2018, pp. 271–292. ISBN: 9780128111970. DOI: 10.1016/B978-0-12-811197-0.00007-5.

[8] Aliakbar Hassanpouryouzband, Mark Wilkinson, and Robert Stuart Haszeldine. *Chemical Society Reviews* 53.5 (Mar. 2024), pp. 2258–2263. ISSN: 1460-4744. DOI: 10.1039/D3CS00723E.

[9] Ibrahim Dincer and Canan Acar. *International Journal of Hydrogen Energy* 40.34 (Sept. 2015), pp. 11094–11111. ISSN: 0360-3199. DOI: 10.1016/J.IJHYDENE.2014.12.035.

[10] N. Z. Muradov and T. N. Veziroğlu. *International Journal of Hydrogen Energy* 30.3 (Mar. 2005), pp. 225–237. ISSN: 0360-3199. DOI: 10.1016/J.IJHYDENE.2004.03.033.

[11] Arthur J. Shih et al. *Nature Reviews Methods Primers* 2.1 (Oct. 2022), pp. 1–19. ISSN: 2662-8449. DOI: 10.1038/s43586-022-00164-0.

[12] Harun Tüysüz. *Accounts of Chemical Research* (2023). ISSN: 15204898. DOI: 10.1021/ACS.ACCOUNTS.3C00709.

[13] Zenan Wu et al. *Energy & Environmental Science* 17.10 (May 2024), pp. 3338–3346. ISSN: 1754-5706. DOI: 10.1039/D3EE04368A.

[14] Aziz Nechache and Stéphane Hody. *Renewable and Sustainable Energy Reviews* 149 (Oct. 2021), p. 111322. ISSN: 1364-0321. DOI: 10.1016/J.RSER.2021.111322.

[15] Kongfa Chen and San Ping Jiang. *Journal of The Electrochemical Society* 163.11 (June 2016), F3070–F3083. ISSN: 0013-4651. DOI: 10.1149/2.0101611JES.

[16] Sergio Yesid Gómez and Dachamir Hotza. *Renewable and Sustainable Energy Reviews* 61 (Aug. 2016), pp. 155–174. ISSN: 1364-0321. DOI: 10.1016/J.RSER.2016.03.005.

[17] *NIST Chemistry WebBook*. URL: https://webbook.nist.gov/chemistry.

[18] Kaveh Mazloomi and Chandima Gomes. *Renewable and Sustainable Energy Reviews* 16.5 (June 2012), pp. 3024–3033. ISSN: 1364-0321. DOI: 10.1016/J.RSER.2012.02.028.

[19] C Raucci et al. "Hydrogen on board ship: a first analysis of key parameters and implications". *SCC Conference 2015*. University of Strathclyde, Nov. 2015.

[20] *Liquefied hydrogen | Fuel Cell Electric Buses*. URL: https://fuelcellbuses.eu/wiki/concept-hydrogen-refueling-station/tank-trailer-liquid-hydrogen.

[21] Qian Cheng et al. *International Journal of Lightweight Materials and Manufacture* 7.2 (Mar. 2024), pp. 269–284. ISSN: 2588-8404. DOI: 10.1016/J.IJLMM.2023.08.002.

[22] Asbjørn Klerke et al. *Journal of Materials Chemistry* 18.20 (May 2008), pp. 2304–2310. ISSN: 09599428. DOI: 10.1039/B720020J.

[23] *Ammonia Technology Roadmap – Analysis - IEA*. URL: https://www.iea.org/reports/ammonia-technology-roadmap.

[24] Borislav Bogdanović et al. *Advanced Materials* 18.9 (May 2006), pp. 1198–1201. ISSN: 1521-4095. DOI: 10.1002/ADMA.200501367.

[25] Leslie J. Murray, Mircea Dinc, and Jeffrey R. Long. *Chemical Society Reviews* 38.5 (Apr. 2009), pp. 1294–1314. ISSN: 03060012. DOI: 10.1039/B802256A.

[26] Myunghyun Paik Suh et al. *Chemical Reviews* 112.2 (Feb. 2012), pp. 782–835. ISSN: 00092665. DOI: 10.1021/cr200274s.

[27] Kamil Wróbel et al. *Energies* 15.23 (Nov. 2022), p. 8937. ISSN: 1996-1073. DOI: 10.3390/EN15238937.

[28] Zbigniew Stępień. *Energies* 14.20 (Oct. 2021), p. 6504. ISSN: 1996-1073. DOI: 10.3390/EN14206504.

[29] A. Kirubakaran, Shailendra Jain, and R. K. Nema. *Renewable and Sustainable Energy Reviews* 13.9 (Dec. 2009), pp. 2430–2440. ISSN: 1364-0321. DOI: 10.1016/J.RSER.2009.04.004.

[30] Omar Z. Sharaf and Mehmet F. Orhan. *Renewable and Sustainable Energy Reviews* 32 (Apr. 2014), pp. 810–853. ISSN: 1364-0321. DOI: 10.1016/J.RSER.2014.01.012.

[31] S. Mekhilef, R. Saidur, and A. Safari. *Renewable and Sustainable Energy Reviews* 16.1 (Jan. 2012), pp. 981–989. ISSN: 1364-0321. DOI: 10.1016/J.RSER.2011.09.020.

[32] A. J. Appleby. *Journal of Power Sources* 29.1-2 (Jan. 1990), pp. 3–11. ISSN: 0378-7753. DOI: 10.1016/0378-7753(90)80002-U.

[33] Tabbi Wilberforce et al. *International Journal of Hydrogen Energy* 41.37 (Oct. 2016), pp. 16509–16522. ISSN: 0360-3199. DOI: 10.1016/J.IJHYDENE.2016.02.057.

[34] Muhammad A. Aminudin et al. *International Journal of Hydrogen Energy* 48.11 (Feb. 2023), pp. 4371–4388. ISSN: 0360-3199. DOI: 10.1016/J.IJHYDENE.2022.10.156.

[35] J. J. Baschuk and Xianguo Li. *International Journal of Energy Research* 25.8 (June 2001), pp. 695–713. ISSN: 1099-114X. DOI: 10.1002/ER.713.

[36] Daniel J.L. Brett et al. *Chemical Society Reviews* 37.8 (July 2008), pp. 1568–1578. ISSN: 1460-4744. DOI: 10.1039/B612060C.

[37] Osamu Yamamoto. *Electrochimica Acta* 45.15-16 (May 2000), pp. 2423–2435. ISSN: 0013-4686. DOI: 10.1016/S0013-4686(00)00330-3.

[38] Yu Zhou. "NdBaInO4 based triple (electronic, ionic and protonic) conductor for solid oxide fuel cell applications". PhD thesis. Imperial College London, 2021.

[39] Qidong Xu et al. *Energy Conversion and Management* 253 (Feb. 2022), p. 115175. ISSN: 0196-8904. DOI: 10.1016/J.ENCONMAN.2021.115175.

[40] J. C. Grenier, J. M. Bassat, and F. Mauvy. "Novel cathodes for solid oxide fuel cells". *Functional Materials for Sustainable Energy Applications*. Woodhead Publishing, Jan. 2012, pp. 402–444. ISBN: 9780857090591. DOI: 10.1533/9780857096371.3.402.

[41] Philippe Moçoteguy and Annabelle Brisse. *International Journal of Hydrogen Energy* 38.36 (Dec. 2013), pp. 15887–15902. ISSN: 0360-3199. DOI: 10.1016/J.IJHYDENE.2013.09.045.

[42] Neelima Mahato et al. *Progress in Materials Science* 72 (July 2015), pp. 141–337. ISSN: 0079-6425. DOI: 10.1016/J.PMATSCI.2015.01.001.

[43] Hui Zhao, Qiang Li, and Liping Sun. *Science China Chemistry* 54.6 (June 2011), pp. 898–910. ISSN: 16747291. DOI: 10.1007/S11426-011-4290-2.

[44] N. Preux, A. Rolle, and R. N. Vannier. *Functional Materials for Sustainable Energy Applications* (Jan. 2012), pp. 370–401. DOI: 10.1533/9780857096371.3.370.

[45] S. W. Tao, P. I. Cowin, and R. Lan. *Functional Materials for Sustainable Energy Applications* (Jan. 2012), pp. 445–477. DOI: 10.1533/9780857096371.3.445.

[46] Brian C.H. Steele and Angelika Heinzel. *Nature* 414.6861 (Nov. 2001), pp. 345–352. ISSN: 1476-4687. DOI: 10.1038/35104620.

[47] Cheng Li. "Structural, surface and electrochemical studies of LaNbO4 based ionic conductors". PhD thesis. Imperial College London, 2016.

[48] N. Kochetova et al. *RSC Advances* 6.77 (Aug. 2016), pp. 73222–73268. ISSN: 20462069. DOI: 10.1039/c6ra13347a.

[49] Lorenzo Malavasi, Craig A.J. Fisher, and M. Saiful Islam. *Chemical Society Reviews* 39.11 (Oct. 2010), pp. 4370–4387. ISSN: 14604744. DOI: 10.1039/b915141a.

[50] Yoshio Matsuzaki et al. *Scientific Reports* 5.1 (July 2015), pp. 1–10. ISSN: 2045-2322. DOI: 10.1038/srep12640.

[51] Muhammad Bilal Hanif et al. *Matter* 6.6 (June 2023), pp. 1782–1830. ISSN: 2590-2385. DOI: 10.1016/J.MATT.2023.04.013.

[52] Inna Zvonareva et al. *Energy & Environmental Science* 15.2 (Feb. 2022), pp. 439–465. ISSN: 1754-5706. DOI: 10.1039/D1EE03109K.

[53] Chuancheng Duan et al. *Applied Physics Reviews* 7.1 (Mar. 2020), p. 11314. ISSN: 19319401. DOI: 10.1063/1.5135319.

[54] Reidar Haugsrud and Truls Norby. *Solid State Ionics* 177.13-14 (May 2006), pp. 1129–1135. ISSN: 01672738. DOI: 10.1016/j.ssi.2006.05.011.

[55] Reidar Haugsrud and Truls Norby. *Nature Materials* 5.3 (Feb. 2006), pp. 193–196. ISSN: 14764660. DOI: 10.1038/nmat1591.

[56] A. D. Brandão et al. *Journal of Solid State Chemistry* 184.4 (Apr. 2011), pp. 863–870. ISSN: 0022-4596. DOI: 10.1016/J.JSSC.2011.02.012.

[57] Chris G. Van De Walle and Jörg Neugebauer. *Annual Review of Materials Research* 36 (June 2006), pp. 179–198. ISSN: 15317331. DOI: 10.1146/ANNUREV.MATSCI.36.010705.155428.

[58] Çetin Kiliç and Alex Zunger. *Applied Physics Letters* 81.1 (June 2002), p. 73. ISSN: 0003-6951. DOI: 10.1063/1.1482783.

[59] Truls Norby and Yngve Larring. *Current Opinion in Solid State and Materials Science* 2.5 (Oct. 1997), pp. 593–599. ISSN: 13590286. DOI: 10.1016/S1359-0286(97)80051-4.

[60] Yuqing Meng et al. *Journal of Materials Science* 54.13 (July 2019), pp. 9291–9312. ISSN: 15734803. DOI: 10.1007/S10853-019-03559-9.

[61] F. A. Kröger and H. J. Vink. *Solid State Physics - Advances in Research and Applications* 3.C (Jan. 1956), pp. 307–435. ISSN: 0081-1947. DOI: 10.1016/S0081-1947(08)60135-6.

[62] Truls Norby et al. *Dalton Transactions* 19 (Sept. 2004), pp. 3012–3018. ISSN: 1477-9234. DOI: 10.1039/B403011G.

[63] D. K. Lim et al. *Acta Materialia* 61.4 (Feb. 2013), pp. 1274–1283. ISSN: 1359-6454. DOI: 10.1016/J.ACTAMAT.2012.11.003.

[64] Emiliana Fabbri, Daniele Pergolesi, and Enrico Traversa. *Chemical Society Reviews* 39.11 (Oct. 2010), pp. 4355–4369. ISSN: 1460-4744. DOI: 10.1039/B902343G.

[65] C. A.J. Fisher and M. S. Islam. *Solid State Ionics* 118.3-4 (Mar. 1999), pp. 355–363. ISSN: 0167-2738. DOI: 10.1016/S0167-2738(98)00391-9.

[66] Truls Norby and Per Kofstad. *Journal of the American Ceramic Society* 69.11 (Nov. 1986), pp. 780–783. ISSN: 1551-2916. DOI: 10.1111/J.1151-2916.1986.TB07359.X.

[67] Morten Huse, Truls Norby, and Reidar Haugsrud. *International Journal of Hydrogen Energy* 37.9 (May 2012), pp. 8004–8016. ISSN: 0360-3199. DOI: 10.1016/J.IJHYDENE.2011.10.020.

[68] Andreas Løken, Tor Svendsen Bjørheim, and Reidar Haugsrud. *Journal of Materials Chemistry A* 3.46 (Nov. 2015), pp. 23289–23298. ISSN: 2050-7496. DOI: 10.1039/C5TA04932F.

[69] Truls Norby and Reidar Haugsrud. "Dense Ceramic Membranes for Hydrogen Separation". *Membranes for Energy Conversion*. Vol. 2. John Wiley & Sons, Ltd, Apr. 2008, pp. 169–216. ISBN: 9783527314812. DOI: 10.1002/9783527622146.CH6.

[70] D. G. Thomas and J. J. Lander. *The Journal of Chemical Physics* 25.6 (Dec. 1956), pp. 1136–1142. ISSN: 0021-9606. DOI: 10.1063/1.1743165.

[71] You Zhou et al. *Nature* 534.7606 (May 2016), pp. 231–234. ISSN: 1476-4687. DOI: 10.1038/nature17653.

[72] Jian Shi, You Zhou, and Shriram Ramanathan. *Nature Communications* 5.1 (Sept. 2014), pp. 1–9. ISSN: 2041-1723. DOI: 10.1038/ncomms5860.

[73] K. P. Mohamed Jibri et al. *Physical Chemistry Chemical Physics* 25.18 (May 2023), pp. 12914–12922. ISSN: 1463-9084. DOI: 10.1039/D2CP04949J.

[74] K. D. Kreuer. *Solid State Ionics* 125.1-4 (Oct. 1999), pp. 285–302. ISSN: 0167-2738. DOI: 10.1016/S0167-2738(99)00188-5.

[75] Takuya Yamaguchi et al. *Solid State Ionics* 392 (Apr. 2023), p. 116164. ISSN: 0167-2738. DOI: 10.1016/J.SSI.2023.116164.

[76] Meagan Papac et al. *Nature Materials* 20.3 (Dec. 2020), pp. 301–313. ISSN: 1476-4660. DOI: 10.1038/s41563-020-00854-8.

[77] K. D. Kreuer. *Annual Review of Materials Research* 33 (Nov. 2003), pp. 333–359. ISSN: 15317331. DOI: 10.1146/ANNUREV.MATSCI.33.022802.091825.

[78] W Münch et al. *Phase Transitions* 68.3 (2006), pp. 567–586. ISSN: 01411594. DOI: 10.1080/01411599908224535.

[79] A. S. Nowick and A. V. Vaysleyb. *Solid State Ionics* 97.1-4 (May 1997), pp. 17–26. ISSN: 0167-2738. DOI: 10.1016/S0167-2738(97)00081-7.

[80] Zetian Tao et al. *Progress in Materials Science* 74 (Oct. 2015), pp. 1–50. ISSN: 0079-6425. DOI: 10.1016/J.PMATSCI.2015.04.002.

[81] C J T De Grotthuss. *Annales de Chimie* 58.1806 (1806), p. 54.

[82] K. D. Kreuer. *Solid State Ionics* 136-137 (Nov. 2000), pp. 149–160. ISSN: 0167-2738. DOI: 10.1016/S0167-2738(00)00301-5.

[83] M. Huse et al. *Journal of Solid State Chemistry* 187 (Mar. 2012), pp. 27–34. ISSN: 0022-4596. DOI: 10.1016/J.JSSC.2011.12.025.

[84] Yirong Gao et al. *Chemical Reviews* 120.13 (July 2020), pp. 5954–6008. ISSN: 15206890. DOI: 10.1021/ACS.CHEMREV.9B00747.

[85] Md Shafiqul Islam et al. *Chemistry of Materials* (July 2022). ISSN: 0897-4756. DOI: 10.1021/ACS.CHEMMATER.2C00867.

[86] Fabian M. Draber et al. *Nature Materials* 19.3 (Dec. 2019), pp. 338–346. ISSN: 1476-4660. DOI: 10.1038/s41563-019-0561-7.

[87] M. Saiful Islam et al. *Dalton Transactions* 0.19 (Sept. 2004), pp. 3061–3066. ISSN: 14779226. DOI: 10.1039/B402669C.

[88] Shihang Guo et al. *Advanced Functional Materials* (2024), p. 2304729. ISSN: 1616-3028. DOI: 10.1002/ADFM.202304729.

[89] Joachim Maier. *Progress in Solid State Chemistry* 23.3 (Jan. 1995), pp. 171–263. ISSN: 0079-6786. DOI: 10.1016/0079-6786(95)00004-E.

[90] Roger A. De Souza et al. *Solid State Ionics* 196.1 (Aug. 2011), pp. 1–8. ISSN: 0167-2738. DOI: 10.1016/J.SSI.2011.07.001.

[91] Zijie Sha et al. *Journal of Materials Chemistry A* 8.40 (Oct. 2020), pp. 21273–21288. ISSN: 2050-7496. DOI: 10.1039/D0TA08899D.

[92] Zijie Sha et al. *Small* (2024), p. 2404702. ISSN: 1613-6829. DOI: 10.1002/SMLL.202404702.

[93] Christian Kjølseth et al. *Solid State Ionics* 181.5-7 (Mar. 2010), pp. 268–275. ISSN: 0167-2738. DOI: 10.1016/J.SSI.2010.01.014.

[94] D. Vignesh and Ela Rout. *Energy and Fuels* 37.5 (Mar. 2023), pp. 3428–3469. ISSN: 15205029. DOI: 10.1021/ACS.ENERGYFUELS.2C03926.

[95] Tarjei Bondevik, Jonathan M. Polfus, and Truls Norby. *Solid State Ionics* 353 (Oct. 2020), p. 115369. ISSN: 0167-2738. DOI: 10.1016/J.SSI.2020.115369.

[96] Xin Guo and Rainer Waser. *Progress in Materials Science* 51.2 (Feb. 2006), pp. 151–210. ISSN: 0079-6425. DOI: 10.1016/J.PMATSCI.2005.07.001.

[97] Mona Shirpour et al. *Journal of Physical Chemistry C* 116.3 (Jan. 2012), pp. 2453–2461. ISSN: 19327447. DOI: 10.1021/JP208213X.

[98] Sangtae Kim et al. *Physical Chemistry Chemical Physics* 11.17 (Apr. 2009), pp. 3035–3038. ISSN: 14639076. DOI: 10.1039/B901623F.

[99] Truls Norby. *MRS Bulletin* 34.12 (Jan. 2009), pp. 923–928. ISSN: 08837694. DOI: 10.1557/MRS2009.214.

[100] J. A. Lane, J. L. Neff, and G. M. Christie. *Solid State Ionics* 177.19-25 (Oct. 2006), pp. 1911–1915. ISSN: 0167-2738. DOI: 10.1016/J.SSI.2006.02.024.

[101] Xin Xu et al. *Nature Materials* 19.8 (Apr. 2020), pp. 887–893. ISSN: 1476-4660. DOI: 10.1038/s41563-020-0656-1.

[102] Maarten C. Verbraeken, Emmanuelle Suard, and John T.S. Irvine. *Journal of Materials Chemistry* 19.18 (Apr. 2009), pp. 2766–2770. ISSN: 09599428. DOI: 10.1039/B820173K.

[103] Maarten C. Verbraeken et al. *Nature Materials* 14.1 (Dec. 2014), pp. 95–100. ISSN: 1476-4660. DOI: 10.1038/nmat4136.

[104] Genki Kobayashi et al. *Science* 351.6279 (Mar. 2016), pp. 1314–1317. ISSN: 10959203. DOI: 10.1126/SCIENCE.AAC9185.

[105] Keiga Fukui et al. *Nature Communications* 10.1 (June 2019), pp. 1–8. ISSN: 2041-1723. DOI: 10.1038/s41467-019-10492-7.

[106] Fumitaka Takeiri et al. *Nature Materials* 21.3 (Jan. 2022), pp. 325–330. ISSN: 1476-4660. DOI: 10.1038/s41563-021-01175-0.

[107] Shu Yamaguchi. *Science* 351.6279 (Mar. 2016), pp. 1262–1263. ISSN: 10959203. DOI: 10.1126/SCIENCE.AAF3361.

[108] Finn W. Poulsen. *Solid State Ionics* 145.1-4 (Dec. 2001), pp. 387–397. ISSN: 0167-2738. DOI: 10.1016/S0167-2738(01)00935-3.

[109] Truls Norby. *Progress in Energy* 6.4 (Aug. 2024), p. 043002. ISSN: 2516-1083. DOI: 10.1088/2516-1083/AD6C9F.

[110] H. Iwahara et al. *Journal of The Electrochemical Society* 135.2 (Feb. 1988), pp. 529–533. ISSN: 0013-4651. DOI: 10.1149/1.2095649.

[111] H. Iwahara. *Solid State Ionics* 28-30.PART 1 (Sept. 1988), pp. 573–578. ISSN: 0167-2738. DOI: 10.1016/S0167-2738(88)80104-8.

[112] K. S. Knight. *Solid State Ionics* 74.3-4 (Dec. 1994), pp. 109–117. ISSN: 0167-2738. DOI: 10.1016/0167-2738(94)90199-6.

[113] Anubhav Jain et al. *APL Materials* 1.1 (July 2013). ISSN: 2166532X. DOI: 10.1063/1.4812323.

[114] V. M. Goldschmidt. *Die Naturwissenschaften* 14.21 (May 1926), pp. 477–485. ISSN: 00281042. DOI: 10.1007/BF01507527.

[115] Zhen Li et al. *Chemistry of Materials* 28.1 (Jan. 2016), pp. 284–292. ISSN: 15205002. DOI: 10.1021/ACS.CHEMMATER.5B04107.

[116] Koichi Momma and Fujio Izumi. *Journal of Applied Crystallography* 44.6 (Oct. 2011), pp. 1272–1276. ISSN: 0021-8898. DOI: 10.1107/S0021889811038970.

[117] Lei Bi and Enrico Traversa. *Journal of Materials Research* 29.1 (2014), pp. 1–15. ISSN: 0884-2914. DOI: 10.1557/JMR.2013.205.

[118] G. B. Zhang and D. M. Smyth. *Solid State Ionics* 82.3-4 (Dec. 1995), pp. 153–160. ISSN: 0167-2738. DOI: 10.1016/0167-2738(95)00199-8.

[119] J. B. Goodenough, J. E. Ruiz-Diaz, and Y. S. Zhen. *Solid State Ionics* 44.1-2 (Dec. 1990), pp. 21–31. ISSN: 0167-2738. DOI: 10.1016/0167-2738(90)90039-T.

[120] Katsuyoshi Kakinuma et al. *Journal of Materials Science* 41.19 (Oct. 2006), pp. 6435–6440. ISSN: 00222461. DOI: 10.1007/S10853-006-0718-Z.

[121] Qiyang Lu and Bilge Yildiz. *Nano Letters* 16.2 (Feb. 2016), pp. 1186–1193. ISSN: 15306992. DOI: 10.1021/ACS.NANOLETT.5B04492.

[122] Nianpeng Lu et al. *Nature* 546.7656 (May 2017), pp. 124–128. ISSN: 1476-4687. DOI: 10.1038/nature22389.

[123] Nianpeng Lu et al. *Nature Energy* 7 (Dec. 2022), pp. 1–9. ISSN: 2058-7546. DOI: 10.1038/s41560-022-01166-8.

[124] Hugo J. Avila-Paredes et al. *Journal of Materials Chemistry* 20.45 (Nov. 2010), pp. 10110–10112. ISSN: 09599428. DOI: 10.1039/C0JM02967J.

[125] Shogo Miyoshi et al. *Chemistry of Materials* 26.18 (Sept. 2014), pp. 5194–5200. ISSN: 15205002. DOI: 10.1021/CM5012923.

[126] Sindre Østby Stub, Einar Vøllestad, and Truls Norby. *Journal of Physical Chemistry C* 121.23 (June 2017), pp. 12817–12825. ISSN: 19327455. DOI: 10.1021/ACS.JPCC.7B03005.

[127] Tetsuo Shimura, Seiichi Fujimoto, and Hiroyasu Iwahara. *Solid State Ionics* 143.1 (June 2001), pp. 117–123. ISSN: 0167-2738. DOI: 10.1016/S0167-2738(01)00839-6.

[128] Sonia Escolastico et al. *ChemSusChem* 6.8 (Aug. 2013), pp. 1523–1532. ISSN: 1864-564X. DOI: 10.1002/CSSC.201300091.

[129] Li Jian and C. M. Wayman. *Journal of the American Ceramic Society* 80.3 (Mar. 1997), pp. 803–806. ISSN: 1551-2916. DOI: 10.1111/J.1151-2916.1997.TB02905.X.

[130] Fride Vullum et al. *Journal of Solid State Chemistry* 181.10 (Oct. 2008), pp. 2580–2585. ISSN: 1095726X. DOI: 10.1016/j.jssc.2008.06.032.

[131] Shamanthini W. Arulnesan et al. *Journal of Solid State Chemistry* 277 (Sept. 2019), pp. 229–239. ISSN: 0022-4596. DOI: 10.1016/J.JSSC.2019.06.014.

[132] Pankaj Sarin et al. *Journal of the American Ceramic Society* 97.10 (Oct. 2014), pp. 3307–3319. ISSN: 1551-2916. DOI: 10.1111/JACE.13095.

[133] Harald Fjeld et al. *Physical Chemistry Chemical Physics* 12.35 (Aug. 2010), pp. 10313–10319. ISSN: 1463-9084. DOI: 10.1039/C002851G.

[134] Zhonghe Bi et al. *International Journal of Hydrogen Energy* 37.17 (Sept. 2012), pp. 12751–12759. ISSN: 03603199. DOI: 10.1016/j.ijhydene.2012.06.014.

[135] Truls Norby and Anna Magrasó. *Journal of Power Sources* 282 (May 2015), pp. 28–33. ISSN: 0378-7753. DOI: 10.1016/J.JPOWSOUR.2015.02.027.

[136] Sebastian Wachowski et al. *Inorganic Chemistry Frontiers* 5.9 (Sept. 2018), pp. 2157–2166. ISSN: 20521553. DOI: 10.1039/c8qi00524a.

[137] A. D. Brandão et al. *Chemistry of Materials* 22.24 (Dec. 2010), pp. 6673–6683. ISSN: 08974756. DOI: 10.1021/CM102705E.

[138] Cheng Li, Ryan D. Bayliss, and Stephen J. Skinner. *Solid State Ionics* 262 (Sept. 2014), pp. 530–535. ISSN: 01672738. DOI: 10.1016/j.ssi.2013.12.023.

[139] Yong Cao et al. *Journal of the European Ceramic Society* 35.6 (June 2015), pp. 1979–1983. ISSN: 1873619X. DOI: 10.1016/j.jeurceramsoc.2015.01.002.

[140] Yong Cao et al. *International Journal of Hydrogen Energy* 41.45 (Dec. 2016), pp. 20633–20639. ISSN: 0360-3199. DOI: 10.1016/J.IJHYDENE.2016.08.056.

[141] A. Mielewczyk-Gryn et al. *Crystal Research and Technology* 45.12 (Dec. 2010), pp. 1225–1228. ISSN: 1521-4079. DOI: 10.1002/CRAT.201000378.

[142] Tommy Mokkelbost et al. *Journal of the American Ceramic Society* 91.3 (Mar. 2008), pp. 879–886. ISSN: 1551-2916. DOI: 10.1111/J.1551-2916.2007.02232.X.

[143] A. Mielewczyk-Gryń et al. *Journal of Non-Crystalline Solids* 356.37-40 (Aug. 2010), pp. 1976–1979. ISSN: 0022-3093. DOI: 10.1016/J.JNONCRYSOL.2010.05.068.

[144] Yong Cao et al. *Solid State Ionics* 278 (Oct. 2015), pp. 152–156. ISSN: 0167-2738. DOI: 10.1016/J.SSI.2015.06.011.

[145] Kacper Dzierzgowski et al. *Crystals* 9.2 (Feb. 2019), p. 91. ISSN: 20734352. DOI: 10.3390/cryst9020091.

[146] Kacper Dzierzgowski et al. *Materials* 15.6 (Mar. 2022), p. 2267. ISSN: 1996-1944. DOI: 10.3390/MA15062267.

[147] R. J. Packer, P. A. Stuart, and S. J. Skinner. *Journal of Solid State Chemistry* 181.6 (June 2008), pp. 1445–1455. ISSN: 0022-4596. DOI: 10.1016/J.JSSC.2008.03.016.

[148] S. Wachowski, A. Mielewczyk-Gryn, and M. Gazda. *Journal of Solid State Chemistry* 219 (Nov. 2014), pp. 201–209. ISSN: 0022-4596. DOI: 10.1016/J.JSSC.2014.07.041.

[149] Aleksandra Mielewczyk-Gryń et al. *Journal of the American Ceramic Society* 103.11 (Nov. 2020), pp. 6575–6585. ISSN: 1551-2916. DOI: 10.1111/JACE.17352.

[150] R. J. Cava et al. *Journal of Solid State Chemistry* 40.3 (Dec. 1981), pp. 318–329. ISSN: 1095726X. DOI: 10.1016/0022-4596(81)90398-4.

[151] Cheng Li et al. *Chemistry of Materials* 32.6 (Mar. 2020), pp. 2292–2303. ISSN: 15205002. DOI: 10.1021/ACS.CHEMMATER.9B04255.

[152] Josie E. Auckett et al. *Journal of Materials Chemistry A* 9.7 (Feb. 2021), pp. 4091–4102. ISSN: 20507496. DOI: 10.1039/d0ta07453e.

[153] Giovanna Canu et al. *Journal of Alloys and Compounds* 697 (Mar. 2017), pp. 392–400. ISSN: 09258388. DOI: 10.1016/j.jallcom.2016.12.111.

[154] Sander van Smaalen. *Incommensurate Crystallography*. Oxford University Press, Jan. 2007, pp. 1–288. ISBN: 9780191718762. DOI: 10.1093/ACPROF:OSO/9780198570820.001.0001.

[155] Yidong Han. "Investigation of structure and conductivity of LaNb0.9Mo0.1O4.05 based materials". PhD thesis. Imperial College London, 2024.

[156] P. M. De Wolff. *Acta Crystallographica Section A: Foundations and Advances* 30.6 (Nov. 1974), pp. 777–785. ISSN: 0567-7394. DOI: 10.1107/S0567739474-010710.

[157] P. M. De Wolff, T. Janssen, and A. Janner. *Acta Crystallographica Section A: Foundations and Advances* 37.5 (Sept. 1981), pp. 625–636. ISSN: 0567-7394. DOI: 10.1107/S0567739481-001447.

[158] Stevin S. Pramana et al. *Journal of the American Chemical Society* 138.4 (Feb. 2016), pp. 1273–1279. ISSN: 15205126. DOI: 10.1021/jacs.5b11373.

[159] Jian Li et al. *Nature Communications* 11.1 (Sept. 2020), pp. 1–9. ISSN: 2041-1723. DOI: 10.1038/s41467-020-18481-x.

[160] Yidong Han and Stephen J. Skinner. *Materials Advances* 4.17 (2023), pp. 3759–3766. ISSN: 2633-5409. DOI: 10.1039/D3MA00268C.

[161] Cheng Li, Stevin S. Pramana, and Stephen J. Skinner. *Dalton Transactions* 48.5 (Jan. 2019), pp. 1633–1646. ISSN: 14779234. DOI: 10.1039/c8dt03958e.

[162] Hege Westvold Johansen. "Defects and transport in donor doped LaNbO4". MSc Thesis. University of Oslo, 2020.

[163] Chiara Ferrara et al. *Journal of Materials Chemistry A* 3.44 (Nov. 2015), pp. 22258–22265. ISSN: 20507496. DOI: 10.1039/c5ta06575e.

[164] Kazuaki Toyoura et al. *Journal of Materials Chemistry A* 6.25 (2018), pp. 12004–12011. ISSN: 20507496. DOI: 10.1039/c8ta02859a.

[165] Yidong Han, Siqi Li, and Stephen Skinner. *Journal of Solid State Chemistry* 332 (Apr. 2024), p. 124590. ISSN: 0022-4596. DOI: 10.1016/J.JSSC.2024.124590.

[166] A. Neumann and D. Walter. *Thermochimica Acta* 445.2 (June 2006), pp. 200–204. ISSN: 0040-6031. DOI: 10.1016/J.TCA.2005.06.013.

[167] W H Bragg et al. "The reflection of X-rays by crystals". *Proceedings of the Royal Society of London. Series A, Containing Papers of a Mathematical and Physical Character*. Vol. 88. 605. The Royal SocietyLondon, July 1913, pp. 428–438. DOI: 10.1098/RSPA.1913.0040.

[168] H. M. Rietveld. *Journal of Applied Crystallography* 2.2 (June 1969), pp. 65–71. ISSN: 0021-8898. DOI: 10.1107/S0021889869006558.

[169] Armel Le Bail. *Powder Diffraction* 20.4 (Dec. 2005), pp. 316–326. ISSN: 1945-7413. DOI: 10.1154/1.2135315.

[170] Brian H. Toby. *Powder Diffraction* 21.1 (Mar. 2006), pp. 67–70. ISSN: 0885-7156. DOI: 10.1154/1.2179804.

[171] G. V. Narasimha Rao et al. *Powder Diffraction* 11.3 (1996), pp. 200–203. ISSN: 1945-7413. DOI: 10.1017/S088571560000912X.

[172] Brian H. Toby and Robert B. Von Dreele. *Journal of Applied Crystallography* 46.2 (Mar. 2013), pp. 544–549. ISSN: 0021-8898. DOI: 10.1107/S0021889813003531.

[173] D. Zagorac et al. *Journal of Applied Crystallography* 52.5 (Sept. 2019), pp. 918–925. ISSN: 16005767. DOI: 10.1107/S160057671900997X.

[174] F. Y. Xie et al. *Journal of Electron Spectroscopy and Related Phenomena* 185.3-4 (Apr. 2012), pp. 112–118. ISSN: 0368-2048. DOI: 10.1016/J.ELSPEC.2012.01.004.

[175] Zijie Sha. "Investigation of mass transport in mixed onducting A-site deficient (La0.8Sr0.2)0.95Cr0.5Fe0.5O3-δ perovskites in humid conditions". PhD thesis. Imperial College London, 2022.

[176] J. J. Rehr and R. C. Albers. *Reviews of Modern Physics* 72.3 (July 2000), p. 621. ISSN: 00346861. DOI: 10.1103/RevModPhys.72.621.

[177] François Farges. *Journal of Non-Crystalline Solids* 204.1 (Aug. 1996), pp. 53–64. ISSN: 0022-3093. DOI: 10.1016/0022-3093(96)00392-4.

[178] Joanna Kowalska and Serena DeBeer. *Biochimica et Biophysica Acta (BBA) - Molecular Cell Research* 1853.6 (June 2015), pp. 1406–1415. ISSN: 0167-4889. DOI: 10.1016/J.BBAMCR.2014.11.027.

[179] C. Marini et al. *Journal of Physics: Condensed Matter* 28.4 (Jan. 2016), p. 045401. ISSN: 0953-8984. DOI: 10.1088/0953-8984/28/4/045401.

[180] Q Bollaert et al. *European Journal of Mineralogy* 36.1 (2024), pp. 55–72. DOI: 10.5194/ejm-36-55-2024.

[181] François Farges and Stéphanie Rossano. *European Journal of Mineralogy* 12.6 (Nov. 2000), pp. 1093–1107. ISSN: 09351221. DOI: 10.1127/0935-1221/2000/0012-1093.

[182] Paula C. Piilonen et al. *Canadian Mineralogist* 44.3 (June 2006), pp. 775–794. ISSN: 00084476. DOI: 10.2113/GSCANMIN.44.3.775.

[183] T. Pauporté, Y. Soldo-Olivier, and R. Faure. *Journal of Physical Chemistry B* 107.34 (Aug. 2003), pp. 8861–8867. ISSN: 15206106. DOI: 10.1021/JP034279S.

[184] Alexei Kuzmin and Juris Purans. *Journal of Physics: Condensed Matter* 5.15 (Apr. 1993), p. 2333. ISSN: 0953-8984. DOI: 10.1088/0953-8984/5/15/006.

[185] Matthew Newville. *Reviews in Mineralogy and Geochemistry* 78.1 (Jan. 2014), pp. 33–74. ISSN: 1529-6466. DOI: 10.2138/RMG.2014.78.2.

[186] J. J. Rehr et al. *Journal of the American Chemical Society* 113.14 (July 1991), pp. 5135–5140. ISSN: 15205126. DOI: 10.1021/JA00014A001.

[187] A J Dent et al. *Journal of Physics: Conference Series* 190.1 (Nov. 2009), p. 012039. ISSN: 1742-6596. DOI: 10.1088/1742-6596/190/1/012039.

[188] B. Ravel and M. Newville. *Journal of Synchrotron Radiation* 12.4 (June 2005), pp. 537–541. ISSN: 0909-0495. DOI: 10.1107/S0909049505012719.

[189] Yoshihiro Yamazaki, Peter Babilo, and Sossina M. Haile. *Chemistry of Materials* 20.20 (Oct. 2008), pp. 6352–6357. ISSN: 08974756. DOI: 10.1021/CM800843S.

[190] Ph Colomban. *Fuel Cells* 13.1 (Feb. 2013), pp. 6–18. ISSN: 1615-6854. DOI: 10.1002/FUCE.201200088.

[191] C. Tsioptsias. *Measurement* 204 (Nov. 2022), p. 112136. ISSN: 0263-2241. DOI: 10.1016/J.MEASUREMENT.2022.112136.

[192] Joseph I. Goldstein et al. *Scanning Electron Microscopy and X-ray Microanalysis*. Boston, MA: Springer US, 2003. ISBN: 978-1-4613-4969-3. DOI: 10.1007/978-1-4615-0215-9.

[193] David B. Williams and C. Barry Carter. *Transmission Electron Microscopy*. Boston, MA: Springer US, 1996. ISBN: 978-0-306-45324-3. DOI: 10.1007/978-1-4757-2519-3.

[194] Dale E. Newbury. *Microscopy and Microanalysis* 4.6 (Dec. 1998), pp. 585–597. ISSN: 1431-9276. DOI: 10.1017/S1431927698980564.

[195] Earl J. Kirkland. *Advanced computing in electron microscopy: Second edition*. Springer US, 2010, pp. 1–289. ISBN: 9781441965325. DOI: 10.1007/978-1-4419-6533-2.

[196] Caroline A. Schneider, Wayne S. Rasband, and Kevin W. Eliceiri. *Nature Methods* 9.7 (June 2012), pp. 671–675. ISSN: 1548-7105. DOI: 10.1038/nmeth.2089.

[197] Alka B. Garg et al. *Journal of Physical Chemistry Letters* 14.7 (Feb. 2023), pp. 1762–1768. ISSN: 19487185. DOI: 10.1021/ACS.JPCLETT.3C00020.

[198] M. Bär et al. *Applied Physics Letters* 93.24 (Dec. 2008). ISSN: 00036951. DOI: 10.1063/1.3046780.

[199] J. Tauc, R. Grigorovici, and A. Vancu. *physica Status Solidi (b)* 15.2 (Jan. 1966), pp. 627–637. ISSN: 1521-3951. DOI: 10.1002/PSSB.19660150224.

[200] E. A. Davis and N. F. Mott. *Philosophical Magazine* 22.179 (1970), pp. 903–922. ISSN: 00318086. DOI: 10.1080/14786437008221061.

[201] Markus Meinert and Günter Reiss. *Journal of Physics: Condensed Matter* 26.11 (Mar. 2014), p. 115503. ISSN: 0953-8984. DOI: 10.1088/0953-8984/26/11/115503.

[202] Jean Luc Bredas. *Materials Horizons* 1.1 (Nov. 2013), pp. 17–19. ISSN: 2051-6355. DOI: 10.1039/C3MH00098B.

[203] Paul Kubelka and Franz Munk. *Zeitschrift für technische Physik* 12 (1931), pp. 593–601.

[204] J. Tauc. *Amorphous and Liquid Semiconductors*. Boston, MA: Springer US, 1974. ISBN: 978-1-4615-8707-1. DOI: 10.1007/978-1-4615-8705-7.

[205] Julian Klein et al. *Advanced Functional Materials* 33.47 (Nov. 2023), p. 2304523. ISSN: 1616-3028. DOI: 10.1002/ADFM.202304523.

[206] Biswajit Choudhury and Amarjyoti Choudhury. *Physica E: Low-dimensional Systems and Nanostructures* 56 (Feb. 2014), pp. 364–371. ISSN: 1386-9477. DOI: 10.1016/J.PHYSE.2013.10.014.

[207] John A. Weil and James R. Bolton. *Electron Paramagnetic Resonance*. Wiley, Dec. 2006. ISBN: 9780471754961. DOI: 10.1002/0470084987.

[208] U. Selvaraj and K. J. Rao. *Chemical Physics* 123.1 (June 1988), pp. 141–150. ISSN: 0301-0104. DOI: 10.1016/0301-0104(88)87039-3.

[209] D. Boudlich et al. *Journal of Non-Crystalline Solids* 224.2 (Mar. 1998), pp. 135–142. ISSN: 0022-3093. DOI: 10.1016/S0022-3093(97)00459-6.

[210] K. Vanheusden et al. *Journal of Applied Physics* 79.10 (May 1996), pp. 7983–7990. ISSN: 0021-8979. DOI: 10.1063/1.362349.

[211] Yi Hu and H. J. Chen. *Journal of Applied Physics* 101.12 (June 2007), p. 124902. ISSN: 00218979. DOI: 10.1063/1.2745301.

[212] Zonghao Shen. "Mass transport in mixed-conducting LSCrF-ScSZ dual phase composites for oxygen transport membrane applications". PhD thesis. Imperial College London, 2017.

[213] P. Terrence Murray and J. Wayne Rabalais. *Journal of the American Chemical Society* 103.5 (1981), pp. 1007–1013. ISSN: 15205126. DOI: 10.1021/JA00395A002.

[214] Zonghao Shen and Sarah Fearn. *Journal of Electroceramics* (Dec. 2024), pp. 1–28. ISSN: 1573-8663. DOI: 10.1007/S10832-024-00375-9.

[215] John A. Kilner, Stephen J. Skinner, and Hidde H. Brongersma. *Journal of Solid State Electrochemistry* 15.5 (May 2011), pp. 861–876. ISSN: 14328488. DOI: 10.1007/S10008-010-1289-0.

[216] J Crank. *The mathematics of diffusion*. 2nd edition. Oxford: Oxford University Press, 1956. ISBN: 9780198534112.

[217] Jingjing Liu. "Mass transport and electrochemical properties of La2Mo2O9 as a fast ionic conductor". PhD thesis. Imperial College London, 2010.

[218] Chen-Yu Tsai. "Phase evolution and reactivity of Pr2NiO4+d and Ce0.9Gd0.1O2-d solid oxide cell electrodes". PhD thesis. Imperial College London, 2020.

[219] John T.S. Irvine, Derek C. Sinclair, and Anthony R. West. *Advanced Materials* 2.3 (Mar. 1990), pp. 132–138. ISSN: 15214095. DOI: 10.1002/adma.19900020304.

[220] M. Schönleber, D. Klotz, and E. Ivers-Tiffée. *Electrochimica Acta* 131 (June 2014), pp. 20–27. ISSN: 0013-4686. DOI: 10.1016/J.ELECTACTA.2014.01.034.

[221] William J. Fleming. *Journal of The Electrochemical Society* 124.1 (Jan. 1976), p. 21. ISSN: 0013-4651. DOI: 10.1149/1.2133235.

[222] Malcolm H Hebb. *The Journal of Chemical Physics* 20.1 (Jan. 1952), pp. 185–190. ISSN: 0021-9606. DOI: 10.1063/1.1700165.

[223] I. Riess. *Solid State Ionics* 91.3-4 (Oct. 1996), pp. 221–232. ISSN: 0167-2738. DOI: 10.1016/S0167-2738(96)83022-0.

[224] Jin Ho Kim and Han Ill Yoo. *Solid State Ionics* 140.1-2 (Mar. 2001), pp. 105–113. ISSN: 0167-2738. DOI: 10.1016/S0167-2738(01)00687-7.

[225] Jin Ho Jang and Gyeong Man Choi. *Solid State Ionics* 154-155.155 (Dec. 2002), pp. 481–486. ISSN: 0167-2738. DOI: 10.1016/S0167-2738(02)00486-1.

[226] Tatsumi Ishihara et al. *Solid State Ionics* 175.1-4 (Nov. 2004), pp. 319–322. ISSN: 0167-2738. DOI: 10.1016/J.SSI.2004.03.036.

[227] Kyung Ryul Lee, Jong Ho Lee, and Han Ill Yoo. *Solid State Ionics* 181.15-16 (June 2010), pp. 724–729. ISSN: 0167-2738. DOI: 10.1016/J.SSI.2010.03.015.

[228] T. Miruszewski et al. *Journal of Materials Chemistry A* 10.13 (Mar. 2022), pp. 7218–7227. ISSN: 2050-7496. DOI: 10.1039/D1TA10916B.

[229] Varley F. Sears. *Neutron News* 3.3 (Jan. 1992), pp. 26–37. ISSN: 19317352. DOI: 10.1080/10448639208218770.

[230] R. Satija et al. *Journal of Power Sources* 129.2 (Apr. 2004), pp. 238–245. ISSN: 0378-7753. DOI: 10.1016/J.JPOWSOUR.2003.11.068.

[231] Walter Langel. *ChemTexts* 9.4 (Dec. 2023), pp. 1–55. ISSN: 21993793. DOI: 10.1007/S40828-023-00184-7.

[232] Yoji Kobayashi et al. *Nature Materials* 11.6 (Apr. 2012), pp. 507–511. ISSN: 1476-4660. DOI: 10.1038/nmat3302.

[233] Aneta Slodczyk et al. *Solid State Ionics* 225 (Oct. 2012), pp. 214–218. ISSN: 0167-2738. DOI: 10.1016/J.SSI.2012.01.023.

[234] Jan Wallis et al. *Journal of Physics Communications* 4.4 (Apr. 2020), p. 045004. ISSN: 2399-6528. DOI: 10.1088/2399-6528/AB852D.

[235] Maciej Krzystyniak et al. *Physical Review B - Condensed Matter and Materials Physics* 88.18 (Nov. 2013), p. 184304. ISSN: 10980121. DOI: 10.1103/PHYSREVB.88.184304.

[236] Aneta Slodczyk et al. *Solid State Ionics* 252 (Dec. 2013), pp. 7–11. ISSN: 0167-2738. DOI: 10.1016/J.SSI.2013.06.012.

[237] M. Krzystyniak et al. *Journal of Physics: Conference Series* 571.1 (Dec. 2014), p. 012002. ISSN: 1742-6596. DOI: 10.1088/1742-6596/571/1/012002.

[238] Maciej Krzystyniak, Giovanni Romanelli, and Felix Fernandez-Alonso. *Analyst* 144.13 (June 2019), pp. 3936–3941. ISSN: 1364-5528. DOI: 10.1039/C8AN01729H.

[239] M. Krzystyniak et al. *Physica Scripta* 98.2 (Jan. 2023), p. 025707. ISSN: 1402-4896. DOI: 10.1088/1402-4896/ACB323.

[240] Erwin Lalik et al. *Energies* 16.14 (July 2023), p. 5496. ISSN: 1996-1073. DOI: 10.3390/EN16145496.

[241] M. Krzystyniak et al. *Journal of Physics: Conference Series* 1055.1 (July 2018), p. 012006. ISSN: 1742-6596. DOI: 10.1088/1742-6596/1055/1/012006.

[242] Carla Andreani et al. *Advances in Physics* 66.1 (Jan. 2017), pp. 1–73. ISSN: 14606976. DOI: 10.1080/00018732.2017.1317963.

[243] Carla Andreani et al. *Advances in Physics* 54.5 (July 2005), pp. 377–469. ISSN: 00018732. DOI: 10.1080/00018730500403136.

[244] Matthew Krzystyniak et al. *Journal of Physics Communications* 8.2 (Feb. 2024), p. 022001. ISSN: 2399-6528. DOI: 10.1088/2399-6528/AD27E0.

[245] Claudia Scatigno et al. *Analytical Chemistry* 94.12 (Mar. 2022), pp. 5023–5028. ISSN: 15206882. DOI: 10.1021/ACS.ANALCHEM.1C04949.

[246] Owen Arnold et al. *Nuclear Instruments and Methods in Physics Research Section A: Accelerators, Spectrometers, Detectors and Associated Equipment* 764 (Nov. 2014), pp. 156–166. ISSN: 0168-9002. DOI: 10.1016/J.NIMA.2014.07.029.

[247] S. Jackson et al. *Journal of Physics: Conference Series* 571.1 (Dec. 2014), p. 012009. ISSN: 1742-6596. DOI: 10.1088/1742-6596/571/1/012009.

[248] J. I. Robledo et al. *Nuclear Instruments and Methods in Physics Research Section A: Accelerators, Spectrometers, Detectors and Associated Equipment* 971 (Aug. 2020), p. 164096. ISSN: 0168-9002. DOI: 10.1016/J.NIMA.2020.164096.

[249] E. S. Buyanova et al. *Russian Journal of Inorganic Chemistry* 62.2 (Feb. 2017), pp. 211–217. ISSN: 00360236. DOI: 10.1134/S0036023617020048.

[250] Kehan Huang et al. *Journal of Materials Chemistry A* 13.6 (Feb. 2025), pp. 4214–4224. ISSN: 2050-7496. DOI: 10.1039/D4TA05501B.

[251] Maria Vasilopoulou et al. *Journal of the American Chemical Society* 134.39 (Oct. 2012), pp. 16178–16187. ISSN: 00027863. DOI: 10.1021/JA3026906.

[252] D. Marrero-López et al. *Electrochimica Acta* 50.22 (Aug. 2005), pp. 4385–4395. ISSN: 0013-4686. DOI: 10.1016/J.ELECTACTA.2005.02.002.

[253] D. Marrero-López et al. *Journal of Solid State Chemistry* 181.2 (Feb. 2008), pp. 253–262. ISSN: 0022-4596. DOI: 10.1016/J.JSSC.2007.11.024.

[254] Gongming Wang et al. *Energy & Environmental Science* 5.3 (Mar. 2012), pp. 6180–6187. ISSN: 1754-5706. DOI: 10.1039/C2EE03158B.

[255] M. F. Sunding et al. *Journal of Electron Spectroscopy and Related Phenomena* 184.7 (July 2011), pp. 399–409. ISSN: 0368-2048. DOI: 10.1016/J.ELSPEC.2011.04.002.

[256] P. A.W. Van Der Heide. *Surface and Interface Analysis* 33.5 (May 2002), pp. 414–425. ISSN: 1096-9918. DOI: 10.1002/SIA.1227.

[257] W. Y. Howng and R. J. Thorn. *Journal of Physics and Chemistry of Solids* 41.1 (Jan. 1980), pp. 75–81. ISSN: 0022-3697. DOI: 10.1016/0022-3697(80)90123-7.

[258] V. Jayaseelan et al. *Journal of Materials Science: Materials in Electronics* 33.11 (Apr. 2022), pp. 8741–8746. ISSN: 1573482X. DOI: 10.1007/S10854-021-06798-2.

[259] V. Seeman et al. *Scientific Reports* 10.1 (Sept. 2020), pp. 1–14. ISSN: 2045-2322. DOI: 10.1038/s41598-020-72958-9.

[260] M. C. Paganini et al. *Surface Science* 421.3 (Feb. 1999), pp. 246–262. ISSN: 0039-6028. DOI: 10.1016/S0039-6028(98)00795-X.

[261] Yeqin Guan et al. *Nature Chemistry* 16.3 (Jan. 2024), pp. 373–379. ISSN: 1755-4349. DOI: 10.1038/s41557-023-01395-8.

[262] Catalina E. Laplaza et al. *Journal of the American Chemical Society* 118.36 (Sept. 1996), pp. 8623–8638. ISSN: 00027863. DOI: 10.1021/JA960574X.

[263] Quentin Bollaert et al. *American Mineralogist* 108.3 (Mar. 2023), pp. 595–605. ISSN: 0003-004X. DOI: 10.2138/AM-2022-8293.

[264] Andrew M. Beale and Gopinathan Sankar. *Chemistry of Materials* 15.1 (Jan. 2003), pp. 146–153. ISSN: 08974756. DOI: 10.1021/CM020463Z.

[265] Seiji Yamazoe et al. *Journal of Physical Chemistry C* 112.17 (May 2008), pp. 6869–6879. ISSN: 19327447. DOI: 10.1021/JP711250F.

[266] M. Nalin et al. *Journal of Non-Crystalline Solids* 353.16-17 (June 2007), pp. 1592–1597. ISSN: 0022-3093. DOI: 10.1016/J.JNONCRYSOL.2007.01.031.

[267] Giovanna Canu et al. *Journal of Alloys and Compounds* 857 (Mar. 2021), p. 157532. ISSN: 09258388. DOI: 10.1016/j.jallcom.2020.157532.

[268] Hui Zhou et al. *Nature Catalysis* 4.10 (Oct. 2021), pp. 860–871. ISSN: 2520-1158. DOI: 10.1038/s41929-021-00684-0.

[269] Hui Zhou et al. *Nature Communications* 12.1 (Sept. 2021), pp. 1–10. ISSN: 2041-1723. DOI: 10.1038/s41467-021-25784-0.

[270] Takashi Yamamoto. *X-Ray Spectrometry* 37.6 (Nov. 2008), pp. 572–584. ISSN: 1097-4539. DOI: 10.1002/XRS.1103.

[271] Ying Chu Chen et al. *ACS Catalysis* 6.4 (Apr. 2016), pp. 2357–2367. ISSN: 21555435. DOI: 10.1021/ACSCATAL.5B02444.

[272] Simon J. Hibble et al. *Inorganic Chemistry* 34.21 (Oct. 1995), pp. 5109–5113. ISSN: 1520510X. DOI: 10.1021/IC00125A006.

[273] Kalpana Singh, Janusz Nowotny, and Venkataraman Thangadurai. *Chemical Society Reviews* 42.5 (Feb. 2013), pp. 1961–1972. ISSN: 1460-4744. DOI: 10.1039/C2CS35393H.

[274] Truls Norby. "Proton Conductivity in Perovskite Oxides". Ed. by Tatsumi Ishihara. Springer, Boston, MA, 2009, pp. 217–241. ISBN: 978-0-387-77708-5. DOI: 10.1007/978-0-387-77708-5_11.

[275] T. Miruszewski et al. *Journal of Solid State Chemistry* 270 (Feb. 2019), pp. 601–607. ISSN: 0022-4596. DOI: 10.1016/J.JSSC.2018.12.034.

[276] Ragnhild Hancke, Zuoan Li, and Reidar Haugsrud. *Journal of Membrane Science* 439 (July 2013), pp. 68–77. ISSN: 0376-7388. DOI: 10.1016/J.MEMSCI.2013.03.049.

[277] Hyun Ho Shin and Steven McIntosh. *Journal of Materials Chemistry A* 1.26 (June 2013), pp. 7639–7647. ISSN: 2050-7496. DOI: 10.1039/C3TA10740J.

[278] M. Khalid Hossain, Takayuki Yamamoto, and Kenichi Hashizume. *Journal of Alloys and Compounds* 903 (May 2022), p. 163957. ISSN: 0925-8388. DOI: 10.1016/J.JALLCOM.2022.163957.

[279] Reidar Haugsrud et al. *Journal of The Electrochemical Society* 153.8 (June 2006), J87. ISSN: 00134651. DOI: 10.1149/1.2203933.

[280] Takeshi Matsukawa and Toru Ishigaki. *Dalton Transactions* 50.22 (June 2021), pp. 7590–7596. ISSN: 1477-9234. DOI: 10.1039/D1DT01259B.

[281] Febrigia Ghana Rinaldi et al. *ACS Omega* 3.8 (Aug. 2018), pp. 8963–8970. ISSN: 24701343. DOI: 10.1021/ACSOMEGA.8B01110.

[282] Kasala Prabhakar Reddy et al. *Journal of Physical Chemistry C* 122.40 (Oct. 2018), pp. 23034–23044. ISSN: 19327455. DOI: 10.1021/ACS.JPCC.8B07024.

[283] Chris G. Van de Walle and J. Neugebauer. *Nature* 423.6940 (June 2003), pp. 626–628. ISSN: 1476-4687. DOI: 10.1038/nature01665.

[284] Masao Arai et al. *Japanese Journal of Applied Physics* 44.9R (Sept. 2005), pp. 6596–6599. ISSN: 00214922. DOI: 10.1143/JJAP.44.6596.

[285] Shoujun Ding et al. *Journal of Materials Science: Materials in Electronics* 29.14 (July 2018), pp. 11878–11885. ISSN: 1573482X. DOI: 10.1007/S10854-018-9288-5.

[286] Shoujun Ding et al. *Journal of Solid State Chemistry* 262 (June 2018), pp. 87–93. ISSN: 0022-4596. DOI: 10.1016/J.JSSC.2018.03.011.

[287] F. Litimein et al. *Journal of Materials Science* 49.22 (Aug. 2014), pp. 7809–7818. ISSN: 15734803. DOI: 10.1007/S10853-014-8491-X.

[288] Patrycja Makuła, Michał Pacia, and Wojciech Macyk. *Journal of Physical Chemistry Letters* 9.23 (Dec. 2018), pp. 6814–6817. ISSN: 19487185. DOI: 10.1021/ACS.JPCLETT.8B02892.

[289] Ioannis Kostis et al. *Journal of Physical Chemistry C* 117.35 (Sept. 2013), pp. 18013–18020. ISSN: 19327447. DOI: 10.1021/JP407354J.

[290] Maria Vasilopoulou et al. *Journal of Physical Chemistry C* 118.24 (June 2014), pp. 12632–12641. ISSN: 19327455. DOI: 10.1021/JP502092H.

[291] M. Vasilopoulou et al. *Journal of Materials Chemistry A* 2.6 (Jan. 2014), pp. 1738–1749. ISSN: 2050-7496. DOI: 10.1039/C3TA13975A.

[292] Ph Colomban and A. Slodczyk. *The European Physical Journal Special Topics* 213.1 (Dec. 2012), pp. 171–193. ISSN: 1951-6401. DOI: 10.1140/EPJST/E2012-01670-7.

[293] A. Parmentier et al. *Frontiers of Physics* 13.1 (Feb. 2018), pp. 1–11. ISSN: 20950470. DOI: 10.1007/S11467-017-0724-4.

[294] Matthew Krzystyniak et al. *Journal of Physics Communications* 5.7 (July 2021), p. 075013. ISSN: 2399-6528. DOI: 10.1088/2399-6528/AC1508.

[295] Zonghao Shen, John A. Kilner, and Stephen J. Skinner. *Physical Chemistry Chemical Physics* 20.27 (July 2018), pp. 18279–18290. ISSN: 1463-9084. DOI: 10.1039/C8CP02797H.

[296] Rongzheng Ren et al. *ACS Applied Energy Materials* 3.5 (May 2020), pp. 4914–4922. ISSN: 25740962. DOI: 10.1021/ACSAEM.0C00486.

[297] Arim Seong et al. *Advanced Science* 8.11 (June 2021), p. 2004099. ISSN: 21983844. DOI: 10.1002/ADVS.202004099.

[298] Albert Tarancón et al. *Journal of Materials Chemistry* 17.30 (Aug. 2007), pp. 3175–3181. ISSN: 1364-5501. DOI: 10.1039/B704320A.

Appendix A

Publication record

Chapters 4 and 5 contain information from:

[250] K. Huang, Y. Han, M. A. Isaacs, S. J. Skinner. Exploring the stability and protonic conductivity in W- and Mo-substituted $LaNbO_4$ under a reducing atmosphere. *Journal of Materials Chemistry A* 13.6 (Feb. 2025), pp. 4214-4224. ISSN: 2050-7496. DOI: 10.1039/D4TA05501B.

Appendix B

Copyright statement

All reproduced figures and tables covered by open access licences that do not require specific copyright permissions are listed below.

Figure 1.1 Classification of hydrogen production routes by specific colours. Reproduced from [8] with permission under a Creative Commons Attribution-NonCommercial 3.0 Unported Licence.

Figure 2.7 The total conductivity of nano-YSZ with different grain sizes measured under wet air (∼2.5% RH). Reproduced from [60, 98] with permission under a Creative Commons CC BY Licence.

Figure 2.11(b) Phase diagrams of (a) LNW and (b) LNMo. Both phases were evaluated via the in-situ X-ray powder diffraction (XRD) technique. Two temperature points extrapolated from dilatometry analysis are marked as "×" on the phase diagram of LNW. Reproduced from [151] with permission from American Chemical Society, and from [152] with permission under a Creative Commons Attribution-NonCommercial 3.0 Unported Licence.

Figure 2.12 Schematic diagrams of (a) an ideal crystal lattice, (b) the (3+1)D-commensurately modulated structure along *a* axis, (c) the (3+1)D-incommensurately modulated structure along *a* axis, and their corresponding reciprocal lattice point patterns, respectively. Adapted from [47, 155] with permission from Imperial College London.

Figure 3.6 (a) The absorption process of an isolated atom. No EXAFS is raised. (b) The photoelectron is scattered by the electrons of the neighbouring atom, which interferes with the photoelectron at the absorbing atom, causing EXAFS. The photoelectron travels as a wave. Reproduced from [185] with permission under a Creative Commons Attribution-ShareAlike 3.0 Licence.

Table 2.2 The activation energy of LNW with a series of substitution levels (1%, 8%, 12% and 16%). The activation energy reduces at around 600 °C. Reproduced from [47] with permission from Imperial College London.

The copyright permissions for all reproduced figures and tables in this thesis are provided below.

Figure 1.2 Schematic diagram of the working principle in a SOFC based on (a) oxide ion-conducting electrolyte and (b) proton-conducting electrolyte. Reproduced from [49] with permission from Royal Society of Chemistry.



CCC Marketplace

This is a License Agreement between Kehan Huang ("User") and Copyright Clearance Center, Inc. ("CCC") on behalf of the Rightsholder identified in the order details below. The license consists of the order details, the Marketplace Permissions General Terms and Conditions below, and any Rightsholder Terms and Conditions which are included below.

All payments must be made in full to CCC in accordance with the Marketplace Permissions General Terms and Conditions below.

Order Date	13-Mar-2025	Type of Use	Republish in a thesis/dissertation
Order License ID	1587977-1	Publisher	ROYAL SOCIETY OF CHEMISTRY
ISSN	1460-4744	Portion	Chart/graph/table/figure

LICENSED CONTENT

Publication Title	Chemical Society reviews	Rightsholder	Royal Society of Chemistry
Article Title	Oxide-ion and proton conducting electrolyte materials for clean energy applications: structural and mechanistic features.	Publication Type	e-Journal
		Start Page	4370
		Issue	11
Author / Editor	Royal Society of Chemistry (Great Britain)	Volume	39
Date	01/01/1972	URL	http://www.rsc.org/csr
Language	English		
Country	United Kingdom of Great Britain and Northern Ireland		

REQUEST DETAILS

Portion Type	Chart/graph/table/figure	Distribution	Worldwide
Number of Charts / Graphs / Tables / Figures Requested	1	Translation	Original language plus one translation
		Copies for the Disabled?	No
Format (select all that apply)	Print, Electronic	Minor Editing Privileges?	Yes
Who Will Republish the Content?	Academic institution	Incidental Promotional Use?	No
Duration of Use	Life of current edition	Currency	GBP
Lifetime Unit Quantity	Up to 499		
Rights Requested	Main product		

NEW WORK DETAILS

Title	PhD Thesis: Redox Stability and Ionic Conduction in Donor-Substituted LaNbO4 under Hydrogen Environments	Institution Name	Imperial College London
		Expected Presentation Date	2025-07-01
Instructor Name	Kehan Huang		

ADDITIONAL DETAILS

Order Reference Number	47	The Requesting Person / Organization to Appear on the License	Kehan Huang

REQUESTED CONTENT DETAILS

Title, Description or Numeric Reference of the Portion(s)	Figure 1.2	Title of the Article / Chapter the Portion Is From	Oxide-ion and proton conducting electrolyte materials for clean energy applications: structural and mechanistic features.
Editor of Portion(s)	Malavasi, Lorenzo; Fisher, Craig A. J.; Islam, M. Saiful	Author of Portion(s)	Malavasi, Lorenzo; Fisher, Craig A. J.; Islam, M. Saiful
Volume / Edition	39 / ONLINE		
Page or Page Range of Portion	4370	Issue, if Republishing an Article From a Serial	11
		Publication Date of Portion	2010-11-01

Figure 2.1 Helmholtz energy of proton transport of $BaCeO_3$ as a function of the O-O distance and the O-H···O bond length. Reproduced from [74] with permission from Elsevier.

ELSEVIER LICENSE
TERMS AND CONDITIONS

May 29, 2025

This Agreement between Kehan Huang ("You") and Elsevier ("Elsevier") consists of your license details and the terms and conditions provided by Elsevier and Copyright Clearance Center.

License Number	6038270685629
License date	May 29, 2025
Licensed Content Publisher	Elsevier
Licensed Content Publication	Solid State Ionics
Licensed Content Title	Aspects of the formation and mobility of protonic charge carriers and the stability of perovskite-type oxides
Licensed Content Author	K.D Kreuer
Licensed Content Date	Oct 1, 1999
Licensed Content Volume	125
Licensed Content Issue	1-4
Licensed Content Pages	18
Start Page	285
End Page	302
Type of Use	reuse in a thesis/dissertation
Portion	figures/tables/illustrations
Number of figures/tables/illustrations	1
Format	both print and electronic
Are you the author of this Elsevier article?	No
Will you be translating?	No
Title of new work	PhD thesis: Redox Stability and Ionic Conduction in Donor-Substituted LaNbO4 under Hydrogen Environments
Institution name	Imperial College London
Expected presentation date	Jul 2025
Portions	Figure 2.1
The Requesting Person / Organization to Appear on the License	Kehan Huang
Requestor Location	Mr. Kehan Huang Imperial College London London, SW7 2AZ United Kingdom
Publisher Tax ID	GB 494 6272 12
Total	**0.00 GBP**
Terms and Conditions	

Figure 2.2 Proton migration pathways and their energy barriers in (a) Y-Zr-Y configuration and (b) Y-Zr-Zr configuration. Reproduced from [86] with permission from Springer Nature.

SPRINGER NATURE LICENSE
TERMS AND CONDITIONS

May 19, 2025

This Agreement between Kehan Huang ("You") and Springer Nature ("Springer Nature") consists of your license details and the terms and conditions provided by Springer Nature and Copyright Clearance Center.

License Number	5987110067430
License date	Mar 13, 2025
Licensed Content Publisher	Springer Nature
Licensed Content Publication	Nature Materials
Licensed Content Title	Nanoscale percolation in doped BaZrO3 for high proton mobility
Licensed Content Author	Fabian M. Draber et al
Licensed Content Date	Dec 23, 2019
Type of Use	Thesis/Dissertation
Requestor type	academic/university or research institute
Format	print and electronic
Portion	figures/tables/illustrations
Number of figures/tables/illustrations	1
Would you like a high resolution image with your order?	no
Will you be translating?	no
Circulation/distribution	1 - 29
Author of this Springer Nature content	no
Title of new work	PhD thesis: Redox Stability and Ionic Conduction in Donor-Substituted LaNbO4 under Hydrogen Environments
Institution name	Imperial College London
Expected presentation date	Jul 2025
Portions	Figure 2.2
The Requesting Person / Organization to Appear on the License	Kehan Huang
Requestor Location	Mr. Kehan Huang Imperial College London London, SW7 2AZ United Kingdom
Order reference number	86
Billing Type	Invoice
Billing Address	Imperial College London Imperial College London London, United Kingdom SW7 2AZ
Total	**0.00 GBP**

Figure 2.3 (a) Polycrystalline perovskite morphology, (b) enlarged grain boundary area, and (c) detailed schematic diagram. Reproduced from [94] with permission from American Chemical Society.

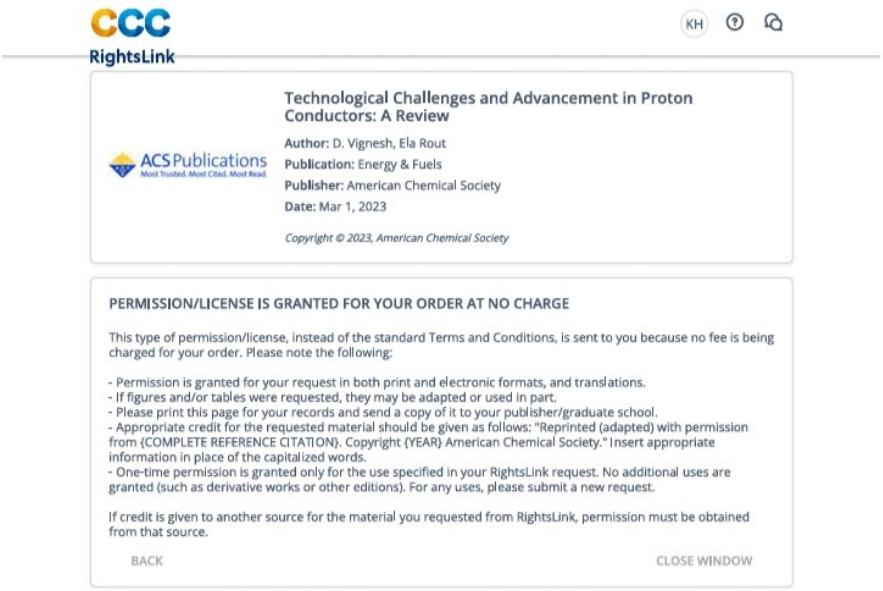
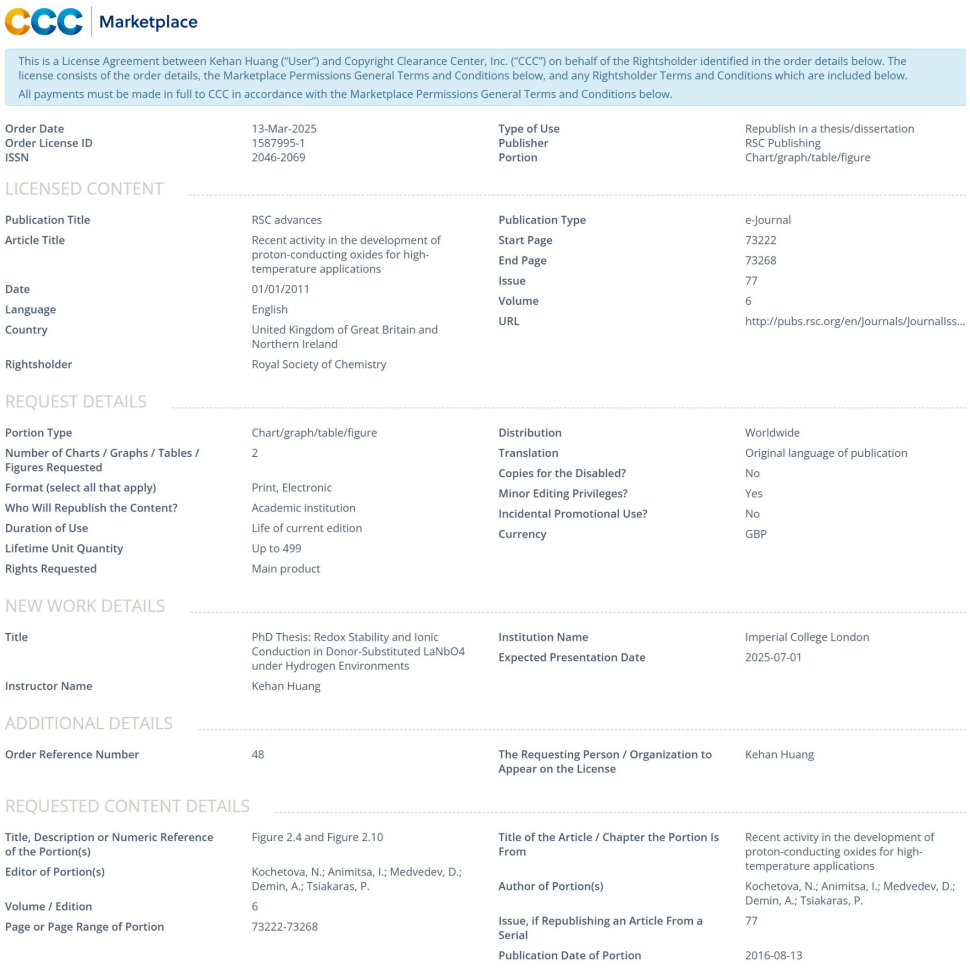


Figure 2.4 The proton-conducting mechanism in the ABO_3 perovskite structure. Reproduced from [48] with permission from Royal Society of Chemistry.

Figure 2.10 Linear thermal expansion of pristine $LaNbO_4$ and its corresponding monoclinic and tetragonal phase structures. Red and green balls and blue polyhedra denote O^{2-}, La^{3+} and NbO_4 tetrahedra, respectively. Reproduced from [48, 49, 135] with permission from Royal Society of Chemistry.



CCC Marketplace

This is a License Agreement between Kehan Huang ("User") and Copyright Clearance Center, Inc. ("CCC") on behalf of the Rightsholder identified in the order details below. The license consists of the order details, the Marketplace Permissions General Terms and Conditions below, and any Rightsholder Terms and Conditions which are included below.

All payments must be made in full to CCC in accordance with the Marketplace Permissions General Terms and Conditions below.

Order Date	13-Mar-2025	Type of Use	Republish in a thesis/dissertation
Order License ID	1587995-1	Publisher	RSC Publishing
ISSN	2046-2069	Portion	Chart/graph/table/figure

LICENSED CONTENT

Publication Title	RSC advances	Publication Type	e-Journal
Article Title	Recent activity in the development of proton-conducting oxides for high-temperature applications	Start Page	73222
		End Page	73268
Date	01/01/2011	Issue	77
Language	English	Volume	6
Country	United Kingdom of Great Britain and Northern Ireland	URL	http://pubs.rsc.org/en/Journals/JournalIss...
Rightsholder	Royal Society of Chemistry		

REQUEST DETAILS

Portion Type	Chart/graph/table/figure	Distribution	Worldwide
Number of Charts / Graphs / Tables / Figures Requested	2	Translation	Original language of publication
		Copies for the Disabled?	No
Format (select all that apply)	Print, Electronic	Minor Editing Privileges?	Yes
Who Will Republish the Content?	Academic institution	Incidental Promotional Use?	No
Duration of Use	Life of current edition	Currency	GBP
Lifetime Unit Quantity	Up to 499		
Rights Requested	Main product		

NEW WORK DETAILS

Title	PhD Thesis: Redox Stability and Ionic Conduction in Donor-Substituted LaNbO4 under Hydrogen Environments	Institution Name	Imperial College London
		Expected Presentation Date	2025-07-01
Instructor Name	Kehan Huang		

ADDITIONAL DETAILS

Order Reference Number	48	The Requesting Person / Organization to Appear on the License	Kehan Huang

REQUESTED CONTENT DETAILS

Title, Description or Numeric Reference of the Portion(s)	Figure 2.4 and Figure 2.10	Title of the Article / Chapter the Portion Is From	Recent activity in the development of proton-conducting oxides for high-temperature applications
Editor of Portion(s)	Kochetova, N.; Animitsa, I.; Medvedev, D.; Demin, A.; Tsiakaras, P.	Author of Portion(s)	Kochetova, N.; Animitsa, I.; Medvedev, D.; Demin, A.; Tsiakaras, P.
Volume / Edition	6		
Page or Page Range of Portion	73222-73268	Issue, if Republishing an Article From a Serial	77
		Publication Date of Portion	2016-08-13

Figure 2.6 Comparison of ionic conductivity of a series of solid oxide electrolytes. The solid line shows the protonic conductivity of the proton-conducting oxides, while the dashed line indicates the oxygen ionic conductivity of the comparative oxides. The arrow shows the optimising direction of solid oxide electrolytes, *i.e.*, higher ionic conductivity at lower working temperatures. Reproduced from [123] with permission from Springer Nature.

SPRINGER NATURE LICENSE
TERMS AND CONDITIONS

May 19, 2025

This Agreement between Kehan Huang ("You") and Springer Nature ("Springer Nature") consists of your license details and the terms and conditions provided by Springer Nature and Copyright Clearance Center.

License Number	5987110598618
License date	Mar 13, 2025
Licensed Content Publisher	Springer Nature
Licensed Content Publication	Nature Energy
Licensed Content Title	Enhanced low-temperature proton conductivity in hydrogen-intercalated brownmillerite oxide
Licensed Content Author	Nianpeng Lu et al
Licensed Content Date	Dec 8, 2022
Type of Use	Thesis/Dissertation
Requestor type	academic/university or research institute
Format	print and electronic
Portion	figures/tables/illustrations
Number of figures/tables/illustrations	1
Would you like a high resolution image with your order?	no
Will you be translating?	no
Circulation/distribution	1 - 29
Author of this Springer Nature content	no
Title of new work	PhD thesis: Redox Stability and Ionic Conduction in Donor-Substituted LaNbO4 under Hydrogen Environments
Institution name	Imperial College London
Expected presentation date	Jul 2025
Portions	Figure 2.6
The Requesting Person / Organization to Appear on the License	Kehan Huang
Requestor Location	Mr. Kehan Huang Imperial College London London, SW7 2AZ United Kingdom
Order reference number	123
Billing Type	Invoice
Billing Address	Imperial College London Imperial College London London, United Kingdom SW7 2AZ
Total	**0.00 GBP**

Figure 2.8 Distorted NbO_6 octahedra (left) possesses four short Nb-O bonds similar to NbO_4 tetrahedra (middle) and two long Nb-O bonds, forming a corner-sharing configuration along c axis. Grey and green balls and dark green polyhedra denote O^{2-}, La^{3+} and NbO_4/NbO_6 polyhedra, respectively. Reproduced from [131] with permission from Elsevier.

ELSEVIER LICENSE
TERMS AND CONDITIONS

May 19, 2025

This Agreement between Kehan Huang ("You") and Elsevier ("Elsevier") consists of your license details and the terms and conditions provided by Elsevier and Copyright Clearance Center.

License Number	5987120607990
License date	Mar 13, 2025
Licensed Content Publisher	Elsevier
Licensed Content Publication	Journal of Solid State Chemistry
Licensed Content Title	Studies of the fergusonite to scheelite phase transition in LnNbO4 orthoniobates
Licensed Content Author	Shamanthini William Arulnesan,Paula Kayser,Justin A. Kimpton,Brendan J. Kennedy
Licensed Content Date	Sep 1, 2019
Licensed Content Volume	277
Licensed Content Issue	n/a
Licensed Content Pages	11
Start Page	229
End Page	239
Type of Use	reuse in a thesis/dissertation
Portion	figures/tables/illustrations
Number of figures/tables/illustrations	1
Format	both print and electronic
Are you the author of this Elsevier article?	No
Will you be translating?	No
Title of new work	PhD thesis: Redox Stability and Ionic Conduction in Donor-Substituted LaNbO4 under Hydrogen Environments
Institution name	Imperial College London
Expected presentation date	Jul 2025
Portions	Figure 2.8
The Requesting Person / Organization to Appear on the License	Kehan Huang
Requestor Location	Mr. Kehan Huang Imperial College London London, SW7 2AZ United Kingdom
Order reference number	131
Publisher Tax ID	GB 494 6272 12
Total	**0.00 GBP**

Figure 2.9 Proton transport paths 1-4 in (a) t-$LaNbO_4$ and 1′-5′ in (b) m-$LaNbO_4$ (0 K). The green balls and green polyhedra denote La^{3+} cations and NbO_4 tetrahedra, respectively, while the black, white and grey balls denote the stable proton sites in both phases. The layer distance ratio between O1 and O2 in m-$LaNbO_4$ is 3:2. Reproduced from [133] with permission from Royal Society of Chemistry.

CCC Marketplace

This is a License Agreement between Kehan Huang ("User") and Copyright Clearance Center, Inc. ("CCC") on behalf of the Rightsholder identified in the order details below. The license consists of the order details, the Marketplace Permissions General Terms and Conditions below, and any Rightsholder Terms and Conditions which are included below.
All payments must be made in full to CCC in accordance with the Marketplace Permissions General Terms and Conditions below.

Order Date	13-Mar-2025	Type of Use	Republish in a thesis/dissertation
Order License ID	1588024-1	Publisher	ROYAL SOCIETY OF CHEMISTRY
ISSN	1463-9084	Portion	Chart/graph/table/figure

LICENSED CONTENT

Publication Title	Physical chemistry chemical physics	Rightsholder	Royal Society of Chemistry
Article Title	Proton mobility through a second order phase transition: theoretical and experimental study of LaNbO4.	Publication Type	e-Journal
		Start Page	10313
Author / Editor	Royal Society of Chemistry (Great Britain)	Issue	35
Date	01/01/1999	Volume	12
Language	English	URL	http://firstsearch.oclc.org/journal=1463-9...
Country	United Kingdom of Great Britain and Northern Ireland		

REQUEST DETAILS

Portion Type	Chart/graph/table/figure	Distribution	Worldwide
Number of Charts / Graphs / Tables / Figures Requested	1	Translation	Original language of publication
		Copies for the Disabled?	No
Format (select all that apply)	Print, Electronic	Minor Editing Privileges?	Yes
Who Will Republish the Content?	Academic institution	Incidental Promotional Use?	No
Duration of Use	Life of current edition	Currency	GBP
Lifetime Unit Quantity	Up to 499		
Rights Requested	Main product		

NEW WORK DETAILS

Title	PhD Thesis: Redox Stability and Ionic Conduction in Donor-Substituted LaNbO4 under Hydrogen Environments	Institution Name	Imperial College London
		Expected Presentation Date	2025-07-01
Instructor Name	Kehan Huang		

ADDITIONAL DETAILS

Order Reference Number	133	The Requesting Person / Organization to Appear on the License	Kehan Huang

REQUESTED CONTENT DETAILS

Title, Description or Numeric Reference of the Portion(s)	Figure 2.9	Title of the Article / Chapter the Portion Is From	Proton mobility through a second order phase transition: theoretical and experimental study of LaNbO4.
Editor of Portion(s)	Fjeld, Harald; Toyoura, Kazuaki; Haugsrud, Reidar; Norby, Truls	Author of Portion(s)	Fjeld, Harald; Toyoura, Kazuaki; Haugsrud, Reidar; Norby, Truls
Volume / Edition	12		
Page or Page Range of Portion	10313	Issue, if Republishing an Article From a Serial	35
		Publication Date of Portion	2010-09-21

Figure 2.11(a) Phase diagrams of (a) LNW and (b) LNMo. Both phases were evaluated via the *in-situ* X-ray powder diffraction (XRD) technique. Two temperature points extrapolated from dilatometry analysis are marked as "×" on the phase diagram of LNW. Reproduced from [151] with permission from American Chemical Society, and from [152] with permission under a Creative Commons Attribution-NonCommercial 3.0 Unported Licence.

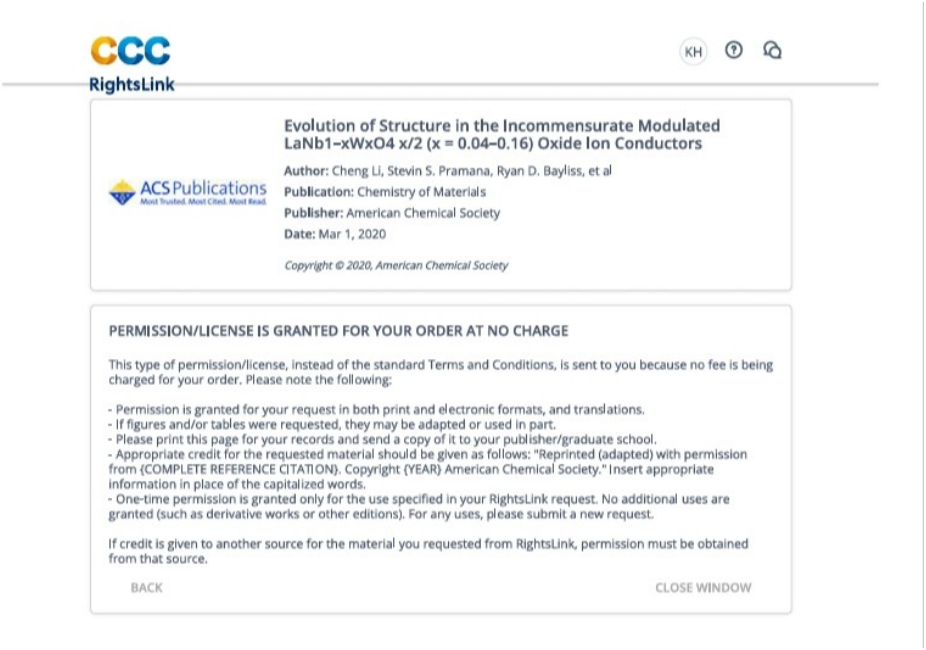


Figure 2.13 (a) XRD pattern of pristine $LaNbO_4$ and LNW08. The insert shows the satellite peaks marked as "asterisk" (*) from the modulated structure. (b) SAED pattern of LNW08 from [010] zone axis. The satellite reflections from the modulated structure are clearly observed. The estimated additional lattice vectors are $\boldsymbol{q_1} = 0.263\boldsymbol{a}^* + 0.106\boldsymbol{c}^*$ and $\boldsymbol{q_2} = 0.082\boldsymbol{a}^* + 0.243\boldsymbol{c}^*$. Reproduced from [138] with permission from Elsevier.

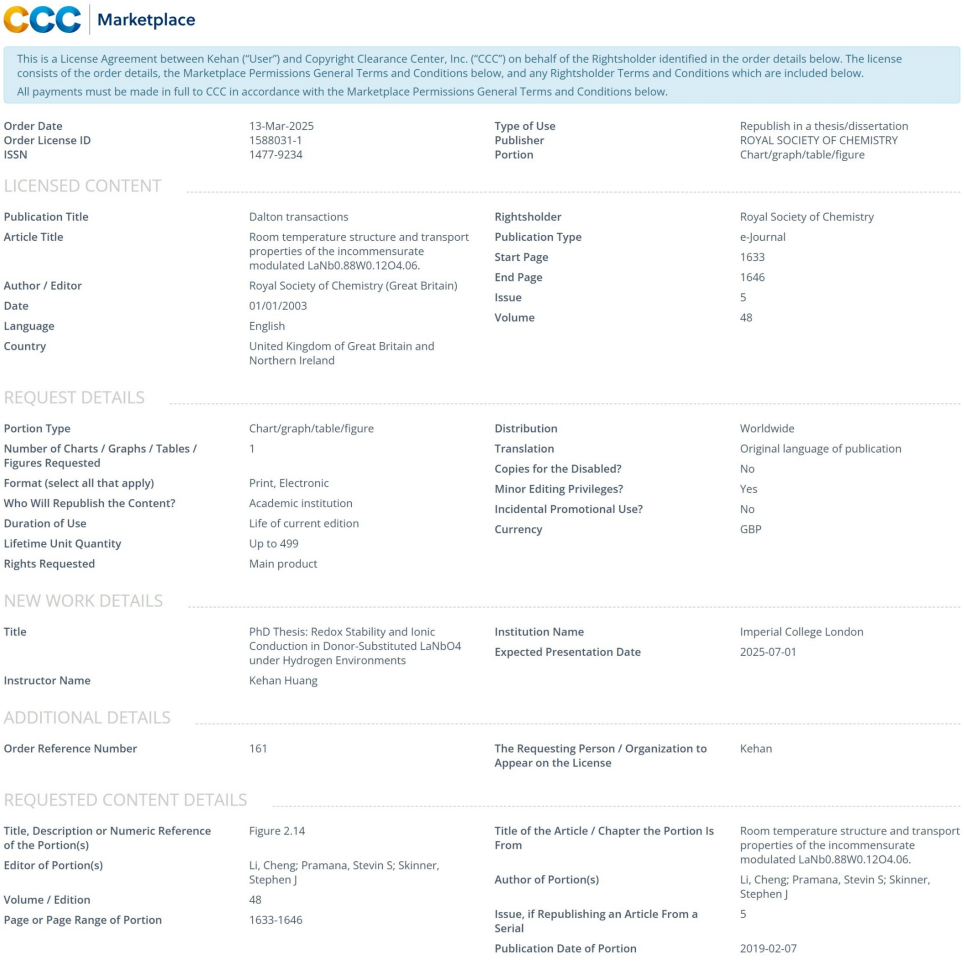
ELSEVIER LICENSE
TERMS AND CONDITIONS

May 19, 2025

This Agreement between Kehan Huang ("You") and Elsevier ("Elsevier") consists of your license details and the terms and conditions provided by Elsevier and Copyright Clearance Center.

License Number	5987130606793
License date	Mar 13, 2025
Licensed Content Publisher	Elsevier
Licensed Content Publication	Solid State Ionics
Licensed Content Title	Crystal structure and potential interstitial oxide ion conductivity of LnNbO4 and LnNb0.92 W0.08O4.04 (Ln=La, Pr, Nd)
Licensed Content Author	Cheng Li,Ryan D. Bayliss,Stephen J. Skinner
Licensed Content Date	Sep 1, 2014
Licensed Content Volume	262
Licensed Content Issue	n/a
Licensed Content Pages	6
Start Page	530
End Page	535
Type of Use	reuse in a thesis/dissertation
Portion	figures/tables/illustrations
Number of figures/tables/illustrations	1
Format	both print and electronic
Are you the author of this Elsevier article?	No
Will you be translating?	No
Title of new work	PhD thesis: Redox Stability and Ionic Conduction in Donor-Substituted LaNbO4 under Hydrogen Environments
Institution name	Imperial College London
Expected presentation date	Jul 2025
Portions	Figure 2.13
The Requesting Person / Organization to Appear on the License	Kehan Huang
Requestor Location	Mr. Kehan Huang Imperial College London London, SW7 2AZ United Kingdom
Order reference number	152
Publisher Tax ID	GB 494 6272 12
Total	**0.00 GBP**

Figure 2.14 Total conductivity of LNW with a series of substitution levels (1%, 8%, 12% and 16%) under the ambient condition. The separate solid lines in LNW08 represent the activation energy difference between unmodulated and modulated scheelite structures, while such difference is diminished in LNW16. Reproduced from [161] with permission from Royal Society of Chemistry.



CCC Marketplace

This is a License Agreement between Kehan ("User") and Copyright Clearance Center, Inc. ("CCC") on behalf of the Rightsholder identified in the order details below. The license consists of the order details, the Marketplace Permissions General Terms and Conditions below, and any Rightsholder Terms and Conditions which are included below.

All payments must be made in full to CCC in accordance with the Marketplace Permissions General Terms and Conditions below.

Order Date	13-Mar-2025	Type of Use	Republish in a thesis/dissertation
Order License ID	1588031-1	Publisher	ROYAL SOCIETY OF CHEMISTRY
ISSN	1477-9234	Portion	Chart/graph/table/figure

LICENSED CONTENT

Publication Title	Dalton transactions	Rightsholder	Royal Society of Chemistry
Article Title	Room temperature structure and transport properties of the incommensurate modulated LaNb0.88W0.12O4.06.	Publication Type	e-Journal
		Start Page	1633
Author / Editor	Royal Society of Chemistry (Great Britain)	End Page	1646
Date	01/01/2003	Issue	5
Language	English	Volume	48
Country	United Kingdom of Great Britain and Northern Ireland		

REQUEST DETAILS

Portion Type	Chart/graph/table/figure	Distribution	Worldwide
Number of Charts / Graphs / Tables / Figures Requested	1	Translation	Original language of publication
		Copies for the Disabled?	No
Format (select all that apply)	Print, Electronic	Minor Editing Privileges?	Yes
Who Will Republish the Content?	Academic institution	Incidental Promotional Use?	No
Duration of Use	Life of current edition	Currency	GBP
Lifetime Unit Quantity	Up to 499		
Rights Requested	Main product		

NEW WORK DETAILS

Title	PhD Thesis: Redox Stability and Ionic Conduction in Donor-Substituted LaNbO4 under Hydrogen Environments	Institution Name	Imperial College London
		Expected Presentation Date	2025-07-01
Instructor Name	Kehan Huang		

ADDITIONAL DETAILS

Order Reference Number	161	The Requesting Person / Organization to Appear on the License	Kehan

REQUESTED CONTENT DETAILS

Title, Description or Numeric Reference of the Portion(s)	Figure 2.14	Title of the Article / Chapter the Portion Is From	Room temperature structure and transport properties of the incommensurate modulated LaNb0.88W0.12O4.06.
Editor of Portion(s)	Li, Cheng; Pramana, Stevin S; Skinner, Stephen J	Author of Portion(s)	Li, Cheng; Pramana, Stevin S; Skinner, Stephen J
Volume / Edition	48		
Page or Page Range of Portion	1633-1646	Issue, if Republishing an Article From a Serial	5
		Publication Date of Portion	2019-02-07

Figure 2.16 Two short interstitial oxygen ion transport paths via interstitial mechanism along the *ab* plane, 1 and 3, and one long interstitial oxygen ion transport path via interstitialcy mechanism along the *c* axis, 4. The yellow and black balls represent the stable interstitial oxygen sites, while the blue balls represent the transition interstitial oxygen sites. For simplicity, the interstitialcy path 4 is represented by the blue lines. Path 2 is excluded due to its unfavourable energy barrier. Reproduced from [164] with permission from Royal Society of Chemistry.



CCC Marketplace

This is a License Agreement between Kehan Huang ("User") and Copyright Clearance Center, Inc. ("CCC") on behalf of the Rightsholder identified in the order details below. The license consists of the order details, the Marketplace Permissions General Terms and Conditions below, and any Rightsholder Terms and Conditions which are included below.
All payments must be made in full to CCC in accordance with the Marketplace Permissions General Terms and Conditions below.

Order Date	13-Mar-2025	Type of Use	Republish in a thesis/dissertation
Order License ID	1588033-1	Publisher	Royal Society of Chemistry
ISSN	2050-7496	Portion	Chart/graph/table/figure

LICENSED CONTENT

Publication Title	Journal of materials chemistry. A, Materials for energy and sustainability	Publication Type	e-Journal
Article Title	Oxide-ion conduction via interstitials in scheelite-type LaNbO4: a first-principles study	Start Page	12004
		End Page	12011
		Issue	25
Author / Editor	Royal Society of Chemistry (Great Britain)	Volume	6
Date	01/01/2013	URL	http://pubs.rsc.org/en/journals/journaliss...
Language	English		
Country	United Kingdom of Great Britain and Northern Ireland		
Rightsholder	Royal Society of Chemistry		

REQUEST DETAILS

Portion Type	Chart/graph/table/figure	Distribution	Worldwide
Number of Charts / Graphs / Tables / Figures Requested	1	Translation	Original language of publication
		Copies for the Disabled?	No
Format (select all that apply)	Print, Electronic	Minor Editing Privileges?	Yes
Who Will Republish the Content?	Academic institution	Incidental Promotional Use?	No
Duration of Use	Life of current edition	Currency	GBP
Lifetime Unit Quantity	Up to 499		
Rights Requested	Main product		

NEW WORK DETAILS

Title	PhD Thesis: Redox Stability and Ionic Conduction in Donor-Substituted LaNbO4 under Hydrogen Environments	Institution Name	Imperial College London
		Expected Presentation Date	2025-07-01
Instructor Name	Kehan Huang		

ADDITIONAL DETAILS

Order Reference Number	164	The Requesting Person / Organization to Appear on the License	Kehan Huang

REQUESTED CONTENT DETAILS

Title, Description or Numeric Reference of the Portion(s)	Figure 2.16	Title of the Article / Chapter the Portion Is From	Oxide-ion conduction via interstitials in scheelite-type LaNbO4: a first-principles study
Editor of Portion(s)	Toyoura, Kazuaki; Sakakibara, Yusuke; Yokoi, Tatsuya; Nakamura, Atsutomo; Matsunaga, Katsuyuki	Author of Portion(s)	Toyoura, Kazuaki; Sakakibara, Yusuke; Yokoi, Tatsuya; Nakamura, Atsutomo; Matsunaga, Katsuyuki
Volume / Edition	6		
Page or Page Range of Portion	12004-12011	Issue, if Republishing an Article From a Serial	25
		Publication Date of Portion	2018-01-01

Figure 3.8 (a) Typical Tauc plot of an oxide; (b) Density of states $N(E)$ as a function of energy. Adapted from [204, 205] with permission from John Wiley and Sons.

JOHN WILEY AND SONS LICENSE
TERMS AND CONDITIONS

May 19, 2025

This Agreement between Kehan Huang ("You") and John Wiley and Sons ("John Wiley and Sons") consists of your license details and the terms and conditions provided by John Wiley and Sons and Copyright Clearance Center.

License Number	5987140674777
License date	Mar 13, 2025
Licensed Content Publisher	John Wiley and Sons
Licensed Content Publication	Advanced Functional Materials
Licensed Content Title	Limitations of the Tauc Plot Method
Licensed Content Author	Gerd Bacher, Jennifer Strunk, Malte Behrens, et al
Licensed Content Date	Sep 3, 2023
Licensed Content Volume	33
Licensed Content Issue	47
Licensed Content Pages	19
Type of Use	Dissertation/Thesis
Requestor type	University/Academic
Format	Print and electronic
Portion	Figure/table
Number of figures/tables	1
Will you be translating?	No
Title of new work	PhD thesis: Redox Stability and Ionic Conduction in Donor-Substituted LaNbO4 under Hydrogen Environments
Institution name	Imperial College London
Expected presentation date	Jul 2025
Portions	Figure 3.8
The Requesting Person / Organization to Appear on the License	Kehan Huang
Requestor Location	Mr. Kehan Huang Imperial College London London, SW7 2AZ United Kingdom
Order reference number	205
Publisher Tax ID	EU826007151
Total	**0.00 GBP**

Figure 3.12 Schematic diagram of the bricklayer model. The notation "gb" is short for grain boundary. Adapted from [219] with permission from John Wiley and Sons.

Table 3.2 Capacitance value ranges and their possible corresponding response. Adapted from [219] with permission from John Wiley and Sons.

JOHN WILEY AND SONS LICENSE
TERMS AND CONDITIONS

May 19, 2025

This Agreement between Kehan Huang ("You") and John Wiley and Sons ("John Wiley and Sons") consists of your license details and the terms and conditions provided by John Wiley and Sons and Copyright Clearance Center.

License Number	6032700620294
License date	May 19, 2025
Licensed Content Publisher	John Wiley and Sons
Licensed Content Publication	Advanced Materials
Licensed Content Title	Electroceramics: Characterization by Impedance Spectroscopy
Licensed Content Author	Anthony R. West, Derek C. Sinclair, John T. S. Irvine
Licensed Content Date	Sep 15, 2004
Licensed Content Volume	2
Licensed Content Issue	3
Licensed Content Pages	7
Type of Use	Dissertation/Thesis
Requestor type	University/Academic
Format	Print and electronic
Portion	Figure/table
Number of figures/tables	2
Will you be translating?	No
Title of new work	PhD thesis: Redox Stability and Ionic Conduction in Donor-Substituted LaNbO4 under Hydrogen Environments
Institution name	Imperial College London
Expected presentation date	Jul 2025
Portions	Figure 3.12 and Table 3.2
The Requesting Person / Organization to Appear on the License	Kehan Huang
Requestor Location	Mr. Kehan Huang Imperial College London London, SW7 2AZ United Kingdom
Publisher Tax ID	EU826007151
Total	**0.00 GBP**

Figure 3.14 Schematic comparison of the relative total cross sections of various elements for X-rays and neutrons. Reproduced from [230] with permission from Elsevier.

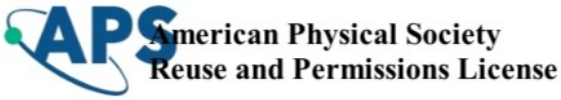
ELSEVIER LICENSE
TERMS AND CONDITIONS

May 19, 2025

This Agreement between Kehan Huang ("You") and Elsevier ("Elsevier") consists of your license details and the terms and conditions provided by Elsevier and Copyright Clearance Center.

License Number	6032700965648
License date	May 19, 2025
Licensed Content Publisher	Elsevier
Licensed Content Publication	Journal of Power Sources
Licensed Content Title	In situ neutron imaging technique for evaluation of water management systems in operating PEM fuel cells
Licensed Content Author	R. Satija,D.L. Jacobson,M. Arif,S.A. Werner
Licensed Content Date	Apr 22, 2004
Licensed Content Volume	129
Licensed Content Issue	2
Licensed Content Pages	8
Start Page	238
End Page	245
Type of Use	reuse in a thesis/dissertation
Portion	figures/tables/illustrations
Number of figures/tables/illustrations	1
Format	both print and electronic
Are you the author of this Elsevier article?	No
Will you be translating?	No
Title of new work	PhD thesis: Redox Stability and Ionic Conduction in Donor-Substituted LaNbO4 under Hydrogen Environments
Institution name	Imperial College London
Expected presentation date	Jul 2025
Portions	Figure 3.14
The Requesting Person / Organization to Appear on the License	Kehan Huang
Requestor Location	Mr. Kehan Huang Imperial College London London, SW7 2AZ United Kingdom
Publisher Tax ID	GB 494 6272 12
Total	**0.00 GBP**

Figure 3.16 Schematic diagram of VESUVIO spectrometer. The foil changers are placed in between the sample and sensors to fix the value of the final energy of the neutrons in the so-called inverted-geometry configuration. Reproduced from [235] with permission from American Physical Society.



19-May-2025

This license agreement between the American Physical Society ("APS") and Kehan Huang ("You") consists of your license details and the terms and conditions provided by the American Physical Society and SciPris.

Licensed Content Information

License Number:	**RNP/25/MAY/091437**
License date:	19-May-2025
DOI:	10.1103/PhysRevB.88.184304
Title:	Mass-selective neutron spectroscopy of lithium hydride and deuteride: Experimental assessment of the harmonic and impulse approximations
Author:	Maciej Krzystyniak et al.
Publication:	Physical Review B
Publisher:	American Physical Society
Cost:	USD $ 0.00

Request Details

Does your reuse require significant modifications: No

Specify intended distribution locations:	Worldwide
Reuse Category:	Reuse in a thesis/dissertation
Requestor Type:	Student
Items for Reuse:	Figures/Tables
Number of Figure/Tables:	1
Figure/Tables Details:	Figure 3.16
Format for Reuse:	Print and Electronic
Total number of print copies:	Up to 1000

Information about New Publication:

University/Publisher:	Imperial College London
Title of dissertation/thesis:	Redox Stability and Ionic Conduction in Donor-Substituted $LaNbO_4$ under Hydrogen Environments
Author(s):	Kehan Huang
Expected completion date:	Jul. 2025

License Requestor Information

Name:	Kehan Huang
Affiliation:	Individual
Email Id:	kehan.huang20@imperial.ac.uk
Country:	United Kingdom

Table 1.1 Summary of fuel cell types. Adapted from [36–38] with permission from Elsevier.

ELSEVIER LICENSE
TERMS AND CONDITIONS

May 19, 2025

This Agreement between Kehan Huang ("You") and Elsevier ("Elsevier") consists of your license details and the terms and conditions provided by Elsevier and Copyright Clearance Center.

License Number	5987091130419
License date	Mar 13, 2025
Licensed Content Publisher	Elsevier
Licensed Content Publication	Electrochimica Acta
Licensed Content Title	Solid oxide fuel cells: fundamental aspects and prospects
Licensed Content Author	Osamu Yamamoto
Licensed Content Date	3 May 2000
Licensed Content Volume	45
Licensed Content Issue	15-16
Licensed Content Pages	13
Start Page	2423
End Page	2435
Type of Use	reuse in a thesis/dissertation
Portion	figures/tables/illustrations
Number of figures/tables/illustrations	1
Format	both print and electronic
Are you the author of this Elsevier article?	No
Will you be translating?	No
Title of new work	PhD thesis: Redox Stability and Ionic Conduction in Donor-Substituted LaNbO4 under Hydrogen Environments
Institution name	Imperial College London
Expected presentation date	Jul 2025
Portions	Table 1.1
The Requesting Person / Organization to Appear on the License	Kehan Huang
Requestor Location	Mr. Kehan Huang Imperial College London London, SW7 2AZ United Kingdom
Order reference number	8
Publisher Tax ID	GB 494 6272 12
Total	**0.00 GBP**